Precision predictions for vector-boson scattering

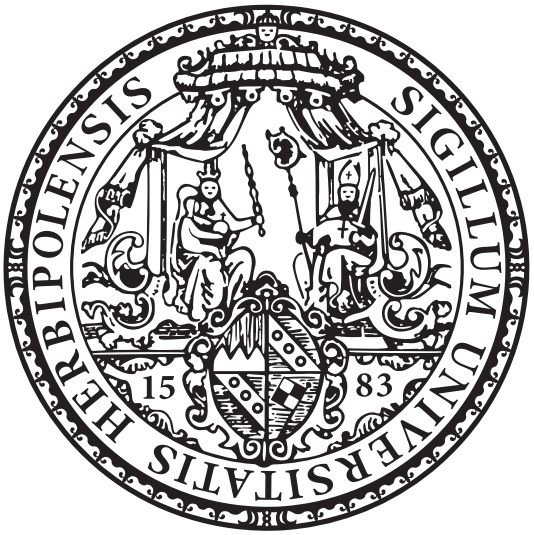

Dissertation zur Erlangung des naturwissenschaftlichen Doktorgrades
an der Fakultät für Physik und Astronomie
der Julius-Maximilians-Universität Würzburg

vorgelegt
von

Christoph Haitz
aus Schaffhausen, Schweiz

Würzburg, im April 2025

Eingereicht bei der Fakultät für Physik und Astronomie am 15.04.2025

Gutachter der Dissertation

1. Gutachter: Prof. Dr. Ansgar Denner
2. Gutachter: Prof. Dr. Raimund Ströhmer
3. Gutachter: _____

Prüfer des öffentlichen Promotionskolloquiums

1. Prüfer: Prof. Dr. Ansgar Denner
2. Prüfer: Prof. Dr. Raimund Ströhmer
3. Prüfer: Prof. Dr. Karl Mannheim
4. Prüfer: _____
5. Prüfer: _____

Tag des öffentlichen Promotionskolloquiums 18.07.2025
Doktorurkunde ausgehändigt am _____

Abstract

This thesis investigates the polarisation states of intermediate vector bosons in di-boson processes at the Large Hadron Collider (LHC). Of particular importance are vector-boson scattering (VBS) processes, because VBS processes with longitudinally polarised bosons are very sensitive to unitarity cancellations. This allows for precise tests of the Standard Model. The Monte Carlo code BBMC was extended to compute processes with polarised vector bosons at next-to-leading-order (NLO) quantum chromodynamics (QCD) and electroweak (EW) accuracy using the double-pole approximation (DPA). This included the implementation of the local and integrated massive-resonance counterterms needed to compute the EW real-emission corrections in the presence of charged resonances. This has been the missing part in the computation of NLO EW accurate predictions for polarised processes with electrically charged W bosons in the DPA.

As vector-boson production processes are simpler than VBS processes they were studied first, in order to test the implementation of the DPA formalism. The production of a Z and W^+ boson with semi-leptonic decay was the first process calculated. The computation was done including the NLO QCD corrections. The second process that was studied was W^+W^- production with purely leptonic decays including the NLO EW corrections. To compute this process some of the massive-resonance counterterms had to be used. Then the focus was put on the main goal, polarised VBS. Therefore, the third process studied was the scattering of two polarised W^+ bosons at NLO QCD and EW accuracy with both bosons decaying into different flavour leptons. In VBS all of the massive-resonance counterterms are needed to subtract the infrared (IR) divergences.

For the three processes both the integrated and differential cross-sections were calculated. The computations were done with both bosons unpolarised and all combinations of transversely and longitudinally polarised bosons. For all the studied processes, measurable LHC observables were found that are sensitive to the polarisation of the resonant vector bosons. A selection of the found observables is: the decay angle of the positron for ZW^+ production, the angular separation of positron and muon for W^+W^- production and the ratio of transverse momenta of the subleading and leading charged lepton for W^+W^+ scattering. These observables are well suited to be used for polarised templates to distinguish the polarisation states in measurements.

The inclusion of NLO corrections is very important since their effects can differ considerably between polarisation states. Particularly large differences were found for ZW^+ production where the NLO QCD corrections range from -5% to $+200\%$ depending on the polarisation state. For W^+W^- production the NLO EW corrections extend from -0.2% to -2.5% and in W^+W^+ scattering the NLO EW+QCD corrections reach from -15% to -21%. Furthermore, the NLO corrections have been shown to change the normalised shapes of some differential cross-sections.

Kurzzusammenfassung

Diese Dissertation behandelt die Polarisationszustände virtueller Vektorbosonen in Vektorbosonpaarproduktions- und Vektorbosonstreuprozessen am LHC. Hierbei sind Vektorbosonstreuprozesse von besonderer Wichtigkeit, denn die Streuung longitudinal polarisierter Vektorbosonen ist besonders empfindlich für die Unitaritätskompensationen. Diese ermöglichen die Untersuchung des Standardmodells mit hoher Präzision. Der Monte Carlo Code BBMC wurde erweitert, um polarisierte Prozesse in der Doppelpolnäherung mit Vektorbosonen bis zur nächstführenden Ordnung zu berechnen. Dies beinhaltete die Implementierung der reellen und integrierten massiven Resonanzgegenterme, die gebraucht werden, um die elektroschwachen Korrekturen durch reelle Emissionen in der Anwesenheit von geladenen Resonanzen zu berechnen. Das war Vorrausetzung, um Vorhersagen für Prozesse mit polarisierten Vektorbosonen machen zu können, die bis zur nächstführenden elektroschwachen Ordnung akkurat sind.

Da Vektorbosonpaarproduktionsprozesse einfacher als Vektorbosonstreuprozesse sind, wurden sie zuerst untersucht, um die Implementierung der Doppelpolnäherung zu testen. Zuerst wurde die Produktion eines Z und W^+ Bosons mit semileptonischem Zerfall berechnet. In der Berechnung wurden die nächstführenden QCD Korrekturen berücksichtigt. Der zweite untersuchte Prozess war die W^+W^- Paarproduktion, bei der beide Bosonen leptonisch zerfallen. Für diesen Prozess wurden einige der massiven Resonanzgegenterme benötigt. Als nächstes wurde der Fokus auf das Hauptziel, polarisierte Vektorbosonstreuung, gelegt. Hierfür wurde als dritter Prozess die Streuung von zwei W^+ Bosonen bis zur nächstführenden QCD und elektroschwachen Ordnung berechnet. In dem untersuchten Prozess zerfallen beide Bosonen in Leptonen unterschiedlicher Familien. In Vektorbosonstreuprozessen werden alle massiven Resonanzgegenterme benötigt.

Für die drei analysierten Prozesse wurden die integrierten und die differenziellen Wirkungsquerschnitte ermittelt. Die Berechnungen wurden für den unpolarisierten Prozess und für alle Kombinationen von transversaler und longitudinaler Polarisation durchgeführt. Für alle drei Prozesse wurden messbare LHC Observablen gefunden, die sensitiv auf die Polarisation der Vektorbosonen sind. Eine Auswahl der gefunden Observablen ist: der Zerfallswinkel des Positrons für ZW^+ Produktion, der Winkel zwischen dem Positron und dem Muon für W^+W^- Produktion und das Verhältnis der transversalen Impulse des nächstführenden und führenden geladenen Leptons für W^+W^+ Streuung. Mit diesen Observablen können Templates erstellt werden. In Messungen kann mit ihnen zwischen den Polarisationszuständen unterschieden werden.

Das Miteinbeziehen der nächstführenden Korrekturen ist entscheidend, da sie sich sehr unterschiedlich auf die Polarisationszustände auswirken können. Besonders große Unterschiede wurden für die ZW^+ Produktion gefunden. Die relativen nächstführenden QCD Korrekturen sind je nach Polarisationszustand -5% bis $+200\%$. Die elektroschwachen Korrekturen

zur W^+W^- Produktion reichen von -0.2% bis -2.5%. Die W^+W^+ Streuung erhält eine -15% bis -21% Korrektur von der nächstführenden elektroschwachen und QCD Ordnung. Insbesondere können die Korrekturen auch die Form der differenziellen Wirkungsquerschnitte ändern.

Contents

Chapter 1

Introduction

1.1 Standard Model

The Standard Model of particle physics is the most successful model to describe the interactions of particles at very small distances. In its form today it encompasses the electroweak (EW) theory and quantum chromodynamics (QCD). To get to the well known form of the Standard Model, prominently displayed on the European Organization for Nuclear Research (CERN) coffee mug, much work by many great physicists was needed.

The construction of the Standard Model started with the formulation of quantum electrodynamics (QED) [1–3] in the late 1920s. This allowed for a consistent explanation of the emission and absorption of photons off and by electrons. This was the first interacting quantum theory that included special relativity that could be tested in nature. In the non-relativistic theory of atoms, giving electrons a spin degree of freedom was needed to explain why two electrons could occupy the same energy state. However, it lacked a fundamental motivation for the existence of spin. In a relativistic quantum theory the spin is a consequence of particle states transforming in unitary representations of the Poincaré group. In QED electrons are Dirac fermions and have four intrinsic degrees of freedom: two for the spin states and two for the antiparticle states. The corresponding antiparticle of the electron, the positron, was discovered in cosmic rays [4] soon after.

Despite the initial success of QED in explaining many phenomena in nature, when attempting to compute higher perturbative orders divergences appeared rendering the predictions unusable. In higher-order corrections loop diagrams are present. In loop diagrams not all momenta are fixed by the external momenta and four-momentum conservation. Instead, an integration over all loop momenta is performed. These integrals in general do not have well-defined solutions as they can be divergent. There are two types of divergences that can be present: ultraviolet (UV) divergences and infrared (IR) divergences. The UV divergences stem from an insufficiently fast fall-off of the integrand in the limit where the loop momentum approaches infinity. The IR divergences originate from the denominator of a loop propagator vanishing when the loop momentum is zero or collinear to one of the external legs of the loop. The treatment of the divergences boils down to the in principle trivial statement that only physical observables, quantities that are measured in experiments, have to be finite. The loop integrals are not physical observables. Therefore, as long as the final result of the prediction is finite, the divergences in intermediate steps of the calculation pose no fundamental problem. To deal with the IR divergences it has to be taken into account

that not all final-state particles are observable as separated tracks or energy deposits in the detector. Any detector will have an energy threshold below which it will not register a particle and a separation threshold below which multiple particles are detected as one. The mere existence of these fundamental detector limitations requires the inclusion of processes with degenerate final states. In practice this means that processes with additional massless final-state particles that can produce the same signal in the detector have to be considered. These are called the real-emission contributions. Like the contributions from loops they also feature IR singularities. However, they do not stem from the integration over unconstrained momenta in loops, instead they arise from the phase-space integration over the momenta of the additional final-state particles. When a final-state particle is produced with vanishing momentum or in the same direction as another particle internal propagators can become singular. For QED the IR divergences of the loop integrals and the real-emission processes are shown to cancel order by order [5]. The cancellation of the IR divergences in more general theories is shown by the Kinoshita-Lee-Nauenberg (KLN) theorem [6, 7]. When both the virtual and real-emission contributions are included the final result is free of IR divergences. The UV divergences have to be treated in a different manner. Renormalisation allows for the removal of the UV divergences by shifting them to the unobservable bare parameters. The predictions of observables are then only dependent on measured quantities, which are by definition finite and not on unobservable bare quantities. This keeps the predictions of measurable observables finite. With the singularities removed also loop effects such as the Lamb shift could be measured [8].

The inclusion of the weak and the strong force was accompanied by additional conceptional challenges. By the 1950s a large number of particles that are today classified as hadrons had been discovered in collider and cosmic ray experiments. This diverse assortment of particles was called the particle zoo. The formulation of the quark model in 1964 [9, 10] allowed for the disentanglement of all the discovered particles. In the quark model the discovered hadrons are bound states of quarks. Among the discovered hadrons were also spin three half particles like the Δ^{++} [11] that are symmetric in all quantum numbers known at that time. The contradiction of having a fermionic half integer spin particle that is symmetric could be resolved by introducing a colour quantum number. This sparked the formulation of QCD as a local $SU(3)_{\text{colour}}$ gauge theory. QCD predicts a gauge boson, the gluon, that mediates the strong interaction. The theory was backed up when experiments at Positron-Electron-Tandem-Ring Accelerator (PETRA) found three-jet events that confirmed the existence of the gluon [12–15].

The last building block of the Standard Model came with the unification of the electromagnetic and the weak interaction to the EW part of the Standard Model. The first model of the weak interaction, the Fermi theory [16], was very successful in describing beta decays and the decay of the muon. But the theory was soon found to be non-renormalisable meaning it could only be used as an effective theory at low energies. To make predictions that remain valid at high energies a new theory was needed. The Glashow-Salam-Weinberg (GSW) model [17–20] with the local symmetry $SU(2) \otimes U(1)$ seemed to be a promising candidate. In gauge theories the invariance under the chosen symmetry forbids explicit mass terms for the vector bosons. The GSW model circumvents this problem by introducing a spontaneous breaking of the gauge symmetry [21–24]. This added an additional scalar particle, later named the Higgs boson, that through its interaction with the gauge bosons gives them their mass. The predicted heavy gauge bosons were discovered in 1983 at Super Proton Syn-

chrotron (SPS) experiments (W boson [25, 26], Z boson [27, 28]). Finding the scalar boson proved more difficult as its potential mass range was much less constrained by existing measurements and theoretical considerations. In 2012 first indications of the Higgs boson were discovered at the Large Hadron Collider (LHC) in Geneva by the A Toroidal LHC Apparatus (ATLAS) [29] and Compact Muon Solenoid (CMS) collaborations [30] completing the particle set of the Standard Model.

Today's Standard Model is a quantum field theory (QFT) containing fermion fields, vector-boson fields and one scalar boson field. It has Lorentz symmetry making it a relativistic QFT. The interactions are described as gauge interactions with the symmetry group

$$SU(3)_{\text{colour}} \otimes SU(2)_{\text{weak isospin}} \otimes U(1)_{\text{hypercharge}} . \tag{1.1}$$

This symmetry is spontaneously broken via the Higgs mechanism.

The Standard Model has given us a theoretical description of many observed phenomena in nature. It has been tested to great precision in many different experimental setups like high-energy collider experiments, cosmic ray experiments, atomic physics and many others. So far it has been confirmed by these experiments; however, the Standard Model cannot describe all phenomena observed in nature. Its first shortcoming is that the Standard Model does not include gravity. In our goal to find a theory of everything a theory that only covers three of the four fundamental forces is only a partial success. So far none of the proposed theories that combine gravity and the Standard Model could be experimentally verified. Furthermore, the Standard Model does not give any explanation for dark-matter phenomena observed in astrophysical measurements. The observed motion of stars in a galaxy cannot be explained by visible objects alone. From extensive astrophysical measurements we can conclude that dark matter cannot be made solely from Standard Model particles. Also the observed phenomenon of dark energy, detected when measuring the rate of expansion of the universe, cannot be explained by the Standard Model. In the most primitive form of the Standard Model the neutrinos are massless which contradicts the findings from neutrino-oscillation experiments. It was found that neutrinos could be measured with a different flavour than the one they were initially created with. This is only permitted if the weak eigenstates in which they are created are different from the mass eigenstates in which they travel long distances. The weak eigenstates and the mass eigenstates can only be different when the neutrinos are massive. Additionally there are many that argue that the Standard Model lacks naturalness as it does not give any reason why the theory input parameters have the values that they have.

The before listed problems make it clear that the Standard Model cannot be the final answer in physics and that some form of extension or an entirely new theory is needed. Today there is no shortage of theories that claim to give explanations to some or all of the shortcomings of the Standard Model previously mentioned. Yet so far there is no clear indication which of these if any are realised in nature. Therefore, it is important to understand where the Standard Model starts to break down. This requires very precise experimental measurements which can be compared to equally precise theoretical predictions of the Standard Model.

1.2 Testing the Standard Model with vector-boson pair-production and vector-boson-scattering processes

There are numerous ways to test the validity of the Standard Model in the field of high-energy physics. The focus here is providing precise predictions for polarised di-boson processes: vector-boson pair production and vector-boson scattering (VBS). In vector-boson pair production final states are studied that can stem from the decay of two intermediate EW vector bosons. The final state of VBS entails particles that can stem from the decay of two intermediate vector bosons and two jets. These processes are well suited to test the Standard Model because of their sensitivity to the exact method of EW spontaneous symmetry breaking. In VBS and to a lesser extent also in vector-boson pair-production processes there are contributions which individually would cause violations to the unitarity of the perturbative S-matrix [31, 32]. These stem from the high-energy behaviour of the polarisation vectors. While the transverse polarisation vectors are constant in the high-energy limit, the longitudinal polarisation vectors grow with the energy. The high-energy behaviour of the transverse and longitudinal polarisation vectors is a general property and is seen in their explicit form used in the performed calculations [33]. The polarisation vector of a vector boson with mass M and four-momentum

$$p = \begin{pmatrix} p_0 \\ \vec{p} \end{pmatrix} = \begin{pmatrix} p_0 \\ p_x \\ p_y \\ p_z \end{pmatrix} \tag{1.2}$$

reads

$$\epsilon_\pm = \frac{1}{\sqrt{2}|\vec{p}|\sqrt{p_x^2+p_y^2}} \begin{pmatrix} 0 \\ \mp p_x p_z + \mathrm{i} p_y |\vec{p}| \\ \mp p_y p_z - \mathrm{i} p_x |\vec{p}| \\ \pm(p_x^2+p_y^2) \end{pmatrix}, \qquad \epsilon_0 = \frac{1}{M|\vec{p}|} \begin{pmatrix} |\vec{p}|^2 \\ p_x p_0 \\ p_y p_0 \\ p_z p_0 \end{pmatrix}. \tag{1.3}$$

The right- and left-handed polarisation vectors are $\epsilon_\pm$ and the longitudinal one is ϵ_0. In the high-energy limit the longitudinal polarisation vector grows with $\mathcal{O}\left(\frac{p_0}{M}\right)$.

Therefore, in principle the amplitude for the scattering of longitudinally polarised vector bosons could grow with the fourth power of the center of mass (CM) energy $\sqrt{s}$. The unitarity of the S-matrix restricts how fast an amplitude can grow with the energy. In the Standard Model at high energies the problematic contributions cancel, keeping the theory perturbative and the S-matrix unitary. These are the unitarity cancellations.

Using the derivation from Ref. [34] it can be shown how perturbation theory breaks down when the amplitude grows with the energy. From the requirement that the time evolution of the quantum states is unitary follows the optical theorem

$$\mathrm{Im}\left(\mathcal{M}\left(A \to A\right)\right) = 2\sqrt{s}|\vec{p}_i| \sum_X \sigma\left(A \to X\right). \tag{1.4}$$

It relates the imaginary part of the forward scattering amplitude of a transition from a two-particle state A to itself to a sum of scattering cross-sections of the transition from the state A to an arbitrary state X. Here $\vec{p}_i$ is the three-momentum of one of the initial states in the CM frame and $\sqrt{s}$ is the CM energy. The optical theorem holds for arbitrary two-particle

states A. To derive a threshold for the amplitude one first uses that the cross-section of any physical process has to be greater or equal to zero; therefore,

$$\mathrm{Im}\left(\mathcal{M}\left(A \to A\right)\right) \geq 2\sqrt{s}|\vec{p_i}|\sigma\left(A \to A\right) . \tag{1.5}$$

Inserting that the cross-section for two particle scattering is the absolute value of the amplitude square times a kinematic factor integrated over the decay phase space gives

$$\mathrm{Im}\left(\mathcal{M}\left(A \to A; \theta = 0\right)\right) \geq 2\sqrt{s}|\vec{p_i}| \int \frac{1}{64\pi^2 s} \left|\mathcal{M}\left(A \to A; \theta\right)\right|^2 d\cos(\theta) d\varphi \,. \tag{1.6}$$

Carrying out the integration over the angle φ results in

$$\mathrm{Im}\left(\mathcal{M}\left(A \to A; \theta = 0\right)\right) \geq \frac{|\vec{p_i}|}{16\pi\sqrt{s}} \int_{-1}^{1} \left|\mathcal{M}\left(A \to A; \theta\right)\right|^2 d\cos(\theta) \,. \tag{1.7}$$

To get a threshold where perturbation theory can be used consistently the amplitude is expanded in a sensible set of functions. Afterwards the integral over $\cos(\theta)$ is performed. This results in a criterion for the expansion coefficients.

A criterion that is very useful for longitudinal VBS is the partial-wave unitarity bound. To derive the partial-wave unitarity bound the amplitude is expanded in Legendre polynomials of $\cos(\theta)$

$$\mathcal{M}\left(A \to A; \theta\right) = 16\pi \sum_{j=0}^{\infty} a_j \left(2j+1\right) P_j\left(\cos(\theta)\right) . \tag{1.8}$$

Using the orthogonality of the Legendre polynomials the integration over $\cos(\theta)$ is performed giving

$$\sum_{j=0}^{\infty} \left(2j+1\right) \mathrm{Im}\left(a_j\right) \geq \frac{2|\vec{p_i}|}{\sqrt{s}} \sum_{j=0}^{\infty} \left(2j+1\right) \left|a_j\right|^2 . \tag{1.9}$$

When considering the scattering of angular-momentum eigenstates the inequality holds for all terms in the series individually [35] giving

$$\mathrm{Im}\left(a_j\right) \geq \frac{2|\vec{p_i}|}{\sqrt{s}} \left|a_j\right|^2 . \tag{1.10}$$

In the limit where the process $(A \to X)$ is dominated by elastic scattering $(A \to A)$ the equality is fulfilled; furthermore, taking the limit of large energies $\sqrt{s} = 2|\vec{p_i}|$ holds simplifying the expression to

$$\mathrm{Im}\left(a_j\right) = \left|a_j\right|^2 . \tag{1.11}$$

So far the coefficients a_j are those of the amplitude computed to all orders. To obtain a criterion for the amplitude computed to a fixed order an expansion in a generic coupling constant g

$$a_j = \sum_{k=0}^{\infty} g^{2(k+1)} a_{j,k} \,, \tag{1.12}$$

where k runs over the number of loops in the amplitude, is inserted resulting in

$$\sum_{k=0}^{\infty} g^{2(k+1)} \mathrm{Im}\left(a_{j,k}\right) = \left|\sum_{k=0}^{\infty} g^{2(k+1)} a_{j,k}\right|^2 . \tag{1.13}$$

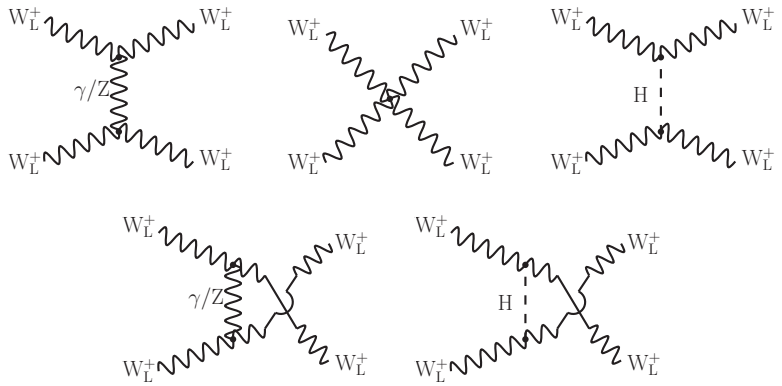

Figure 1.1: Tree-level contributions to the scattering of longitudinally polarised W^+ bosons. Individually all of them violate the unitarity of the S-matrix.

Taking the terms with equal powers in the coupling of the amplitude results in the relation

$$g^4 \operatorname{Im}(a_{j,1}) = g^4 |a_{j,0}|^2 \tag{1.14}$$

for the imaginary part of the one-loop coefficient and the absolute value squared of the tree-level coefficient.

This means that the unitarity of the S-matrix allows one to get an estimate of the potential size of the higher-order contributions to the amplitude. Therefore, when the tree-level coefficient is of order one, the coefficient from the loop contribution will also be at least of order one. When this is the case, all terms in the perturbative expansion are of similar size and the theory is non-perturbative. This results in the condition for the coefficient of the tree-level amplitude

$$|a_{j,0}| \leq 1\,. \tag{1.15}$$

This relation restricts the possible range of coefficients in a unitary theory where perturbation theory is valid. This is only a rough bound where perturbation theory definitely breaks down, as already a too slow fall-off of the higher-order terms prevents convergence. By computing the scattering amplitude for the processes of interest, here the scattering of longitudinally polarised vector bosons, with pertubation theory and expanding the result in Legendre polynomials an explicit kinematic bound can be derived. Having an amplitude that grows with the CM energy will lead to an energy threshold. When the perturbative amplitude is beyond the bound given by the unitarity of the S-matrix, perturbation theory breaks down and the perturbatively computed amplitude is wrong.

For longitudinal W^+W^+ scattering the problematic contributions are depicted in Figure 1.1. For same-sign W^+ scattering

$$W_L^+(p_1) + W_L^+(p_2) \to W_L^+(p_3) + W_L^+(p_4) \tag{1.16}$$

the momenta and polarisation vectors can be written as

$$\begin{aligned} p_1 &= \frac{1}{2}\begin{pmatrix} \sqrt{s} \\ \sqrt{s-4M_{\mathrm{W}}^2} \\ 0 \\ 0 \end{pmatrix}, & p_2 &= \frac{1}{2}\begin{pmatrix} \sqrt{s} \\ -\sqrt{s-4M_{\mathrm{W}}^2} \\ 0 \\ 0 \end{pmatrix}, \\ p_3 &= \frac{1}{2}\begin{pmatrix} \sqrt{s} \\ \cos(\theta)\sqrt{s-4M_{\mathrm{W}}^2} \\ 0 \\ \sin(\theta)\sqrt{s-4M_{\mathrm{W}}^2} \end{pmatrix}, & p_4 &= \frac{1}{2}\begin{pmatrix} \sqrt{s} \\ -\cos(\theta)\sqrt{s-4M_{\mathrm{W}}^2} \\ 0 \\ -\sin(\theta)\sqrt{s-4M_{\mathrm{W}}^2} \end{pmatrix} \end{aligned} \tag{1.17}$$

and

$$\begin{aligned} \epsilon_0(p_1) &= \frac{1}{2M_{\mathrm{W}}}\begin{pmatrix} \sqrt{s-4M_{\mathrm{W}}^2} \\ \sqrt{s} \\ 0 \\ 0 \end{pmatrix}, & \epsilon_0(p_2) &= \frac{1}{2M_{\mathrm{W}}}\begin{pmatrix} \sqrt{s-4M_{\mathrm{W}}^2} \\ -\sqrt{s} \\ 0 \\ 0 \end{pmatrix}, \\ \epsilon_0(p_3) &= \frac{1}{2M_{\mathrm{W}}}\begin{pmatrix} \sqrt{s-4M_{\mathrm{W}}^2} \\ \cos(\theta)\sqrt{s} \\ 0 \\ \sin(\theta)\sqrt{s} \end{pmatrix}, & \epsilon_0(p_4) &= \frac{1}{2M_{\mathrm{W}}}\begin{pmatrix} \sqrt{s-4M_{\mathrm{W}}^2} \\ -\cos(\theta)\sqrt{s} \\ 0 \\ -\sin(\theta)\sqrt{s} \end{pmatrix}. \end{aligned} \tag{1.18}$$

Applying the Feynman rules to the diagrams depicted in Figure 1.1 results in the following amplitudes. The t-channel photon- and Z-boson-exchange diagrams give

$$\begin{aligned} \mathcal{M}_1 =& \frac{1}{16M_{\mathrm{W}}^4}\left(\frac{e^2}{(\cos(\theta)-1)\left(4M_{\mathrm{W}}^2-s\right)} + \frac{e^2\cot^2(\vartheta_{\mathrm{W}})}{(\cos(\theta)-1)\left(4M_{\mathrm{W}}^2-s\right)+2M_{\mathrm{Z}}^2}\right) \\ &\times \left(s^2\cos^3(\theta)\left(4M_{\mathrm{W}}^2-s\right) - s\cos^2(\theta)\left(160M_{\mathrm{W}}^4-36M_{\mathrm{W}}^2s+s^2\right)\right. \\ &\quad + \cos(\theta)\left(64M_{\mathrm{W}}^6+112M_{\mathrm{W}}^4s-52M_{\mathrm{W}}^2s^2+5s^3\right) \\ &\quad \left. + 64M_{\mathrm{W}}^6 - 16M_{\mathrm{W}}^4s + 12M_{\mathrm{W}}^2s^2 - 3s^3\right). \end{aligned} \tag{1.19}$$

The quartic-gauge-boson-coupling diagram gives

$$\mathcal{M}_2 = \frac{e^2 s\left(6s - 2s\cos^2(\theta) - 16M_{\mathrm{W}}^2\right)}{16\sin^2(\vartheta_{\mathrm{W}})M_{\mathrm{W}}^4}. \tag{1.20}$$

The t-channel Higgs-exchange diagram gives

$$\mathcal{M}_3 = \frac{e^2\left(s\left(\cos(\theta)-1\right)+4M_{\mathrm{W}}^2\right)^2}{8\sin^2(\vartheta_{\mathrm{W}})M_{\mathrm{W}}^2\left(\left(\cos(\theta)-1\right)\left(4M_{\mathrm{W}}^2-s\right)+2M_{\mathrm{H}}^2\right)}. \tag{1.21}$$

The u-channel photon- and Z-boson-exchange diagrams give

$$\begin{aligned} \mathcal{M}_4 =& \frac{1}{16M_{\mathrm{W}}^4}\left(\frac{e^2}{(\cos(\theta)+1)\left(4M_{\mathrm{W}}^2-s\right)} + \frac{e^2\cot^2(\vartheta_{\mathrm{W}})}{(\cos(\theta)+1)\left(4M_{\mathrm{W}}^2-s\right)-2M_{\mathrm{Z}}^2}\right) \\ &\times \left(s^2\cos^3(\theta)\left(4M_{\mathrm{W}}^2-s\right) + s\cos^2(\theta)\left(160M_{\mathrm{W}}^4-36M_{\mathrm{W}}^2s+s^2\right)\right. \\ &\quad + \cos(\theta)\left(64M_{\mathrm{W}}^6+112M_{\mathrm{W}}^4s-52M_{\mathrm{W}}^2s^2+5s^3\right) \\ &\quad \left. - 64M_{\mathrm{W}}^6 + 16M_{\mathrm{W}}^4s - 12M_{\mathrm{W}}^2s^2 + 3s^3\right). \end{aligned} \tag{1.22}$$

The u-channel Higgs-exchange diagram gives

$$\mathcal{M}_5 = -\frac{e^2\left(s(\cos(\theta)+1)-4M_{\mathrm{W}}^2\right)^2}{8\sin^2(\vartheta_{\mathrm{W}})M_{\mathrm{W}}^2\left((\cos(\theta)+1)\left(4M_{\mathrm{W}}^2-s\right)-2M_{\mathrm{H}}^2\right)}\,. \tag{1.23}$$

As expected, individually these amplitudes grow with the CM energy $\sqrt{s}$. Expanding the expressions for large CM energies ($\sqrt{s} \gg M_{\mathrm{W}}, M_{\mathrm{Z}}, M_{\mathrm{H}}$) results in

$$\begin{aligned}\mathcal{M}_1 = {} & \frac{e^2\left(\cos^2(\theta)+2\cos(\theta)-3\right)s^2}{16\sin^2(\vartheta_{\mathrm{W}})M_{\mathrm{W}}^4} - \frac{2e^2\cos(\theta)s}{M_{\mathrm{W}}^2} \\ & + \frac{e^2\left(3M_{\mathrm{Z}}^2+(M_{\mathrm{Z}}^2-16M_{\mathrm{W}}^2)\cos(\theta)\right)\cos^2(\vartheta_{\mathrm{W}})s}{8\sin^2(\vartheta_{\mathrm{W}})M_{\mathrm{W}}^4} + \mathcal{O}\big(s^0\big)\,,\end{aligned} \tag{1.24}$$

$$\mathcal{M}_2 = -\frac{e^2\left(2\cos^2(\theta)-6\right)s^2}{16\sin^2(\vartheta_{\mathrm{W}})M_{\mathrm{W}}^4} - \frac{e^2 s}{\sin^2(\vartheta_{\mathrm{W}})M_{\mathrm{W}}^2} + \mathcal{O}\big(s^0\big)\,, \tag{1.25}$$

$$\mathcal{M}_3 = -\frac{e^2(\cos(\theta)-1)s}{8\sin^2(\vartheta_{\mathrm{W}})M_{\mathrm{W}}^2} + \mathcal{O}\big(s^0\big)\,, \tag{1.26}$$

$$\begin{aligned}\mathcal{M}_4 = {} & \frac{e^2\left(\cos^2(\theta)-2\cos(\theta)-3\right)s^2}{16\sin^2(\vartheta_{\mathrm{W}})M_{\mathrm{W}}^4} + \frac{2e^2\cos(\theta)s}{M_{\mathrm{W}}^2} \\ & + \frac{e^2\left(3M_{\mathrm{Z}}^2+(16M_{\mathrm{W}}^2-M_{\mathrm{Z}}^2)\cos(\theta)\right)\cos^2(\vartheta_{\mathrm{W}})s}{8\sin^2(\vartheta_{\mathrm{W}})M_{\mathrm{W}}^4} + \mathcal{O}\big(s^0\big)\,,\end{aligned} \tag{1.27}$$

$$\mathcal{M}_5 = \frac{e^2(\cos(\theta)+1)s}{8\sin^2(\vartheta_{\mathrm{W}})M_{\mathrm{W}}^2} + \mathcal{O}\big(s^0\big)\,. \tag{1.28}$$

The amplitudes from the quartic-gauge-boson-coupling and the vector-boson-exchange diagrams grow with $\mathcal{O}(s^2)$ in the high-energy limit. The Higgs-exchange diagrams grow with $\mathcal{O}(s)$. Summing all the diagrams with purely vector-boson exchanges results in

$$\mathcal{M}_1 + \mathcal{M}_2 + \mathcal{M}_4 = -\frac{e^2 s}{4\sin^2(\vartheta_{\mathrm{W}})M_{\mathrm{W}}^2} + \mathcal{O}\big(s^0\big)\,, \tag{1.29}$$

where the relation $M_{\mathrm{W}} = \cos(\vartheta_{\mathrm{W}})M_{\mathrm{Z}}$ was used to simplify the expression. The $\mathcal{O}(s^2)$ terms cancel. This is a consequence of relations between the couplings of the triple- and quartic-gauge-boson vertices, which themselves are required by gauge invariance. Summing the contributions to the amplitude from the t- and u-channel Higgs exchanges gives

$$\mathcal{M}_3 + \mathcal{M}_5 = \frac{e^2 s}{4\sin^2(\vartheta_{\mathrm{W}})^2 M_{\mathrm{W}}^2} + \mathcal{O}\big(s^0\big)\,. \tag{1.30}$$

This is the same expression as Eq. (1.29) up to an opposite overall sign; therefore, in the full Standard Model no problematic terms remain. By using the partial-wave unitarity bound it is possible to get an estimate for the CM energy where a Standard Model without Higgs would become non-perturbative. Taking the $\mathcal{O}(s)$ term and expanding it in Legendre polynomials results in

$$16\pi\sum_{j=0}^{\infty} a_{j,0}\,(2j+1)\,P_j\left(\cos(\theta)\right) = -\frac{e^2 s}{4\sin^2(\vartheta_{\mathrm{W}})M_{\mathrm{W}}^2}\,, \tag{1.31}$$

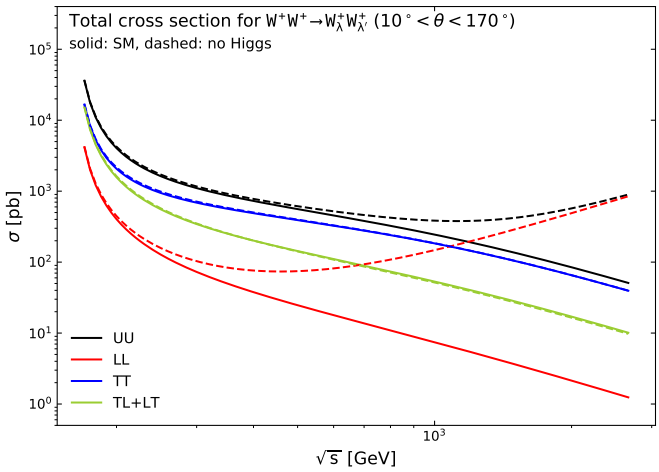

Figure 1.2: Total cross-sections for on-shell $\mathrm{W}^+\mathrm{W}^+ \to \mathrm{W}^+_\lambda \mathrm{W}^+_{\lambda'}$ scattering at tree level, as functions of the di-boson CM energy. The two initial bosons are unpolarised, while the two final ones can be in a longitudinal (L) or transverse (T) polarisation state. Numerical results have been obtained with RECOLA 1 [33, 36] for the complete Standard Model (solid curves) and in the absence of Higgs-mediated diagrams (dashed curves). Figure taken from Ref. [37].

with

$$a_{0,0} = -\frac{1}{16\pi}\frac{e^2}{4\sin^2(\vartheta_\mathrm{W})}\frac{s}{M_\mathrm{W}^2} \quad \text{and} \quad a_{j,0} = 0, \quad j > 0\,. \tag{1.32}$$

The partial-wave unitarity bound $|a_{j,0}| \leq 1$ is then applied to the computed coefficients resulting in the expression

$$\frac{64\pi\sin^2(\vartheta_\mathrm{W})}{e^2} \geq \frac{s}{M_\mathrm{W}^2} \tag{1.33}$$

as a bound on the energy. Plugging in the numerical values leads to that for CM energies $\sqrt{s} \gtrsim 1.8\,\mathrm{TeV}$ the Standard Model without a Higgs bosons is non-perturbative.

The discussion of the unitarity cancellation so far only focussed on the amplitude. The amplitude is not directly measurable; therefore, it is important to understand how the cancellation or the non-cancellation affects physical observables. In Figure 1.2 the cross-section for the scattering of two polarised W^+ bosons is shown. When all Standard Model contributions are included the cross-section decreases with the CM energy as is required by the unitarity of the S-matrix. When the contributions from the Higgs exchange are omitted the cross-sections of the transverse transverse (TT), transverse longitudinal (TL) and longitudinal transverse (LT) states only change slightly. For the longitudinal longitudinal (LL) polarisation state the cross-section increases very fast with the energy. This is caused by the missing diagrams that prevent the cancellation resulting in a cross-section that grows with the energy. As the transverse polarisation vectors feature a constant behaviour in the high-energy limit the scattering of transversely polarised bosons is not sensitive to the unitarity cancellations. The unpolarised cross-section also has an enhancement at high energies as it contains a contribution from both W bosons being longitudinally polarised. In contrast to the LL polarisation state the energy at which the curves with Higgs and without Higgs show significant differences is much higher. As the unpolarised cross-section contains contributions from all polarisation states, the effects of the unitarity cancellations become obscured.

This is particularly apparent in VBS processes where the contribution from the TT state is generally much larger than the one from the LL state.

Since their effects are more apparent, when all vector bosons taking part in the scattering are longitudinally polarised, explicitly searching for the purely longitudinal signal grants additional sensitivity to the unitarity cancellations. Extensions of the EW sector of the Standard Model can affect the unitarity cancellations. In particular, additional particles that couple to the vector bosons or modified couplings of the vector bosons can disrupt the unitarity cancellations. Such extensions of the Standard Model could shift the scale at which the unitarity cancellations happen to much higher energies or prevent the cancellations entirely. When this is the case in processes like VBS, that are very sensitive to the unitarity cancellations, even nominally small deviations from the Standard Model are enhanced in the high-energy regions. This makes the study of polarised VBS processes a very crucial building block in understanding the Standard Model. The sensitivity of vector-boson pair-production processes to the unitarity cancellations and therefore to beyond the Standard Model contributions is smaller than for VBS processes. For vector-boson pair-production processes the diagrams containing a Higgs boson are suppressed by the light quark masses at leading-order (LO). Diagrams with a Higgs exchange between vector bosons only contribute at the one-loop order and higher. However, vector-boson pair-production processes have less final-state particles simplifying their study. This makes them ideal to test both the computational tools needed for the calculation of next-to-leading-order (NLO) corrections and experimental analysis methods needed to measure them.

1.3 Polarisation of virtual particles

In the previous section it has been explained why the study of longitudinally polarised vector bosons is an integral part for testing the Standard Model. However, only the polarisation of stable external particles is defined unambiguously and can be measured in experiments. The polarisation of intermediate virtual particles is not a well defined observable and is not directly experimentally accessible. The W and Z bosons, which are of interest here, have a mean lifetime of $\tau \approx 3 \cdot 10^{-25}$s; therefore, they cannot be treated as stable final-state particles. To define the polarised signal in theoretical calculations a special framework is needed. In this framework the vector bosons have to be treated as if they were on-shell external particles to assign polarisation vectors to them. Furthermore, it has to select, gauge invariantly, the diagrams that contain the intermediated particle studied. One such method is the double-pole approximation (DPA) detailed in Chapter 2. This means that the polarisation states of the vector bosons are only uniquely defined within such a framework using a different method will give a different polarisation definition. While the polarisation cannot be measured experimentally, the polarisation fractions can be extracted by measuring the cross-sections and fitting them to polarisation templates. The polarisation fractions are the ratios at which each polarisation state contributes to the unpolarised signal. The extracted polarisation fractions can then be compared to the theoretical predictions.

The polarised templates are the normalised shapes of differential cross-section distributions. For the creation of polarised templates that can be used for polarisation discrimination it is crucial to find observables for which the shape of the differential cross-section varies greatly with the polarisation. It is important to note that the polarisation templates depend on the exact model they were created with. In particular, it is expected that beyond

the Standard Model physics does not only change the polarisation fractions but also the shapes of the distributions. This means that ideally one should choose observables where the shape of the distribution is insensitive to beyond the Standard Model effects. Templates from such observables can be created in a purely Standard Model computation and can be used to measure the polarisation fractions also in beyond the Standard Model analyses. Generally these are observables which only depend on the decay of one of the studied resonances. It is expected that the new physics only results in very small corrections to the decays. Observables which have a large dependence on the production of the resonances can feature considerable shape changes from the inclusion of beyond the Standard Model physics. Therefore, these observables are only suited to discriminate polarisation states in an analysis that uses the same model as the one that was used to create the templates. Therefore the polarised templates would have to be recomputed when performing an analysis in a different model.

The thesis is structured as follows:

- In Chapter 2 the method, the DPA, that is used to define polarised cross-sections is detailed. In particular, it is shown how to select the polarisation of a virtual particle in a gauge-invariant way.
- In Chapter 3 the treatment of IR divergences present in the NLO EW corrections to DPA processes with charged resonances is discussed. This includes how the needed subtraction counterterms both local and integrated are constructed.
- In Chapter 4 the methods described in Chapter 2 and Chapter 3 are used to compute the polarised cross-section for vector-boson pair-production processes. The particular processes discussed are ZW^+ and W^+W^- production.
- In Chapter 5 the results of the computation of polarised W^+ W^+ scattering are studied.
- Chapter 6 concludes the thesis with some final remarks.

Chapter 2

Double-pole approximation

To compute polarised cross-sections the DPA is used. This chapter explains the details of the DPA applied in the calculations carried out in Chapters 4 and 5. The methods used in the calculations follow the DPA definition from Refs. [37–39].

The DPA used in the computations here is the special case of a general pole approximation (PA) with two resonances. Originally the main use of the PA formalism was as an approximation of a full off-shell process. The PA is a valid approximation in phase-space regions dominated by contributions from s-channel resonances that are close to on-shell. Nominally the PA reproduces the full off-shell process up to terms of $\mathcal{O}\left(\frac{\Gamma_{\text{res}}}{M_{\text{res}}}\right)$, where Γ_{res} and M_{res} are the decay width and the mass of the studied resonances. The main use of the PA is simplifying the computations of higher-order corrections. The PA is particularly useful when the NLO non-resonant effects are smaller than the wanted accuracy of the predictions. When the PA is performed, the contributing loop diagrams that need to be evaluated are considerably simpler compared to the full off-shell computation.

When computing the cross-sections of polarised processes the PA is not used as an approximation but to define the on-shell signal. To compute processes with polarised intermediate particles polarisation vectors need to be assigned to them. This is only possible when said particle is present as an s-channel resonance in all contributing diagrams. For most processes there will be diagrams that do not have all the wanted resonances of which the polarisation is studied. These diagrams have to be removed in a consistent and gauge invariant manner to have a meaningful definition of the polarisation of intermediate particles. The naive approach of simply discarding the non-resonant contributions leads to a gauge-dependent amplitude and cross-section. To remove the non-resonant contributions and keeping the amplitude gauge independent a PA [40–43] can be used.

2.1 General method

In a full off-shell computation all diagrams corresponding to the chosen initial and final state are included. In a PA a set of intermediate massive s-channel resonances, that is present in the process, is chosen. The PA amplitude is split into a production part, decay parts and the propagators of the chosen resonances. The diagrams that cannot be split in this manner are discarded. This removes any diagrams that do not have the wanted resonances. To preserve gauge invariance the momenta of the resonant particles are projected on-shell $\{p\} \Rightarrow \{\tilde{p}\}$:

$\tilde{p}^2_{\text{res},i} = \left(\sum_{j=1}^{n_i} \tilde{p}_{\text{decay},i,j}\right)^2 = M^2_{\text{res},i}$. The PA amplitude takes the form

$$\mathcal{M}_{\text{PA}}\left(\{\tilde{p}\}, p^2_{\text{res}}\right) = \mathcal{M}^{\mu_1\cdots\mu_n}_{\text{production}}\left(\{\tilde{p}\}\right) \prod_{i=1}^{n} \frac{\mathcal{N}_{\mu_i\nu_i}\left(\{\tilde{p}\}\right)}{p^2_{\text{res},i} - M^2_{\text{res},i} + \mathrm{i}M_{\text{res},i}\Gamma_{\text{res},i}} \mathcal{M}^{\nu_i}_{\text{decay}}\left(\{\tilde{p}\}\right) . \tag{2.1}$$

While the production amplitude, the decay amplitudes and the numerators of the resonant propagators are evaluated with the on-shell projected momenta (denoted with a tilde), the denominators of the resonant propagators are evaluated with the off-shell momenta (without a tilde). The explicit functional form of the numerator of the propagator $\mathcal{N}$ depends on the type of the resonant particle. Similarly the type of indices that μ_i and ν_i are also depends on the type of the resonant particle, for resonant vector bosons they are Lorenz indices, for fermionic resonances they are spinor indices. In the production and decay subprocesses the resonances are external particles; therefore, to conserve gauge invariance their decay width is set to zero in the production and decay amplitude. Keeping the off-shell momenta of the resonances in the denominators of the propagators, preserves some of the off-shell effects like the Breit-Wigner shape of the resonance. Off-shell effects in the numerator of the propagator and in the production and the decay subprocesses are not included in a PA. Such effects are considered beyond the accuracy of the PA. The phase-space integration is performed over the off-shell phase space giving

$$\sigma_{\text{PA}} = \int \frac{1}{\left(2E_1\right)\left(2E_2\right)\left|\vec{v}_1 - \vec{v}_2\right|} \left|\mathcal{M}_{\text{PA}}\left(\left\{\tilde{p}\left(\{p\}\right)\right\}, p^2_{\text{res}}\right)\right|^2 d\Pi\left(\{p\}\right) . \tag{2.2}$$

This means that any phase-space cuts are applied to the off-shell momenta. Furthermore, the histogram binning used to compute differential cross-sections is done with the off-shell momenta. This ensures that the Breit-Wigner shape is recovered in differential cross-sections with respect to the invariant mass of a resonance.

Which diagrams contribute can be best seen with an example. Taking the process of $\mathrm{W}^+\mathrm{W}^+$ scattering, where the two W bosons are set as resonant, the full off-shell process is

$$\mathrm{uu} \to \mathrm{e}^+\nu_\mathrm{e}\mu^+\nu_\mu\mathrm{dd} . \tag{2.3}$$

In the full off-shell computation all of the diagrams resonant and non-resonant depicted in Figure 2.1 are included. The PA process is

$$\mathrm{uu} \to \mathrm{W}^+\left(\to \mathrm{e}^+\nu_\mathrm{e}\right)\mathrm{W}^+\left(\to \mu^+\nu_\mu\right)\mathrm{dd} . \tag{2.4}$$

In a PA computation only the diagrams with one W^+ boson decaying into a positron and an electron neutrino and one W^+ boson decaying into an antimuon and a muon neutrino as depicted in Figure 2.1(a) are included. Diagrams of the type shown in Figure 2.1(b) have the same final-state particles and are a needed in a full off-shell computation. They, however, do not contain the required s-channel W bosons; therefore, they do not contribute to a PA calculation and are a part of the non-resonant background. Furthermore, this means that also interferences of resonant and non-resonant diagrams are not part of a PA. The PA amplitude factorises as

$$\begin{aligned}\mathcal{M}_{\text{PA}} = \underbrace{\mathcal{M}\left(\mathrm{uu} \to \mathrm{W}^+\mathrm{W}^+\mathrm{dd}\right)}_{\text{production}} \times \text{propagator 1} \times \underbrace{\mathcal{M}\left(\mathrm{W}^+ \to \mathrm{e}^+\nu_\mathrm{e}\right)}_{\text{decay 1}} \\ \times \text{propagator 2} \times \underbrace{\mathcal{M}\left(\mathrm{W}^+ \to \mu^+\nu_\mu\right)}_{\text{decay 2}} .\end{aligned} \tag{2.5}$$

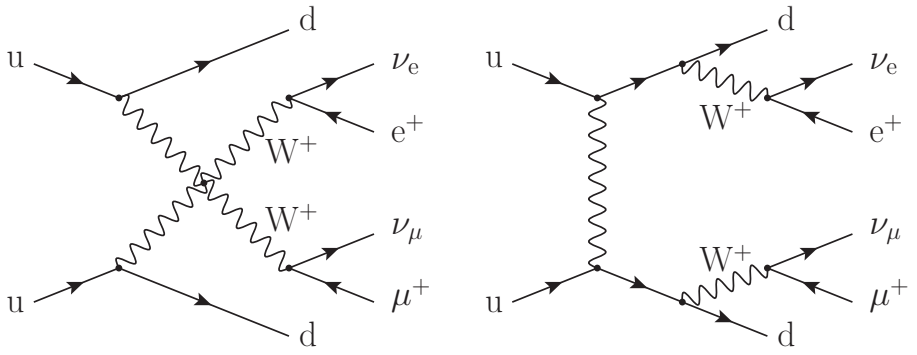

(a) Doubly resonant diagrams

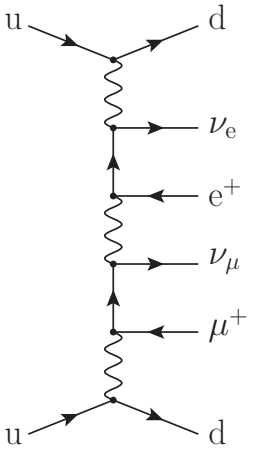

(b) Non-resonant diagram

Figure 2.1: Sample resonant diagrams that are included in a PA and non-resonant diagrams that are excluded in a PA. The diagrams depicted here are for the sample process of W^+W^+ scattering.

The on-shell projection modifies the external momenta $(p_{u,1}, p_{u,2}, p_{e^+}, p_{\nu_e}, p_{\mu^+}, p_{\nu_\mu}, p_{d,1}, p_{d,2})$ such that

$$(\tilde{p}_{e^+} + \tilde{p}_{\nu_e})^2 = M_W^2\,, \qquad \left(\tilde{p}_{\mu^+} + \tilde{p}_{\nu_\mu}\right)^2 = M_W^2 \tag{2.6}$$

holds.

So far all diagrams that do not feature the wanted resonance are removed. In general one has to distinguish between factorisable and non-factorisable contributions. In the calculations carried out in the following chapters only the factorisable contributions are treated as part of the PA. The non-factorisable contributions are removed and treated as part of the non-resonant background. Non-factorisable are those contributions that feature the wanted s-channel resonances, but that do not factorise into production and decay. Figure 2.2 shows sample contributions that are non-factorisable. The non-factorisable contributions can be loop diagrams where a massless propagator connects the production and the decay or different decays. The diagram shown in Figure 2.2(a) is non-factorisable since the photon connects the production subprocess $\left(q\overline{q}^{'} \to W^+W^+q\overline{q}^{'}\right)$ and the decay subprocess $\left(W^+ \to e^+\nu_e\right)$. Another type of non-factorisable contribution is the interference of diagrams where a massless final-state particle is emitted from one sub-process in one diagram, but from another sub-

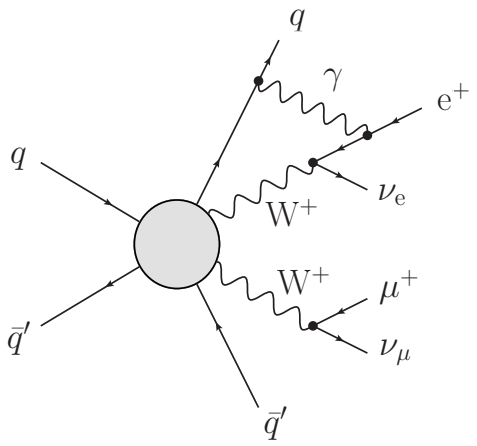

(a) Non-factorisable loop diagram

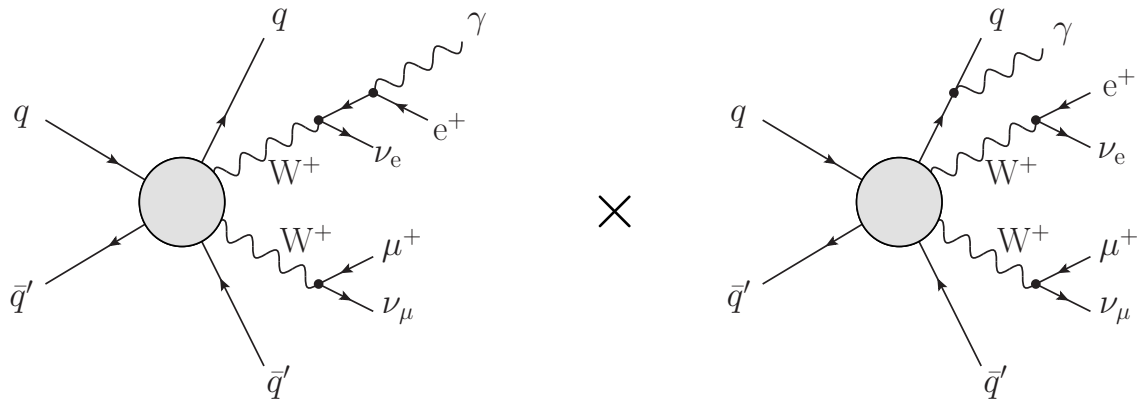

(b) Non-factorisable interferences

Figure 2.2: Non-factorisable contributions of the types shown here are neglected and not part of the PA signal. The diagrams depicted here are for the sample process of W^+W^+ scattering.

process in the second diagram. This is shown in Figure 2.2(b). In the first diagram the photon is emitted from one of the decays and in the second diagram the photon is emitted from the production. When both the non-factorisable virtual contributions and real-emission contributions are removed simultaneously their sum is generally small [44–46]. When observables are studied that are inclusive regarding the decay products of the resonances the non-factorisable real and virtual contributions cancel against each other [47–49]. This means that treating the non-factorisable contributions as non-resonant background effectively only changes the result by terms that are smaller than the intrinsic uncertainty of the PA.

As stated in the beginning of this chapter the size of the non-resonant background is nominally of $\mathcal{O}\left(\frac{\Gamma_{\text{res}}}{M_{\text{res}}}\right)$. How close to the full off-shell result the PA result ends up, depends largely on the process studied. There are many effects that can worsen the performance of a PA, in particular when there are other resonances besides the considered ones that contribute to the same final state. An example of this in the context of di-boson processes, is the s-channel Higgs resonance present in opposite sign W boson scattering. In the DPA calculation, the two decay bosons are projected on-shell; therefore, only contributions where

the Higgs is far off-shell are included. In the full off-shell computation contributions, where an on-shell Higgs decays into the two W bosons with one being off-shell, are also included. Underlying resonances like the Higgs can cause larger non-resonant backgrounds. Different underlying resonances are also important when studying vector bosons decaying into jets. Here the contributions from resonant W^+, W^- and Z bosons cannot be distinguished by the types of the decay particles. The contributions from the different resonances have to be computed separately in different DPA calculations. Another important point to consider are the phase-space cuts. If the event selection does not favour the resonant regions over the non-resonant background, there can be larger differences between the PA and full off-shell computation. How well the resonant contribution can be selected depends primarily on the process. Having decays that include neutrinos that can only be treated as missing transverse momentum can complicate the selection of the resonant regions.

2.2 On-shell projection

To evaluate the production and decay matrix elements as well as the numerators of the resonant propagators a phase-space point with on-shell resonant particles is needed. There are many ways of constructing a phase-space point with on-shell resonances from one with off-shell resonances. The cross-sections computed with the PA will depend on the specific choice of on-shell projection. This means in particular the polarisation definition depends on the chosen on-shell projection.

However, not all of them will produce equally good results. Primarily one is interested in a physically meaningful result. Therefore, the constructed on-shell phase-space point must satisfy four-momentum conservation. Furthermore, the squares of the external momenta (initial-state particles, decay particles of resonances and other final-state particles) must remain equal to their respective masses squared. Without four-momentum conservation and on-shell external particles the amplitudes of the production and decay sub-processes are not well defined. In the limit where the phase-space point is already close to on-shell the projection should become trivial and return the same phase-space point. A discontinuous on-shell projection could lead to potentially large unphysical artefacts when integrating over the phase space. If these requirements are considered, the explicit choice of on-shell projection leads only to differences that are beyond the intrinsic accuracy of the PA.

On top of these mandatory constraints, a number of additional conserved quantities are chosen for the on-shell projection used in the computations here. In particular, the on-shell projection should conserve some of the angles between particles. Firstly the angle between the two resonant particles in their CM frame should be conserved by the on-shell projection. Secondly the angles between the decay products in the rest frame of their resonance are left unchanged. These conditions will ensure that the collinear limits of possible real radiation are approached smoothly. This allows for a proper cancellation of the IR singularities present in real-emission processes with the local subtraction counterterms. By keeping the angles between the decay particles constant, the angular part of the radiation phase-space measure remains the same for the on- and off-shell momenta. This will become important in Chapter 3 when the correspondence of the local and integrated counterterms is studied in more detail. Lastly the external momenta that are not associated to the decay of a resonance are chosen be the same for the on- and off-shell phase-space point. This prevents the on-shell projection from shifting the phase-space point too far. Furthermore, in combination with

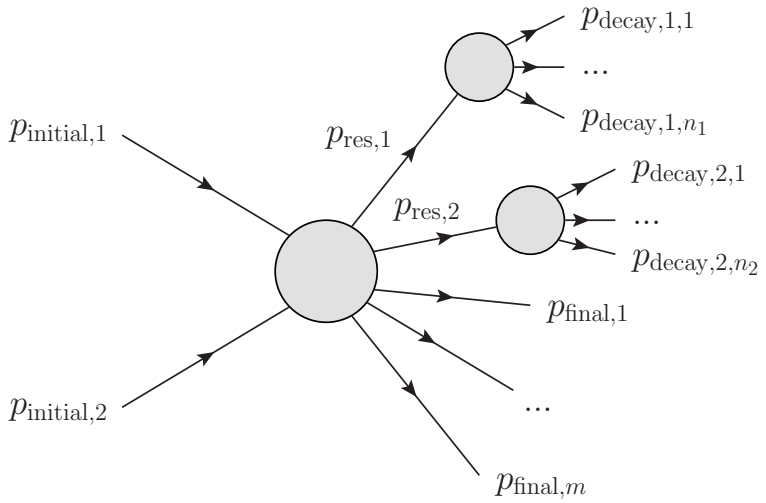

Figure 2.3: Generic doubly-resonant process with the momenta that are projected on-shell. The arrows indicate the direction of the momentum flow.

four-momentum conservation this preserves the sum of the resonant momenta.

The selected conserved quantities are tailored to processes with two resonances. The method can be generalised to processes with more particles set as resonant as done in Ref. [50].

2.2.1 Numerical implementation of the on-shell projection

With the before mentioned constraints the on-shell projection for two resonances is defined. The implementation follows the steps performed in Ref. [39]. The formulas of the on-shell projection are constructed for the generic doubly-resonant process

$$\begin{aligned} p_{\text{initial},1} + p_{\text{initial},2} \to\ & p_{\text{res},1}\,(\to p_{\text{decay},1,1} + ... + p_{\text{decay},1,n_1}) \\ & + p_{\text{res},2}\,(\to p_{\text{decay},2,1} + ... + p_{\text{decay},2,n_2}) \\ & + p_{\text{final},1} + ... + p_{\text{final},m} \end{aligned} \tag{2.7}$$

shown diagramatically in Figure 2.3. The momenta of the initial-state particles are labelled as $p_{\text{initial},1}$ and $p_{\text{initial},2}$. The momenta of the resonances $p_{\text{res},1}$ and $p_{\text{res},2}$ are the sum of the decay particle momenta from the generated off-shell phase-space point

$$p_{\text{res},1} = \sum_{i=1}^{n_1} p_{\text{decay},1,i}\,, \quad p_{\text{res},2} = \sum_{i=1}^{n_2} p_{\text{decay},2,i}\,. \tag{2.8}$$

The momenta $p_{\text{final},j}$ $j \in \{1, ..., m\}$ correspond to other final-state particles that are not decay particles of one of the resonances. After the on-shell projection, the resonances should have the masses

$$\tilde{p}^2_{\text{res},1} = M^2_{\text{res},1}\,, \quad \tilde{p}^2_{\text{res},2} = M^2_{\text{res},2}\,. \tag{2.9}$$

The chosen criteria cannot be fulfilled by all valid off-shell phase-space points. The square of the combined momenta of the two resonances must be at least the square of the sum of the masses they are to be projected on. If

$$(M_{\text{res},1} + M_{\text{res},2})^2 \leq (p_{\text{res},1} + p_{\text{res},2})^2 \tag{2.10}$$

is not satisfied, an on-shell phase-space point with the required conditions does not exist. When the off-shell phase-space point cannot be projected on-shell, the DPA amplitude is set to zero.

To project the resonances on-shell, first the on-shell momenta of the resonances are computed. From those the on-shell projected decay momenta are constructed. First a boost is performed into the CM frame of the two resonances (denoted with a prime). In the CM frame of the two resonances, their three-momenta are exactly back to back. Since the angle between the two resonances in the CM frame is conserved, the resonances remain back to back after the on-shell projection giving

$$\vec{p}'_{\text{res},1} = -\vec{p}'_{\text{res},2}\,, \qquad \vec{\tilde{p}}'_{\text{res},1} = -\vec{\tilde{p}}'_{\text{res},2}\,. \tag{2.11}$$

From this and from the fact that the sum of the resonant momenta are not changed follows

$$\left(E'_{\text{res},1} + E'_{\text{res},2}\right)^2 = \left(p_{\text{res},1} + p_{\text{res},2}\right)^2 = \left(\tilde{p}_{\text{res},1} + \tilde{p}_{\text{res},2}\right)^2 = \left(\tilde{E}'_{\text{res},1} + \tilde{E}'_{\text{res},2}\right)^2 . \tag{2.12}$$

To satisfy the on-shell condition $\tilde{p}^2_{\text{res},i} = M^2_{\text{res},i}$ the energy in the CM frame is given by

$$\tilde{E}'_{\text{res},1} = \sqrt{|\vec{\tilde{p}}'_{\text{res},1}|^2 + M^2_{\text{res},1}}\,, \quad \tilde{E}'_{\text{res},2} = \sqrt{|\vec{\tilde{p}}'_{\text{res},1}|^2 + M^2_{\text{res},2}}\,. \tag{2.13}$$

Inserting the energy expressions into Eq. (2.12) and solving for the absolute value squared of the on-shell projected three-momentum in the CM frame gives

$$|\vec{\tilde{p}}'_{\text{res},1}|^2 = \frac{\left(\left(p_{\text{res},1} + p_{\text{res},2}\right)^2\right)^2 - 2\left(p_{\text{res},1} + p_{\text{res},2}\right)^2\left(M^2_{\text{res},1} + M^2_{\text{res},2}\right) + \left(M^2_{\text{res},1} - M^2_{\text{res},2}\right)^2}{4\left(p_{\text{res},1} + p_{\text{res},2}\right)^2}\,. \tag{2.14}$$

The three-momenta of both resonances are then rescaled to their new lengths keeping their spatial directions fixed. This ensures that the requirement of preserving the angle in the resonance CM frame is fulfilled. The on-shell energies of the resonances are then computed from the on-shell condition in Eq. (2.13). Now the momenta of the resonances have the desired masses. As initially the phase-space point was constructed in the lab frame the newly on-shell projected resonant momenta are boosted back to the lab frame. This results in the on-shell resonant momenta in the lab frame $\tilde{p}_{\text{res},1}$ and $\tilde{p}_{\text{res},2}$.

In the next step the on-shell projection first applied to the resonant momenta needs to be applied to the decay momenta, which will be needed in the amplitude evaluation. To do this one starts by taking the off-shell decay momenta of one of the resonances. The decay momenta are then boosted into the CM frame of their off-shell resonance (denoted with a double prime). Here only the case of massless decay particles is treated, the general case of massive decay particles is considered in Ref. [50]. The decay momenta are then rescaled with

$$\tilde{p}''_{\text{decay},j,i} = \frac{M_{\text{res},j}}{\sqrt{p^2_{\text{res},j}}} p''_{\text{decay},j,i}\,. \tag{2.15}$$

The rescaling of the decay momenta keeps the angle between the decay particles of one resonance untouched fulfilling the requirement. The rescaled decay momenta are then boosted back to the lab frame. This is done with the inverse of the boost to the CM frame of the on-shell resonance. The on-shell decay momenta are then computed completely analogously

for the other resonance. After this all on-shell momenta of the decay particles have been calculated. The other external momenta are not changed by the on-shell projection giving

$$\tilde{p}_{\text{initial},1} = p_{\text{initial},1}, \quad \tilde{p}_{\text{initial},2} = p_{\text{initial},2} \tag{2.16}$$

and

$$\tilde{p}_{\text{final},j} = p_{\text{final},j}\,, \quad j \in \{1, ..., m\}\,. \tag{2.17}$$

The on-shell phase-space point needed to compute amplitudes in the DPA is now complete. As a shorthand notation the on-shell projection with two resonances, the first decaying into i and the second into j particles is labelled as $\text{DPA}^{(i,j)}$.

2.3 Polarisation definition

With the methods described so far the calculation of unpolarised processes in the DPA can be carried out. The primary focus of this thesis are polarised processes. The step from unpolarised DPA to polarised DPA calculations is fairly straight-forward. In the DPA the resonances are on-shell. Massive vector bosons have three physical polarisation states and the unphysical auxiliary state that cancels against the contribution from the Goldstone boson. Therefore, the numerator of the propagator only contains a sum over the physical polarisation states (longitudinal (L), left ($-$) and right ($+$))

$$\sum_{\lambda'=\text{L},\pm} \varepsilon_\mu^{(\lambda')}(\tilde{p}_{\text{res}})\, \varepsilon_\nu^{*\,(\lambda')}(\tilde{p}_{\text{res}}) = -g_{\mu\nu} + \frac{\tilde{p}_{\text{res}\,\mu}\tilde{p}_{\text{res}\,\nu}}{M_{\text{res}}^2}\,. \tag{2.18}$$

For a resonant W boson the unpolarised PA amplitude reads

$$\mathcal{M}_{\text{PA}}\left(\{\tilde{p}\}, p_{\text{res}}^2\right) = \mathcal{M}^{\mu}_{\text{production}}\left(\{\tilde{p}\}\right) \frac{\mathrm{i}\left(-g_{\mu\nu} + \dfrac{\tilde{p}_{\text{res}\,\mu}\tilde{p}_{\text{res}\,\nu}}{M_{\text{W}}^2}\right)}{p_{\text{res}}^2 - M_{\text{W}}^2 + \mathrm{i}M_{\text{W}}\Gamma_{\text{W}}} \mathcal{M}^{\nu}_{\text{decay}}\left(\{\tilde{p}\}\right)\,. \tag{2.19}$$

This expression is obtained from the general form shown in Eq. (2.1) by replacing the generic numerator of the resonant propagator, masses and decay widths with the ones of the W boson. For simplification only one resonant propagator is studied. For the case of more resonances the polarisation selection is performed for each resonance separately. The polarisation split is performed by replacing the polarisation sum with the desired physical polarisation state λ [51, 52] in the numerator of the propagator,

$$\sum_{\lambda'=\text{L},\pm} \varepsilon_\mu^{(\lambda')}(\tilde{p}_{\text{res}})\, \varepsilon_\nu^{*\,(\lambda')}(\tilde{p}_{\text{res}}) \;\longrightarrow\; \varepsilon_\mu^{(\lambda)}(\tilde{p}_{\text{res}})\, \varepsilon_\nu^{*\,(\lambda)}(\tilde{p}_{\text{res}})\,. \tag{2.20}$$

As in the PA the resonant propagators are on-shell, the polarised amplitudes are defined independently of the chosen gauge. The unpolarised PA amplitude is then written as the sum over the polarised PA amplitudes

$$\mathcal{M}_{\text{PA}} = \sum_{\lambda'=\text{L},\pm} \mathcal{M}_{\text{PA}}^{(\lambda')}\,. \tag{2.21}$$

To compute cross-sections the absolute value squared of an amplitude is needed. Squaring the unpolarised PA amplitude results in

$$|\mathcal{M}_{\mathrm{PA}}|^2 = \sum_{\lambda'} \left|\mathcal{M}_{\mathrm{PA}}^{(\lambda')}\right|^2 + \sum_{\lambda' \neq \lambda''} \mathcal{M}_{\mathrm{PA}}^{(\lambda')} \mathcal{M}_{\mathrm{PA}}^{(\lambda'')*}, \tag{2.22}$$

where the first term is the incoherent sum over the squared amplitudes with a fixed polarisation state, the second term contains the interferences of different polarisation states.

There is a further aspect where unpolarised and polarised amplitudes differ. As for the full off-shell amplitude the unpolarised PA amplitude is frame independent. However, the polarisation vectors $\varepsilon_\mu^{(\lambda)}(\tilde{p}_{\mathrm{res}})$ of a polarisation λ do not transform as four-vectors. Therefore, the polarised PA amplitude and cross-sections calculated from it are inherently frame dependent. This means that what is treated as the signal from a specific polarisation will depend on this choice of frame used to define the polarisation vectors. In principle, all frame choices give equally valid polarised cross-sections. For di-boson processes, as the ones studied in more detail in Chapters 4 and 5, a commonly used choice is the CM frame of the two bosons. This frame is directly related to the interactions of the resonant vector bosons; therefore, it might offer more sensitivity to the EW symmetry breaking. Another frame choice that has been used in the past is the lab frame. The lab frame was used as it is the simplest frame choice. Today it is only used very rarely in polarisation studies of di-boson processes.

2.4 Exceptions

The DPA, as explained so far, cannot be used in a straight-forward manner for all processes. Problems can arise when the studied final state allows for more resonances than the ones explicitly treated as resonant in the PA. This is particularly relevant for VBS processes, while for vector-boson pair-production processes additional resonances can only appear beyond NLO accuracy. To preserve the gauge invariance of the amplitude for the production of W and/or Z bosons the decay width of all internal W and Z propagators needs to be set to zero. When studying a final state, where another W or Z boson can be in the s-channel, setting the width to zero will result in a divergent amplitude.

Another issue is that the on-shell projection defined in Section 2.2 can shift certain invariants. Even though the definition of the on-shell projection is chosen in a way to avoid large shifts in the relevant invariants some changes are necessary. A type of invariant that can be subject to change is the one corresponding to the momenta of one decay and other final-state momenta. In the notation from Section 2.2.1 this would for example be an invariant like $(p_{\mathrm{res},1} + p_{\mathrm{final},1} + p_{\mathrm{final},2})^2$. This can become problematic when the studied final state allows for an underlying resonance that is not treated in a PA. The shift of invariants from the on-shell projection can shift the underlying resonance closer to being on-shell. In the numerical integration of the process carried out with a Monte Carlo code this can lead to large event weights that cause the convergence to become very unstable. For VBS processes the invariant that can be problematic is the one of the decay particles of one vector boson and the two jets. In partonic processes that have a triple-resonant background this invariant corresponds to a s-channel Higgs boson that decays into an on-shell vector boson and two jets. The on-shell projection can shift the invariant of the Higgs to or away from the reson-

ance peak giving large enhancements or suppressions of the DPA cross-section compared to the full of-shell process.

How these exceptions are handled for W^+W^+ scattering is discussed in Section 5.2.2.

Chapter 3

Subtraction method for divergences from unresolved real radiation in the presence of charged resonances

This Chapter is based on the methods of Ref. [37]. In the previous chapter, the general structure of the DPA has been explained. For predictions that are only LO accurate this is enough. But to achieve accurate theoretical predictions higher-order corrections have to be included. For contributions that feature the Born topology, such as virtual and integrated-dipole contributions, the LO DPA can be applied analogously. More care has to be taken when computing the NLO subtracted-real contributions. For chargeless resonances, like the Z boson as seen in Figure 3.1, the computation of the NLO EW corrections is fairly straightforward. The treatment of the IR singularities from unresolved real radiation can be done with the same dipole structures used for the full off-shell process. Compared to the full off-shell process only a subset of the dipoles (combinations of emitter, spectator and emissus) are necessary. As in the DPA only diagrams are included that factorise into production and decay, it matters from which subprocess the real radiation is emitted. This means that only dipoles, where emitter, spectator and emissus are all external particles of the same subprocess, are needed. In particular, only dipoles where emitter, spectator and emissus all stem from the production or the same decay are included. Since non-factorisable contributions are not considered in the DPA this is sufficient. To apply the DPA on-shell projection to a process with real radiation from one of the decays the on-shell projection must include the additional decay particle. The NLO QCD corrections with colour neutral resonances as the W and the Z boson can be computed in the same manner. This has been used in the past for vector-boson pair-production processes [39, 52, 53].

The calculation of the NLO EW corrections for processes with charged resonances is more involved. With charged resonances new singular structures appear that are not present in the full off-shell process. In the DPA the resonances are projected on-shell and the decay widths of the resonant particles are set to zero everywhere, but in the two propagators explicitly set as resonant. Therefore, the emission of soft photons can cause the denominators of the intermediate propagators, corresponding to the particle of the charged resonance, to vanish resulting in a divergence. In the full off-shell process the emission of a soft photon from a W boson is not singular as the divergence is regulated by the decay width in the denominator of the W propagator. This is different in the DPA where the emission of a soft photon from

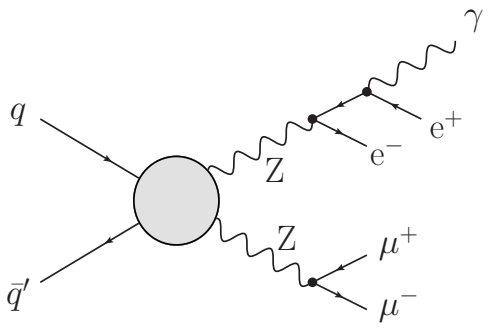

(a) Real emission off the decay

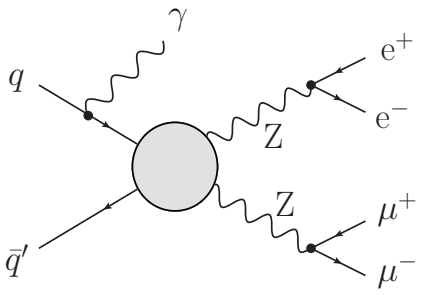

(b) Real emission off the initial state of the production

Figure 3.1: Types of real-emission diagrams contributing in the case of chargeless resonances, here displayed with the sample process ZZ pair production.

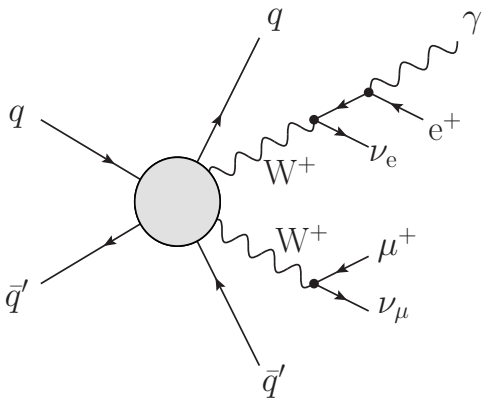

(a) Real emission off the decay

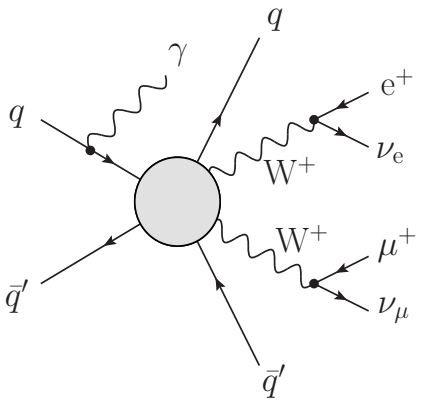

(b) Real emission off the initial state of the production

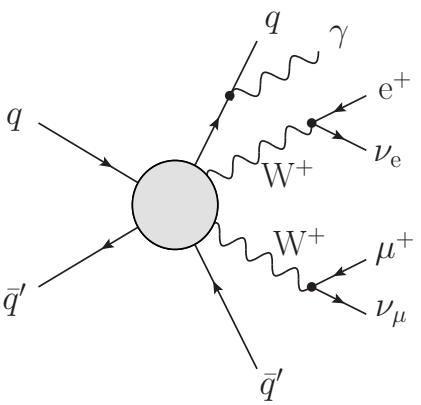

(c) Real emission off the final state of the production

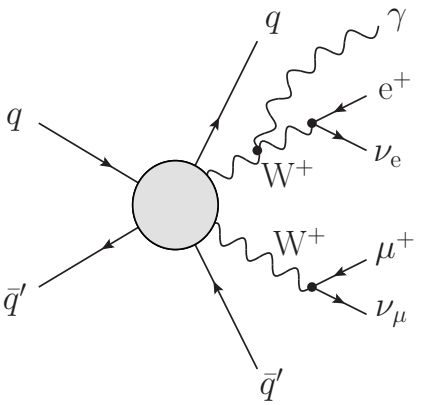

(d) Real emission off the resonant propagator

Figure 3.2: Types of real-emission diagrams contributing in the case of charged resonances, here displayed for the sample process of W^+W^+ scattering.

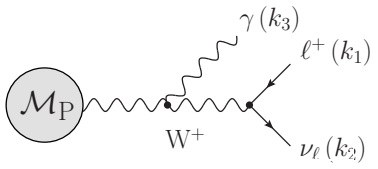

Figure 3.3: Photon-radiation off a W-boson propagator.

a W boson is singular. Therefore, simply removing the dipoles connecting production and decay or different decays is not enough in the presence of charged resonances. When the real radiation can be emitted from one of the resonances, additional counterterms are needed to cancel the IR divergences. The methods to deal with the IR divergences in the presence of charged resonances have been published in Refs. [37, 54, 55]. Not all real-emission partonic processes have singular structures not present in the full off-shell process. Partonic processes that have real-quark radiation do not have additional singularities. The IR singularities can be treated in the same manner as for electrically neutral resonances.

In processes with chargeless resonances it is clear whether a diagram contributes to the process with the radiation emitted from the production or from one of the decays. For charged resonances this is not necessarily the case. For diagrams of the type depicted in Figure 3.2(a) the radiation is part of the decay. For diagrams of the type shown in Figures 3.2(b) and 3.2(c) the real radiation is evidently from the production. But for diagrams with real radiation off the resonant propagators as shown in Figure 3.2(d), it is not inherently clear whether this diagram should contribute to the production or the decay subprocess. They are not uniquely part of the process with emission from the production or the decay as they contribute to both processes. The diagram has to be split into two contributions one for the production and one for the decay subprocess. The split is done with a partial-fraction decomposition described in more detail in Section 3.1.

After the partial fraction split is performed, additional counterterms can be used to cancel all IR singularities. These additional soft singularities need to be cancelled with subtraction counterterms tailored to resonance processes. Their exact form and use is discussed in Sections 3.2 and 3.3.

3.1 Splitting real-emission diagrams with a partial fractioning

As mentioned before, to cancel the IR singularities present in the contributions with real radiation off the resonant propagators, a split into a part associated with emission from the decay and one with emission from the production is needed. The discussion follows the example of the emission of a photon from a W boson but is completely analogous for photons emitted from other charged resonances. Putting aside the DPA for a moment, the off-shell amplitude for the subdiagram in Figure 3.3 is

$$\begin{aligned}\mathcal{M}_{\mathrm{prop}} = &\quad \mathcal{N}_{\mathrm{prop}}(k_1,k_2,k_3)\,\frac{1}{s_{123}-M_{\mathrm{W}}^2+\mathrm{i}M_{\mathrm{W}}\Gamma_{\mathrm{W}}}\cdot\frac{1}{s_{12}-M_{\mathrm{W}}^2+\mathrm{i}M_{\mathrm{W}}\Gamma_{\mathrm{W}}}\\ = &-\frac{\mathcal{N}_{\mathrm{prop}}(k_1,k_2,k_3)}{s_{13}+s_{23}}\left(\frac{1}{s_{123}-M_{\mathrm{W}}^2+\mathrm{i}M_{\mathrm{W}}\Gamma_{\mathrm{W}}}-\frac{1}{s_{12}-M_{\mathrm{W}}^2+\mathrm{i}M_{\mathrm{W}}\Gamma_{\mathrm{W}}}\right).\end{aligned} \tag{3.1}$$

Here k_1, k_2 and k_3 are the decay momenta of the charged lepton, neutrino and photon with corresponding invariants $s_{ab} = 2k_a \cdot k_b$ and $s_{abc} = s_{ab} + s_{bc} + s_{ac}$. The amplitude features a product of the two W-boson propagators with different momentum invariants. This product is then rewritten as a sum with the help of a partial fraction decomposition. The two terms have different invariants (s_{123} and s_{12}) in the propagators.

The discussion so far only concerned the full off-shell amplitude. Now the DPA is applied to the amplitude but with treating different propagators as the resonant one. When the W boson with momentum k_1+k_2 is set as resonant, the invariant s_{12} is projected on-shell. Here the on-shell projection with two decay particles is needed, resulting in the DPA amplitude

$$\begin{aligned}\tilde{\mathcal{M}}^{(2)}_{\text{prop}} =& \frac{1}{s_{12} - M_{\text{W}}^2 + \mathrm{i}M_{\text{W}}\Gamma_{\text{W}}} \\ & \left[\frac{\mathcal{N}_{\text{prop}}(k_1,k_2,k_3)}{s_{13}+s_{23}}\left(1 - \frac{s_{12} - M_{\text{W}}^2 + \mathrm{i}M_{\text{W}}\Gamma_{\text{W}}}{s_{123} - M_{\text{W}}^2 + \mathrm{i}M_{\text{W}}\Gamma_{\text{W}}}\right)\right]_{s_{12}=M_{\text{W}}^2,\Gamma_{\text{W}}=0} \\ =& \frac{1}{s_{12} - M_{\text{W}}^2 + \mathrm{i}M_{\text{W}}\Gamma_{\text{W}}}\left[\frac{\mathcal{N}_{\text{prop}}(\tilde{k}_1^{(12)},\tilde{k}_2^{(12)},\tilde{k}_3^{(12)})}{\tilde{s}_{13}^{(12)}+\tilde{s}_{23}^{(12)}}\right].\end{aligned} \tag{3.2}$$

This amplitude is part of the process, where the photon is emitted from the production sub-process. Following the notation from Section 2.2, the tilded momenta denote the on-shell projected momenta with the superscript indicating the invariant that is projected on shell. Subsequently, the IR-singular behaviour is only in the production sub-process.

The propagator with then momentum $k_1+k_2+k_3$ can also be treated as the resonant one. Therefore, the on-shell projection with three decay particles sets the invariant s_{123} on-shell. The DPA amplitude reads

$$\begin{aligned}\tilde{\mathcal{M}}^{(3)}_{\text{prop}} =& \frac{1}{s_{123} - M_{\text{W}}^2 + \mathrm{i}M_{\text{W}}\Gamma_{\text{W}}} \\ & \left[-\frac{\mathcal{N}_{\text{prop}}(k_1,k_2,k_3)}{s_{13}+s_{23}}\left(1 - \frac{s_{123} - M_{\text{W}}^2 + \mathrm{i}M_{\text{W}}\Gamma_{\text{W}}}{s_{12} - M_{\text{W}}^2 + \mathrm{i}M_{\text{W}}\Gamma_{\text{W}}}\right)\right]_{s_{123}=M_{\text{W}}^2,\Gamma_{\text{W}}=0} \\ =& \frac{1}{s_{123} - M_{\text{W}}^2 + \mathrm{i}M_{\text{W}}\Gamma_{\text{W}}}\left[-\frac{\mathcal{N}_{\text{prop}}(\tilde{k}_1^{(123)},\tilde{k}_2^{(123)},\tilde{k}_3^{(123)})}{\tilde{s}_{13}^{(123)}+\tilde{s}_{23}^{(123)}}\right].\end{aligned} \tag{3.3}$$

This amplitude is part of the process with the photon being emitted from the decay of the W boson. The IR singularities are only in the decay sub-process.

The two terms from the partial fractioned amplitude in Eq. (3.1) are the ones that are treated in the DPA by projecting different momenta on-shell. For the first term the momentum $k_1 + k_2 + k_3$ is projected on-shell giving the contributions in (3.3). For the second term the momentum $k_1 + k_2$ is projected on-shell giving the contribution in (3.2).

3.2 Production counterterms

The typical energy scales of the hard scattering at the LHC are of a similar order of magnitude as the W mass. Therefore, the W bosons are treated as massive and only the limit where the emitted photons become soft is singular. The limit where the photon is collinear to a W boson is finite. With only soft singularities present the singular limits are spin independent.

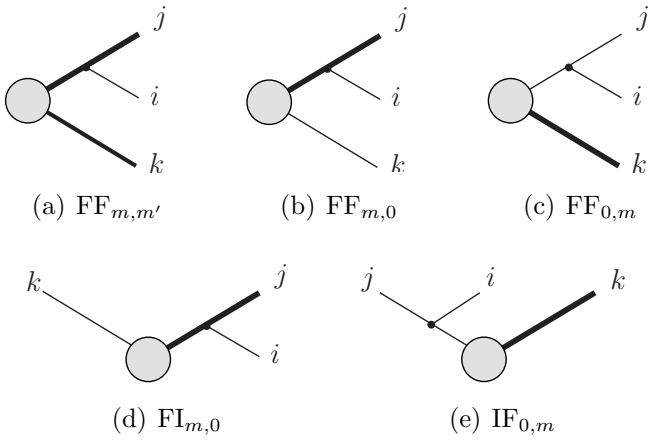

Figure 3.4: QED subtraction dipoles involving one or two massive external particles (highlighted as bold lines) with emitter j, emissus i and spectator k. The indices indicate the masses of emitters (first indices) and spectators (second indices) and the labels F and I stand for final and initial state.

Because of the spin independence, the IR singularities can be cancelled with the same dipoles as for soft radiation off massive fermions [56].

As seen in Figure 3.4 there are five types of dipoles needed to cancel all additional soft singularities from the charged resonance. In these dipoles a charged resonance takes the role of the emitter and/or the spectator.

In order for the subtraction scheme to work properly the local dipoles must cancel all IR singularities of the real matrix element. Additionally, the finite part of the local counterterms must be exactly added back in the integrated counterterms. These requirements for every valid subtraction scheme lead to constraints on how the dipoles need to be evaluated. In particular, the interplay of the subtraction mapping and the on-shell projection needs to be analysed carefully to prevent a mismatch between the local and integrated dipoles. The detailed understanding of how the subtraction mapping and the on-shell projection interact is very important as the pole in dimensional regularisation from soft-photon emission is only present for on-shell resonances.

To study this in more detail the partonic process

$$q\,q \to \underbrace{\mu^+(k_1)\,\nu_\mu(k_2)}_{\mathrm{W}^+(k_{12})}\ \underbrace{\mathrm{e}^+(k_3)\,\nu_\mathrm{e}(k_4)}_{\mathrm{W}^+(k_{34})}\ q(k_5)\,q(k_6)\,\gamma(k_7) \tag{3.4}$$

is considered. In this process a closer look is taken at the dipole $\mathcal{D}_{[12]7,5}$ which has the first W^+ boson (momentum k_{12}) as the emitter, the massless quark (momentum k_5) as the spectator and the photon (momentum k_7) as the emissus. This dipole corresponds to the type depicted in Figure 3.4(b) with massive emitter and massless spectator. The following argument is done explicitly for this dipole to simplify the used formulas. The same arguments also apply to the other types of dipoles featuring a resonance as an emitter and/or spectator. Following the notation from Section 2.2 the on-shell projected momenta are denoted with a tilde. The momenta with the subtraction mapping applied to them are denoted with a bar. The subtraction mapping here is the massive-Catani-Seymour (CS)-dipole mapping [56]. To simplify the following formulas the absolute value squared of the denominator of the

Breit-Wigner propagator is abbreviated as

$$\mathrm{BW}(k_{ij}) = \left(k_{ij}^2 - M_\mathrm{W}^2\right)^2 + \left(\Gamma_\mathrm{W} M_\mathrm{W}\right)^2 . \tag{3.5}$$

To begin the discussion one starts from the real-emission contribution $\mathcal{R}$ to the differential cross-section including the phase-space measure. In the DPA the phase-space integration is performed over the off-shell phase space giving a phase-space measure of the off-shell momenta. To keep the focus on the main point, the correct use of the subtraction dipoles, the flux factor and possible symmetry factors have been omitted giving

$$\begin{aligned}
\mathcal{R} &\propto \frac{\left|\mathcal{M}^{(7)}\left(Q; \tilde{k}_1, .., \tilde{k}_4, k_5, k_6, k_7\right)\right|^2}{\mathrm{BW}(k_{12})\,\mathrm{BW}(k_{34})}\,\mathrm{d}\Phi_7\left(Q; k_1, .., k_5, k_6, k_7\right) \\
&= \frac{\left|\mathcal{M}^{(7)}\left(Q; \tilde{k}_1, .., \tilde{k}_4, k_5, k_6, k_7\right)\right|^2}{\mathrm{BW}(k_{12})\,\mathrm{BW}(k_{34})}\,\mathrm{d}\Phi_5\left(Q; k_{12}, k_{34}, k_5, k_6, k_7\right) \\
&\quad \times \frac{\mathrm{d}k_{12}^2}{2\pi}\frac{\mathrm{d}k_{34}^2}{2\pi}\,\mathrm{d}\Phi_2\left(k_{12}; k_1, k_2\right)\mathrm{d}\Phi_2\left(k_{34}; k_3, k_4\right) .
\end{aligned} \tag{3.6}$$

While the phase-space measure depends on the off-shell momenta, the numerator is evaluated with the on-shell projected momenta. Using the on-shell projection detailed in Section 2.2 the momenta k_5, k_6, k_7 are left unchanged. Therefore, the tilde is omitted. The integration measure over the seven final-state particles is split up into two two-particle phase-space measures for the decays of the two resonances and a five-particle phase-space measure for the production. Next the numerator is split into the production, the decay parts and the polarisation vectors of the resonances. Here an unpolarised DPA process is studied; therefore, a sum over all possible polarisations is present in the real amplitude squared

$$\begin{aligned}
\left|\mathcal{M}^{(7)}\left(Q; \tilde{k}_1, .., \tilde{k}_4, k_5, k_6, k_7\right)\right|^2 = \sum_{\lambda_{12},\lambda_{34}} &\left|\mathcal{M}^{(5)}_{\mathrm{P},\mu\nu}\left(Q; \tilde{k}_{12}, \tilde{k}_{34}, k_5, k_6, k_7\right)\tilde{\varepsilon}_{12}^{\mu,*}\tilde{\varepsilon}_{34}^{\nu,*}\right|^2 \\
&\times \left|\tilde{\varepsilon}_{12}^{\mu}\mathcal{M}^{(2)}_{\mathrm{D},\mu}\left(\tilde{k}_{12}; \tilde{k}_1, \tilde{k}_2\right)\right|^2 \left|\tilde{\varepsilon}_{34}^{\mu}\mathcal{M}^{(2)}_{\mathrm{D},\mu}\left(\tilde{k}_{34}; \tilde{k}_3, \tilde{k}_4\right)\right|^2 .
\end{aligned} \tag{3.7}$$

The split into production and decay is then inserted into the formula for the real-emission contribution from Eq. (3.6) resulting in

$$\begin{aligned}
\mathcal{R} \propto \sum_{\lambda_{12},\lambda_{34}} &\frac{\left|\mathcal{M}^{(5)}_{\mathrm{P},\mu\nu}\left(Q; \tilde{k}_{12}, \tilde{k}_{34}, k_5, k_6, k_7\right)\tilde{\varepsilon}_{12}^{\mu,*}\tilde{\varepsilon}_{34}^{\nu,*}\right|^2}{\mathrm{BW}(k_{12})\,\mathrm{BW}(k_{34})} \\
&\times \left|\tilde{\varepsilon}_{12}^{\mu}\mathcal{M}^{(2)}_{\mathrm{D},\mu}\left(\tilde{k}_{12}; \tilde{k}_1, \tilde{k}_2\right)\right|^2 \left|\tilde{\varepsilon}_{34}^{\mu}\mathcal{M}^{(2)}_{\mathrm{D},\mu}\left(\tilde{k}_{34}; \tilde{k}_3, \tilde{k}_4\right)\right|^2 \\
&\times \mathrm{d}\Phi_5\left(Q; k_{12}, k_{34}, k_5, k_6, k_7\right)\frac{\mathrm{d}k_{12}^2}{2\pi}\frac{\mathrm{d}k_{34}^2}{2\pi}\,\mathrm{d}\Phi_2\left(k_{12}; k_1, k_2\right)\mathrm{d}\Phi_2\left(k_{34}; k_3, k_4\right) .
\end{aligned} \tag{3.8}$$

In dimensional regularisation the two-particle decay phase-space measure takes the form

$$\mathrm{d}\Phi_2\left(k_{12}; k_1, k_2\right) = \frac{\left(k_{12}^2\right)^{-\epsilon}}{2\left(4\pi\right)^{2-2\epsilon}}\,\mathrm{d}\Omega_2^{(2-2\epsilon)} , \tag{3.9}$$

when the DPA$^{(2,2)}$ is applied, the decay phase-space measure is

$$\mathrm{d}\Phi_2\left(\tilde{k}_{12};\tilde{k}_1,\tilde{k}_2\right) = \frac{\left(\tilde{k}_{12}^2\right)^{-\epsilon}}{2\,(4\pi)^{2-2\epsilon}}\,\mathrm{d}\Omega_2^{(2-2\epsilon)}\,. \tag{3.10}$$

The on-shell projection chosen conserves the angles of the decay momenta in the CM frame of the decaying resonance. This leaves the angular part of the phase-space measure unchanged, when projecting the momenta on-shell. Therefore, the two expressions only differ in the square of the decay momentum.The off-shell phase-space measure features the off-shell momentum $\left(k_{12}^2\right)^{-\epsilon}$ while the on-shell phase-space measure has $\left(\tilde{k}_{12}^2\right)^{-\epsilon}$. Here the real radiation is emitted from the production; therefore, the decay, both matrix element and phase-space measure, is LO like. This means that they are always evaluated in four space-time dimensions ($\epsilon = 0$) resulting in equal phase-space measures for the decays.

To remove the IR singularities the local counterterms are subtracted from the real-emission contribution. To evaluate the local counterterms first the subtraction mapping, the massive-CS mapping generalised to off-shell momenta, is applied. Afterwards the on-shell projection is performed on the reduced kinematics. This order is chosen since the reverse order leads to a discrepancy between the local and integrated counterterms that is not necessarily beyond the accuracy of the DPA. A detailed discussion of the approach with first projecting the momenta on-shell and applying the subtraction mapping second is found in App. A. Subtracting the local counterterms $\mathcal{D}$ from the real-emission contribution $\mathcal{R}$ gives the subtracted real

$$\begin{aligned}
\mathcal{R}-\mathcal{D} \propto \sum_{\lambda_{12},\lambda_{34}} \Bigg[& \left|\mathcal{M}^{(5)}_{\mathrm{P},\mu\nu}\left(Q;k_{12},k_{34},k_5,k_6,k_7\right)\varepsilon_{12}^{\mu,*}\varepsilon_{34}^{\nu,*}\right|^2 \\
& \times \frac{1}{\mathrm{BW}(k_{12})}\left|\varepsilon_{12}^{\mu}\mathcal{M}^{(2)}_{\mathrm{D},\mu}\left(k_{12};k_1,k_2\right)\right|^2 \\
& \times \mathrm{d}\Phi_5\left(Q;k_{12},k_{34},k_5,k_6,k_7\right)\frac{\mathrm{d}k_{12}^2}{2\pi}\mathrm{d}\Phi_2\left(k_{12};k_1,k_2\right) \\
& - \mathcal{D}_{[12]7,5}(\bar{k}_{12},\bar{k}_5;y,z,\phi)\left|\mathcal{M}^{(4)}_{\mathrm{P},\mu\nu}\left(Q;\bar{k}_{12},k_{34},\bar{k}_5,k_6\right)\bar{\varepsilon}_{12}^{\mu,*}\varepsilon_{34}^{\nu,*}\right|^2 \\
& \times \frac{1}{\mathrm{BW}(\bar{k}_{12})}\left|\bar{\varepsilon}_{12}^{\mu}\mathcal{M}^{(2)}_{\mathrm{D},\mu}\left(\bar{k}_{12};\bar{k}_1,\bar{k}_2\right)\right|^2 \\
& \times \mathrm{d}\Phi_{\mathrm{rad}}\left(\bar{k}_{12}+\bar{k}_5;z,y,\phi\right)\mathrm{d}\Phi_4\left(Q;\bar{k}_{12},k_{34},\bar{k}_5,k_6\right)\frac{\mathrm{d}\bar{k}_{12}^2}{2\pi}\mathrm{d}\Phi_2\left(\bar{k}_{12};\bar{k}_1,\bar{k}_2\right)\Bigg] \\
& \times \frac{1}{\mathrm{BW}(k_{34})}\left|\varepsilon_{34}^{\mu}\mathcal{M}^{(2)}_{\mathrm{D},\mu}\left(k_{34};k_3,k_4\right)\right|^2\frac{\mathrm{d}k_{34}^2}{2\pi}\,\mathrm{d}\Phi_2\left(k_{34};k_3,k_4\right)\,.
\end{aligned} \tag{3.11}$$

Only the dipole $\mathcal{D}_{[12]7,5}$, studied here in detail, is given, the others needed for a finite subtracted-real contribution are omitted for simplicity. The dipole depends on the radiation variables y, z and ϕ that parametrise the radiation phase space. As seen by the absence of any tilded momenta, all present momenta are still off-shell.

To have a final result that is independent of the subtraction scheme the term subtracted with the local counterterms has to be added back with the integrated counterterms. This

results in the integrated counterterm, before on-shell projection,

$$\begin{aligned}\mathcal{I} = \sum_{\lambda_{12},\lambda_{34}} & \mathcal{I}_{[12]7,5}(\bar{k}_{12},\bar{k}_5)\frac{1}{\mathrm{BW}(\bar{k}_{12})\,\mathrm{BW}(k_{34})}\left|\mathcal{M}^{(4)}_{\mathrm{P},\mu\nu}\left(Q;\bar{k}_{12},k_{34},\bar{k}_5,k_6\right)\bar{\varepsilon}^{\mu,*}_{12}\varepsilon^{\nu,*}_{34}\right|^2 \\ & \times\left|\bar{\varepsilon}^{\mu}_{12}\mathcal{M}^{(2)}_{\mathrm{D},\mu}\left(\bar{k}_{12};\bar{k}_1,\bar{k}_2\right)\right|^2\left|\varepsilon^{\mu}_{34}\mathcal{M}^{(2)}_{\mathrm{D},\mu}\left(k_{34};k_3,k_4\right)\right|^2 \\ & \times\mathrm{d}\Phi_4\left(Q;\bar{k}_{12},k_{34},\bar{k}_5,k_6\right)\frac{\mathrm{d}\bar{k}^2_{12}}{2\pi}\frac{\mathrm{d}k^2_{34}}{2\pi}\mathrm{d}\Phi_2\left(\bar{k}_{12};\bar{k}_1,\bar{k}_2\right)\mathrm{d}\Phi_2\left(k_{34};k_3,k_4\right),\end{aligned} \tag{3.12}$$

with the dipole kernel

$$\mathcal{I}_{[12]7,5}(\bar{k}_{12},\bar{k}_5) = \int_{d=4-2\epsilon}\mathcal{D}_{[12]7,5}(\bar{k}_{12},\bar{k}_5;y,z,\phi)\,\mathrm{d}\Phi_{\mathrm{rad}}\left(\bar{k}_{12}+\bar{k}_5;z,y,\phi\right). \tag{3.13}$$

The explicit poles that cancel with those present in the virtual contributions arise, when the d-dimensional integral over the radiation phase space is performed.

So far the counterterms and real amplitude are evaluated with the off-shell momenta. To have a subtracted-real contribution in the DPA, the momenta of the resonant particles are projected on-shell leading to the subtracted real contribution

$$\begin{aligned}\mathcal{R}-\mathcal{D} \propto \sum_{\lambda_{12},\lambda_{34}}\Bigg[& \left|\mathcal{M}^{(5)}_{\mathrm{P},\mu\nu}\left(Q;\tilde{k}_{12},\tilde{k}_{34},k_5,k_6,k_7\right)\tilde{\varepsilon}^{\mu,*}_{12}\tilde{\varepsilon}^{\nu,*}_{34}\right|^2 \\ & \times\frac{1}{\mathrm{BW}(k_{12})}\left|\tilde{\varepsilon}^{\mu}_{12}\mathcal{M}^{(2)}_{\mathrm{D},\mu}\left(\tilde{k}_{12};\tilde{k}_1,\tilde{k}_2\right)\right|^2\mathrm{d}\Phi_7\left(Q;k_1,\ldots,k_7\right) \\ & -\mathcal{D}_{[12]7,5}(\tilde{\bar{k}}_{12},\bar{k}_5;\tilde{y},\tilde{z},\tilde{\phi})\left|\mathcal{M}^{(4)}_{\mathrm{P},\mu\nu}\left(Q;\tilde{\bar{k}}_{12},\tilde{k}_{34},\bar{k}_5,k_6\right)\tilde{\bar{\varepsilon}}^{\mu,*}_{12}\tilde{\varepsilon}^{\nu,*}_{34}\right|^2 \\ & \times\frac{1}{\mathrm{BW}(\bar{k}_{12})}\left|\tilde{\bar{\varepsilon}}^{\mu}_{12}\mathcal{M}^{(2)}_{\mathrm{D},\mu}\left(\tilde{\bar{k}}_{12};\tilde{\bar{k}}_1,\tilde{\bar{k}}_2\right)\right|^2 \\ & \times\mathrm{d}\Phi_{\mathrm{rad}}\left(\bar{k}_{12}+\bar{k}_5;z,y,\phi\right)\mathrm{d}\Phi_6\left(Q;\bar{k}_1,\bar{k}_2,k_3,k_4,\bar{k}_5,k_6\right)\Bigg] \\ & \times\frac{1}{\mathrm{BW}(k_{34})}\left|\tilde{\varepsilon}^{\mu}_{34}\mathcal{M}^{(2)}_{\mathrm{D},\mu}\left(\tilde{k}_{34};\tilde{k}_3,\tilde{k}_4\right)\right|^2.\end{aligned} \tag{3.14}$$

As before, only the dipole $\mathcal{D}_{[12]7,5}$ is considered while the other dipoles are omitted for simplicity. Performing the integration over the radiation phase space gives the integrated dipole

$$\begin{aligned}\mathcal{I} \propto \sum_{\lambda_{12},\lambda_{34}}\Bigg[& \mathcal{I}_{[12]7,5}(\tilde{\bar{k}}_{12},\bar{k}_5)\left|\mathcal{M}^{(4)}_{\mathrm{P},\mu\nu}\left(Q;\tilde{\bar{k}}_{12},\tilde{k}_{34},\bar{k}_5,k_6\right)\tilde{\bar{\varepsilon}}^{\mu,*}_{12}\tilde{\varepsilon}^{\nu,*}_{34}\right|^2 \\ & \times\frac{1}{\mathrm{BW}(\bar{k}_{12})\,\mathrm{BW}(k_{34})}\left|\tilde{\bar{\varepsilon}}^{\mu}_{12}\mathcal{M}^{(2)}_{\mathrm{D},\mu}\left(\tilde{\bar{k}}_{12};\tilde{\bar{k}}_1,\tilde{\bar{k}}_2\right)\right|^2\left|\tilde{\varepsilon}^{\mu}_{34}\mathcal{M}^{(2)}_{\mathrm{D},\mu}\left(\tilde{k}_{34};\tilde{k}_3,\tilde{k}_4\right)\right|^2 \\ & \times\mathrm{d}\Phi_6\left(Q;\bar{k}_1,\bar{k}_2,k_3,k_4,\bar{k}_5,k_6\right)\Bigg],\end{aligned} \tag{3.15}$$

with kernel

$$\mathcal{I}_{[12]7,5}(\tilde{\bar{k}}_{12},\bar{k}_5) = \int_{d=4-2\epsilon}\mathcal{D}_{[12]7,5}(\tilde{\bar{k}}_{12},\bar{k}_5;\tilde{y},\tilde{z},\tilde{\phi})\,\mathrm{d}\Phi_{\mathrm{rad}}\left(\tilde{\bar{k}}_{12}+\bar{k}_5;\tilde{z},\tilde{y},\tilde{\phi}\right)\Bigg]. \tag{3.16}$$

Comparing the functional form of the on-shell integrated-dipole kernel with the off-shell one in Eq. (3.13) one finds a few differences. The shift from the off-shell radiation variables (y, z, ϕ) to their on-shell counterparts $\left(\tilde{z}, \tilde{y}, \tilde{\phi}\right)$ does not affect the kernel as this is only a relabelling of variables. The real difference comes from the momenta that are used to evaluate the kernels. The off-shell kernel is evaluated with the off-shell momenta while the on-shell kernel is evaluated with on-shell momenta.

In the limit of soft-photon emission the CS mapping becomes trivial resulting in $\left\{\bar{k}_{12}, k_{34}, \bar{k}_5, k_6\right\} \to \{k_{12}, k_{34}, k_5, k_6\}$. Omitting the phase-space measure and decay subamplitudes, which are not affected by CS mapping, the on-shell projection in four space-time dimensions results in the subtracted real in the soft limit

$$\begin{aligned}
&\frac{\left|\mathcal{M}^{(5)}_{\mathrm{P},\mu\nu}\left(Q; \tilde{k}_{12}, \tilde{k}_{34}, k_5, k_6, k_7\right) \tilde{\varepsilon}^{\mu,*}_{12} \tilde{\varepsilon}^{\nu,*}_{34}\right|^2}{\mathrm{BW}(k_{12})\,\mathrm{BW}(k_{34})} \\
&\quad - \frac{\mathcal{D}_{[12]7,5}(\tilde{\bar{k}}_{12}, \bar{k}_5; \tilde{y}, \tilde{z}, \tilde{\phi}) \left|\mathcal{M}^{(4)}_{\mathrm{P},\mu\nu}\left(Q; \tilde{\bar{k}}_{12}, \tilde{k}_{34}, \bar{k}_5, k_6\right) \tilde{\varepsilon}^{\mu,*}_{12} \tilde{\varepsilon}^{\nu,*}_{34}\right|^2}{\mathrm{BW}(\bar{k}_{12})\,\mathrm{BW}(k_{34})} \\
\to & \\
&\frac{\left|\mathcal{M}^{(5)}_{\mathrm{P},\mu\nu}\left(Q; \tilde{k}_{12}, \tilde{k}_{34}, k_5, k_6, k_7\right) \tilde{\varepsilon}^{\mu,*}_{12} \tilde{\varepsilon}^{\nu,*}_{34}\right|^2}{\mathrm{BW}(k_{12})\,\mathrm{BW}(k_{34})} \\
&\quad - \frac{\mathcal{D}_{[12]7,5}(\tilde{k}_{12}, k_5; \tilde{y}, \tilde{z}, \tilde{\phi}) \left|\mathcal{M}^{(4)}_{\mathrm{P},\mu\nu}\left(Q; \tilde{k}_{12}, \tilde{k}_{34}, k_5, k_6\right) \tilde{\varepsilon}^{\mu,*}_{12} \tilde{\varepsilon}^{\nu,*}_{34}\right|^2}{\mathrm{BW}(k_{12})\,\mathrm{BW}(k_{34})}.
\end{aligned} \tag{3.17}$$

Here the correct cancellation of the IR singularities in the soft-photon limit is shown. This means that the constructed local counterterms work as intended.

After demonstrating that the local counterterms function as needed, it is required to test, if they feature the correct correspondence between the integrated and local counterterms. To this end the two expressions

$$\begin{aligned}
\text{Eq. (3.14)}: &\quad \int_{(d=4)} \mathcal{D}_{[12]7,5}(\tilde{\bar{k}}_{12}, \bar{k}_5; \tilde{y}, \tilde{z}, \tilde{\phi})\, \mathrm{d}\Phi_{\mathrm{rad}}\left(\bar{k}_{12} + \bar{k}_5; z, y, \phi\right), \\
\text{Eq. (3.16)}: &\quad \int_{(d=4-2\epsilon)} \mathcal{D}_{[12]7,5}(\tilde{\bar{k}}_{12}, \bar{k}_5; \tilde{y}, \tilde{z}, \tilde{\phi})\, \mathrm{d}\Phi_{\mathrm{rad}}\left(\tilde{\bar{k}}_{12} + \bar{k}_5; \tilde{z}, \tilde{y}, \tilde{\phi}\right) \\
&\qquad = \mathcal{I}_{[12]7,5}(\tilde{\bar{k}}_{12}, \bar{k}_5),
\end{aligned} \tag{3.18}$$

are compared. The first equation is the local-counterterm kernel. The numerical integration over the radiation phase space is done in $d = 4$ space-time dimensions. Also the integration is performed over the off-shell phase space. The second equation shows the integrated-counterterm kernel that is added back. Here the integration is done over the $d = 4 - 2\epsilon$ dimensional on-shell radiation phase space. That the phase-space integration is done over the off-shell phase space for the local counterterms and over the on-shell one for the integrated counterterms introduces a mismatch between them. In principle this means that the approach of using massive dipoles from the literature [56] to cancel the IR divergences from charged resonances is not applicable and one would have to carry out the analytic $d = 4 - 2\epsilon$ dimensional integration over the off-shell phase space.

However, when the counterterms are evaluated with the on-shell projection applied to the subtraction mapped momenta, the mismatch is beyond the accuracy of the DPA. The change from off-shell to on-shell phase space results in a Jacobian factor of the on-shell projection in the integration. When using the on-shell projection defined in Section 2.2 it follows from Eq. (2.15) that the Jacobian factor is of order $\mathcal{O}(M_{\mathrm{W}}^2/k_{12}^2)$. At the fully differential level this Jacobian can be fairly large and cause a significant mismatch between the local and integrated counterterms. At the integrated level this has a much smaller effect because the regions of phase space, where the W boson is far off-shell are suppressed by the Breit-Wigner modulation. The same argument holds in case of differential cross-sections, where the contributions to each bin are dominated by contributions where the W boson is close to on-shell.

While first applying the subtraction mapping comes with the advantage of a nominally smaller discrepancy between the integrated and local counterterms there is an additional subtlety. This occurs when taking an off-shell real phase-space point where the invariants are too small so that it is below the threshold of the on-shell projection given in Eq. (2.10). As the on-shell projection and the subtraction mapping do not commute, the subtraction mapping can push a phase-space point above the threshold. This can happen only in the presence of hard-real radiation. Additional soft radiation can only shift the relevant invariant by a very small amount resulting in the CS mapping and on-shell projection commuting. Normally the kernel of the local counterterms are evaluated with the radiation variables constructed from the on-shell projected real momenta. Since the real phase-space point is below threshold, this cannot be done here. For these phase-space points the kernel part of the dipoles is evaluated with the off-shell real momenta. As the emitted photon needs to be hard these phase-space points are all far from the singular regions. Therefore, the exact treatment of these events has no effect on the local subtraction. Also any discrepancies between the local and integrated dipoles that arise from this are beyond the accuracy of the DPA. Furthermore, it has been shown that this effect is numerically small for $\mathrm{W}^+\mathrm{W}^+$ scattering detailed in Chapter 5.

An important point has been ignored so far. How does the subtraction mapping for the momenta of the resonances translate to a mapping of the decay momenta? The mapped decay momenta are needed to evaluate the decay amplitudes. To apply the mapping to decay momenta the decay momenta are first boosted into the rest frame of the unmapped resonance momentum. Afterwards they are boosted back using the inverse of the boost to the rest frame of the mapped resonance momentum. This gives the mapped decay momenta

$$\bar{k}_i = \Lambda(\bar{k}_{12})^{-1} \cdot \Lambda(k_{12}) \cdot k_i \quad \text{for } i = 1, 2\,, \tag{3.19}$$

where $\Lambda(p)$ denotes the boost to the rest frame of the momentum p.

3.2.1 Dipoles

Following the general discussion from the previous section this section details the explicit functional form of the dipoles used to cancel the IR divergences. The dipoles here are adapted from the massive-fermion dipoles from Refs. [56, 57]. This can be done since photons emitted off W bosons only result in soft divergences and not collinear ones. For the processes studied in more detail in Chapters 4 and 5 the charged resonance will always be a W boson. The

dipoles, however, are more general and can be used for any DPA process with charged resonances.

3.2.2 Final-state massive emitter and final-state massive spectator

The first production level dipole has both as the emitter (label: j) and the spectator (label: k) a massive charged resonance. Following the reasoning from Section 3.2 the CS mapping is applied to the off-shell momenta. Therefore, in general the momentum squared of the resonances will not be equal to their mass squared. This means in contrast to the formulas from the literature [56] the squared masses of the emitter and the spectator are replaced by their momenta squared. For NLO EW the emissus (label: i) will always be a massless photon, allowing us to set $p_i^2 = m_i^2 = 0$. The mass of the mapped emitter m_{ij}^2 is set to p_j^2. The momentum $Q = p_i + p_j + p_k = \bar{p}_j + \bar{p}_k$ is the sum of the emissus, emitter and spectator momenta. This results in the off-shell CS mapping taking the form

$$\begin{aligned} \bar{p}_k &= \sqrt{\frac{\lambda\left(Q^2, p_j^2, p_k^2\right)}{\lambda\left(Q^2, \left(p_i + p_j\right)^2, p_k^2\right)}}\left(p_k - \frac{Q\cdot p_k}{Q^2}Q\right) + \frac{Q^2 + p_k^2 - p_j^2}{2Q^2}Q\,, \\ \bar{p}_j &= Q - \bar{p}_k\,, \end{aligned} \tag{3.20}$$

where $\lambda(x,y,z) = x^2 + y^2 + z^2 - 2xy - 2xz - 2yz$ is used. In the following, the Lorentz invariant radiation variables defined as

$$z \equiv z_i = \frac{p_i\cdot p_k}{p_i\cdot p_k + p_j\cdot p_k}\,, \quad z_j = 1 - z_i\,, \quad y \equiv y_{ij,k} = \frac{p_i\cdot p_j}{p_i\cdot p_j + p_i\cdot p_k + p_j\cdot p_k} \tag{3.21}$$

are used. Furthermore, the rescaled masses

$$\mu_j^2 = \frac{p_j^2}{Q^2}\,, \qquad \mu_k^2 = \frac{p_k^2}{Q^2} \tag{3.22}$$

and the quantities

$$\begin{aligned} \bar{v}_{ij,k} &= \frac{\sqrt{\lambda\left(1, \mu_j^2, \mu_k^2\right)}}{1 - \mu_j^2 - \mu_k^2} = \frac{\sqrt{1 + \left(\mu_j^2\right)^2 + \left(\mu_k^2\right)^2 - 2\left(\mu_j^2 + \mu_k^2 + \mu_j^2\mu_k^2\right)}}{1 - \mu_j^2 - \mu_k^2}\,, \\ v_{ij,k} &= \frac{\sqrt{\left[2\mu_k^2 + \left(1 - \mu_j^2 - \mu_k^2\right)(1-y)\right]^2 - 4\mu_k^2}}{\left(1 - \mu_j^2 - \mu_k^2\right)(1-y)} \end{aligned} \tag{3.23}$$

are utilised to simplify the formulas. The momenta used to compute the radiation variables, rescaled masses, $\bar{v}_{ij,k}$ and $v_{ij,k}$ are the on-shell projected real momenta, when both the real and reduced phase-space point can be projected on-shell. For the special case, where only the reduced phase-space point can be projected on-shell, the quantities are computed in the same functional form with the off-shell real momenta. With all these quantities defined, the local dipole takes the form

$$\begin{aligned} \mathcal{D}_{ij,k} =& (8\pi\alpha)\mu^{2\epsilon}\frac{\theta_{[ij]}\theta_k Q_{[ij]} Q_k}{-yQ^2\left(1 - \mu_j^2 - \mu_k^2\right)} \\ & \left[\frac{2}{1 - (1-z)(1-y)} - \frac{\bar{v}_{ij,k}}{v_{ij,k}}\left(2 - z(1-\epsilon) + \frac{2\mu_j^2}{y\left(1 - \mu_j^2 - \mu_k^2\right)}\right)\right]. \end{aligned} \tag{3.24}$$

Here α is the EW coupling constant and μ is the IR-regularisation scale. The $\theta_{[ij]}\theta_k Q_{[ij]}Q_k$ term is the charge correlation factor. The θ_a take the value -1 when a is an initial-state particle and $+1$ when a is a final-state particle. For this dipole, since the resonances can only be in the final state, $\theta_{[ij]} = \theta_k = +1$ holds. The Q_a denote the electric charge of the particle a in multiples of the elementary charge. For the dipole with a W boson as emitter and spectator studied here the factor takes the values ± 1. To also accommodate the case, where the reduced momenta can be projected on-shell but the real momenta cannot and the dipole kernel is evaluated with the off-shell momenta, the local-dipole kernel is written in a form, where all masses of the resonances are replaced by their corresponding momenta squared. Therefore, this expression of the local-dipole kernel is valid independent of whether p_j and p_k are on- or off-shell. The corresponding integrated dipole is given as

$$\begin{aligned}
\int \mathrm{d}\Phi_{\mathrm{rad}}^{(4-2\epsilon)} \mathcal{D}_{ij,k} \;=\; & \left(-\theta_{[ij]}\theta_k Q_{[ij]}Q_k\right) \frac{\alpha}{2\pi} \frac{(4\pi)^\epsilon}{\Gamma(1-\epsilon)} \left(\frac{\mu^2}{Q^2}\right)^\epsilon \\
& \times \Bigg[\frac{1}{\epsilon}\left(\frac{\ln(\rho)}{\bar{v}_{ij,k}} + 1\right) + \frac{1}{\bar{v}_{ij,k}} \Bigg(-2\ln(\rho)\ln\left(1-(\mu_j+\mu_k)^2\right) - \ln(\rho_j)^2 \\
& - \ln(\rho_k)^2 + \frac{\pi^2}{3} + 4\mathrm{Li}_2(-\rho) - 4\mathrm{Li}_2(1-\rho) - \mathrm{Li}_2(1-\rho_j^2) - \mathrm{Li}_2(1-\rho_k^2) \Bigg) \\
& + \frac{1}{2}\ln(\mu_j^2) - 2 - 2\ln\left((1-\mu_k)^2 - \mu_j^2\right) + \ln(1-\mu_k) \\
& - \frac{2\mu_j^2}{1-\mu_j^2-\mu_k^2}\ln\left(\frac{\mu_j}{1-\mu_k}\right) + 5 - \frac{\mu_k}{1-\mu_k} - \frac{2\mu_k(1-2\mu_k)}{1-\mu_j^2-\mu_k^2} + O(\epsilon) \Bigg],
\end{aligned} \tag{3.25}$$

where

$$\rho_n = \sqrt{\frac{1-\bar{v}_{ij,k} + \dfrac{2\mu_n^2}{1-\mu_j^2-\mu_k^2}}{1+\bar{v}_{ij,k} + \dfrac{2\mu_n^2}{1-\mu_j^2-\mu_k^2}}}, \quad n = j,k, \qquad \rho = \sqrt{\frac{1-\bar{v}_{ij,k}}{1+\bar{v}_{ij,k}}}. \tag{3.26}$$

The formula of the integrated dipole only features a single pole in ϵ. This is a consequence of the massive emitter that only leads to soft and not to collinear singularities.

For the types of processes studied here the charged resonance will always be a W boson. The kernels of the integrated dipoles are always evaluated with the on-shell momenta. Therefore, it can be used that

$$\mu_j^2 = \mu_k^2 = \frac{M_{\mathrm{W}}^2}{Q^2}. \tag{3.27}$$

For standard phase-space points, where the local dipole kernels are evaluated with the on-shell real momenta, this simplification can also be used for the local dipoles.

3.2.3 Final-state massless emitter and final-state massive spectator

Now the case, where the emitter is a massless final-state particle (label: j) and the spectator is a massive resonance (label: k), is discussed. This dipole is very similar to the one in Section 3.2.2 with both emitter and spectator massive. Unless explicitly mentioned the

notation from the massive-massive dipole is reused. For this dipole the emitter is massless; therefore, $p_j^2 = m_j^2 = 0$ simplifies the mapping. The mass squared of the spectator is set to its momentum squared following the same argument as for the massive-massive dipole. Therefore, the CS mapping adapted from the literature [56] is given as

$$\begin{aligned} \bar{p}_k &= \frac{Q}{2}\left(1+\mu_k^2\right) + \frac{1}{2}\frac{Q^2-p_k^2}{\sqrt{(Q\cdot p_k)^2 - Q^2 p_k^2}}\left(p_k - Q\frac{Q\cdot p_k}{Q^2}\right), \\ \bar{p}_j &= Q - \bar{p}_k\,. \end{aligned} \tag{3.28}$$

The radiation variables and invariants are defined in the same way as for the case with a resonance as the emitter and spectator in Eqs. (3.21), (3.22) and (3.23). Also for this dipole, when only the reduced momenta can be projected on-shell and not the real momenta, the off-shell momenta are used to evaluate the invariants. This gives the kernel of the local dipoles

$$\mathcal{D}_{ij,k} = (8\pi\alpha)\mu^{2\epsilon}\,\frac{\theta_{[ij]}\theta_k Q_{[ij]}Q_k}{-y\,Q^2(1-\mu_k^2)}\left[\frac{2}{1-(1-z)(1-y)} - \frac{1}{v_{ij,k}}\left(2-z\,(1-\epsilon)\right)\right]. \tag{3.29}$$

The functional form of the local dipole kernel was constructed in a way to have the same functional form independent of being evaluated with on- or off-shell spectator momenta. The integrated dipole is given as

$$\begin{aligned} \int \mathrm{d}\Phi_{\mathrm{rad}}^{(4-2\epsilon)}\mathcal{D}_{ij,k} = (-\theta_{[ij]}\theta_k Q_{[ij]}Q_k)\frac{\alpha}{2\pi}\frac{(4\pi)^\epsilon}{\Gamma(1-\epsilon)}\left(\frac{\mu^2}{Q^2}\right)^\epsilon \\ \times\left[\frac{1}{\epsilon^2} - \frac{2}{\epsilon}\log\left(1-\mu_k^2\right) - \frac{5\pi^2}{6} + 2\log^2\left(1-\mu_k^2\right) + 2\mathrm{Li}_2\left(1-\mu_k^2\right)\right. \\ \left. + \frac{3}{2\epsilon} + 2 + \frac{3}{1+\mu_k} - 3\log(1-\mu_k) + \mathcal{O}(\epsilon)\right]. \end{aligned} \tag{3.30}$$

The emitter of this dipole is massless; therefore, it not only regularises the singularities from soft-photon emission but also those from photons that are produced collinear to the emitter. In the integrated dipoles this leads to an ϵ^{-2} pole. For W-boson processes the rescaled momenta can be replaced with the rescaled W mass $\mu_k^2 = \frac{M_{\mathrm{W}}^2}{Q^2}$ in the integrated dipoles and the local dipoles when the real phase-space point can be projected on-shell.

3.2.4 Final-state massive emitter and final-state massless spectator

In the dipole detailed here the emitter is a massive resonance (label: j) and the spectator is a massless final-state particle (label: k). The CS mapping from literature [56] is adapted for this dipole. This dipole has a massless spectator; therefore, the equations are simplified by setting $p_k^2 = m_k^2 = 0$. The off-shell CS mapping is defined as

$$\bar{p}_k = p_k\frac{Q^2-p_j^2}{2\,Q\cdot p_k}, \qquad \bar{p}_j = Q - p_k\frac{Q^2-p_j^2}{2\,Q\cdot p_k}\,. \tag{3.31}$$

Again using the radiation variables defined before in Eqs. (3.21), (3.22) and (3.23) the local dipole kernel reads

$$\mathcal{D}_{ij,k} = (8\pi\alpha)\mu^{2\epsilon}\,\frac{\theta_{[ij]}\theta_k Q_{[ij]}Q_k}{-y\,Q^2(1-\mu_j^2)}\left[\frac{2}{1-(1-z)(1-y)} - 2 + z\,(1-\epsilon) - \frac{2\mu_j^2}{y\,(1-\mu_j^2)}\right], \tag{3.32}$$

while its integrated counterpart is given by

$$\begin{aligned}\int \mathrm{d}\Phi_{\mathrm{rad}}^{(4-2\epsilon)} \mathcal{D}_{ij,k} = (-\theta_{[ij]}\theta_k Q_{[ij]} Q_k) \frac{\alpha}{2\pi} \frac{(4\pi)^\epsilon}{\Gamma(1-\epsilon)} \left(\frac{\mu^2}{Q^2}\right)^\epsilon \\ \times \left[\frac{2}{\epsilon}\log\mu_j - 2\log^2\mu_j - 4\log\mu_j \log\left(1-\mu_j^2\right) - 4\mathrm{Li}_2\left(1-\mu_j^2\right)\right. \\ \left. + \frac{1}{\epsilon} + 3 + \frac{3\mu_j^2-1}{\mu_j^2-1}\log\mu_j - 2\log\left(1-\mu_j^2\right) + \mathcal{O}(\epsilon)\right].\end{aligned} \tag{3.33}$$

As for the case of a massive resonance emitter and spectator the absence of a collinear singularity only results in a single pole in ϵ in the integrated dipole.

3.2.5 Final-state massive emitter and initial-state massless spectator

The dipoles discussed so far were all with final-state emitters and spectators. This dipole has an emitter that is a massive resonance (label: j) and a spectator that is a massless initial-state particle (label: a). The CS mapping is adapted from literature [56]. As for the final-final dipoles the subtraction mapping is applied to the off-shell momenta. Defining as $Q = p_i + p_j - p_a = \bar{p}_j - \bar{p}_a$, the mapped momenta are

$$\bar{p}_j = p_i + p_j - (1 - x_{ij,a})\, p_a, \qquad \bar{p}_a = x_{ij,a}\, p_a\,. \tag{3.34}$$

The radiation variables

$$x \equiv x_{ij,a} = \frac{p_i{\cdot}p_a + p_j{\cdot}p_a - p_i{\cdot}p_j}{p_i{\cdot}p_a + p_j{\cdot}p_a}\,, \quad z \equiv z_i = \frac{p_i{\cdot}p_a}{p_i{\cdot}p_a + p_j{\cdot}p_a}\,, \quad z_j = 1 - z_i \tag{3.35}$$

used to compute the dipole kernels are defined in the same functional form as for the equivalent massless dipoles [56, 58]. It is useful to define the quantity

$$\mu_j^2 = \frac{p_j^2}{2\bar{p}_j{\cdot}p_a} = \frac{p_j^2}{2\left(p_i{\cdot}p_a + p_j{\cdot}p_a\right)} = x\frac{p_j^2}{p_j^2 - Q^2}\,. \tag{3.36}$$

When the real phase-space point can be projected on-shell the invariants are all constructed from the on-shell momenta. The off-shell real momenta are used, when this is not possible. The local dipole reads

$$\mathcal{D}_{ij,a} \;=\; (8\pi\alpha)\mu^{2\epsilon} \frac{\theta_{[ij]}\theta_a Q_{[ij]} Q_a}{(1-x)\left(Q^2 - p_j^2\right)} \left(\frac{2}{1-x+z} + z\,(1-\epsilon) - 2 - \frac{2p_j^2}{p_j^2 - Q^2}\frac{x}{1-x}\right), \tag{3.37}$$

and its integration leads to the integrated counterterm

$$\begin{aligned}\int \mathrm{d}\Phi_{\mathrm{rad}}^{(4-2\epsilon)} \mathcal{D}_{ia,j} = \theta_{[ij]}\theta_a Q_{[ij]} Q_a \frac{\alpha}{2\pi} \frac{(4\pi)^2}{\Gamma(1-\epsilon)} \left(\frac{\mu^2}{2\bar{p}_j \cdot p_a}\right)^{\epsilon} \\ \times \Bigg\{ \left[\frac{1-x}{2\left(1-x+\mu_j^2\right)^2} - \frac{2}{1-x}\Big(1+\log\left(1-x+\mu_j^2\right)\Big) \right]_+ \\ + \left(\frac{2}{1-x}\right)_+ \log(2+\mu_j^2-x) \\ + \delta(1-x)\Bigg[\frac{1}{\epsilon}\left(\log\left(\frac{\mu_j^2}{1+\mu_j^2}\right)+1\right) - \frac{1}{2}\log^2\left(\mu_j^2\right) + \frac{1}{2}\log\left(\mu_j^2\right) \\ + \frac{3}{2} - \frac{2\pi^2}{3} + \frac{1}{2}\log^2(1+\mu_j^2) - 2\log(\mu_j^2)\log(1+\mu_j^2) \\ - 4\mathrm{Li}_2(-\mu_j^2) + \frac{1}{2}\log(1+\mu_j^2) + \frac{\mu_j^2}{2\left(1+\mu_j^2\right)} \Bigg] + \mathcal{O}(\epsilon) \Bigg\},\end{aligned} \tag{3.38}$$

where the plus distribution is defined as

$$\int_{-1}^{1} a(x)_+ \, b(x) \, \mathrm{d}x = \int_{-1}^{1} a(x) \big[b(x) - b(1) \big] \mathrm{d}x \,. \tag{3.39}$$

The integrated dipole will always be evaluated with on-shell projected momenta. Therefore, for resonant W bosons the simplification

$$\mu_j^2 \;=\; \mu_{\mathrm{W}}^2 = x \frac{M_{\mathrm{W}}^2}{M_{\mathrm{W}}^2 - Q^2} \tag{3.40}$$

can be used.

3.2.6 Initial-state massless emitter and final-state massive spectator

In the last production-level dipole the emitter is a massless initial-state particle (label: a) and the spectator is a massive resonance (label: j). The definition of this dipole follows the results of Ref. [56]. By setting $Q = p_i + p_j - p_a = \bar{p}_j - \bar{p}_a$ the CS mapping with the off-shell phase-space point is defined as

$$\bar{p}_j = p_i + p_j - (1 - x_{ij,a})\, p_a \,, \qquad \bar{p}_a = x_{ij,a} p_a \,. \tag{3.41}$$

The radiation variables are taken from Eq. (3.35). The formula for the rescaled momentum of the spectator is the same as for the emitter from Eq. (3.36). The on-shell projected momenta are used unless the real phase-space point cannot be projected on-shell. The local dipole takes the form

$$\mathcal{D}_{ia,j} = (8\pi\alpha)\mu^{2\epsilon} \frac{\theta_{[ia]}\theta_j Q_{[ia]} Q_j}{z\left(Q^2 - p_j^2\right)} \left(\frac{2}{1-x+z} - (1+x) - \epsilon\,(1-x) \right) , \tag{3.42}$$

while the integrated counterpart can be written as

$$\begin{aligned}\int \mathrm{d}\Phi_{\mathrm{rad}}^{(4-2\epsilon)} \mathcal{D}_{ia,j} = \theta_{[ia]}\theta_j Q_{[ia]} Q_j \frac{\alpha}{2\pi} \frac{(4\pi)^\epsilon}{\Gamma(1-\epsilon)} \left(\frac{\mu^2}{2\bar{p}_j \cdot p_a}\right)^\epsilon \\ \left\{ -\frac{2}{\epsilon}\left(\frac{1}{1-x}\right)_+ + 4\left(\frac{\log(1-x)}{1-x}\right)_+ + 2\left(\frac{1}{1-x}\right)_+ \log\left(\frac{2-x}{2-x+\mu_j^2}\right) \right. \\ + \frac{1}{\epsilon}(1+x) - (1+x)\log(1-x) + (1-x) - (1+x)\log\left(\frac{1-x}{1-x+\mu_j^2}\right) \\ - \frac{2}{1-x}\log(2-x) + \delta(1-x)\left[\frac{1}{\epsilon^2} + \frac{1}{\epsilon}\log(1+\mu_j^2) + \frac{1}{2}\log^2(1+\mu_j^2)\right. \\ \left.\left. + 2\mathrm{Li}_2\left(\frac{1}{1+\mu_j^2}\right) - \frac{\pi^2}{6}\right] + \mathcal{O}(\epsilon)\right\}.\end{aligned} \tag{3.43}$$

Like for all other dipoles the integrated dipole is evaluated with the on-shell momenta. Therefore, Eq. (3.40) can be used to simplify the expression for resonant W bosons.

3.2.7 Additional dipoles with a massive resonant spectator

There are types of EW dipoles that only need one spectator as a recoiler for the CS mapping. Therefore, all singularities associated to them can be cancelled with one choice of spectator. These are dipoles of the types:

- where a photon is emitted from the reduced process and afterwards splits into a fermion-antifermion pair,
- where an initial-state fermion splits into a fermion and a photon and the photon enters the reduced process,
- where an initial-state photon splits into a fermion-antifermion pair.

In principle one could use a resonance as a spectator for these dipoles. This is, however, not necessary as one can always choose one of the massless external particles as the spectator. Doing so will cancel this specific singularity with a standard massless CS dipole. When generalising this method to NLO QCD with colour charged resonances like the top quark care must be taken. The corresponding QCD dipoles with gluons replacing the photons feature colour correlations; therefore, a dipole for each possible spectator including the colour charged resonance is needed. Therefore, dedicated dipoles with a massive spectator would be needed for a generalisation. These dipoles are known in the literature [56] and can be adapted to the DPA.

3.3 Decay counterterms

So far the focus has been on the IR singularities in the production part of the amplitude and their treatment. Unresolved radiation can also be emitted from the decay sub-process of one of the resonances. As for the production, having charged resonances leads to additional singular configurations. The emission of a photon from a massless decay particle leads to both

soft and collinear singularities. When a photon is emitted off the W-boson propagator, this results only in soft divergences. These divergences need to be subtracted with a counterterm.

The subtraction method of equivalent IR singularities present in top-quark decays [59] can also be used for W-boson decays. As the emission of soft photons from top quarks and W bosons does not give rise to spin-dependent singularities the top-quark dipoles can also be used for W bosons. This approach has been used successfully in the calculations from Refs. [54, 60]. Similar to the production counterterms studied previously the typical energy scales of the hard scattering at the LHC are of a similar order as the masses of the resonances. Therefore, the quasi-collinear configurations do not cause problems [57].

Here a slightly different approach is chosen. A subtraction counterterm is used that reproduces the decay of the W boson into a photon and a charged lepton and the corresponding neutrino. This counterterm uses a mapping, where the charged lepton takes the role of emitter and the neutrino takes the role of spectator. With k_1 the momentum of the charged lepton, q the momentum of the parent W boson, k_3 the momentum of the photon and k_2 the momentum of the neutrino, the mapping takes the form

$$\bar{k}_1^\mu = k_1^\mu + k_3^\mu - \frac{s_{13}}{q^2 - s_{13}} k_2^\mu \,, \qquad \bar{k}_2^\mu = k_2^\mu \frac{q^2}{q^2 - s_{13}} \tag{3.44}$$

known from massless final-final dipoles [58]. The radiation variables are defined in the usual way as

$$y = \frac{s_{13}}{q^2} \,, \qquad z = \frac{s_{12}}{s_{12} + s_{23}} = \frac{s_{12}}{q^2 - s_{13}} \,. \tag{3.45}$$

This gives the local counterterm

$$\mathcal{D}^{(\mathrm{dec})}(q^2, y, z) = \frac{8\pi\alpha}{q^2\, y} \frac{(1-y)\,(1-z)\,[1 + (1-y)(z^2 - y(2 - 2z + z^2))]}{[1 - z(1-y)]^2} \,. \tag{3.46}$$

This counterterm cancels the soft and collinear singularities from the photon emitted from the charged lepton as well as the soft singularity, when the photon is emitted from the W boson. To get the functional expression of the integrated counterterm an analytic integration over the radiation phase space in $d = 4 - 2\epsilon$ dimensions is performed. This gives the integrated counterterm

$$\int \mathrm{d}\Phi_{\mathrm{rad}}\, \mathcal{D}^{(\mathrm{dec})}(q^2, y, z) \;= \frac{\alpha}{2\pi} \frac{(4\pi)^\epsilon}{\Gamma(1-\epsilon)} \left(\frac{\mu^2}{q^2}\right)^\epsilon \left[\frac{1}{\epsilon^2} + \frac{5}{2\epsilon} + \left(\frac{95}{12} - \frac{\pi^2}{2}\right) + \mathcal{O}(\epsilon)\right] . \tag{3.47}$$

The same ϵ poles are found as for top-quark dipoles from Ref. [59]

The decay counterterm is explicitly constructed for a W boson decaying into a photon, a charged lepton and a neutrino. But it can also be used to cancel the divergences present, when the W boson decays hadronically into a photon, a quark and an antiquark. In this case the decay counterterm is needed twice, once with the quark as the emitter in the mapping and the antiquark as the spectator and once with the antiquark as the emitter and the quark as the spectator. Additionally, two massless CS dipoles with the quark and antiquark as emitter and spectator are needed.

The subtraction mapping of the counterterm is only designed for the case, where the spectator of the mapping is massless. For processes with resonant W bosons decaying into two massless fermions at LO this is always given. When studying processes with charged

resonances that decay into three or more particles at LO, such as the top quark, the given mapping cannot be used. Here the spectator momentum is the sum of the final-state decay momenta that are not the emitter or emissus. Therefore, in general the spectator momentum is not lightlike. This requires a generalised mapping that includes massive spectators.

The Eqs. (3.44)−(3.47) keep q^2 as the mass squared of the W boson. As for the production dipoles the subtraction mapping is applied to the off-shell real momenta. The on-shell projection $\mathrm{DPA}^{(2,2)}$ is applied to the reduced kinematics which are then used to evaluate the reduced process. The real momenta are projected on-shell with the $\mathrm{DPA}^{(2,3)}$ or $\mathrm{DPA}^{(3,2)}$ because of the additional decay particle present. The on-shell projection was designed in a way not to change the ratios of the decay invariants. Therefore, the radiation variables from Eq. (3.45) that are used in the kernel evaluation are left unchanged by the on-shell projection. Furthermore also the integration measure does not change resulting in the same pole structure in the integrated counterterm independent of whether $q^2 = M_{\mathrm{W}}^2$ holds or not. Since the numerical integration of the local counterterms is performed over the off-shell phase space and the analytic integration of the integrated counterterms is performed over the on-shell phase space, there is a mismatch between them. This means that the term that is subtracted from the real-emission contribution is not exactly added back by the integrated counterterms. The mismatch stems from the Jacobian of the on-shell projection. This Jacobian can be large for phase-space points where the resonances are far off-shell. Following the same argument as for the production counterterms, when the phase-space integration is performed these regions are suppressed by the Breit-Wigner propagator. Therefore, this only results in a discrepancy that is beyond the accuracy of the DPA and can be neglected.

The method of first projecting the real phase-space point on-shell and afterwards applying the subtraction mapping, which was used for ZZ production [39], also produces a mismatch between the local and integrated counterterms. Other than for the production counterterms for the decay counterterms this mismatch is also beyond the accuracy of the DPA. Therefore, for the decay counterterms both methods give nominally equally valid results. In particular, for $\mathrm{W}^+\mathrm{W}^+$ scattering, detailed in Chapter 5, it has been found that the difference is beyond the numerical uncertainty of the integration. This is different from the production dipoles. There the different order of on-shell projection and subtraction mapping can lead to sizeable differences.

3.4 Generalisation to NLO QCD

So far the discussion has only been about the NLO EW real-emission corrections in the presence of electrically charged resonances. The used method can be generalised to also treat the NLO QCD real-emission corrections. For colour neutral resonances like the W and Z boson, similar to the EW case with chargeless resonances, no additional IR-singular structures associated to the resonance appear. All present IR divergences can be treated with the same dipole structures used for full off-shell processes. As done in the EW case the dipoles connecting different decays or production and decay are not needed. This has been successfully done in the past as seen in Refs. [39, 52, 53].

The case of colour charged resonances like the top quark is more involved. Here additional IR-singular structures appear that need to be subtracted with counterterms. The general method is the same as for the EW case. Also here contributions with real emission from the resonant propagators are present. The emission of a photon is replaced by the emission of a

gluon. The same partial fractioning used for the EW emission can also be used to split the diagrams into a contribution where the gluon is emitted from the production and one where it is emitted from the decay. After the split is performed the IR divergences can be cancelled by massive dipoles. The EW dipoles seen before can be adapted to the QCD case. The reduced amplitude squared is replaced by its colour correlated equivalent. The charge correlation factors are replaced by the colour correlations. Also for QCD dipoles the order in which the on-shell projection and the subtraction mapping are applied matters. The argument made for first applying the subtraction mapping in Section 3.2, that the mismatch between the local and integrated dipoles is beyond the accuracy of the DPA, remains valid for QCD dipoles. Therefore, the ordering of first applying the subtraction mapping and afterwards projecting the reduced momenta on-shell should also be used for QCD dipoles. As in the EW case this choice comes with the subtlety that there are phase-space points where the reduced momenta can be projected on-shell but the real momenta cannot be projected on-shell. Evaluating the dipole kernel with the off-shell momenta for these phase-space points can also be done for QCD dipoles.

There are some differences to the EW case already noted before. The colour correlations require that the kinds of dipoles in Section 3.2.7 with gluons replacing the photons are needed. The basic structure of these dipoles is known in the literature [56] and can be adapted to DPA in the same manner as the EW dipoles. For a resonant top quark, that decays into three particles at LO, the mapping of the decay counterterm needs to be extended to massive spectators.

Chapter 4

Vector-boson pair production

The first class of processes to study polarisation are vector-boson pair-production processes. They are not as sensitive to the intricate details of vector-boson interactions as VBS processes, since the effects of the unitary cancellations are reduced. However, they are much simpler to study. Compared to VBS processes vector-boson pair-production processes only have four instead of six final-state particles at LO. Furthermore, the number of partonic channels that contribute is much smaller. Their simpler structure makes them ideal to test the methods both theoretical and experimental, later used for the study of VBS processes. The investigation of their polarisations is nevertheless suited to test the EW part of the Standard Model. In Section 4.1 the production of a Z and W^+ boson in the semi-leptonic decay mode is treated. The presented results of this computation have previously been published in Ref. [61]. In Section 4.2 the production of a W^+W^- pair with fully leptonic decay is discussed. The results of this calculation have already been published in Ref. [60].

4.1 Polarised ZW^+ production with semi-leptonic decay at NLO QCD

The primary focus of polarisation studies both experimental [62–72] and phenomenological [39, 51–55, 73–97] in vector-boson pair production has been on processes where both bosons decay leptonically. Studying hadronic final states at the LHC comes with several advantages and disadvantages compared to purely leptonic final states. Hadronic decays of W bosons do not contain any unobservable neutrinos that can only be treated as missing transverse momentum in experimental measurements. This allows for better reconstruction of the W-boson momentum. Hadronic decays benefit from a higher event rate at collider experiments compared to leptonic decays because of the larger branching ratio. The main drawback of the study of hadronic decays is the more complicated reconstruction of jets compared to charged leptons. In particular, charged leptons can be distinguished by their charge and flavour. For jets this is much more complicated, as in general the type of quark that initiated the jet cannot be reconstructed. This means contributions from resonant W^+, Z and W^- bosons cannot be distinguished. In a polarisation study they would all have to be treated as separate contributions to the same final state. In experiments the hadronic decays result in an overall increase in hadronic activity. This makes it much harder to associate the measured signals in the detector to the final states of the hard scattering. Another downside is the

large QCD background present that has to be subtracted before any polarisation study can be done.

Nevertheless there has been an increased interest in measuring gauge-boson polarisation at the LHC also in semi-leptonic decays. This has brought about a few phenomenological studies [98–101] of hadronically decaying bosons. The focus of past polarisation studies has been the discrimination of longitudinal and transverse bosons in boosted kinematic configurations [98–100]. The focus on boosted setups is driven by the interest in the substructure of fat jets. Much information on the polarisation of the parent vector boson can be extracted from the boosted-fat-jet substructure with traditional observables like N-subjettiness [98] and soft-drop [100], or machine-learning [99] techniques. The jet constituents can up to a degree be associated to the decay quarks. Therefore, these methods are expected to extract the maximal amount of information on the polarisation of the parent vector boson. Another method that has recently been proposed for polarisation discrimination are energy correlators [101]. There may also be LHC observables that are sensitive to the polarisation without having any dependence on the jet substructure [71] as existing polarisation studies targeting the purely leptonic decay channels suggest.

So far only sensitivity studies for polarisation measurements in di-boson processes with semi-leptonic decays have been performed, for the high-energy [102] and high-luminosity (HL) [103] runs of the LHC. The main focus of these studies was on VBS processes rather than vector-boson production. No actual measurements have been conducted so far for semi-leptonic vector-boson production.

However, there have been other studies conducted for di-boson production with semi-leptonic decay. In particular, searches for potential new resonances [104–108] have been carried out with the 13 TeV LHC data. Including a polarisation split in these measurements could further constrain new physics effects [109] and the spin of the potential new resonance decaying into two vector bosons. For di-boson processes with purely leptonic decays many studies both unpolarised [110–131] and polarised [39, 52–55, 88] exist that include higher-order corrections. The methods needed to compute the NLO QCD corrections to polarised di-boson production with semi-leptonic decays are known [132, 133]. Despite this so far only LO or LO + parton shower (PS) accurate studies exist but no NLO accurate computations in a realistic LHC setting.

4.1.1 Setup

The considered process is the inclusive production of a Z and a W^+ boson at the LHC:

$$\mathrm{pp} \to \mathrm{Z}\,(\to \ell^+\ell^-)\,\mathrm{W}^+\,(\to \mathrm{jj}) + X\,, \qquad \mathrm{pp} \to \mathrm{Z}\,(\to \ell^+\ell^-)\,\mathrm{W}^+\,(\to \mathrm{J}) + X\,, \tag{4.1}$$

where the Z boson decays leptonically and the W^+ boson decays hadronically. The two decay channels differ in the treatment of the decay jets. The first process corresponds to the resolved setup where the W^+ boson decays into two separated jets and the second one to the unresolved setup where the W^+ decays into one fat jet. The details of the two setups are explained later in this section. The LO contribution $\mathcal{O}(\alpha^4)$ and the NLO QCD corrections $\mathcal{O}(\alpha_\mathrm{s}\alpha^4)$ are computed in the Standard Model for the two setups. The calculation of the polarised and unpolarised cross-sections is done using the DPA as explained in Chapter 2. The polarisation split is performed according to Section 2.3. For the non-resonant, QCD, interference, ZW^- and ZZ backgrounds only a LO accurate calculation is performed. As

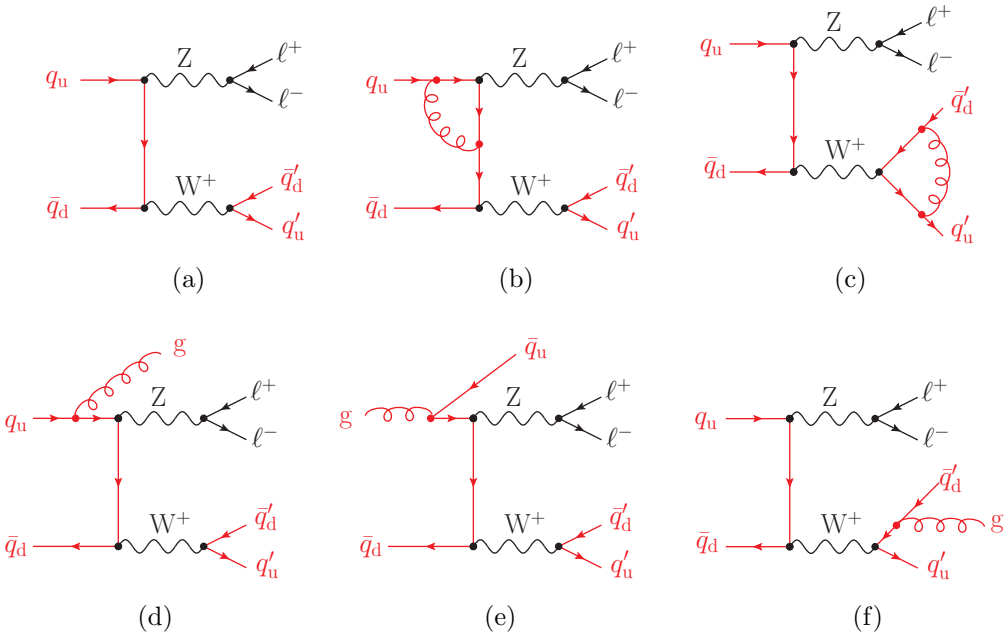

Figure 4.1: Sample tree-level (a), one-loop (b-c), and real-radiation (d-f) diagrams contributing to di-boson production at the LHC in the semi-leptonic decay channel at NLO QCD. Particles carrying colour charge are highlighted in red.

emphasised before the novelty of this calculation compared to previous polarisation studies targeting ZW$^+$ production [53] is the treatment of a semi-leptonic decay mode. Unlike fully leptonic decay modes where QCD real radiation can only stem from the production subprocess, for semi-leptonic decays the real emission can also be emitted from one of the decays. A selection of the diagrams contributing to the process are shown in Figure 4.1. Figure 4.1(a) shows one of the tree-level diagrams. The diagrams in Figures 4.1(b) and 4.1(c) depict contributions to the factorisable virtuals. The Figures 4.1(d) and 4.1(e) depict real-emission diagrams where the real radiation is emitted from the production. Diagrams of this type are also present in purely leptonic decay modes. Figure 4.1(f) shows one of the diagrams with real radiation from the decay subprocess.

The calculation is done in the five flavour scheme with no quark-family mixing assuming a unit Cabibbo-Kobayashi-Maskawa (CKM) matrix. The masses of all light quarks and leptons are set to zero. The on-shell masses and decay widths taken from the Particle Data Group (PDG) [134] are as follows:

$$\begin{aligned} M_{\mathrm{W}}^{\mathrm{OS}} &= 80.379\,\mathrm{GeV}, & M_{\mathrm{Z}}^{\mathrm{OS}} &= 91.1876\,\mathrm{GeV}, \\ \Gamma_{\mathrm{W}}^{\mathrm{OS}} &= 2.085\,\mathrm{GeV}, & \Gamma_{\mathrm{Z}}^{\mathrm{OS}} &= 2.4952\,\mathrm{GeV}. \end{aligned} \tag{4.2}$$

The on-shell masses are then converted to their pole equivalents with the formula [135]

$$M_V = \frac{M_V^{\mathrm{OS}}}{\sqrt{1+\left(\frac{\Gamma_V^{\mathrm{OS}}}{M_V^{\mathrm{OS}}}\right)^2}}, \quad \Gamma_V = \frac{\Gamma_V^{\mathrm{OS}}}{\sqrt{1+\left(\frac{\Gamma_V^{\mathrm{OS}}}{M_V^{\mathrm{OS}}}\right)^2}}. \tag{4.3}$$

No diagrams containing the Higgs boson or the top quark contribute at the considered orders; therefore, their masses and widths have no effect on the results. To calculate the

EW coupling α the G_μ scheme [43] with real masses is employed giving

$$\alpha = \frac{\sqrt{2}}{\pi} G_\mu M_\mathrm{W}^2 \left(1 - \frac{M_\mathrm{W}^2}{M_\mathrm{Z}^2}\right), \qquad G_\mu = 1.16638 \cdot 10^{-5}\,\mathrm{GeV}^{-2}. \tag{4.4}$$

The `NNPDF31_nlo_as_0118` [136, 137] parton-distribution functions (PDFs) are used. The LHAPDF package [138] is utilised to interface the PDFs with the Monte Carlo code. Furthermore, the built-in routines of LHAPDF are used to compute the running of α_s. The CS-dipole subtraction scheme [56, 58, 139], that has been adapted to the DPA, treats the IR singularities of QCD origin. The initial-state collinear singularities are treated with the $\overline{\mathrm{MS}}$ factorisation scheme. To estimate the size of the QCD scale uncertainties a seven-point scale variation is performed. The renormalisation and factorisation scales are varied by factors of

$$(\mu_\mathrm{R}/\mu_0, \mu_\mathrm{F}/\mu_0) = (1/2, 1/2), (1/2, 1), (1, 1/2), (1, 1), (1, 2), (2, 1), (2, 2). \tag{4.5}$$

The smallest and largest value obtained give the scale uncertainty bands.

The CMS analysis in Ref. [108] (see Table 1 therein) is taken as a template for the event selection and reconstruction. The jets are clustered with the anti-k_T algorithm [140] with a maximal rapidity of 5. The analysis is carried out in two slightly different setups: the resolved setup and the unresolved setup. Their main difference is the recombination method of the final-state jets and how the jets from the W^+ boson decay are identified. Furthermore, they differ slightly in the way the phase-space cuts are applied to the jets. In the resolved setup the final state consists of:

- at least two final-state jets (jet clustering radius $R_0 = 0.4$) fulfilling $p_{\mathrm{T,j}} > 30\,\mathrm{GeV}$, $|y_\mathrm{j}| < 2.4$ and $\Delta R_{\mathrm{j}\ell^\pm} > 0.4$,
- the system of decay jets (jet system: J) is defined as the two jets after clustering which feature an invariant mass closest to the pole mass of the W boson,
- with the jet system fulfilling $p_{\mathrm{T,J}} > 200\,\mathrm{GeV}$ and $65\,\mathrm{GeV} < M_\mathrm{J} < 106\,\mathrm{GeV}$,
- two same flavour opposite charged leptons satisfying $p_{\mathrm{T},\ell^\pm} > 40\,\mathrm{GeV}$, $|y_{\ell^\pm}| < 2.4$, $p_{\mathrm{T},\ell\ell} > 200\,\mathrm{GeV}$ and $76\,\mathrm{GeV} < M_{\ell\ell} < 106\,\mathrm{GeV}$.

In the unresolved setup the final state consists of:

- at least one massive wide jet (jet system: J) (jet clustering radius $R_0 = 0.8$),
- with the jet system fulfilling $|y_\mathrm{J}| < 2.4$, $\Delta R_{\mathrm{J},\ell^\pm} > 0.8$, $p_{\mathrm{T,J}} > 200\,\mathrm{GeV}$ and $65\,\mathrm{GeV} < M_\mathrm{J} < 105\,\mathrm{GeV}$,
- two same flavour opposite charged leptons satisfying $p_{\mathrm{T},\ell^\pm} > 40\,\mathrm{GeV}$, $|y_{\ell^\pm}| < 2.4$, $p_{\mathrm{T},\ell\ell} > 200\,\mathrm{GeV}$ and $76\,\mathrm{GeV} < M_{\ell\ell} < 106\,\mathrm{GeV}$.

By requiring that the transverse momentum of the jet system and the electron-positron pair is large, this setup focuses on a regime where both vector bosons are very boosted. No jet veto is applied in either setup as the logarithmically-enhanced real corrections with soft-boson radiation [121, 141, 142] are suppressed. This is caused by the transverse-momentum cuts

on the jet system and the electron-positron pair. The symmetric nature of the transverse-momentum cuts, which are applied to the jet system and the electron-positron pair, introduces a strong sensitivity to quasi-soft and quasi-collinear QCD initial-state radiation. This sensitivity causes large higher order corrections in transverse-momentum distributions close to the cut [143–147]. The renormalisation and factorisation scales are set to

$$\mu_{\mathrm{R}} = \mu_{\mathrm{F}} = \frac{M_{\mathrm{T,Z}} + M_{\mathrm{T,J}}}{2}\,. \tag{4.6}$$

Here $M_{\mathrm{T,Z}}$ and $M_{\mathrm{T,J}}$ denote the transverse masses of the Z boson and jet system defined as

$$M_{\mathrm{T,Z}} = \sqrt{p^2_{\mathrm{T},\ell\ell} + M^2_{\ell\ell}}\,, \qquad M_{\mathrm{T,J}} = \sqrt{p^2_{\mathrm{T,J}} + M^2_{\mathrm{J}}}\,. \tag{4.7}$$

The polarisation states of virtual particles are frame dependent. To define the polarisation of the W and Z boson their CM frame is used. This frame choice allows for a good interpretation of the results. In this frame the Goldstone-boson equivalence theorem [31,32] can be directly used to explain features seen in the results.

4.1.2 Integrated Results

This section lists the numerical results at the integrated level of doubly-polarised and unpolarised ZW^+ production as described in Section 4.1.1. The computation was performed independently with the two Monte Carlo codes MoCaNLO and BBMC, finding agreement within the integration uncertainties. The shown results here are those calculated with MoCaNLO. Here the Z boson has been chosen to decay into an electron-positron pair. However, the results are equivalent to processes where the Z boson decays into pairs of other massless charged leptons like muons.

Table 4.1 shows the computed integrated cross-sections in the resolved and unresolved setups as specified in Section 4.1.1. The LO results show the comparably large contribution from the purely longitudinal polarisation state contributing at $\approx 35\%$ to the unpolarised result. In contrast to ZZ production in W^+Z production diagrams containing the triple-gauge coupling contribute at LO. Therefore, the production of Goldstone bosons is unsuppressed. In the high-energy limit, which is given by the transverse-momentum requirement, the two longitudinally polarised bosons behave as would-be-Goldstone bosons [31, 32]. Therefore, unlike for ZZ pair production there is no suppression of the LL signal. The purely transverse polarisation state contributes at $\approx 50\%$ giving the dominant contribution. The mixed polarisation states TL and LT contribute at $\approx 4\%$ each. In the high-energy limit the LO amplitudes of the mixed polarisation states are subject to a strong unitarity suppression [148,149]. The unitarity suppression causes the amplitude of the mixed polarisation to be diminished by the energy of the longitudinal vector-boson. In the resolved setup the LO contributions from the mixed polarisation states are very similar while in the unresolved setup the TL polarisation state is $\approx 15\%$ larger. Since the decay quarks of a longitudinal W^+ boson are mainly produced orthogonal to the direction of the W^+ boson in its CM frame they are more likely to be recombined into one jet. For a transversely polarised W^+ boson the decay quarks are mostly emitted in and opposite to the direction of the W^+ boson in the bosons rest frame. Therefore, in the lab frame they tend to have a larger separation compared to the decay particles from a longitudinally polarised W^+ boson. The two quarks are thus less

state	σ_{LO} [fb]	f_{LO}[%]	σ_{NLO} [fb]	f_{NLO}[%]	K_{NLO}	$K_{\text{NLO}}^{(\text{no g})}$
resolved, $Z(e^+e^-)W^+(jj)$						
unpol.	$1.8567(2)^{+1.2\%}_{-1.4\%}$	100	$3.036(2)^{+6.8\%}_{-5.3\%}$	100	1.635	1.033
$Z_L W_L^+$	$0.64603(5)^{+0.2\%}_{-0.6\%}$	34.8	$0.6127(4)^{+0.9\%}_{-0.7\%}$	20.2	0.948	1.031
$Z_L W_T^+$	$0.08687(1)^{+0.2\%}_{-0.6\%}$	4.7	$0.17012(6)^{+8.6\%}_{-6.8\%}$	5.6	1.958	0.967
$Z_T W_L^+$	$0.08710(1)^{+0.1\%}_{-0.6\%}$	4.7	$0.24307(7)^{+10.2\%}_{-8.2\%}$	8.0	2.791	1.017
$Z_T W_T^+$	$0.97678(7)^{+2.0\%}_{-2.2\%}$	52.6	$2.0008(7)^{+8.9\%}_{-7.1\%}$	65.8	2.048	1.059
interf.	0.0595(1)	3.2	0.009(2)	0.4	–	–
unresolved, $Z(e^+e^-)W^+(J)$						
unpol.	$1.6879(2)^{+1.9\%}_{-2.1\%}$	100	$3.112(2)^{+7.6\%}_{-6.1\%}$	100	1.843	1.193
$Z_L W_L^+$	$0.61653(5)^{+1.0\%}_{-1.3\%}$	36.5	$0.6799(5)^{+0.9\%}_{-0.7\%}$	21.9	1.103	1.170
$Z_L W_T^+$	$0.06444(1)^{+0.7\%}_{-1.0\%}$	3.8	$0.17584(6)^{+10.8\%}_{-8.6\%}$	5.7	2.729	1.158
$Z_T W_L^+$	$0.07437(1)^{+0.6\%}_{-0.9\%}$	4.4	$0.24742(8)^{+11.0\%}_{-8.9\%}$	8.0	3.327	1.193
$Z_T W_T^+$	$0.88233(9)^{+2.9\%}_{-2.9\%}$	52.3	$2.0041(8)^{+9.6\%}_{-7.7\%}$	64.3	2.271	1.227
interf.	0.0503(3)	3.0	0.004(2)	0.1	–	–

Table 4.1: Integrated cross-sections (in fb) in the resolved and unresolved fiducial setups described in Section 4.1.1 for unpolarised and doubly-polarised ZW^+ production in the semi-leptonic decay channel. Polarisations are defined in the di-boson CM frame. Numerical errors (in parentheses) and QCD-scale uncertainties from 7-point scale variations (in percentages) are shown. The fractions (in percentage) are computed as ratios of polarised cross-sections over the unpolarised one. K-factors are defined as ratios of the NLO QCD cross-sections with (K_{NLO}) and without ($K_{\text{NLO}}^{(\text{no g})}$) gluon-induced contributions over the LO ones.

likely to be combined into one jet making it harder to fulfil the massive jet requirement. This favours the TL polarisation state in the unresolved setup. Another interesting feature is the very small contribution of $\approx 3\%$ from the interferences between the longitudinal and transverse polarisation states. The contribution from the interferences cancels to zero when the full decay phase space of the resonances is considered. The phase-space cuts prevent the exact cancellation resulting only in a suppression of the interferences.

Shifting the focus to the results including the NLO QCD corrections one notices that, if at least one transversely polarised boson is present, the NLO QCD corrections are very large. In the resolved setup the NLO QCD corrections for the LT and TT polarisation states are at $\approx 100\%$ compared to the LO contribution. For the TL state they receive a correction of $\approx 200\%$. For the unresolved setup the corrections are slightly larger. In contrast the LL polarisation state gets a much smaller correction of $\approx -5\%$ in the resolved setup and $\approx 10\%$ in the unresolved setup. The large corrections are caused by real-emission processes with initial-state gluons [141]. These processes receive an enhancement from the large gluon PDFs of the proton. When the partonic processes with initial-state gluons are excluded, the K-factors become much smaller as shown in column $K_{\text{NLO}}^{(\text{no g})}$ of Table 4.1. The LL polarisation state only receives small corrections from the gluon-induced real-emission processes. This has

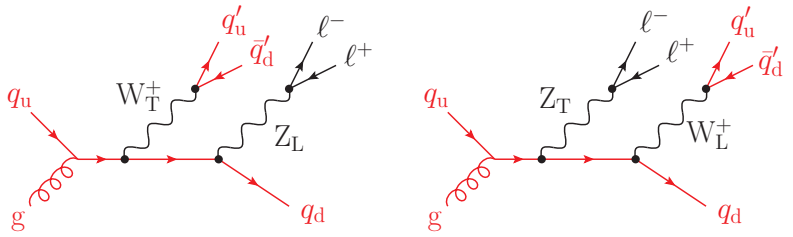

(a) $Z_L W_T^+$ (b) $Z_T W_L^+$

Figure 4.2: Leading QCD-radiation contributions in the q_ug partonic channel for LT and TL ZW$^+$ production at the LHC in the semi-leptonic decay channel. Particles carrying colour charge are highlighted in red.

already been shown for ZW production with leptonic decays [53, 54]. As shown in Ref. [142] the dominant contribution to the gluon-induced process stems from diagrams where the quark absorbs the gluon and afterwards emits the two vector bosons. In the subprocess g$q \to$ Vq' the production of an energetic longitudinally polarised vector boson is suppressed. From the Goldstone-boson equivalence theorem [31, 32, 150] follows that the energetic longitudinal vector boson behaves like a Goldstone boson. Owing to the massless quark, there are no non-vanishing diagrams of the subprocess, where the longitudinal boson is replaced by a would-be Goldstone boson; therefore, the emission of high-transverse-momentum longitudinally polarised bosons is suppressed. This means the contributions that give the large corrections to the polarisation states with at least one transversely polarised boson are suppressed in the LL state. As the NLO QCD corrections affect the polarisation states very differently, the fractions, at which the individual polarisation states contribute to the unpolarised cross-section, also change considerably. The contribution of the purely longitudinal polarisation state is reduced to $\approx 20.0\%$ while the contributions of the mixed polarisation states increase to $\approx 6\%$ for the LT state and $\approx 8\%$ for the TL state. The increase in the differences of the mixed polarisation states from LO to NLO is caused by a larger contribution from gluon-induced real emission to the TL state. Both mixed polarisation states are subject to a suppression from unitarity cancellations in the high-transverse-momentum region of the longitudinal boson. This suppression remains when real radiation is included. Therefore, the preferred kinematic configurations are those, where the longitudinally polarised boson is emitted very close in direction to the real radiation. In these configurations the transverse momentum of the transversly polarised boson is split between the longitudinal boson and the real radiation. Therefore, the TL state prefers real radiation that is emitted close to the decay jets and the LT favours real emission close to the electron-positron pair. It has been verified that the Monte Carlo integration channels, corresponding to the diagrams depicted in Figures 4.2(a) and 4.2(b), give the dominant contribution to the real-emission corrections of the LT and TL states. When the real radiation is emitted close to the decay jets of the longitudinal W$^+$ boson, as preferred by the TL state, it frequently occurs that the selected jet system is not constructed from the decay jets of the W$^+$ boson. Because of the preference of producing the real radiation close to the electron-positron pair, the wrong reconstruction of the W$^+$ decay is less frequent in the LT state. When the jet system does not correctly identify the decay jets, the production of low-transverse-momentum W$^+$ bosons is not forbidden by the event selection. In the TL state the W$^+$ boson is longitudinally polarised

causing such events to be much less effected by unitarty cancellations. In the LT state the Z boson is longitudinally polarised and must fulfil the 200 GeV transverse-momentum requirement giving a stronger unitartiy cancellation. Therefore, the misidentification of the W^+ boson weakens the suppression from unitarity cancellations in the TL state causing the seen larger NLO QCD corrections. The effects of the misidentification are even more prominent in differential observables. The distribution of the invariant mass of the jet system, depicted in Figure 4.8, is particularly distorted by them. The contribution from the purely transverse polarisation state increases to $\approx 65\%$. The TT polarisation state features an approximate amplitude zero effect [109, 148] at tree level that is spoiled by the inclusion of NLO real-emission corrections. The detailed effects of this are seen much better in differential observables like the scattering angle in Figure 4.4. Including the NLO QCD corrections decreases the size of the interferences to the sub percent level. The LO scale uncertainties are small as the LO process is purely EW; therefore, the scale variation only enters in the different factorisation scales. Additionally, selecting a regime, where the bosons are very boosted, further reduces the scale uncertainties by about a factor of 4 compared to more inclusive setups [53, 54]. This is independent of the semi-leptonic decay mode, as it has been checked numerically that the same effect is also present in purely leptonic decay modes. Including the NLO QCD corrections increases the scale uncertainties greatly ($\approx 7\% - 11\%$) for the processes with at least one transversely polarised boson while for the purely longitudinal state they remain of similar order ($\approx 1\%$). The cause of this is that at NLO also the renormalisation scale dependence of the strong coupling enters the computation. On top of that the large real corrections further enhance the scale uncertainties. As at LO ZW^+ production is a purely EW process, to get a scale variation that is truly NLO QCD the next-to-next-to-leading-order (NNLO) QCD corrections need to be included. With the methods used in Ref. [88] this is possible. The inclusion of the NNLO QCD corrections would also increase the reliability of the computed scale uncertainties.

The main difference between the resolved setup and the unresolved setup are the effects of the recombination. For an event to be accepted in the resolved setup the decay jets of the W boson need to have a large enough separation that they are not recombined together into one jet. In the unresolved setup it is the other way around, the two decay particles of the W boson need to be emitted close enough together to be recombined to fulfil the mass requirement of the jet. This means that at LO the low-transverse-momentum region is favoured in the resolved setup compared to the unresolved setup. The high-transverse-momentum region is favoured in the unresolved setup compared to the resolved setup. As the low-transverse-momentum region contributes more to the total cross-section, the cross-section for the resolved setup is larger at LO. At NLO QCD the large real-emission corrections for the polarisation states with at least one transversely polarised boson reduce the difference significantly. This is particularly apparent for the mixed polarisation states. This suggests that the effects of the different recombination procedures are less relevant for the real-emission corrections.

Both the resolved and the unresolved setup apply a 200 GeV transverse-momentum cut on the lepton pair and the jet system. This prevents the NLO corrections from becoming too large by acting as a veto on additional jets. The symmetric nature of the cut can, however, cause unphysical artefacts in the regions of phase space close to the cut threshold from real QCD radiation [147]. When the transverse-momentum cut on the jet system is omitted, such effects can be prevented. In Table 4.2 the integrated cross-section in the

state	σ_{LO} [fb]	f_{LO}[%]	σ_{NLO} [fb]	f_{NLO}[%]	K_{NLO}	$K_{\text{NLO}}^{(\text{no g})}$
resolved (no minimum $p_{\text{T,jj}}$ cut), $Z(e^+e^-)W^+(jj)$						
unpol.	$1.8564(1)^{+1.2\%}_{-1.4\%}$	100	$5.5388(8)^{+10.6\%}_{-8.6\%}$	100	2.984	1.371
$Z_L W_L^+$	$0.64605(3)^{+0.2\%}_{-0.6\%}$	34.8	$0.7525(4)^{+1.5\%}_{-1.2\%}$	13.6	1.165	1.194
$Z_L W_T^+$	$0.08687(1)^{+0.2\%}_{-0.6\%}$	4.7	$0.3057(1)^{+11.4\%}_{-9.2\%}$	5.5	3.519	1.462
$Z_T W_L^+$	$0.08710(1)^{+0.1\%}_{-0.6\%}$	4.7	$1.0486(1)^{+14.6\%}_{-11.9\%}$	18.9	12.04	2.408
$Z_T W_T^+$	$0.97677(7)^{+2.0\%}_{-2.2\%}$	52.6	$3.5506(9)^{+11.8\%}_{-9.6\%}$	64.1	3.635	1.424
interf.	0.0595(1)	3.2	−0.119(2)	−2.1	–	–

Table 4.2: Integrated cross-sections (in fb) in the resolved setup described in Section 4.1.1 without the minimum $p_{\text{T,jj}}$ cut of 200 GeV. Polarisations are defined in the di-boson CM frame. Numerical errors (in parentheses) and QCD-scale uncertainties from 7-point scale variations (in percentages) are shown. The fractions (in percentage) are computed as ratios of polarised cross-sections over the unpolarised one. K-factors are defined as ratios of the NLO QCD cross-sections with (K_{NLO}) and without ($K_{\text{NLO}}^{(\text{no g})}$) gluon-induced contributions over the LO ones.

resolved setup without the cut on the transverse momentum of the jet system is shown. At LO the bosons are always produced back to back in the transverse direction; therefore, the LO cross-sections remain unchanged. The NLO QCD corrections become larger without the transverse-momentum cut on the jet system. This effect is particularly extreme for the TL polarisation state increasing its contribution from 5% at LO to 19%. The K-factor of the purely longitudinal polarisation state is only increased slightly and remains the smallest. Similar to the base setup with the transverse momentum cut also in this setup the large NLO QCD corrections mainly stem from gluon-induced real-emission processes. This is seen best in the $K_{\text{NLO}}^{(\text{no g})}$ column in Table 4.2 displaying the K-factors excluding the gluon-induced partonic channels. The absence of large NLO enhancements for LL polarisation state cause its polarisation fraction to reduce to 13.6% compared to the 20.2% in the default resolved setup. Without the transverse momentum cut on the jet system the transverse momentum of the electron-positron pair is absorbed by the entire hadronic system including the decay and additional real radiation. This causes the much larger K-factors, when at least one boson is transversely polarised, confirming the argument from before that the cut restricts the size of the NLO corrections. The much larger enhancement of the TL polarisation state compared to the LT polarisation state is a result of the requirement that the Z boson is still very boosted but the W boson no longer needs to be boosted. This leads to a much smaller unitarity suppression for the TL polarisation state compared to the LT polarisation state.

It is important to know how large the non-resonant background is, as only the full off-shell result is accessible experimentally. To test how well the DPA describes the full result, a LO accurate study of the background processes is done. The results are presented in Table 4.3. An important difference of hadronic decays compared to leptonic decays is that the final states of W^+, Z and W^- decays cannot be distinguished. This means that on top of the non-resonant background there is also background from other resonances. The LO accurate cross-sections for ZW^+ and ZZ production in the DPA are shown in Table 4.3. Their size is of the

	resolved		unresolved	
process	σ_{LO} [fb]	ratio over full $\mathcal{O}(\alpha^4)$	σ_{LO} [fb]	ratio over full $\mathcal{O}(\alpha^4)$
DPA ZW^+	$1.8567(2)^{+1.2\%}_{-1.4\%}$	0.353	$1.6879(2)^{+1.9\%}_{-2.1\%}$	0.425
DPA ZW^-	$1.0527(1)^{+1.3\%}_{-1.6\%}$	0.200	$0.9003(1)^{+2.0\%}_{-2.1\%}$	0.227
DPA ZZ	$2.1430(3)^{+1.3\%}_{-1.6\%}$	0.408	$1.2804(2)^{+2.6\%}_{-2.7\%}$	0.323
DPA ZV	$5.0523(4)^{+1.3\%}_{-1.5\%}$	0.961	$3.8685(3)^{+2.2\%}_{-2.3\%}$	0.975
full $\mathcal{O}(\alpha^4)$	$5.253(1)^{+1.2\%}_{-1.5\%}$	1.000	$3.967(2)^{+2.1\%}_{-2.3\%}$	1.000
full $\mathcal{O}(\alpha_{\text{s}}\alpha^3)$	$-0.3124(6)^{+9.2\%}_{-10.7\%}$	-0.059	$-0.2145(6)^{+9.7\%}_{-11.4\%}$	-0.054
full $\mathcal{O}(\alpha_{\text{s}}^2\alpha^2)$	$97.91(7)^{+24.3\%}_{-18.4\%}$	18.638	$62.55(7)^{+25.0\%}_{-18.8\%}$	15.768

Table 4.3: Integrated LO cross-sections (in fb) in the resolved and unresolved fiducial setups described in Section 4.1.1 for: the signal process (DPA ZW^+), the background processes with a resonant W^- boson (DPA ZW^-) and with two resonant Z bosons (DPA ZZ), the full off-shell process at the three perturbative orders in α_{s}. The result dubbed DPA ZV is understood as the sum of the three DPA contributions ($\text{ZW}^+ + \text{ZW}^- + \text{ZZ}$).

same order as the one from ZW^+ production treated as the signal here. In both the resolved and the unresolved setup the ZW^- production contribution is the smallest. The contribution from ZW^+ production is the largest in the unresolved setup while in the resolved setup the one from ZZ production is larger. Since the Z boson is more massive than the W boson the decay quarks of the Z boson will be more energetic in the frame of the decaying boson than those of the W boson. Therefore in the lab frame the separation of the decay quarks of the Z boson will be larger making it harder to fulfil the massive jet requirement in the unresolved setup. When all the resonant contributions ZW^+ production, ZW^- production and ZZ production are summed up they agree with the EW full off-shell result $\mathcal{O}(\alpha^4)$ up to 2% - 4%. This is the expected accuracy of the DPA of $\mathcal{O}(\Gamma_V/M_V)$. But not only the purely EW contribution is part of the full result. There are also the interference background $\mathcal{O}(\alpha_s\alpha^3)$ and the QCD background $\mathcal{O}(\alpha_s^2\alpha^2)$ that contribute to the same final state. The interference background only gives a contribution of $\approx 6\%$ compared to the full off-shell EW contribution. The QCD background is much larger resulting in a contribution that is 15 to 20 times larger than the EW signal. In the resolved setup the QCD background is larger than in the unresolved setup. As the jets in the QCD background do not stem from a resonance there is no strong preference for them to be emitted in a similar direction; therefore, the jets are less often recombined into a fat jet suppressing the unresolved result. To measure the polarisation these two background contributions would need to be subtracted beforehand. All three resonant processes contribute to the same off-shell EW signal. They, however, feature different resonance structures and spin structures that can cause very different LO suppressions in the polarised signals and/or phase-space regions. This can lead to spin-specific details in the differential cross-sections being washed out or a reduced sensitivity to new physics from effects originating from one of the other Standard Model resonances. Therefore, the three resonant contributions must be treated separately either by removing them as background or using separate templates for all possible resonances.

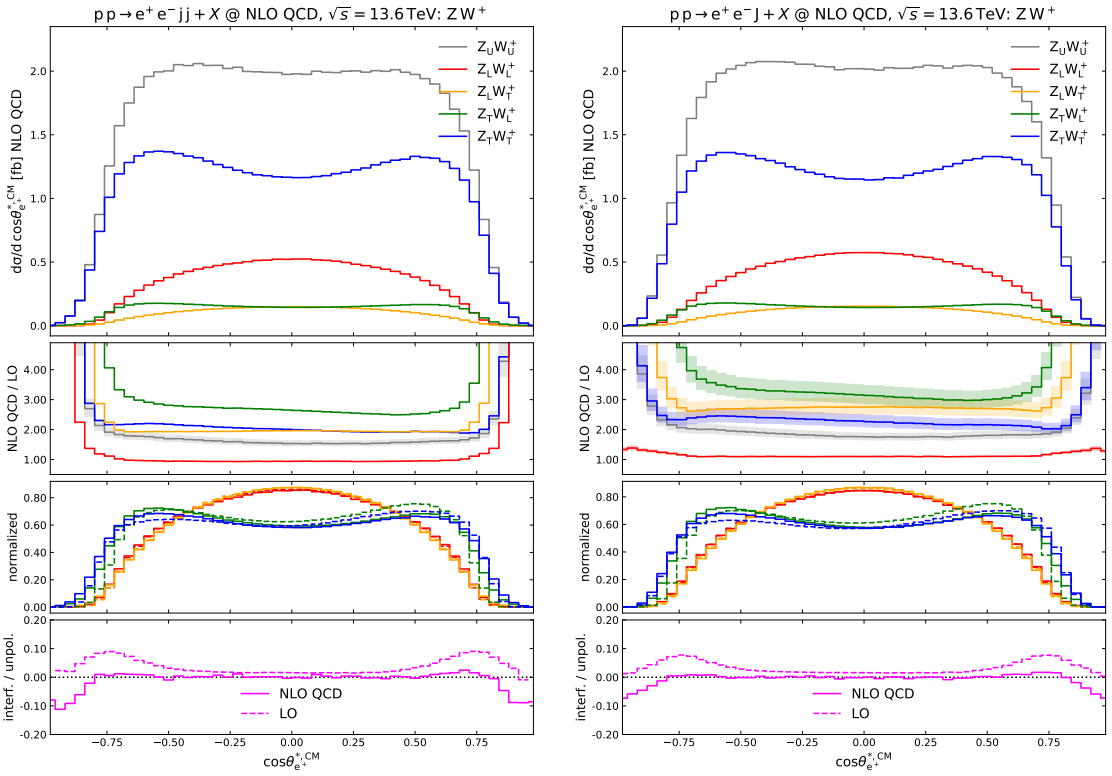

(a) Resolved topology

(b) Unresolved topology

Figure 4.3: Distribution in the cosine of the polar decay angle of the positron in semi-leptonic ZW$^+$ production at the LHC. The definition of this angle is given in Eq. (4.8). Details are described in the main text (first paragraphs of Section 4.1.3)

4.1.3 Differential Results

To study the effects of the different polarisation states and the different setups, differential cross-sections are analysed. The default resolved and unresolved setups given in Section 4.1.1 are used in the plots if not stated otherwise. The plots are structured in two columns. With the exception of Figures 4.9 and 4.12 the left column corresponds to the resolved and the right one to the unresolved setup. Each column of the plots (Figures 4.3–4.12) contains four individual plots. The top one displays the NLO accurate differential cross-sections with respect to the given observable for the unpolarised (gray) and the polarised LL (red), LT (yellow), TL (green), TT (blue) DPA process. The first polarisation label represents the polarisation of the Z boson and the second label the polarisation of the W$^+$ boson. The second plot shows the NLO QCD K-factors, including the uncertainty bands from the scale variation, of the polarised and unpolarised processes. The third panel presents the normalised shapes of the LO cross-sections (dashed) and the NLO cross-sections (full). The bottom panel displays the interference contribution normalised to the unpolarised contribution at LO (dashed, magenta) and at NLO (solid, magenta).

Observables that are very well suited to distinguish the polarisation states of the Z boson are the decay angles of the electron and the positron. These observables have been used in several polarisation studies [39, 53, 55, 151] to distinguish the different polarisation states. In

Figure 4.3 the decay angle of the positron is depicted. The decay angle of the electron or positron is defined as

$$\cos\left(\theta^{*,\mathrm{CM}}_{\mathrm{e}^{\pm}}\right) = \frac{\vec{p}^{\,*}_{\mathrm{e}^{\pm}} \cdot \vec{p}^{\,\mathrm{CM}}_{\mathrm{e}^{+}\mathrm{e}^{-}}}{|\vec{p}^{\,*}_{\mathrm{e}^{\pm}}||\vec{p}^{\,\mathrm{CM}}_{\mathrm{e}^{+}\mathrm{e}^{-}}|}. \tag{4.8}$$

Here $\vec{p}^{\,*}_{\mathrm{e}^{\pm}}$ is the three-momentum of the positron or electron in the CM of the recombined Z boson. The vector $\vec{p}^{\,\mathrm{CM}}_{\mathrm{e}^{+}\mathrm{e}^{-}}$ denotes the three-momentum of the electron-positron pair in the CM frame of the recombined Z boson and the jet system. When studying the normalised shapes of the distributions, clear differences between the cases where the Z boson is transversely polarised and longitudinally polarised are visible. In case of a transverse polarised Z boson the distribution has peaks at $\cos\left(\theta^{*,\mathrm{CM}}_{\mathrm{e}^{+}}\right) = \pm 0.6$. The LL and LT polarisation states have a single peak at $\cos\left(\theta^{*,\mathrm{CM}}_{\mathrm{e}^{+}}\right) = 0$. The decay particles of a longitudinally polarised boson are predominantly emitted orthogonal to the direction of the boson in the boson rest frame. In case of a transversely polarised boson one of the decay particles is generally emitted in the direction of the boson and one opposite to its direction in the Z boson rest frame. The cuts on the transverse momentum of the charged leptons greatly suppress the contributions close to the edges. This shifts the peaks of the distributions of transversely polarised Z bosons from $\cos\left(\theta^{*,\mathrm{CM}}_{\mathrm{e}^{+}}\right) = \pm 1$, as expected in a fully inclusive setup, to the observed value. The small differences in shape between the TT and TL or LL and LT polarisation state are the effect of left-right interferences and spin-correlations. The left-right interferences, which are part of the transverse polarisation state, do not cancel when phase-space cuts are applied. The phase-space cuts on the jets cause the spin correlations to depend on the decay angle giving a different shape depending on the W^{+} boson polarisation. The plots of the K-factors show that in the central region the NLO QCD corrections only rescale the cross-section and do not change the shape. At the edges of the plot this is different, here the NLO QCD corrections become large compared to the LO contribution. This is the kinematic region that is influenced the most by the phase-space cuts. That the differential cross-section only depends on the decay dynamics of the Z boson and the small shape changes make the observable well suited to distinguish the different polarisation states also in extensions of the Standard Model. The beyond the Standard Model contributions to the Z decay are assumed to be small. There are only very minor differences between the resolved and the unresolved setup. The interferences are very small in the central region. At the edges, where the effects of the phase-space cuts are the strongest, they can reach up to -10%. Here the effects of the phase-space cuts, that prevent the cancellation of the interferences, are the largest.

Figure 4.4 shows the differential cross-section with respect to the cosine of the scattering angle, defined as

$$\cos\left(\theta_{\mathrm{scatt}}\right) = \frac{|p^{\mathrm{CM}}_{\mathrm{e}^{+}\mathrm{e}^{-},z}|}{|\vec{p}^{\,\mathrm{CM}}_{\mathrm{e}^{+}\mathrm{e}^{-}}|} \tag{4.9}$$

where $\vec{p}^{\,\mathrm{CM}}_{\mathrm{e}^{+}\mathrm{e}^{-}}$ is the momentum of the electron-positron pair in the CM frame of the electron-positron pair and the jet system and $p^{\mathrm{CM}}_{\mathrm{e}^{+}\mathrm{e}^{-},z}$ is its z component (beam direction). Like the decay angle seen before this observable is well suited for the discrimination between the polarisation states as evidenced by the different shapes of the normalised distributions. In contrast to the decay angle that was primarily sensitive to the decay of the Z boson the scattering angle is mainly sensitive to the production dynamics of the W^{+} and Z boson. Its dependence on the decay is limited to small effects from the reconstruction of the decay

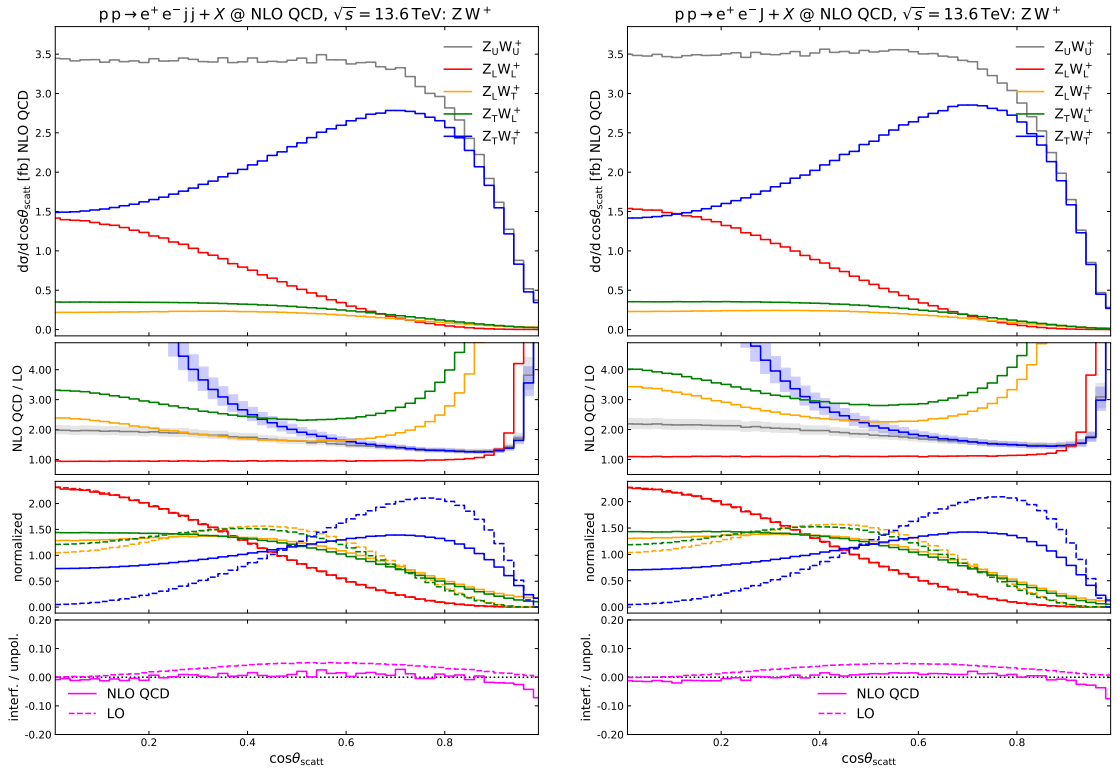

(a) Resolved topology

(b) Unresolved topology

Figure 4.4: Distribution in the cosine of the scattering angle in semi-leptonic ZW$^+$ production at the LHC. The scattering angle is defined according to Eq. (4.9). Details are described in the main text (first paragraphs of Section 4.1.3).

products. The dependence on the production part of the amplitude makes the scattering angle only directly usable to distinguish the polarisation states in a Standard Model analysis. The inclusion of beyond the Standard Model physics could give very different normalised shapes. Therefore, in any beyond the Standard Model analysis the distribution would have to be recalculated. In the region of large $\cos(\theta_{\text{scatt}}) > 0.6$ the cross-section is dominated by the purely transverse polarisation state. In the region of small scattering angles the purely longitudinal polarisation state has a contribution that is of similar size as the one of the TT state. When studying the normalised shapes of the distributions a considerable shape change from LO to NLO can be observed for the TT polarisation state and to a lesser extent for the mixed polarisation states LT, TL. The large shape change of the TT polarisation state is caused by a suppression of the LO contribution in the low-$\cos(\theta_{\text{scatt}})$ range. The LO contribution is suppressed because of an approximate amplitude zero effect [109, 148]. The inclusion of real-emission corrections spoils this effect giving the large K-factors that are shown in the plot. The mixed polarisation states also have large K-factors in the region $\cos(\theta_{\text{scatt}}) > 0.75$. The unitarity suppression of the mixed polarisation states already seen at the integrated level further diminishes the LO contribution for small scattering angles. When the electron-positron pair is emitted with a small scattering angle they must be very energetic to fulfil the transverse-momentum requirement enhancing the unitarity suppression. Close to $\cos(\theta_{\text{scatt}}) = 1$ the K-factors of all polarisation states become very large. This is caused

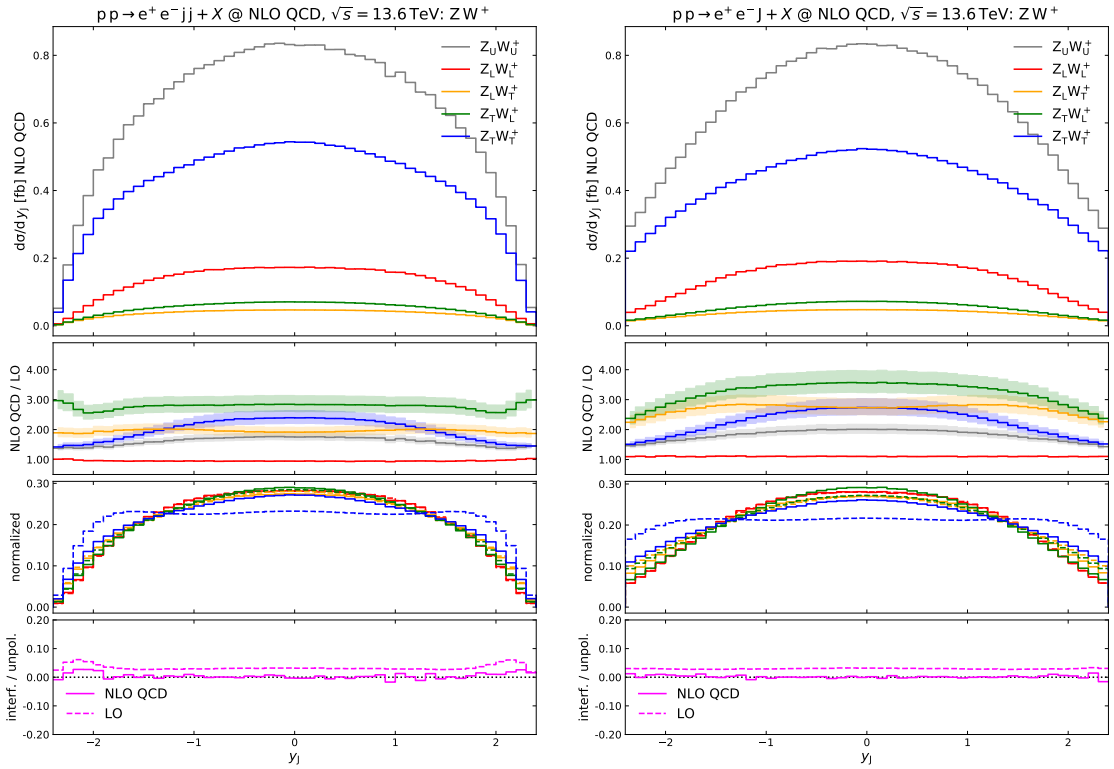

(a) Resolved topology

(b) Unresolved topology

Figure 4.5: Rapidity distribution of the jet system J in semi-leptonic ZW^+ production at the LHC. The identification of the jet system J is described in Section 4.1.1. Details are described in the main text (first paragraphs of Section 4.1.3).

by real radiation allowing momentum configurations where the momenta of the electron-positron pair are closer to the beam direction without being cut away by the rapidity cuts. At NLO the interferences are very small except for the region close to $\cos(\theta_{\text{scatt}}) = 1$ where the interferences reach -7% of the unpolarised contribution. There are only very small differences in the resolved and unresolved setup. The larger K-factors in the unresolved setup of the mixed polarisation states already seen at the integrated level are seen differentially here.

The plots in Figure 4.5 show the differential cross-section with respect to the rapidity of the jet system. The TT polarisation state undergoes a significant shape change from LO to NLO. At LO there is a plateau in the central region ($|y_J| < 1.8$) while at NLO the curve has a peak similar to the other polarisation states. This is indirectly caused by the approximate amplitude zero effect seen in the distribution with respect to the scattering angle, shown in Figure 4.4, that suppresses the TT state at LO. At NLO real radiation fills the suppressed regions. Another effect of this suppression of the LO is that the K-factors of the TT polarisation state are peaked in the central region. In the resolved setup the K-factors of the mixed polarisation states are close to flat only having slight deviation from the flat behaviour at $|y_J| \approx 2$. The K-factors in the unresolved setup are only flat in the central region ($|y_J| < 1.3$) and decrease towards the edges. The cause for the differences seen in the shape of the resolved and unresolved setup stem from the rapidity cut on the

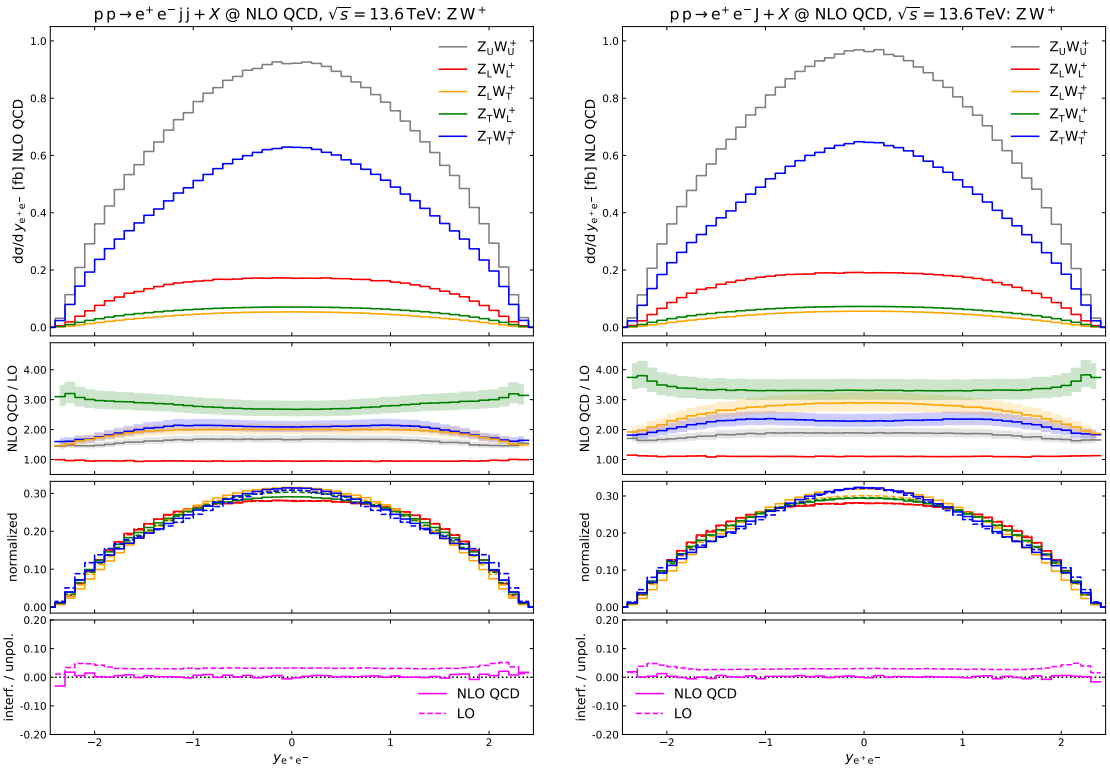

(a) Resolved topology

(b) Unresolved topology

Figure 4.6: Rapidity distribution of the electron–positron pair in semi-leptonic ZW$^+$ production at the LHC. Details are described in the main text (first paragraphs of Section 4.1.3).

jets. In the resolved setup individual cuts are applied to the two jets while in the unresolved setup the cut is directly applied to the momentum of the massive fat jet that constitutes the jet system. This results in a steeper fall-off in phase-space region close to the cut in the resolved setup compared to the unresolved setup. The NLO QCD corrections to the purely longitudinal polarisation state are very small over the whole rapidity range mirroring the picture seen at the integrated level. The interferences are also small over the studied rapidity range.

Figure 4.6 shows the rapidity distribution of the electron-positron pair. As mentioned before, at LO the electron-positron pair and the jet system are produced back to back in the transverse direction causing this observable to be highly correlated to the rapidity of the jet system. The shape of the distributions only changes very slightly translating to the mostly flat NLO QCD K-factors. Only at the edge of the allowed rapidity region the shape is mildly affected by the NLO QCD corrections. This effect is slightly larger in the resolved setup compared to the unresolved setup. The normalised shapes of the polarised signals are very similar.

In Figure 4.7 the differential cross-section with respect to the absolute value of the rapidity difference of the positron and the jet system is depicted. This observable is strongly correlated to the scattering angle from Figure 4.4. The correlation can be motivated as follows. In the CM frame the jet system and the electron-positron pair are emitted back to back. Therefore, an event with small $\cos(\theta_{\text{scatt}})$ will generally have a small rapidity separ-

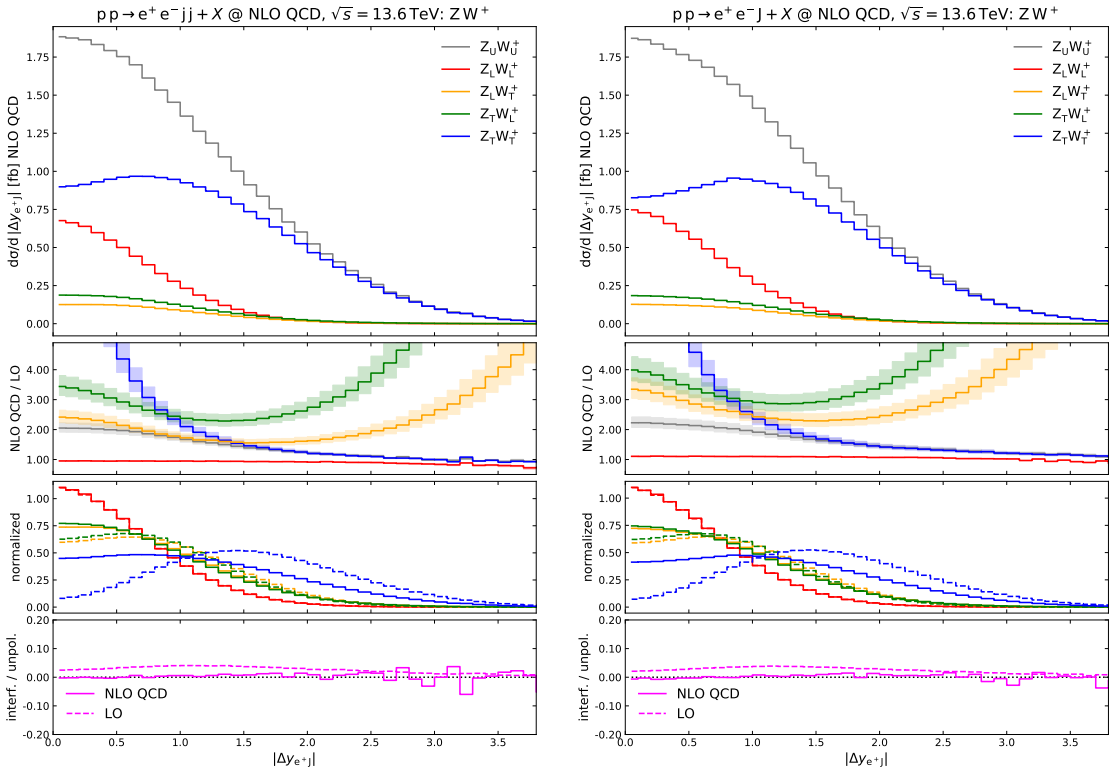

(a) Resolved topology

(b) Unresolved topology

Figure 4.7: Distribution in the rapidity separation between the positron and the hadronic system J in semi-leptonic ZW^+ production at the LHC. The identification of the hadronic system J is described in Section 4.1.1. Details are described in the main text (first paragraphs of Section 4.1.3).

ation between the jet system and the electron-positron pair when boosted back to the lab frame. Since the electron and positron are emitted in very similar directions, because of the large transverse-momentum requirement, also the rapidity separation of the positron and the jet system will be small. Similarly, a large $\cos(\theta_{\text{scatt}})$ often corresponds to a large rapidity separation between the jet system and the positron. The rapidity separation is similarly well suited for the discrimination of the polarisation of the W and Z boson as the scattering angle. It is also mainly sensitive to the production of the W and Z bosons; therefore, the shape would have to be recomputed for a beyond the Standard Model polarisation analysis. The LL, LT and TL polarisation states are all peaked at $|\Delta y_{e^+J}| = 0$. The TT polarisation state has a peak at $|\Delta y_{e^+J}| = 0.8$ in the resolved and $|\Delta y_{e^+J}| = 1.0$ in the unresolved setup. The normalised shapes show a large change in the shape of the distributions with at least one transversely polarised boson from LO to NLO. The reasons for the shape changes are the same as for the ones seen in the scattering angle. The LO contribution to the TT state is suppressed by the approximate amplitude zero effect in the phase-space region close to $|\Delta y_{e^+J}| = 0$. The LO contributions to the mixed polarisation states are subject to the unitarity suppression. This effect is particularly strong, when the rapidity separation is large $|\Delta y_{e^+J}| \gtrsim 2.5$, resulting in the shape change and large K-factors. For large rapidity separations between the positron and the jet system the contributions of all polarisation states

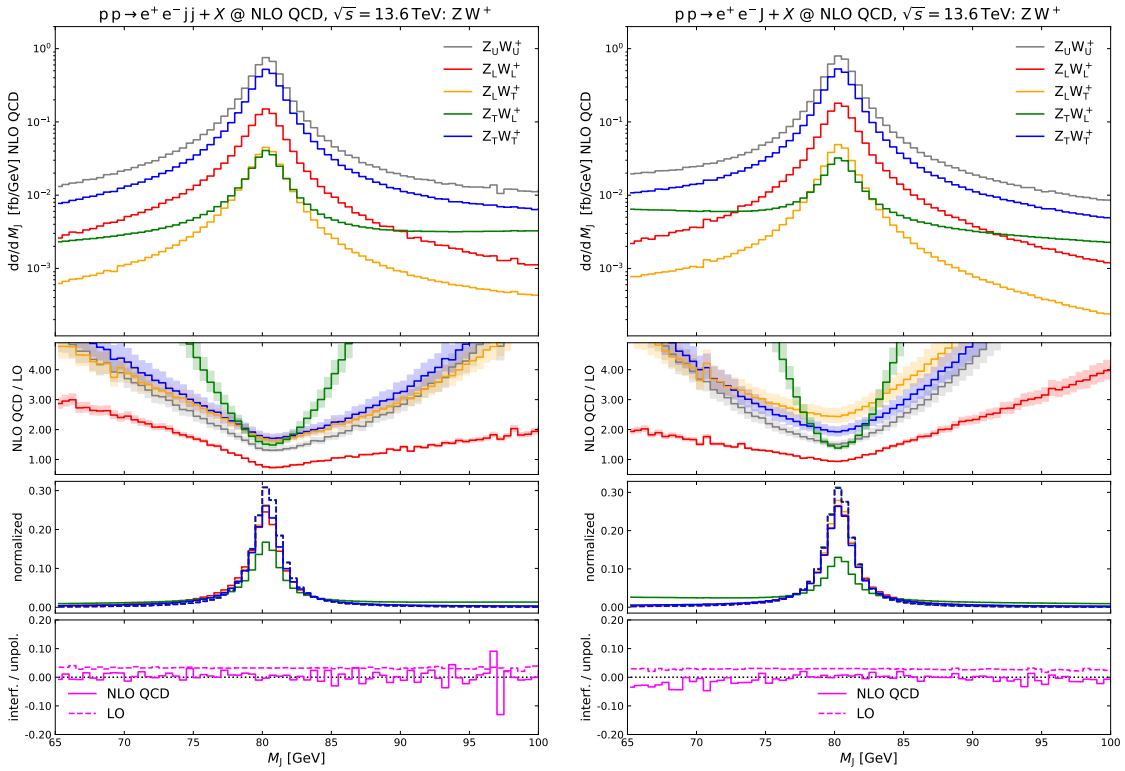

(a) Resolved topology

(b) Unresolved topology

Figure 4.8: Invariant-mass distribution of the hadronic system J in semi-leptonic ZW$^+$ production at the LHC. The identification of the hadronic system J is described in Section 4.1.1. Details are described in the main text (first paragraphs of Section 4.1.3).

become suppressed by the cuts on the rapidity. The contribution from the interferences of different polarisation states is small. There are only very small differences in the distributions in the resolved and unresolved setup.

Figure 4.8 shows the differential cross-section with respect to the invariant mass of the jet system. Close to the mass of the W boson the distributions follow the expected Breit-Wigner shape. Further away from the resonance peak the distributions of the TT, LT and LL polarsation state fall off very quickly as expected by the Breit-Wigner modulation. The behaviour of the TL polarisation state differs considerably from that of a pure Breit-Wigner peak by not falling off when the invariant mass of the jet system is far from the W mass. With the inclusion of NLO real-emission processes the decay jets of the W boson are no longer uniquely defined. Therefore, it can happen that the chosen jet system is not actually constructed from the decay jets of the W boson. This misidentification of the W boson introduces a background to the expected Breit-Wigner shape and adds a strong dependence on how successful the identification of the W decay is to the distribution. All polarisation states receive a background contribution from this misidentification. The reasoning behind this has already been hinted at in Section 4.1.2 for the integrated results. For the TL polarisation the effect is much larger compared to the other polarisation states, because here the emission of the real radiation from the production in a similar direction as the W boson is preferred. Both the TL and LT polarisation state are unitarity suppressed at LO. Therefore,

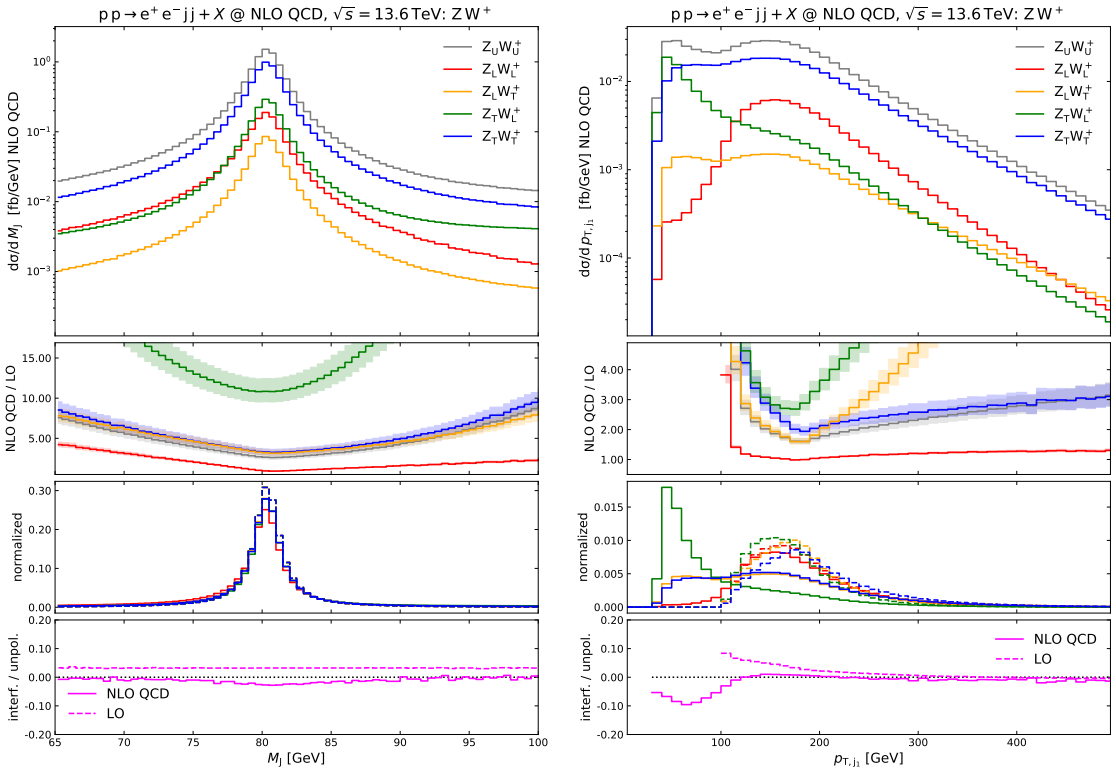

(a) M_{J} (b) $p_{\mathrm{T,j_1}}$

Figure 4.9: Distribution in the invariant mass of the hadronic system J (a) and in the transverse momentum of the hardest decay jet (b) in semi-leptonic ZW^+ production at the LHC. The identification of the hadronic system J is described in Section 4.1.1. The resolved setup is considered, but no minimum cut is applied on $p_{\mathrm{T,jj}}$. The panels of the subfigures have the same structure as described in the main text (first paragraphs of Section 4.1.3).

the gluon-induced real-emission contributions are responsible for the very large corrections. For the TL polarisation state the additional final-state quark is preferably produced in the direction of the W boson, while for the LT polarisation state it is preferably produced opposite to the direction of the W boson. With the additional quark often being emitted in a similar direction as the W boson misidentifications happen much more frequently for the TL polarisation state. For the other polarisation states the misidentification happens more rarely resulting in the more prominent feature in the TL state. The root cause of this effect is the transverse-momentum cut on the jet system that discards events where the W boson has low to moderate transverse momentum. This is shown in more detail in Figure 4.9(a).

Figure 4.9(a) shows the distributions of the invariant mass of the jet system in the resolved loose setup without the 200 GeV transverse-momentum cut on the jet system. Without the transverse-momentum requirement the shape of the TL distribution is much closer to ones of the other polarisation states. The background from misidentified W bosons still exists as is shown in the $M_{\mathrm{J}} > 90\,\mathrm{GeV}$ range for the TL polarisation state. The effect on the overall shape of the distribution is much smaller compared to the standard setup with the transverse-momentum cut on the jet system. This confirms that the cause of the large background is the transverse-momentum cut on the jet system.

The removal of the 200 GeV transverse-momentum requirement allows for real-radiation events with a low transverse momentum of the jet system to be accepted. In Figure 4.9(b) the differential cross-section with respect to the transverse momentum of the hardest decay jet in the loose setup is depicted. Here the effect of the transverse-momentum cut on the jet system is shown very clearly. The transverse-momentum cut on the jet system would remove all events with $p_{\mathrm{T,j_1}} < 100\,\mathrm{GeV}$. The TL polarisation state has a clear peak at $p_{\mathrm{T},Pj_1} = 50\,\mathrm{GeV}$ causing it to be affected the most by the transverse-momentum cut. In the low-transverse-momentum region the emission of the real radiation in a similar direction as the jets system is less favoured. Therefore, the chance of misidentifying the decay jets of the W boson is smaller. With the inclusion of the low-transverse-momentum events the peak is now included giving a normalised shape for the invariant mass of the jet system that is much closer to the expected Breit-Wigner shape. In the low-transverse-momentum region the interference contribution reaches up to -10%. This causes the negative interference contribution seen at the integrated level.

Circling back to the invariant mass of the jet system in the default setup in Figure 4.8, the misidentification background is different in the resolved and the unresolved setup. The size of the flat background compared to the Breit-Wigner peak is larger in the unresolved setup as seen by the lower peak in the normalised shapes. This is a consequence of the different reconstruction of the jets. In the resolved setup jets are recombined with a radius $R_0 = 0.4$ and in the unresolved setup with a radius $R_0 = 0.8$. The larger recombination radius allows for more of the QCD radiation to become part of the jet system in the unresolved setup. Therefore, in the unresolved setup more events with misidentified W bosons will be present. While the relative size of the misidentification background was greatly reduced for the TL state by omitting the transverse-momentum cut on the jet system the shapes of the other polarisation states only receive very small changes. The misidentification background of the other polarisation states are not enhanced by a single cut; therefore, its removal is not expected to result in large changes. The cross-sections of the TT and the LT state are very similar up to an overall normalisation previously seen at the integrated level. This remains valid at NLO accuracy as the QCD real radiation only has a very small effect on the polarisation of the leptonically decaying Z boson. The K-factors of the polarisation states with at least one transversely polarised boson are always greater than one. The ones of the purely longitudinal polarisation state are less than one close to the peak and increase, when the invariant mass is further away from the W mass. The increase of the K-factors is very different in the resolved and the unresolved setup. In the resolved setup the K-factors increase more steeply for $M_{\mathrm{J}} < M_{\mathrm{W}}$ because of events, where not all of the decay jets of the W boson are included in the jet system. In the unresolved setup the increase is steeper for $M_{\mathrm{J}} > M_{\mathrm{W}}$. This results from events where real radiation from the initial state is recombined as part of the jet system. The different behaviour of the NLO real-emission corrections in the LL state is an effect of the different recombination radii used.

Figure 4.10 shows the invariant mass of the positron and the jet system. The shape of the distributions is sensitive to the polarisation of the bosons. When the Z boson is longitudinally polarised, the distribution features a peak at $M_{\mathrm{e^+J}} \approx 400\,\mathrm{GeV}$. This peak is sharper for the LL polarisation state than for the LT polarisation state. The TT polarisation state has a plateau in the region of $250\,\mathrm{GeV} < M_{\mathrm{e^+J}} < 500\,\mathrm{GeV}$. The shape of the TL polarisation state has features of the longitudinal and the transverse polarisation state, having a plateau in the region $300\,\mathrm{GeV} < M_{\mathrm{e^+J}} < 350\,\mathrm{GeV}$ and a small peak at $M_{\mathrm{e^+J}} \approx 400\,\mathrm{GeV}$. The NLO QCD

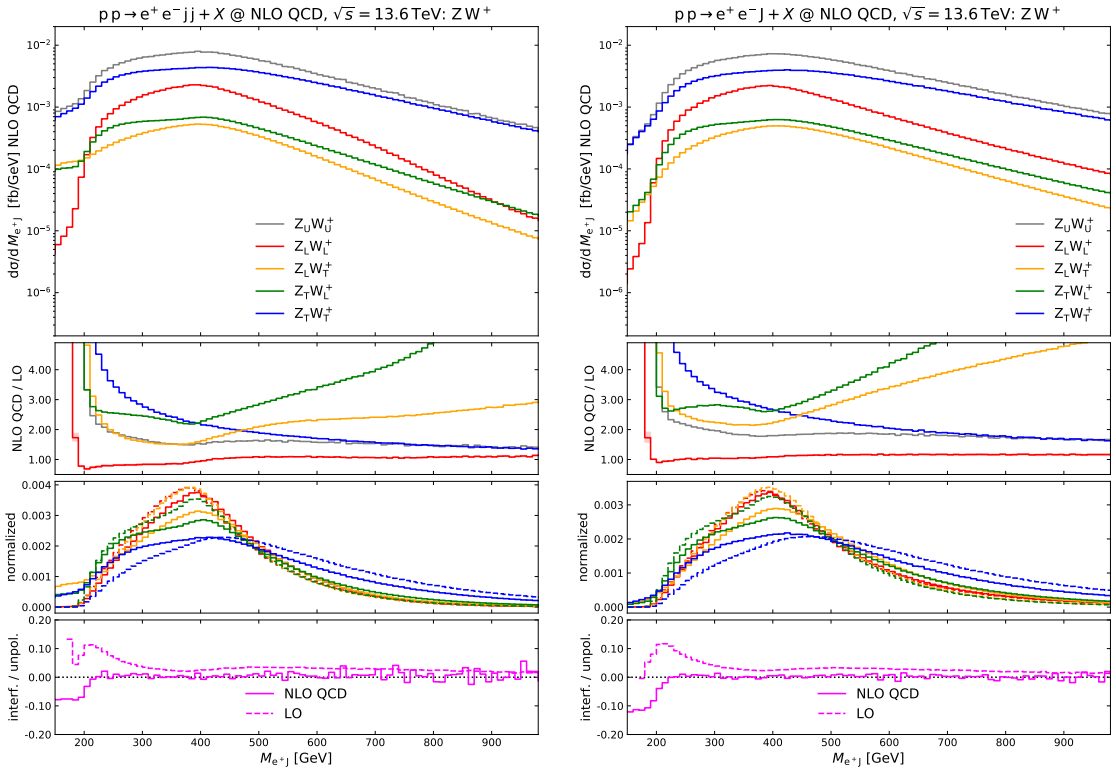

(a) Resolved topology

(b) Unresolved topology

Figure 4.10: Invariant-mass distributions of the system formed by the hadronic system J and the positron in semi-leptonic ZW^+ production at the LHC. The identification of the hadronic system J is described in Section 4.1.1. Details are described in the main text (first paragraphs of Section 4.1.3).

corrections considerably change the shape of the distributions. At high invariant masses the TT polarisation state falls off slower than the other polarisation states. The purely longitudinal polarisation state falls off faster in the resolved setup compared to the unresolved setup causing the LL cross-section to be almost one order of magnitude smaller at $M_{\mathrm{e^+J}} = 1\,\mathrm{TeV}$. The reason is that the LL polarisation state only receives small NLO corrections and behaves more LO like. In the high-invariant-mass region the decay jets of the W boson are emitted very close together, making it much easier for them to be recombined into one jet. This results in a suppression of the LO contribution of the resolved setup compared to unresolved setup. While for the pure polarisation states the NLO QCD K-factors are comparably small in the high-invariant-mass range the ones of the mixed polarisation states increase steadily. This is an effect of the LO unitarity suppression of the mixed polarisation states. In the low-invariant-mass region ($M_{\mathrm{e^+J}} < 200\,\mathrm{GeV}$) the NLO QCD K-factors become very large. Here the cross-section is dominated by real-radiation contributions. The additional final-state particle in real-emission processes allows for lower invariant masses, since they permit configurations where the W and Z boson are not back to back in the partonic CM frame. This contribution is larger in the resolved setup compared to the unresolved setup, since the larger recombination radius clusters more of the real emission into the jet system. The low-invariant-mass region also features a sizeable interference contribution ($\approx -10\%$).

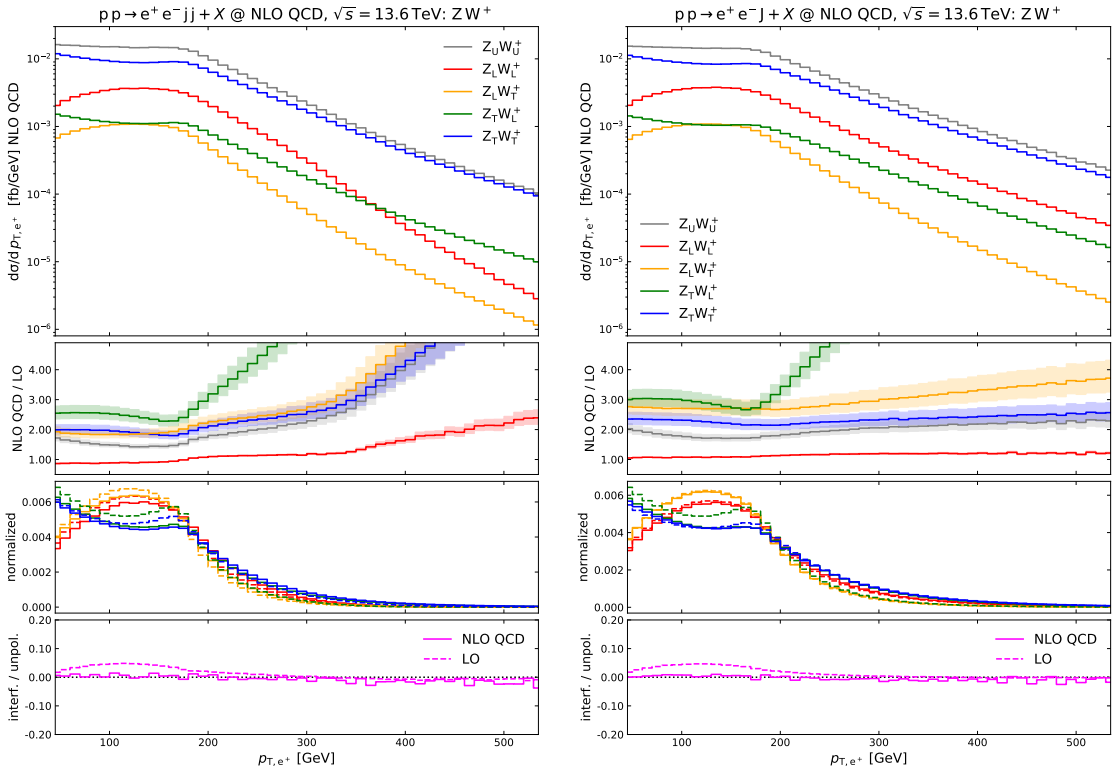

(a) Resolved (b) Unresolved topology

Figure 4.11: Transverse-momentum distributions of the positron in semi-leptonic ZW$^+$ production at the LHC. Details are described in the main text (first paragraphs of Section 4.1.3).

In Figure 4.11 the differential cross-section with respect to the transverse momentum of the positron is presented. The low-transverse-momentum region ($p_{\mathrm{T,e^+}} < 200\,\mathrm{GeV}$) is very sensitive to the polarisation of the Z boson. The distributions with a longitudinally polarised Z boson display a peak at $p_{\mathrm{T,e^+}} \approx 120\,\mathrm{GeV}$. When the Z boson is transversely polarised the distributions have two small peaks at $p_{\mathrm{T,e^+}} = 20\,\mathrm{GeV}$ and $p_{\mathrm{T,e^+}} \approx 180\,\mathrm{GeV}$. The cause is the same as for the different shapes in the decay angle of the Z boson shown in Figure 4.3. When the Z boson is longitudinally polarised the decay particles are predominantly emitted orthogonal to the direction of the Z boson in its rest frame. This leads to the decay products receiving similar amounts of transverse momentum, resulting in the one peak shape seen in the plot. For a transversely polarised Z boson in its CM frame the decay particles are mostly emitted in and opposite to its direction. This results in one of the decay particles getting more transverse momentum than the other one resulting in the two peak structure that is shown in the figure. The shape differences and the small interference contribution make the transverse momentum of the positron a suited observable for the discrimination of the polarisation states of the Z boson. Studying the behaviour at large transverse momenta the differences between the resolved and the unresolved setup can be understood. The NLO QCD K-factors increase much faster in the resolved setup than in the unresolved setup. This is caused by a suppression of the LO contribution of the resolved setup compared to the unresolved setup. When the positron has a large transverse momentum at LO this causes the W boson to also have a large transverse momentum. In the kinematic region, where the

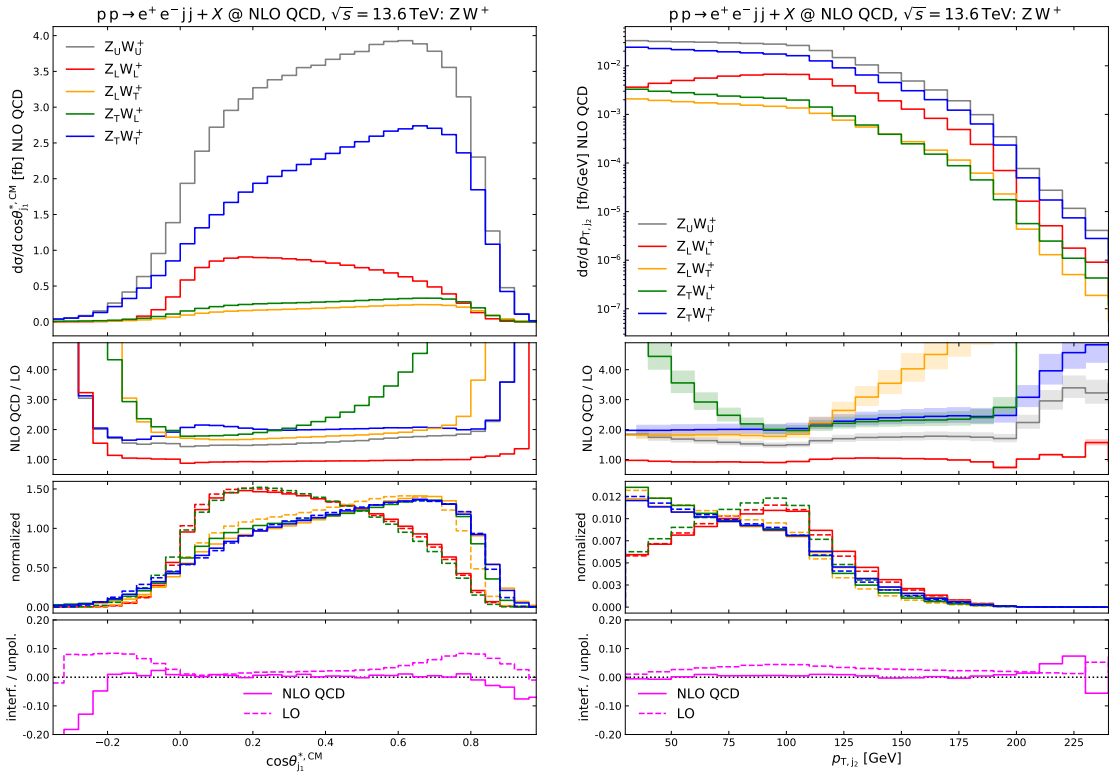

(a) (b)

Figure 4.12: Distributions in the leading-jet decay angle (left) and in the subleading-jet transverse momentum (right) in semi-leptonic ZW^+ production at the LHC. The identification of the leading and subleading jet is discussed in Section 4.1.1 and the decay-angle definition is given in Eq. (4.10). Results for the unpolarised and doubly-polarised process are shown in the resolved setup described in Section 4.1.1. The panels of the subfigures have the same structure as described in the main text (first paragraphs of Section 4.1.3).

W boson is strongly boosted, the two decay jets are emitted very close together in the lab frame resulting in a high probability that they will be recombined into one jet. The resolved setup requires two separated jets in the final state resulting in more of these events being cut away. The unresolved setup only requires one jet in the final state; therefore, these events pass the cuts. Another effect of the suppression of the LO in the unresolved setup at high transverse momenta is the faster fall-off of the LL polarisation state at large transverse momenta. For the polarisation states with at least one transversely polarised boson the large real-emission corrections reduce the differences between the resolved and unresolved setup at LO. The real-radiation contributions to the LL state are much smaller resulting in the suppression of the LO also being visible at NLO. Similar effects are found in the high-energy tails of correlated observables like the transverse momentum of the jet system or the electron-positron pair.

In the resolved setup the two decay jets of the W boson can be distinguished by their transverse momenta. This allows one to study observables that depend on the momenta of the individual jets forming the jet system. Analogous to the decay angle of the positron one

can define the decay angle of the decay jet with the largest transverse momentum as

$$\cos\left(\theta^{*,\mathrm{CM}}_{\mathrm{j}_1}\right) = \frac{\vec{p}^{\,*}_{\mathrm{j}_1} \cdot \vec{p}^{\,\mathrm{CM}}_{\mathrm{J}}}{\left|\vec{p}^{\,*}_{\mathrm{j}_1}\right| \left|\vec{p}^{\,\mathrm{CM}}_{\mathrm{J}}\right|}. \tag{4.10}$$

Similarly to the decay angle of the positron $\vec{p}^{\,*}_{\mathrm{j}_1}$ denotes the three-momentum of the jet with the largest transverse momentum making up the jet system in the CM frame of the jet system. The three-momentum of the jet system in the CM frame of the jet system and the electron-positron pair is labelled as $\vec{p}^{\,\mathrm{CM}}_{\mathrm{J}}$. The corresponding distributions are shown in Figure 4.12(a). The most significant difference to the decay angle of the positron is that the jets cannot be distinguished by their quark flavour. This means that the largest transverse-momentum jet can be an up-type or down-type quark. The distribution is not symmetric around $\cos\left(\theta^{*,\mathrm{CM}}_{\mathrm{j}_1}\right) = 0$ but instead there is a strong preference for the jet to be emitted in the direction of the jet system. The cause is that the largest transverse-momentum jet generally contributes the most to the momentum of the jet system. The decay angle of the subleading decay jet features the opposite behaviour with a clear preference to be emitted opposite to the direction of the jet system. Analogous to the decay angle of the positron this observable is very sensitive to the polarisation of the W boson. The TT and the LT have a peak at $\cos\left(\theta^{*,\mathrm{CM}}_{\mathrm{j}_1}\right) = 0.7$, while the LL has a peak at $\cos\left(\theta^{*,\mathrm{CM}}_{\mathrm{j}_1}\right) = 0.1$. The reason for the observed shapes is the same as for the decay angle of the positron. Taking the hardest transverse-momentum jet primarily shifts the distributions. Transversely polarised bosons preferably emit their decay particles in and opposite to their direction, while longitudinal ones emit their decay particles orthogonal to their direction. The decay angle of the hardest decay jet is very sensitive to the correct identification of the decay jets by the jet system.As shown for the invariant mass of the jet system in Figure 4.8 the TL polarisation state receives the largest misidentification background. At LO the shape of the TL distribution is identical to the LO one of the LL state. This is expected since the decay angle is insensitive to the polarisation of the Z boson. At NLO the TL distribution resembles the shape of the distributions with a transversely polarised W boson. This is caused by misidentification of the decay jets of the W boson. The contribution from the interferences are very small in the most populated regions. Close to the edges of the plot, where the effects from the phase-space cuts are the largest, they are large and negative.

In Figure 4.12(b) the differential cross-section with respect to the transverse momentum of the second largest transverse momentum decay jet is shown. All polarisation states feature a very fast fall-off at moderate transverse momenta. The LL polarisation state has a peak at $p_{\mathrm{T,j}_2} \approx 100\,\mathrm{GeV}$. The LT polarisation features the same peak but only at LO. The 100 GeV of the peak is exactly half of the minimum transverse momentum required for the jet system. As seen in Figure 4.4 the longitudinally polarised W boson is mostly produced with a large scattering angle. As the decay particles of longitudinally polarised bosons are predominantly emitted orthogonal to the bosons direction the transverse momentum of the boson is split evenly between the decay particles resulting in the observed peak. For the other polarisation states the NLO cross-section steadily decreases with increasing transverse momentum. The distribution of the TL polarisation state follows the shape of the LL polarisation state at LO featuring the same peak at $p_{\mathrm{T,j}_2} \approx 100\,\mathrm{GeV}$ but when including the NLO QCD corrections the shape of the distribution drastically changes. The shape of the TL at NLO is very similar to the ones from the transversely polarised W bosons. The decay particles of transversely

polarised bosons are predominantly emitted in and opposite to its direction resulting in one decay particle having more transverse momentum then the other one. This causes the subleading decay jet to be preferably produced with very low transverse momentum. This considerable change in shape is caused by misidentification of the decay jets of the W boson as already seen for the decay angle of the hardest jet in Figure 4.12(a). The gluon-induced partonic real-emission processes that give the main contribution to the NLO corrections of the TL state prefer a boosted Z boson that recoils against the W boson, decaying into low-transverse-momentum jets, and a hard-real-radiation parton. When the real-radiation jet from the production is treated as a decay jet of the W boson the jet system is composed of one high-transverse-momentum jet and one low-transverse-momentum jet. This enhances the cross-section in the low-transverse-momentum region causing the shape to resemble the ones from transverse W bosons.

4.2 Polarised W^+W^- pair production at NLO EW

To further the understanding of the Higgs sector of the Standard Model, additional vector-boson pair-production processes can be studied. An interesting example for such a process is W^+W^- pair production. In particular,

$$\mathrm{pp} \to \mathrm{e}^+\nu_\mathrm{e}\mu^-\nu_\mu + X \tag{4.11}$$

for the full process and the process

$$\mathrm{pp} \to \mathrm{W}^+\left(\to \mathrm{e}^+\nu_\mathrm{e}\right)\mathrm{W}^-\left(\to \mu^-\nu_\mu\right) + X \tag{4.12}$$

in the DPA are studied. The two initial-state protons collide and produce a W^+ and a W^- boson. For the full off-shell process many higher-order accurate predictions exist. In particular, the QCD corrections are known up to NNLO [152–154]. The EW corrections have been calculated up to NLO [154–156]. Additionally the matching to PS has been performed [127, 128, 157]. For the purpose of a polarisation study using the DPA the NLO [52] and NNLO [88] QCD corrections have been calculated. The NLO QCD accurate calculation has been matched to PS [158]. The missing piece is the calculation of the NLO EW corrections in the DPA.

The NLO EW corrections to W^+W^- pair production include real-emission diagrams with an unresolved photon radiated off one of the W boson propagators. To cancel the IR divergences present in diagrams as the ones from Figure 4.13 the charged resonance counterterms given in Chapter 3 are required. In particular, to cancel the divergence from a soft photon that is emitted from one of the initial-state quarks seen in Figure 4.13(a), dipoles with the resonant W bosons taking the role of the spectator are needed. For diagrams like Figure 4.13(b), where the photon is emitted form the resonant propagator, a partial fraction decomposition as described in Section 3.1 is performed to split the divergence between production and decay. For the process with the photon emitted from the production, dipoles with the resonance as emitter and either the other resonance or one of the initial states as spectator are needed. The divergence in the process with the photon emitted from the decay is cancelled together with the divergences arising from diagrams like in Figure 4.13(c) with the decay dipoles given in Section 3.3. Since at LO the two resonant W bosons and their decay products are the only charged final-state particles the final-final massive-massless and the final-final massless-massive dipoles are not necessary.

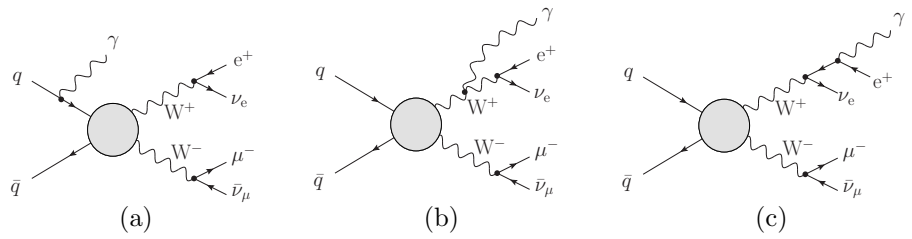

Figure 4.13: Sample photon-radiation diagrams contributing to W^+W^- production and decay at NLO EW.

4.2.1 Setup

In this section the setup chosen for the calculation is discussed. In the full off-shell calculation the partonic processes

$$q\bar{q},\, b\bar{b}\,, \gamma\gamma \to e^+\nu_e\mu^-\nu_\mu \tag{4.13}$$

($q = u, d, s, c$) contribute to the LO cross-section. At NLO EW the real-emission processes

$$\begin{aligned} q\bar{q},\, b\bar{b}\,, \gamma\gamma &\to e^+\nu_e\mu^-\nu_\mu\gamma\,, \\ \gamma\overset{(-)}{q} &\to e^+\nu_e\mu^-\nu_\mu\overset{(-)}{q}\,, \\ \gamma\overset{(-)}{b} &\to e^+\nu_e\mu^-\nu_\mu\overset{(-)}{b} \end{aligned} \tag{4.14}$$

contribute.

The contributing partonic processes with an initial-state photon and bottom or antibottom quark receive a large contribution from the production of an s-channel top or antitop quark. The focus of this computation is the polarisation of the W boson from pair production and not from top-quark decays. Therefore, the contribution from these partonic processes is regarded as irreducible background that would have to be subtracted similarly to the non-resonant background. In the DPA calculation these contributions are removed by assuming a perfect b-jet veto. For the full off-shell computation all contributing partonic processes are studied. In the DPA calculation the partonic processes

$$q\bar{q},\, b\bar{b}\,, \gamma\gamma \to W^+\left(\to e^+\nu_e\right) W^-\left(\to \mu^-\nu_\mu\right) \tag{4.15}$$

are present in contributions with Born-like external particles (Born, virtual and integrated-subtraction counterterms). The partonic processes

$$\begin{aligned} q\bar{q},\, b\bar{b}\,, \gamma\gamma &\to W^+\left(\to e^+\nu_e\right) W^-\left(\to \mu^-\nu_\mu\right)\gamma\,, \\ \gamma\overset{(-)}{q} &\to W^+\left(\to e^+\nu_e\right) W^-\left(\to \mu^-\nu_\mu\right)\overset{(-)}{q} \end{aligned} \tag{4.16}$$

contribute to the NLO EW real-emission corrections. These partonic processes are treated with the on-shell projection for two resonances decaying into two particles each. The real-emission processes

$$\begin{aligned} q\bar{q},\, b\bar{b}\,, \gamma\gamma &\to W^+\left(\to e^+\nu_e\gamma\right) W^-\left(\to \mu^-\nu_\mu\right) \\ q\bar{q},\, b\bar{b}\,, \gamma\gamma &\to W^+\left(\to e^+\nu_e\right) W^-\left(\to \mu^-\nu_\mu\gamma\right) \end{aligned} \tag{4.17}$$

are treated with the on-shell projection, where one of the resonances decays into three particles and the other one into two particles. For the DPA calculation the method described in Chapter 2 is followed.

The proton CM energy is set to $\sqrt{s} = 13.6\,\text{TeV}$ corresponding to Run-3 of the LHC. The on-shell values for the W and Z mass and width taken from the PDG [159] are

$$\begin{aligned} M_{\text{Z}}^{\text{OS}} &= 91.1876\,\text{GeV}, & \Gamma_{\text{Z}}^{\text{OS}} &= 2.4952\,\text{GeV}, \\ M_{\text{W}}^{\text{OS}} &= 80.377\,\text{GeV}, & \Gamma_{\text{W}}^{\text{OS}} &= 2.085\,\text{GeV}\,. \end{aligned} \tag{4.18}$$

The values were then converted to the pole values in the same manner as for the calculation of the ZW production in Section 4.1 using Eq. (4.3). The used width and mass of the top quark and the Higgs boson taken from the PDG [159] are

$$\begin{aligned} M_{\text{t}} &= 172.69\,\text{GeV}, & \Gamma_{\text{t}} &= 1.42\,\text{GeV}, \\ M_{\text{H}} &= 125.25\,\text{GeV}, & \Gamma_{\text{H}} &= 0.0041\,\text{GeV}\,. \end{aligned} \tag{4.19}$$

The EW coupling is calculated using the G_μ scheme. For the full off-shell computation the complex masses are used and for the computations in the DPA the real masses are used. The Fermi coupling constant is set to

$$G_\mu = 1.16638 \times 10^{-5}\,\text{GeV}^{-2}\,. \tag{4.20}$$

The calculation is done in the five flavour scheme. The PDF set `NNPDF31_nnlo_as_0118_luxqed` [136, 137] is used. The renormalisation and factorisation scale are set to the fixed scale

$$\mu_{\text{R}} = \mu_{\text{F}} = M_{\text{W}}\,. \tag{4.21}$$

The CMS measurement [160] (*sequential-cut selections* therein) was used as a template for the chosen event selection. To recombine the charged leptons with unresolved photon radiation the anti-k_{T} jet clustering algorithm [140] is applied with a radius of $R = 0.1$. The selected events must fulfil

$$\begin{aligned} &p_{\text{T},\ell_1} > 25\,\text{GeV}, \\ &p_{\text{T},\ell_2} > 20\,\text{GeV}\ , \\ &|\eta_{\text{e}^+}| < 2.5, \\ &|\eta_{\mu^-}| < 2.4, \\ &p_{\text{T},\text{e}^+\mu^-} > 30\,\text{GeV}, \\ &M_{\text{e}^+\mu^-} > 20\,\text{GeV}, \\ &p_{\text{T,miss}} > 20\,\text{GeV}. \end{aligned} \tag{4.22}$$

The final-state particles are ordered with respect to their transverse momentum and $\ell_{1,2}$ denotes the charged lepton with the largest and second largest transverse momentum.

4.2.2 Integrated results

In Table 4.4 the integrated cross-section of the setup described in the previous section is presented. Two independent calculations with the Monte Carlo codes MoCaNLO and

state	σ_{LO} [fb]	$\sigma_{\text{NLO EW}}$ [fb]	δ_{EW}[%]	$f_{\text{NLO EW}}$[%]
$b\bar{b}$, γb, $\gamma\bar{b}$ excluded				
full	254.79(2)	249.88(9)	−1.93	103.5
unp.	245.79(2)	241.48(2)	−1.75	100
LL	18.752(2)	18.510(2)	−1.30	7.7
LT	32.084(3)	32.043(3)	−0.13	13.3
TL	33.244(5)	33.155(5)	−0.27	13.7
TT	182.17(2)	177.83(2)	−2.38	73.6
int.	−20.46(3)	−20.1(1)	−1.96	−8.3
$b\bar{b}$ included, γb, $\gamma\bar{b}$ excluded				
full	259.02(2)	253.95(9)	−1.96	103.4
unp.	249.97(2)	245.49(2)	−1.79	100.0
LL	21.007(2)	20.663(2)	−1.64	8.4
LT	33.190(3)	33.115(3)	−0.23	13.5
TL	34.352(5)	34.230(5)	−0.35	13.9
TT	182.56(2)	178.21(3)	−2.38	72.6
int.	−21.14(5)	−20.6(2)	−2.45	−8.4
$b\bar{b}$, γb, $\gamma\bar{b}$ included				
full	259.02(2)	265.59(9)	+2.54	-

Table 4.4: Fiducial cross-sections (in fb) at LO and NLO EW for full, unpolarised, and doubly polarised W^+W^- production at the LHC in the fully leptonic decay channel. Absolute numbers in parentheses are numerical integration uncertainties. The value δ_{EW} (in percentage) is computed as the EW correction relative to the LO result. The values $f_{\text{NLO EW}}$ are fractions of NLO EW cross-sections over the NLO EW unpolarised result. The γb, $\gamma\bar{b}$ contributions are only included in the full calculation (last row). The interference (int.) is evaluated as the difference between the unpolarised and the sum of the polarised results.

BBMC were performed, finding agreement within the integration uncertainties. The results shown here are those computed with MoCaNLO. The scale variation uncertainties were omitted in the table as the NLO QCD corrections are not considered. Since the LO process and the NLO EW corrections are purely EW processes, only the factorisation scale enters the scale variation. Therefore, the scale variation does not properly reflect the potential uncertainties from higher-order QCD corrections. In a similar calculation [158] the NLO QCD corrections were calculated giving scale uncertainties of 3–5% depending on the polarisation state.

To analyse the effects of certain individual contributions different initial states were studied. Firstly the bottom-antibottom, photon-bottom and photon-antibottom induced processes, were excluded. Secondly only the photon-bottom and photon-antibottom induced

processes were excluded. Lastly only for the full off-shell case all initial states were included. The exclusion of the photon-bottom and photon-antibottom induced processes can be accomplished by applying a perfect bottom-jet veto. The main goal of removing these contributions is the removal of the top W-boson production background. The difference from the bottom-antibottom induced channels is the inclusion of t-channel top-quark diagrams. By studying the different partonic processes the effects of the t-channel top-quark diagrams are analysed.

Comparing the fractions of the full off-shell and unpolarised contribution, the non-resonant background is found to be of the order $\approx 3.5\%$. This is of the expected accuracy of the DPA $\mathcal{O}(\Gamma_\mathrm{W}/M_\mathrm{W})$. As expected for a di-boson process, the TT polarisation state gives by far the largest contribution at over 70%. The contributions from the other polarisation states are notably smaller. The mixed polarisation states have very similar contributions. The small differences in the LT and TL state are primarily caused by the different PDFs for quarks and antiquarks. The purely longitudinal state has the smallest cross-section. There is a fairly large contribution from the longitudinal and transverse interferences that amounts to $\approx -8\%$ of the unpolarised result. The large interference contribution observed in previous $\mathrm{W^+W^-}$ production calculations [52, 88, 158] stems from the phase-space cuts. In particular, the transverse-momentum cuts on the two charged leptons prevent the cancellation of the interference contribution. For W bosons the effect is particularly large as the left-chiral coupling to fermions significantly changes the shape of the decay angle in the most populated regions.

While the NLO EW corrections are negative for all polarisation states their relative size differs considerably. They are the most negative for the TT polarisation state and the least negative for the mixed polarisation states. The LL polarisation state features an intermediate behaviour.

The bottom-antibottom induced partonic processes provide a much larger enhancement to the longitudinal polarisation states than to the transverse polarisation states. The cross-section of the purely longitudinal polarisation states increase by $\approx 2\,\mathrm{fb}$. The mixed polarisation states gain $\approx 1\,\mathrm{fb}$ and the cross-section of the purely transverse polarisation state only increases by $\approx 0.4\,\mathrm{fb}$. The cause of this effect are diagrams with a massive t-channel top-quark exchange. The different helicity structure in contrast to massless t-channel propagators favour the coupling of the top quark to longitudinally polarised W bosons resulting in the seen enhancement of the longitudinal signal.

For the full off-shell process also the photon-bottom/antibottom induced real-emission contributions were computed. These partonic processes are dominated by top/antitop-W production. Even though they are suppressed by the photon and bottom PDFs, they give an almost 5% correction to the full off-shell NLO EW cross-section.

4.2.3 Differential results

For the experimental separation of the polarised signals differential observables are needed that feature very different normalised shapes for the polarised signals. The plots of the differential cross-sections (Figures 4.14–4.16) are organised as follows. The top left panel displays the absolute differential cross-section including the $\mathrm{b\bar{b}}$-induced processes and excluding $\gamma\mathrm{b}(\gamma\bar{\mathrm{b}})$-induced ones for the full off-shell (black), unpolarised (gray), LL (red), LT (yellow), TL (green), TT (blue) and sum of all polarised processes (magenta). Additionally

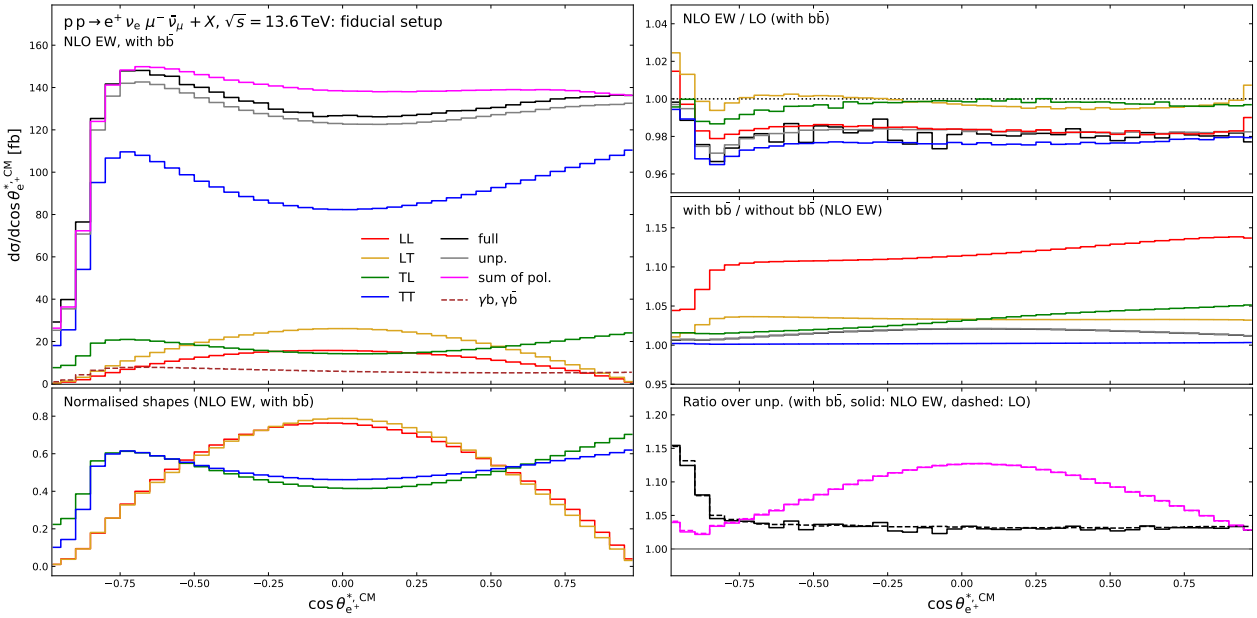

Figure 4.14: Distributions in the polar decay angle of the positron in the W^+ rest frame for W^+W^- production and decay at the LHC with NLO EW accuracy. The setup detailed in Section 4.2.1 is understood. Polarisations are defined in the di-boson CM reference frame. Details are described in the main text (first paragraphs of Section 4.2.3).

the panel also depicts the full off-shell contribution from the $\gamma b(\gamma\bar{b})$-induced partonic processes (dashed, brown). The bottom left panel shows the normalised shapes of the polarised signals. The top right panel presents the NLO EW K-factors. The center right panel shows the relative size of the cross-section including the $b\bar{b}$-induced partonic processes compared to the cross-section without the $b\bar{b}$-induced processes. The bottom right panel depicts the relative size of the full off-shell LO (dashed, black), NLO EW (solid, black) and the sum of all polarisations LO (dashed, magenta), NLO EW (solid, magenta) compared to the unpolarised DPA cross-section.

In Figure 4.14 the differential cross-section with respect to the decay angle of the positron in the CM frame of the W^+ boson is depicted. This is an unobservable quantity as it requires the reconstruction of the two neutrino momenta. Its study is, however, still important as its features translate to other correlated observables that are measurable. The decay angle of the positron is very sensitive to the polarisation of the W^+ boson. The normalised shapes of the plots show the characteristic peak in the central region for a longitudinally polarised W^+ boson and a dip for a transversely polarised W^+ boson already seen in other di-boson processes [39, 53–55, 151]. For decay angles $\cos(\theta^*) < -0.75$ the shape of the distribution is heavily influenced by the transverse-momentum cut on the positron. Since there is no analogous cut on the electron neutrino, there is no similar suppression of the cross-section at $\cos(\theta^*) > +0.75$. The inclusion of the NLO EW corrections only affects the shape of the distributions in the region $\cos(\theta^*) < -0.75$. This is the region of phase space that is affected the most by the transverse-momentum cut on the positron. In the rest of the phase space the NLO K-factor is close to constant and mirrors the results seen at the integrated level. As seen at the integrated level the contribution from the $b\bar{b}$-induced channels is the largest for the LL state and very small for the TT state. For states where the W^- boson

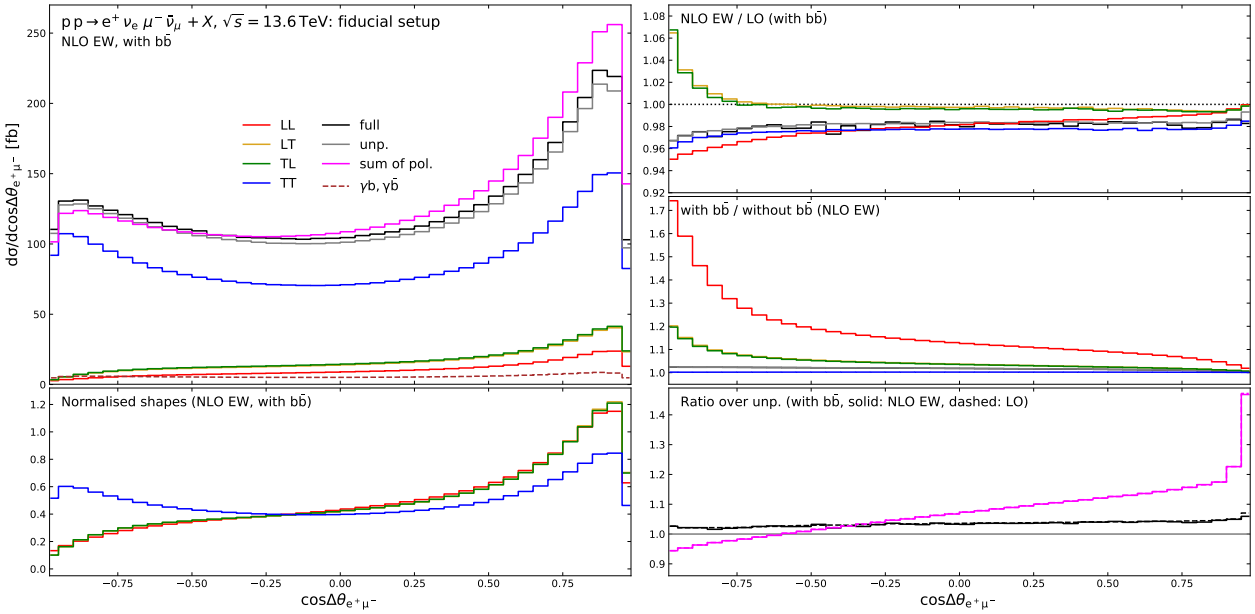

Figure 4.15: Distributions in the cosine of the angular separation between the positron and the muon for W^+W^- production and decay at the LHC with NLO EW accuracy. Details are described in the main text (first paragraphs of Section 4.2.3).

is longitudinally polarised the contribution increases, when the positron is emitted closer to the direction of the W^+ boson. The relative size of the non-resonant background increases to 15%, when the positron is emitted anticollinear to the W^+ boson. This is the phase-space region effected the most by the cuts. In the rest of the phase space the non-resonant background is constant. The size of the interferences is the largest at $\theta_{e^+}^{*,\mathrm{CM}} \approx \pi/2$ where they reach up to -13%. Large interference contributions were already found in setups with the polarisation defined in the lab frame [52, 88]. The origin of the large interferences is the transverse-momentum cut on the two charged leptons, that prevents them from cancelling.

In Figure 4.15 the differential cross-section with respect to the angular separation of the positron and muon momenta is shown. This is a polarisation sensitive observable that can be measured at the LHC. The shapes of all polarisation states feature a peak in the quasi collinear region. The bin with the smallest angular separation is suppressed by the invariant mass requirement $M_{e^+\mu^-} > 20\,\mathrm{GeV}$ for the two charged leptons. The shape of the purely transverse polarisation state is different from the others as it features a second local maximum in the quasi anticollinear region. For the LL, LT and TL polarisation state the cross-section decreases with increasing angular separation. The local maximum in the quasi collinear region is caused by the PDFs. The dominant contribution to the W^+W^- production cross-section originates from valence-quark sea-quark scattering. This means that for most events one of the initial-state partons will be more energetic than the other one resulting in the complete event being boosted into one direction. Therefore, the emission of a positron and a muon in a similar direction is favoured. The additional enhancement for the purely transverse polarisation state, when the positron and the muon are emitted in close to opposite directions, is an effect of the different decay kinematics of transversely polarised bosons. As seen in the plot of the decay angle of the positron in Figure 4.14 the decay particles of a transversely polarised W boson are preferably emitted in and opposite to the direction of the

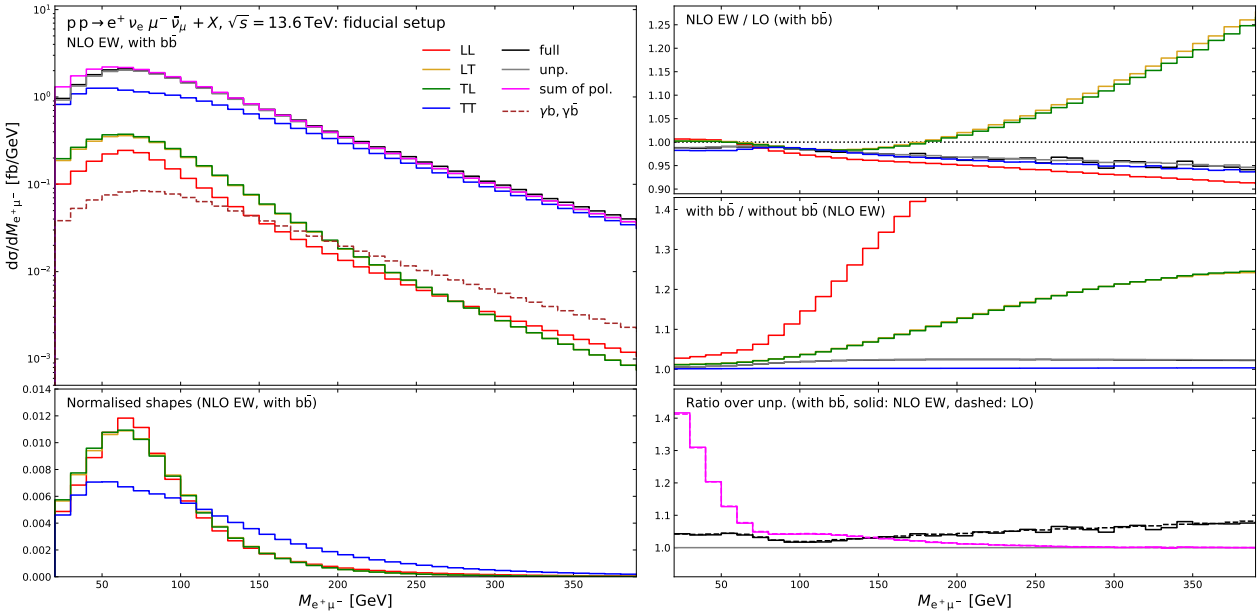

Figure 4.16: Distributions in the invariant mass of the positron–muon pair for W^+W^- production and decay at the LHC with NLO EW accuracy. Details are described in the main text (first paragraphs of Section 4.2.3).

W boson in the di-boson CM frame. When boosting back to the lab frame there is a good chance that one of the charged leptons will be emitted opposite to the direction of the other one resulting in a large angular separation. The angular separation of the positron and the muon is also very well suited to see the effects of the bottom-antibottom induced processes. The plot shows that their relative size for the longitudinal polarisation states becomes very large in the anticollinear region. The reason is that the bottom-antibottom induced processes are sea-quark sea-quark scattering events resulting in a much more symmetric final state in the lab frame. This means that unlike the up-antiup and down-antidown quark induced processes the bottom-antibottom induced processes are not suppressed in the anticollinear region producing the large relative correction (more than 75% for $\Delta\theta_{e^+\mu^-} \approx \pi$). The same effect, though less sizeable, is also seen for the mixed polarisation states. The relative size of the NLO EW corrections are largest in the anticollinear region. The corrections to the mixed polarisation states increase to +6.5%. The anticollinear region is preferably filled with events with a large invariant mass. The positive corrections are an effect of the suppression of the LO cross-section in the high-energy limit. The corrections to the LL polarisation state increase from −5% to −0.1%. The change in the relative size of the NLO EW correction to the TT state is much smaller increasing from −4% in the anticollinear region to −2% in the collinear region. The more negative corrections in the anticollinear region of the LL and TT state are caused by EW logarithms. The smaller effect of the EW logarithms on the TT state is a consequence of the large LO signal in the quasi anticollinear region. The effects from the LO suppression and the EW logarithms in the high-energy region are seen better in the distribution with respect to the invariant mass of the two charged leptons shown in Figure 4.16.

In Figure 4.16 the differential cross-section with respect to the invariant mass of the two charged leptons is presented. This observable is closely related to the angular separation of

the positron and the muon as large angular separations generally result in large invariant masses. The purely transverse polarisation state has a notably different shape compared to the other polarisation states. The cross-section of the TT state falls off slower in the high-invariant-mass region compared to the mixed and purely longitudinal polarisation states. This results in an overall much flatter shape for the purely transverse polarisation state. The position of the peak is also different depending on the polarisation state. The purely longitudinal and the mixed polarisation states are peaked at $M_{e^+\mu^-} \approx 65\,\text{GeV}$, while the purely transverse is peaked at $M_{e^+\mu^-} \approx 50\,\text{GeV}$. The relative NLO EW corrections increase in size in the high-invariant-mass region. The large positive corrections of the mixed polarisation states are the result of a suppression of the LO contribution, that originates from unitarity cancellations and is proportional to the energy of the longitudinally polarised W boson [149]. The increasingly negative corrections to the LL and TT states are caused by large EW logarithms. In the low-invariant-mass region the contribution from the interferences is very large amounting to $\approx 40\%$ of the unpolarised cross-section. In the high-invariant-mass region they become negligible. The reason is that the transverse-momentum cuts on the charged leptons, which spoil the cancellation of the interferences, is much more prominent in the low-invariant-mass region. For small invariant masses the $b\bar{b}$-induced partonic processes only give a very small contribution. At moderate invariant masses their effect becomes very large (+50% at 200 GeV for LL). The relative size of the non-resonant background varies between 3% and 8% increasing with larger invariant masses.

Chapter 5

Vector-boson scattering

5.1 Overview

As already mentioned in the introduction, VBS processes are ideal for studying all possible interactions of the EW gauge bosons and the Higgs. Polarised VBS processes offer additional sensitivity to the delicate unitarity cancellations in the EW sector. This makes them indispensable for precision tests of the Standard Model. Therefore, also the experimental collaborations ATLAS and CMS have invested much to measure VBS at the LHC. This has lead to the successful measurement of $W^{\pm}W^{\pm}$ [161–165], ZZ [166–168], $ZW^{\pm}$ [164, 169–171] and W^+W^- [172, 173] scattering in fully leptonic decay channels. VBS has been used to constrain possible deviations from the Standard Model [161, 174–176]. Recent studies have begun to look into VBS in semi-leptonic decay channels [176–178]. So far only one experimental study of polarised VBS by the CMS collaboration exists [72].

Theoretical predictions for full off-shell VBS exist that are NLO QCD [179–190] and NLO EW [184, 186–191] accurate. Furthermore, the irreducible QCD backgrounds to W^+W^+ and ZZ have been computed up to NLO QCD and EW [184, 188, 190] accuracy. The matching to PS has been performed to NLO QCD accurate fixed-order computations [185, 192–199] and to NLO EW accurate fixed-order computations [200].

The existing theoretical computation for polarised VBS are only LO accurate [51, 85–87, 151]. They have been computed with the publicly available Monte Carlo codes PHANTOM [201], MG5_aMC@NLO [202] and Sherpa [203]. Sherpa is capable of producing approximate NLO QCD accurate predictions [151], this has so far only been used for vector-boson pair production and not VBS. Improving the accuracy to NLO QCD and EW for VBS is urgently needed in the context of the data that is being gathered at LHC experiments.

The particular process that will be discussed in this chapter is the scattering of two W^+ bosons.

5.2 W^+W^+ scattering at NLO EW and QCD

The results that are presented in this section have been published in Ref. [37]. Same-sign W-boson scattering with leptonic decays is the simplest VBS process to study as it features the cleanest signal. It does not have a top-antitop production background as in W^+W^- scattering. Additionally, there is no contribution from on-shell Higgs production at LO. Such contributions can severely disrupt the DPA and lead to large non-resonant backgrounds.

This makes W^+W^+ the ideal VBS process to compute the NLO corrections by applying the methods discussed in Chapter 3.

Here VBS in the purely leptonic decay mode is considered. For the full off-shell calculation the process studied is

$$\mathrm{pp} \to \mathrm{e}^+\nu_\mathrm{e}\mu^+\nu_\mu + \mathrm{jj} + X\,. \tag{5.1}$$

The DPA process is

$$\mathrm{pp} \to \mathrm{W}^+\left(\to \mathrm{e}^+\nu_\mathrm{e}\right)\mathrm{W}^+\left(\to \mu^+\nu_\mu\right) + \mathrm{jj} + X\,. \tag{5.2}$$

At LO there are three different orders that contribute to the processes defined in Eqs. (5.1) and (5.2): the LO VBS signal $\mathcal{O}(\alpha^6)$, the LO interference background $\mathcal{O}(\alpha_\mathrm{s}\alpha^5)$ and the LO QCD background $\mathcal{O}(\alpha_\mathrm{s}^2\alpha^4)$. At NLO there are four different orders that contribute: the NLO EW corrections to the VBS signal $\mathcal{O}(\alpha^7)$, the NLO QCD corrections to the VBS signal $\mathcal{O}(\alpha_\mathrm{s}\alpha^6)$ and the NLO corrections to the irreducible backgrounds $\mathcal{O}(\alpha_\mathrm{s}^2\alpha^5)$ and $\mathcal{O}(\alpha_\mathrm{s}^3\alpha^4)$. At LO all contributions, signal and background, are computed. At NLO only the corrections to the signal $\mathcal{O}(\alpha^7)$ and $\mathcal{O}(\alpha_\mathrm{s}\alpha^6)$ are computed. The contribution denoted as the NLO QCD corrections to the VBS signal also contains EW corrections to the interference background. As these contributions are of the same perturbative order they cannot be split in an unambiguous way. Since the QCD corrections to the VBS signal give the dominant contribution [184] they are referred to as such in the following. The computation of the NLO corrections to the irreducible background is not part of this thesis.

In Figure 5.1 diagrams that feature Born kinematics are shown. These contributions are characterised by the W bosons decaying into a charged lepton and the corresponding neutrino. These are LO contributions to the signal (top left), EW virtual corrections (bottom left), QCD virtual corrections (bottom right) and LO contributions to the irreducible QCD background (top right). The interference of the two top diagrams is part of the interference background. Only some of the partonic processes give an non-zero contribution to the interference-background cross-section. In partonic processes, with two external quarks of the first generation and two from the second generation, the colour algebra causes the colour-averaged product of the amplitudes to vanish.

5.2.1 Setup

The calculation is performed with a CM energy of $\sqrt{s} = 13.6\,\mathrm{TeV}$ corresponding to Run-3 of the LHC. The general methods are the same as for the vector-boson pair-production processes in Chapter 4. The values for the on-shell masses and decay widths of the W and Z bosons are taken from the PDG [159] giving

$$\begin{aligned} M_\mathrm{Z}^\mathrm{OS} &= 91.1876\,\mathrm{GeV}, & \Gamma_\mathrm{Z}^\mathrm{OS} &= 2.4952\,\mathrm{GeV}, \\ M_\mathrm{W}^\mathrm{OS} &= 80.377\,\mathrm{GeV}, & \Gamma_\mathrm{W}^\mathrm{OS} &= 2.085\,\mathrm{GeV}\,. \end{aligned} \tag{5.3}$$

As the calculation requires the pole values of the masses and widths they have been converted according to Eq. (4.3). Furthermore, the mass and width values of the top quark and the Higgs boson taken from the PDG [159] are

$$\begin{aligned} m_\mathrm{t} &= 172.69\,\mathrm{GeV}, & \Gamma_\mathrm{t} &= 1.42\,\mathrm{GeV}, \\ M_\mathrm{H} &= 125.25\,\mathrm{GeV}, & \Gamma_\mathrm{H} &= 0.0041\,\mathrm{GeV}\,. \end{aligned} \tag{5.4}$$

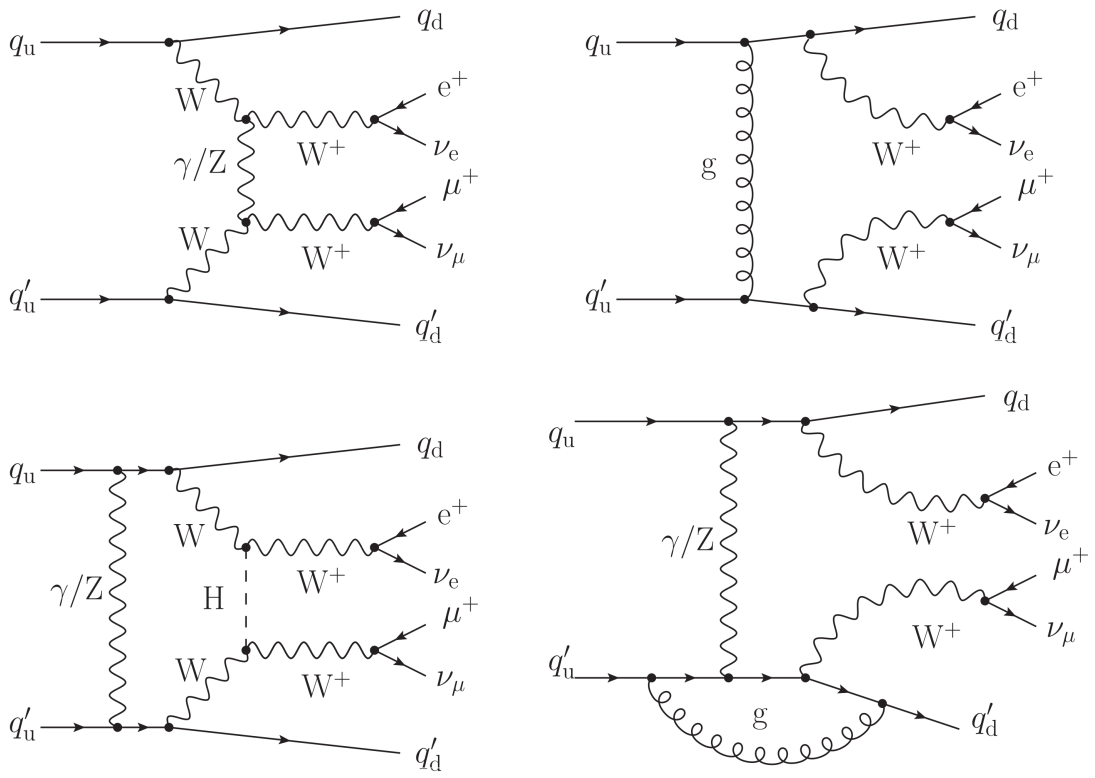

Figure 5.1: Sample doubly-resonant contributions to W^+W^+ scattering at LO EW (top left), NLO EW (bottom left) and NLO QCD (bottom right) accuracy, and to the QCD background at LO (top right).

In the full off-shell calculations the non-zero top-quark width Γ_t is used. For the calculations in the DPA, both polarised and unpolarised, the top width is set to zero $\Gamma_t = 0\,\text{GeV}$. The EW coupling is computed using the G_μ scheme [43, 204] with the Fermi constant

$$G_\mu = 1.16638 \times 10^{-5}\,\text{GeV}^{-2}\,. \tag{5.5}$$

The EW coupling is computed differently in the full off-shell computation compared to the DPA ones. In the full off-shell calculation the EW coupling is calculated with the complex-mass scheme [38, 205, 206] giving

$$\alpha = \frac{\sqrt{2}}{\pi}\,G_\mu \left|\mu_W^2 \left(1 - \frac{\mu_W^2}{\mu_Z^2}\right)\right|\,, \qquad \mu_V^2 = M_V^2 - \mathrm{i}M_V\Gamma_V \quad (V = \text{W, Z})\,. \tag{5.6}$$

The calculations performed in the DPA, both polarised and unpolarised, make use of the real-mass scheme giving the EW coupling

$$\alpha = \frac{\sqrt{2}}{\pi}\,G_\mu\,M_W^2 \left(1 - \frac{M_W^2}{M_Z^2}\right)\,. \tag{5.7}$$

Both the full off-shell and the DPA calculations are performed with five active quark flavours, even though for this process no bottom-quark-induced processes contribute up to NLO. However, photon-induced partonic processes contribute to the real EW corrections. For

the treatment of the initial-state collinear singularities both from EW and QCD the $\overline{\text{MS}}$ factorisation scheme is applied. The `NNPDF40_nnlo_as01180_qed` PDFs [207], linked via the LHAPDF interface [138], are employed. The factorisation and renormalisation scales are dynamically set to

$$\mu_{\text{R}} = \mu_{\text{F}} = \sqrt{p_{\text{T,j}_1}\, p_{\text{T,j}_2}}\,, \tag{5.8}$$

where $p_{\text{T,j}_1}$ and $p_{\text{T,j}_2}$ are the transverse momenta of the hardest and second-hardest transverse-momentum tagged jet. To compute the scale uncertainties a 7-point scale variation with factors

$$(\xi_{\text{F}}, \xi_{\text{R}}) \in \{(1/2, 1/2), (1/2, 1), (1, 1/2), (1, 1), (1, 2), (2, 1), (2, 2)\} \tag{5.9}$$

is performed. The minimal and maximal values, obtained from the scale variation, constitute the uncertainty bands.

The applied phase-space cuts are adapted from the ones in the CMS analysis [72]. A final state with at least one positron, one antimuon and two tagged jets is required. The charged leptons are recombined with photons using the anti-k_{t} algorithm [140] with a radius of $R = 0.1$. Jets are also clustered with the anti-k_{t} algorithm but with a radius $R = 0.4$. Final-state particles with a rapidity $|y| > 5$ are assumed to be lost to the beam pipe and are not recombined. After recombination the charged leptons must satisfy

$$p_{\text{T},\ell_1} > 25\,\text{GeV}\,, \qquad p_{\text{T},\ell_2} > 20\,\text{GeV}\,, \qquad |y_{\ell_{1,2}}| < 2.5\,, \qquad M_{\text{e}^+\mu^+} > 20\,\text{GeV}\,, \tag{5.10}$$

where $\ell_{1(2)}$ is the (sub)leading charged lepton. To be tagged a jet must fulfil

$$p_{\text{T,j}} > 50\,\text{GeV}\,, \qquad |y_{\text{j}}| < 4.7\,, \qquad \Delta R_{\text{e}^+\text{j}} > 0.4\,, \qquad \Delta R_{\mu^+\text{j}} > 0.4\,. \tag{5.11}$$

After jet tagging, the leading and subleading tagged jets must satisfy

$$M_{\text{j}_1\text{j}_2} > 500\,\text{GeV}\,, \qquad |\Delta y_{\text{j}_1\text{j}_2}| > 2.5\,. \tag{5.12}$$

The missing transverse momentum must be at least

$$p_{\text{T,miss}} > 30\,\text{GeV}\,. \tag{5.13}$$

Furthermore, the selected events have to satisfy the rapidity requirement,

$$\max_{\ell} \left| y_\ell - \frac{y_{\text{j}_1} + y_{\text{j}_2}}{2} \right| < 0.75\,|\Delta y_{\text{j}_1\text{j}_2}|\,, \quad \ell = \text{e}^+, \mu^+\,. \tag{5.14}$$

5.2.2 Exception handling

When studying VBS processes at the LHC there is always an unavoidable triple-vector-boson production background. For W^+W^+ scattering the background is $\text{W}^+\text{W}^+\text{W}^-$ production, where the W^- boson decays into jets. These diagrams are present both in the off-shell process and in the DPA process. In the full off-shell calculation they introduce a background to the VBS signal. The background is suppressed by the event selection, in particular the cut on the invariant mass of the two jets, but causes no conceptional problems. This is different in the DPA calculation. In the DPA, to conserve gauge invariance, the decay width of the W and Z bosons must be set to zero everywhere, but in the propagators set as the resonant

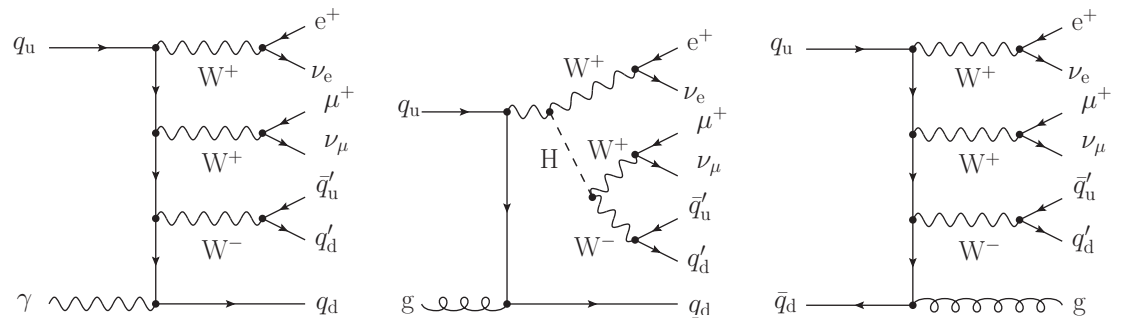

Figure 5.2: Sample real-radiation diagrams of order $\mathcal{O}(\alpha^7)$ (left) and $\mathcal{O}(\alpha_s\alpha^6)$ (middle, right), embedding triple-W-boson production and contributing to the same final state as W^+W^+ scattering at the LHC.

ones. When diagrams contribute with an additional s-channel W boson that is not set as resonant this introduces a singularity when the third W becomes on-shell. In the setup used in this calculation the invariant-mass requirement of the two jets $M_{j_1j_2} > 500\,\text{GeV} > M_W$ prevents the third W from becoming on-shell at LO. When real radiation is considered, final states with three tagged jets are possible. These are photon/gluon-induced or gluon-radiating processes. Sample diagrams of these partonic processes are depicted in Figure 5.2. With three jets in the final state the invariant mass cut can no longer prevent the third W from becoming on-shell.

To deal with the artificial singularity from the third resonance, the decay width of the W and the Z boson is not set to zero in the partonic processes that can have triple-resonant contributions. As stated in Chapter 2 this results in a gauge dependence of the DPA amplitude and the cross-sections calculated from it. To make sure that the effects from the gauge dependence are small, several checks have been performed. Foremost there is the comparison with the full off-shell computation. Comparing the results from the full off-shell computation with those from the unpolarised DPA one finds no discrepancy beyond the intrinsic accuracy of the DPA (see Table 5.4 lines full and unp.). Therefore, the gauge dependence leads at most to contributions of the order of the accuracy of the DPA. A further check that was performed is to estimate the size of the effect by comparing the integrated dipoles. The integrated dipoles feature only Born kinematics; therefore, the integration can be performed with the width set to zero and with keeping the pole value. Comparing the two obtained values it was found that the relative difference is at most 0.3%. This amounts to a total difference for the integrated NLO cross-section of $2.5 \cdot 10^{-4}$ fb which corresponds to a relative difference of 0.021%. For same-sign W scattering the contributions from triple-vector-boson production are smaller than those from VBS diagrams. Therefore, the triple-resonant contributions are suppressed as a whole and thus also the inconsistency from the gauge dependence is suppressed in the final result. This argument and the performed checks are only valid for the specific process and setup treated here.

For general processes with additional resonances the effect of keeping the width non zero does not have to be small. To treat the contributions from additional resonances consistently an improved version of the DPA is needed. A possible idea for such a method would be to remove the triple-resonant diagrams in the DPA calculation and add the contribution back by treating them in a triple-pole approximation (TPA). Such a method would remove the singularities from the triple-resonance contributions. To tune this in a way to have a total

state	$\sigma_{\mathrm{LO}\alpha^6}$ [fb]	$\sigma_{\mathrm{LO}\alpha_\mathrm{s}\alpha^5}$ [fb]	$\delta_{\alpha_\mathrm{s}\alpha^5}$	$\sigma_{\mathrm{LO}\alpha_\mathrm{s}^2\alpha^4}$ [fb]	$\delta_{\alpha_\mathrm{s}^2\alpha^4}$	$\delta_{\alpha_\mathrm{s}\alpha^5+\alpha_\mathrm{s}^2\alpha^4}$	σ_{LO} [fb]
full	1.4863(1)	0.044877(9)	0.03	0.14686(2)	0.10	0.13	1.6780(1)
unp.	1.46455(9)	0.044386(8)	0.03	0.14664(2)	0.10	0.13	1.65558(9)
LL	0.14879(1)	0.006120(1)	0.04	0.012298(2)	0.08	0.12	0.16721(1)
LT	0.23209(2)	0.007284(2)	0.03	0.029465(6)	0.13	0.16	0.26884(2)
TL	0.23208(2)	0.007284(2)	0.03	0.029471(6)	0.13	0.16	0.26884(2)
TT	0.87702(7)	0.026402(6)	0.03	0.07938(2)	0.09	0.12	0.98281(7)
int.	−0.0254(1)	−0.00270(1)	0.11	−0.00398(3)	0.16	0.26	−0.0321(1)

Table 5.1: LO contributions to the integrated cross-section (in fb) for the process $\mathrm{pp} \to \mathrm{e}^+\nu_\mathrm{e}\mu^+\nu_\mu+\mathrm{jj}$ at the LHC. The numbers in columns 4, 6, and 7 give the ratio of the respective background to the LO signal $\mathcal{O}(\alpha^6)$.

result that is gauge independent and has the correct correspondence between the local and integrated counterterms is significantly more complicated and is subject to future research.

Also present in partonic processes that have a triple-resonant contribution are Higgs-strahlung diagrams, where a Higgs boson decays into one W^+ boson and two jets as shown in the middle diagram in Figure 5.2. As stated in Section 2.4 the on-shell projection can shift the invariant corresponding to the Higgs boson closer to or further away from the peak. Large Monte Carlo weights from such events can lead to an unstable integration. While large event weights occur in the chosen setup, they only lead to an integration uncertainty of at most 9% for the individual subtracted-real contributions. Furthermore, as stated before, the contributions from triple-resonant partonic processes are suppressed in the chosen setup; therefore, the individual uncertainties do not affect the final result. Therefore, these partonic processes are not treated differently from other triple-resonant contributions.

5.2.3 Integrated results

Table 5.1 shows the LO cross-sections of the signal $\mathcal{O}(\alpha^6)$, the interference background $\mathcal{O}(\alpha_\mathrm{s}\alpha^5)$, and the QCD background $\mathcal{O}(\alpha_\mathrm{s}^2\alpha^4)$. When performing a polarisation study the contributions to the background would have to be subtracted beforehand. The study of the irreducible background is still very important to analyse the chosen setup, in particular, to what degree it favours the signal contribution. The contribution from the signal is the largest. The interference background only gives a relative contribution of $\approx 3\%$ and the QCD background one of $8-13\%$. The relatively small background contribution is not only caused by the event selection but also by the fact that certain enhancements of the background are absent. In same-sign W scattering there are no gluon-induced processes that contribute to the LO background. The large PDF factors of the gluon have been shown to significantly enhance the backgrounds in opposite-sign W scattering [189]. The phase-space cuts were chosen in a way to prefer contributions from VBS diagrams. The kinematic preferences of the signal and the background are different owing to the different diagram topologies that give the dominant LO contribution. The dominant diagram topology of the signal is where the two quark lines each emit a W^+, which then scatter off each other as shown in the top-left diagram in Figure 5.1. For the QCD background the quark lines exchange a t-channel gluon

state	$f_{\mathrm{LO}\,\alpha^6}$[%]	$f_{\mathrm{LO}\,\alpha_s\alpha^5}$[%]	$f_{\mathrm{LO}\,\alpha_s^2\alpha^4}$[%]	f_{LO}[%]
full	101.5	101.1	100.1	101.4
unp.	100.0	100.0	100.0	100.0
LL	10.2	13.8	8.4	10.1
LT	15.8	16.4	20.1	16.2
TL	15.8	16.4	20.1	16.2
TT	59.9	59.5	54.1	59.4
int.	−1.7	−6.1	−2.7	−1.9

Table 5.2: LO polarisation fractions for the process $pp \to e^+\nu_e\mu^+\nu_\mu + jj$ at the LHC.

and each emit a W^+ boson as seen in the top-right diagram in Figure 5.1. When analysing differential distributions in Section 5.2.4 the effects of the different topologies become more evident.

Table 5.2 shows the polarisation fractions normalised to the unpolarised DPA cross-sections of the LO signal and backgrounds. From the polarisation fractions of the full off-shell cross-section the size of the non-resonant background can be inferred. For the signal, interference background and QCD background it is $\lesssim 1.5\%$, which is within the accuracy of the DPA. As seen in many di-boson processes [39, 53, 60, 61] the TT polarisation state gives by far the largest contribution at $\approx 60\%$ for the signal. The mixed polarisation states LT and TL have identical polarisation fractions. This is a consequence of the symmetric cuts on the two charged leptons. The LL polarisation state has the smallest contribution. The contribution from the interference of longitudinal and transverse polarisations is small and negative. When the whole decay phase space of the W bosons is considered, the contributions from the interferences cancel. The applied phase-space cuts prevent the complete cancellation of the interferences, the setup is still inclusive enough to give a strong suppression. Even though the interference and the QCD background are not part of the VBS signal they are also doubly resonant. Therefore, also for them a polarisation split is performed. The obtained polarisation fractions are similar to the ones of the VBS signal with the interference background having a larger LL contribution and the QCD background having a large contribution from the mixed states. The sensitivity of the irreducible background to the unitarity cancellations is smaller than of the VBS signal. Therefore, only the polarisation states of the signal processes are analysed in more detail.

In Table 5.3 the NLO accurate integrated cross-sections are shown. The relative NLO EW corrections are all fairly large and negative. Their size differs depending on the considered polarisation state. The EW corrections to the TT polarisation state are the most negative at $\approx -15\%$. The ones to the LL polarisation state are the least negative at $\approx -10\%$. For the mixed polarisation states the size is in between the ones from the LL and TT states at $\approx -13\%$. The large negative NLO EW corrections are caused by large Sudakov logarithms [184, 191] present here. The prefactors of the leading double logarithms are the EW Casimir operators [208]. The size of these Casimir operators depends on the W-boson polarisation. When the boson is transversely polarised it is larger than when the W boson is longitudinally polarised. This results in the less negative NLO EW corrections to the LL, LT and TL state.

state	σ_{LO} [fb]	$\Delta\sigma_{\text{NLO EW}}$ [fb]	$\Delta\sigma_{\text{NLO QCD}}$ [fb]	$\sigma_{\text{NLO EW+QCD}}$ [fb]
full	$1.4863(1)^{+9.2\%}_{-7.8\%}$	$-0.2084(6)$	$-0.0704(7)$	$1.208(1)^{+1.6\%}_{-3.1\%}$
unp.	$1.46455(9)^{+9.2\%}_{-7.8\%}$	$-0.2076(2)$	$-0.0733(5)$	$1.1836(5)^{+1.7\%}_{-3.3\%}$
LL	$0.14879(1)^{+8.3\%}_{-7.2\%}$	$-0.01505(2)$	$-0.00660(7)$	$0.12715(8)^{+1.0\%}_{-2.1\%}$
LT	$0.23209(2)^{+9.1\%}_{-7.8\%}$	$-0.03040(4)$	$-0.0098(1)$	$0.1919(1)^{+1.4\%}_{-2.8\%}$
TL	$0.23208(2)^{+9.1\%}_{-7.8\%}$	$-0.03051(4)$	$-0.0097(1)$	$0.1918(1)^{+1.4\%}_{-2.8\%}$
TT	$0.87702(7)^{+9.4\%}_{-8.0\%}$	$-0.1352(1)$	$-0.0474(4)$	$0.6944(4)^{+1.9\%}_{-3.7\%}$
int.	$-0.0254(1)^{-8.9\%}_{+10.6\%}$	0.0035(2)	0.0002(6)	$-0.0217(7)^{-1.6\%}_{+0.7\%}$

state	δ_{EW}	δ_{QCD}	$\delta_{\text{EW+QCD}}$
full	-0.140	-0.047	-0.188
unp.	-0.142	-0.050	-0.192
LL	-0.101	-0.044	-0.145
LT	-0.131	-0.042	-0.173
TL	-0.131	-0.042	-0.173
TT	-0.154	-0.054	-0.208
int.	-0.139	-0.007	-0.147

Table 5.3: NLO contributions to the integrated cross-section (in fb) for the process $pp \to e^+\nu_e\mu^+\nu_\mu + jj$ at the LHC. The numbers in the lower part of the table give the ratio of the given $\mathcal{O}(\alpha^7)$ and $\mathcal{O}(\alpha_s\alpha^6)$ NLO corrections to the corresponding LO signal at $\mathcal{O}(\alpha^6)$.

For the NLO QCD corrections the picture is different. They are negative similar to the EW corrections but their size is smaller than their EW counterparts. In VBS processes the NLO QCD corrections only affect the quark lines; therefore, their dominant behaviour is comparable to the NLO QCD corrections to deep-inelastic electron-proton scattering. For deep-inelastic scattering the NLO QCD corrections have been found to be small [209]. The relative size of the corrections is very similar for the different polarisation states at -4% to -5%. With both W bosons decaying leptonically the NLO QCD corrections only affect the production part of the process. The LO VBS signal is a purely EW process; therefore, only the variation of the factorisation scale enters the LO scale uncertainties. To have a sound estimate of the size of the higher-order QCD corrections the NLO QCD corrections need to be included. This results in scale uncertainties of $1-3\%$ for the NLO EW+QCD prediction. The size of the scale uncertainties only varies slightly with the polarisation state.

Table 5.4 shows the polarisation fractions including the NLO corrections. The relative size of the non-resonant background is slightly larger at NLO compared to LO. The value is still within the expected accuracy of the DPA. Overall the polarisation fractions are only subject to small changes of the order of 1% from LO to NLO. The fractions of the LL, LT, TL polarisation states and the interferences are slightly increased, while the fraction of the TT polarisation state is slightly decreased. This is a consequence of the less negative NLO EW corrections to the states with at least one longitudinally polarised boson compared to the purely transverse state previously discussed in Table 5.3. As at LO, the interference contribution is also small at NLO because of the cancellations, when integrating over the whole decay phase space.

state	f_{LO}[%]	$f_{\text{NLO EW}}$[%]	$f_{\text{NLO QCD}}$[%]	$f_{\text{NLO EW+QCD}}$[%]
full	101.5	101.7	101.8	102.0
unp.	100.0	100.0	100.0	100.0
LL	10.2	10.6	10.2	10.7
LT	15.8	16.0	16.0	16.2
TL	15.8	16.0	16.0	16.2
TT	59.9	59.0	59.6	58.7
int.	−1.7	−1.7	−1.8	−1.8

Table 5.4: NLO polarisation fractions for the process $pp \to e^+\nu_e\mu^+\nu_\mu + jj$ at the LHC.

5.2.4 Differential results

While the integrated cross-sections give a good overview on how large the polarised contributions are, to fully understand the underlying differences between the polarisation states, differential cross-sections have to be studied. Furthermore, their study is necessary in order to judge, which observables are suited to discriminate between the polarisation states. Observables that feature large differences in the normalised shapes of the distributions can be used as polarisation templates.

The histogram plots (Figures 5.3–5.13) are set up as follows. For each observable there are four subplots, each containing three panels. Starting with the top left subplot, the first panel depicts the differential cross-section of the LO accurate signal $\mathcal{O}(\alpha^6)$ with respect to the given observable. The cross-section is given for the full off-shell process (black), the unpolarised DPA process (grey) and the polarised DPA processes (LL red, LT yellow, TL green, TT blue). The panel below shows the relative size of the interference background $\mathcal{O}(\alpha_s\alpha^5)$ compared to the LO signal. The bottom panel of the top left subplot presents the relative size of the LO QCD background $\mathcal{O}(\alpha_s^2\alpha^4)$ compared to the LO signal. The top right subplot is dedicated to the NLO results. The top panel illustrates the differential NLO accurate cross-section containing the LO signal $\mathcal{O}(\alpha^6)$, the NLO EW corrections $\mathcal{O}(\alpha^7)$ and the NLO QCD corrections $\mathcal{O}(\alpha_s\alpha^6)$. The panel below depicts the NLO accurate cross-section normalised to the integrated cross-section. The last panel shows the NLO accurate polarisation fractions. They are depicted for the full off-shell process, the polarised DPA processes and the contribution from interferences of the longitudinal and transverse polarisation states (magenta). The relative sizes of the NLO corrections with respect to the LO signal are shown in the bottom left subplot. The first panel shows the relative NLO EW corrections, the second one the NLO QCD ones and the third NLO EW and QCD combined. The bottom right subplot depicts the relative size of the combined NLO EW and QCD corrections including the uncertainty bands obtained from the QCD scale variation, defined in Eq. (5.9).

Figure 5.3 shows the differential cross-section with respect to the cosine of the decay angle of the positron in the CM frame of the decaying boson. This is a very standard observable for the study of polarisation that has already been used for vector-boson pair production [39, 53, 55, 151]. As the leptonic decays of the W bosons have two final-state neutrinos the decay angle is not experimentally observable. However, there are features of experimentally measurable observables that can be explained by characteristics of the decay angle making

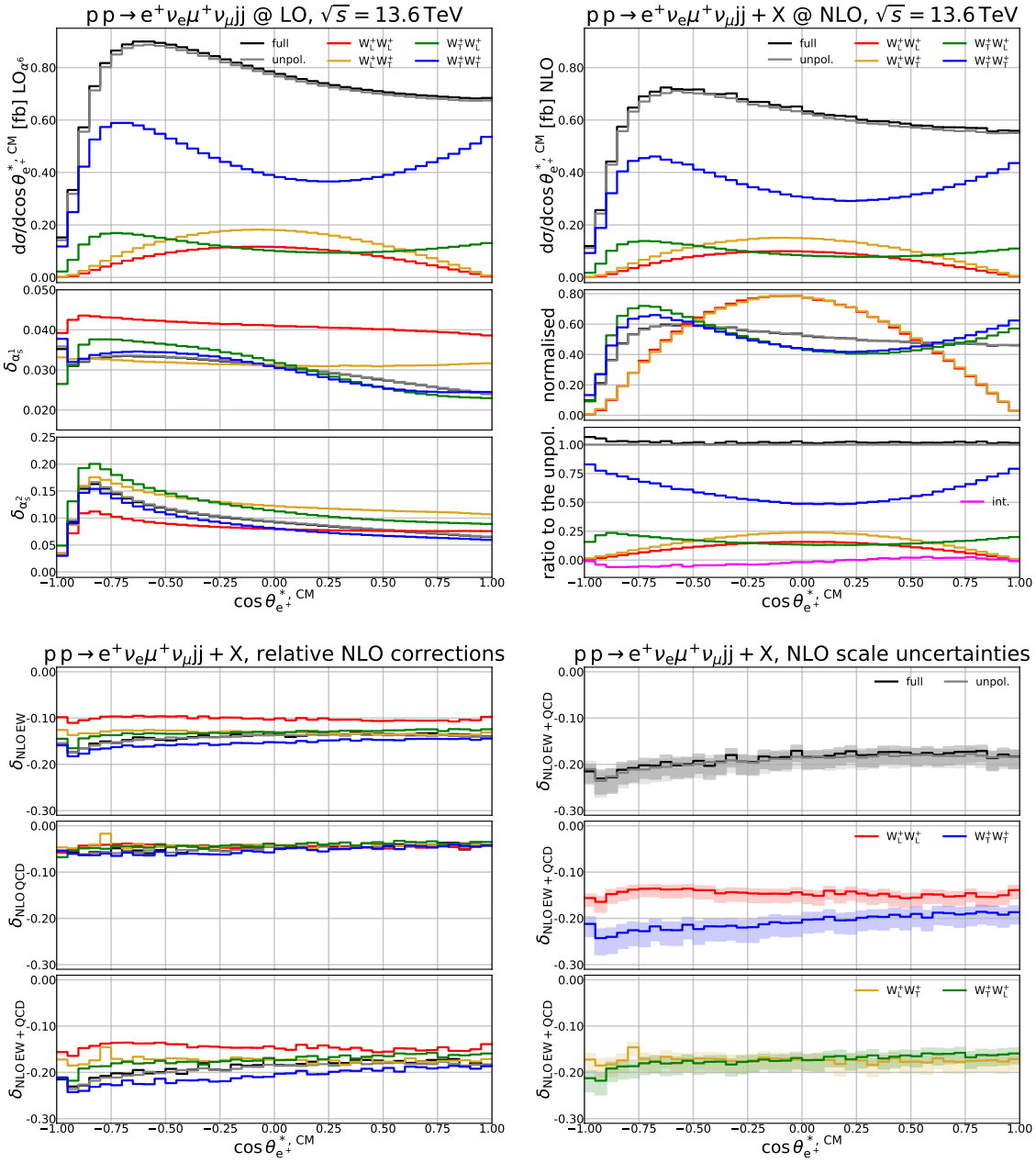

Figure 5.3: Distribution in the polar decay angle of the positron in the rest frame of the decaying W^+ boson. Details are described in the main text (first paragraphs of Section 5.2.4).

its study still worthwhile. The decay angle is directly sensitive to the polarisation of the decaying W^+ boson. Therefore, when investigating the normalised shapes one finds large differences depending on the polarisation of the W^+ boson decaying into the positron. When the W boson is longitudinally polarised the distribution is peaked in the central region. This is caused by the decay particles of longitudinally polarised vector bosons being predominantly emitted orthogonal to the direction of the decaying boson. For a transversely polarised W boson there is a local minimum in the central region. For the decay of a transversely polarised vector boson the decay particles are preferably emitted in and opposite to the direction of the decaying boson. The region close to the edge $-1 < \cos\theta^{*,\mathrm{CM}}_{e^+} < -0.75$ is affected most

by the phase-space cuts. In particular, the cut on the transverse momentum of the positron distorts the shape compared to the one expected in a fully inclusive setup. Since there is no analogous cut on the electron neutrino there is no such distortion at $\cos\theta^{*,\mathrm{CM}}_{e^+} = 1$ resulting in the asymmetric shape seen in the plot. While the shapes of the LL and LT states are almost identical, the ones of the TT and TL state feature some small differences. The peak at $\cos\theta^{*,\mathrm{CM}}_{e^+} = -0.75$ is more prominent in the TL state. The increase close to $\cos\theta^{*,\mathrm{CM}}_{e^+} = 1$ is steeper for the TT state. The relative NLO corrections, both EW and QCD, are very close to flat and mostly mirroring the effects seen at the integrated level. Only in the region $-1 < \cos\theta^{*,\mathrm{CM}}_{e^+} < -0.75$ that is affected most by the cuts some deviation from the flat behaviour is seen in the EW corrections to the TT and TL state.

In Figure 5.4 the differential cross-section with respect to the azimuthal angular separation of the positron and the antimuon is presented. As seen at LO [86] the normalised shapes show significant differences between the different polarisation states. Therefore, this observable is a well suited candidate for the use in polarisation templates to discriminate the different polarisation states. The TT state has a clear preference for the positron and the muon to be produced in opposite directions. This is an effect of the decay leptons from transversely polarised bosons tending to be aligned with their parent W boson. The shapes of the mixed polarisation states are identical and feature only a very small preference for the positron and antimuon to be emitted in opposite hemispheres. The shape of the LL state is close to flat with a small but wide peak at $\Delta\phi_{e^+\mu^+} = 0.75$. The different shapes cause large changes in the polarisation fractions. The relative contribution of the TT state increases to 68% for large separations. As in most angular observables the relative NLO corrections are close to flat reproducing the values seen at the integrated level.

The differential cross-section with respect to the azimuthal angular separation of the leading and the subleading transverse-momentum jet is depicted in Figure 5.5. The normalised shapes show a notably different shape of the LL polarisation state compared to the others. While all polarisation states have a preference for the two jets to be produced at large separations, this preference is much more pronounced when both W bosons are longitudinally polarised. In the polarisation fractions this translates to the fraction of the TT polarisation state decreasing from $\approx 70\%$ to only $\approx 50\%$ over the range of angular separations. The contribution from the LL polarisation state increases from 4% to 15%. The NLO EW corrections to the LL polarisation state give only small negative corrections for small separations. From $\Delta\phi_{j_1 j_2} = 0.8$ the corrections become more negative with increasing separation. The effect of the NLO EW corrections to the other polarisation states is different giving a close to flat correction that becomes slightly less negative for larger separations. The NLO QCD corrections feature no significant differences between the polarisation states and become slightly more negative with increasing separation. Studying the relative sizes of the interference and QCD background it becomes evident that they feature a different shape than the signal. The relative size of the QCD background varies between 5% and 17% depending on the polarisation state, while the interference background has a relative size between -7% and $+6\%$.

The differential cross-section with respect to the rapidity separation of the positron and antimuon is shown in Figure 5.6. The shape of the TT polarisation state, featuring a peak at $|\Delta y_{e^+\mu^+}| = 0$, differs from the other polarised signals. The differential cross-sections with at least one longitudinally polarised W boson have a peak at $|\Delta y_{e^+\mu^+}| = 1.1$. The reason is the different rapidity distributions of the positron and the antimuon from the decay of a

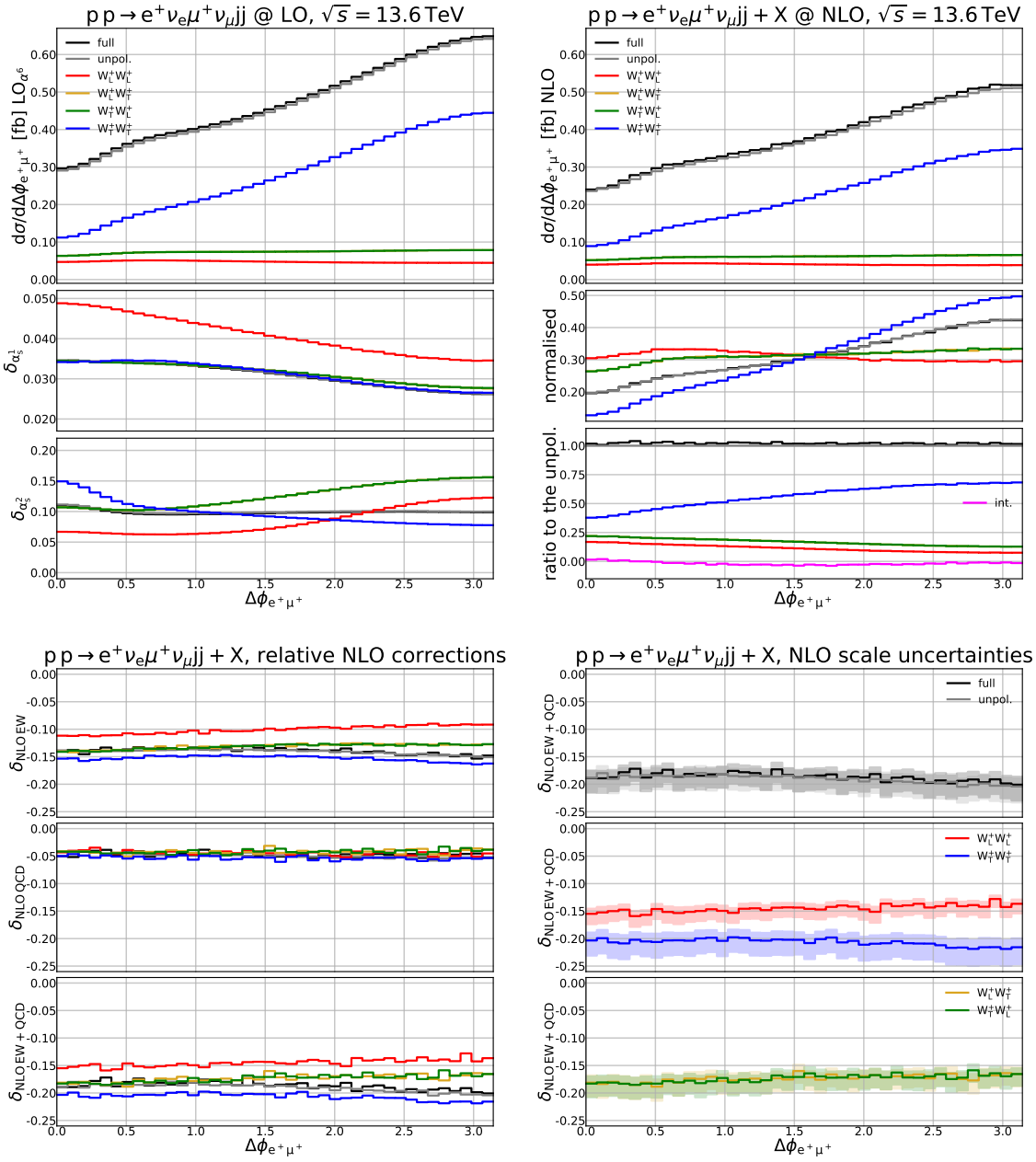

Figure 5.4: Distribution in the azimuthal-angle difference between the two charged leptons. Details are described in the main text (first paragraphs of Section 5.2.4).

longitudinal or transverse W boson. As depicted in Figure 5.8 the rapidity distribution of the positron from a transversely polarised boson has a sharper peak at $y_{e^+} = 0$ than when it is emitted from a longitudinally polarised boson. Therefore, the rapidity difference of the positron and the antimuon will in general be smallest when both W bosons are transversely polarised. This makes the rapidity separation a very good observable to select the TT polarisation state. The different shapes also cause significant changes in the polarisation fractions. The contribution of the TT state decreases from 75% at $|\Delta y_{e^+\mu^+}| = 0$ to 40% at $|\Delta y_{e^+\mu^+}| = 5$. The relative size of the NLO EW corrections are close to constant for all polarisation states. The differences between the polarisation states mirror those seen at

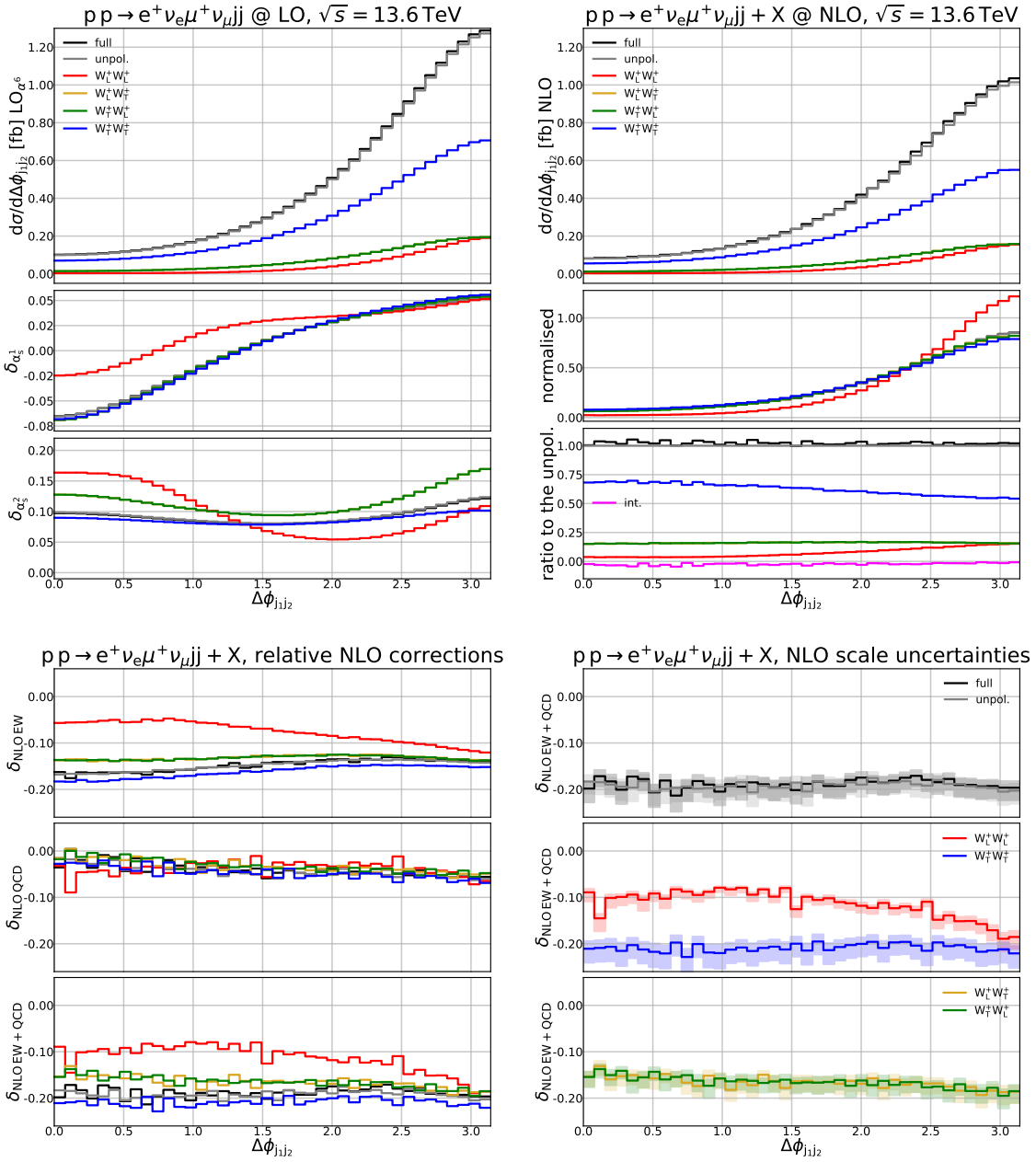

Figure 5.5: Distribution in the azimuthal-angle difference between the two tagged jets. Details are described in the main text (first paragraphs of Section 5.2.4).

the integrated level. The NLO QCD corrections decrease in size with increasing rapidity separation. For large rapidity separations the relative contribution of the QCD background becomes very large. This is caused by the different kinematic preferences of the signal and the QCD background. The cause of the difference can be understood when studying the rapidity distributions of the positron is Figure 5.8. The corresponding plot for the antimuon is not shown here but features an analogous behaviour. The positron and the muon from the QCD background are generally emitted in a more forward/backward direction compared to the signal. This translates to a larger rapidity separation for the QCD background resulting in the seen large relative contribution.

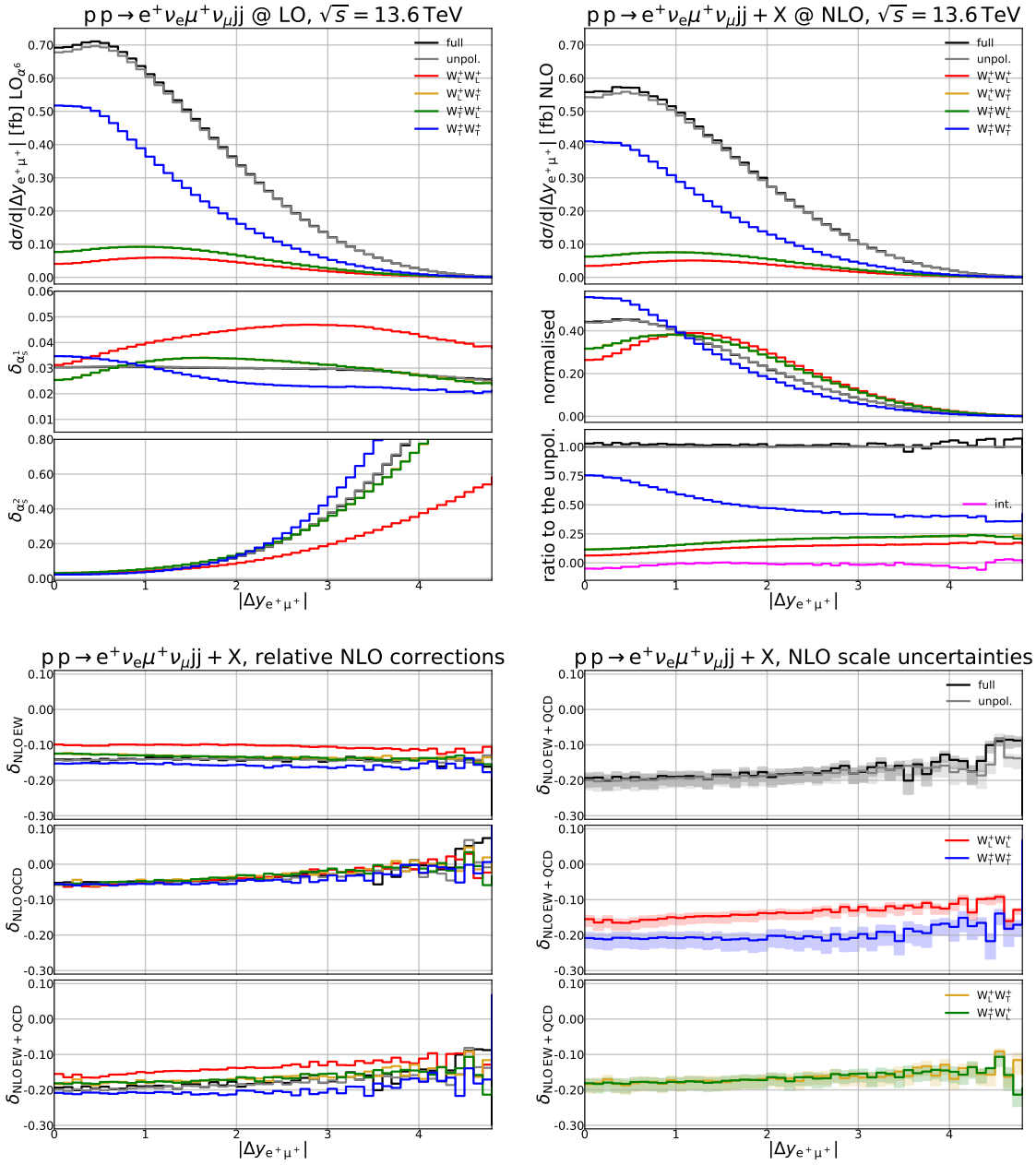

Figure 5.6: Distribution in the absolute value of the rapidity difference between the two charged leptons. Details are described in the main text (first paragraphs of Section 5.2.4).

In Figure 5.7 the differential cross-section with respect to the rapidity of the leading transverse-momentum jet is presented. The dominant feature of the plot is the two peak structure at $y_{j_1} \approx \pm 2.2$ that is present for all polarisation states. For the LL polarisation state the shape is slightly different having an overall shift to more forward/backward directions. These small differences in shape cause the polarisation fractions to be close to constant. The LO irreducible backgrounds, both QCD and interference, have a different shape as seen in the large relative contribution in the central region. While diagrams that have a VBS topology have a strong preference for the jets to be emitted in a very forward/backward direction the jets from topologies of the irreducible background are preferably emitted in

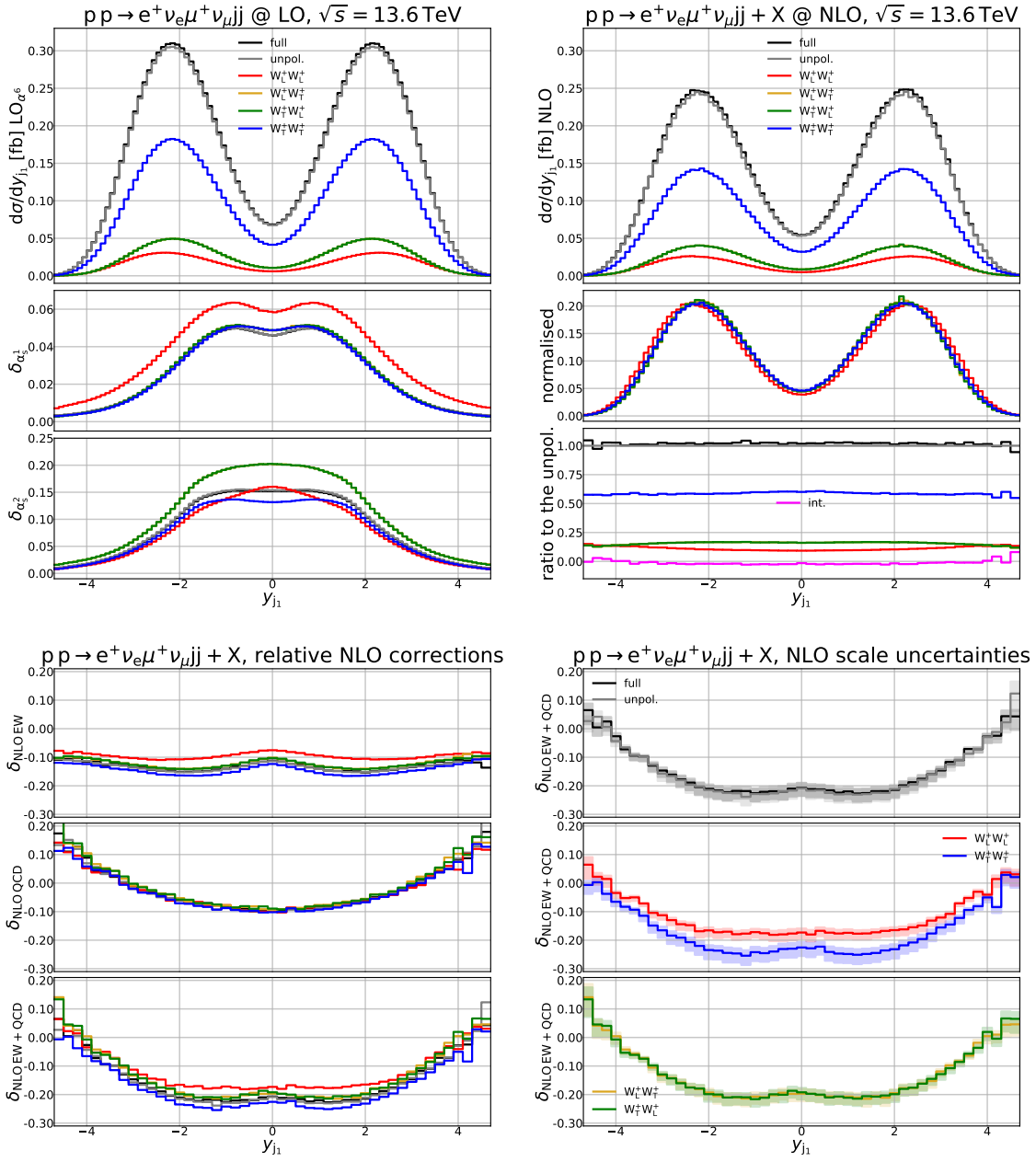

Figure 5.7: Distribution in the rapidity of the leading jet. Details are described in the main text (first paragraphs of Section 5.2.4).

the central region. The relative NLO QCD corrections are negative in the central region at -10% while in the forward/backward region they become positive reaching $+14\%$. This effect has been previously observed for calculations of off-shell W^+W^+ scattering [184]. The relative NLO EW corrections are close to constant featuring only differences of $\approx 4\%$.

Figure 5.8 depicts the differential cross-section with respect to the rapidity of the positron. All polarisation states have a similar overall shape with a peak at $y_{e^+} = 0$. This is caused by the preference of bosons from VBS processes to be emitted in the central region. The sharpness of the peak and the fall-off towards the edges depends on the polarisation of the W^+ boson that emitted the positron. When the W^+ boson is transversely polarised the

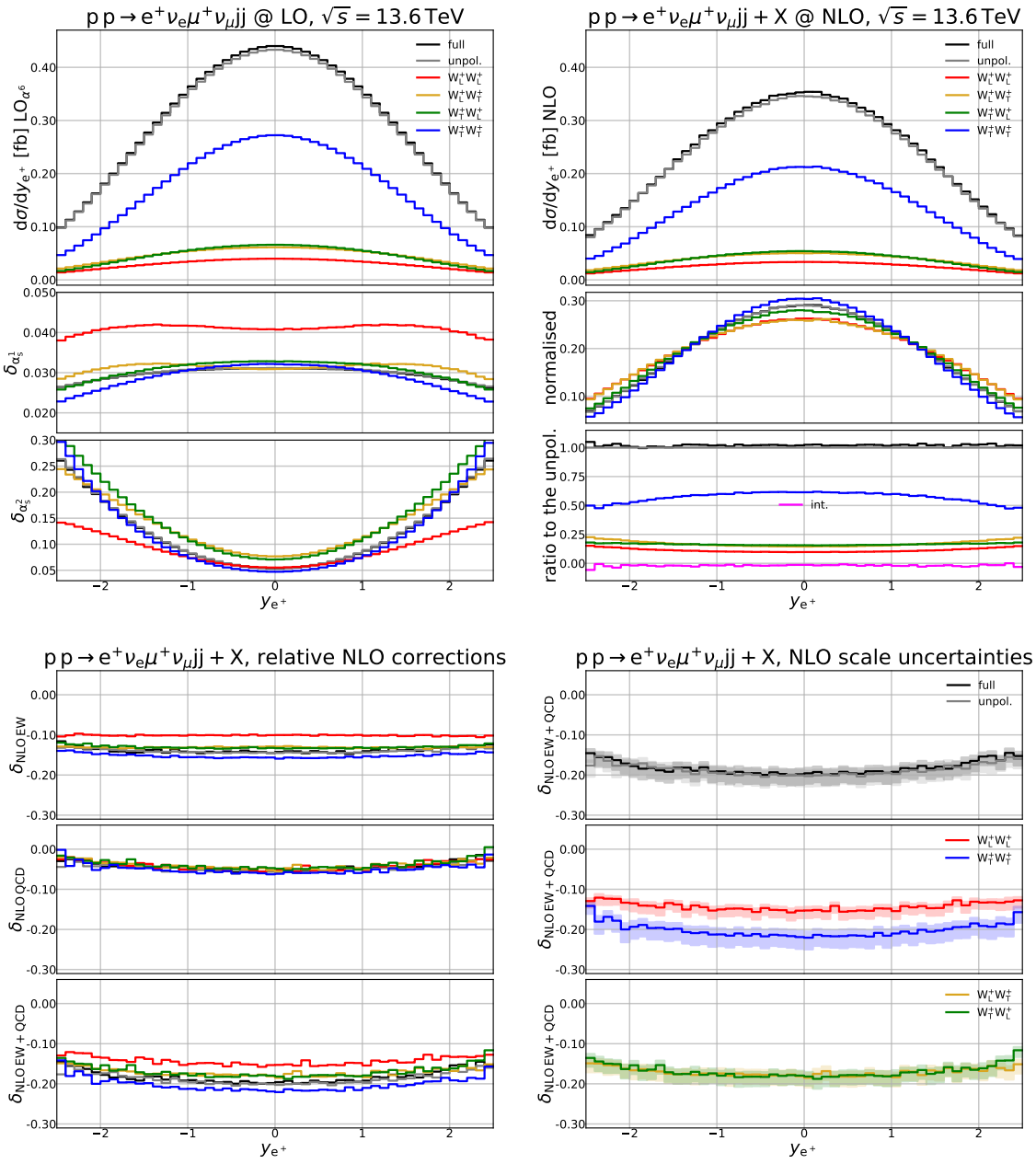

Figure 5.8: Distribution in the rapidity of the positron. Details are described in the main text (first paragraphs of Section 5.2.4).

peak is sharper and the cross-section falls off faster. For a longitudinally polarised W^+ boson the peak is wider and features a slower fall-off. These small differences are caused by the preference of a transversely polarised boson to emit its decay particles in or opposite to its direction in the di-boson CM frame. For longitudinally polarised bosons the decay particles are preferably emitted orthogonal to the direction of the boson. This causes the positron from a transversely polarised boson to be emitted in a more central direction. The QCD background has a very different kinematic preference owing to the t-channel gluon exchange seen in the top right diagram of Figure 5.1. The t-channel gluon exchange diagrams with the two W bosons emitted from different quark lines favour the production of the W bo-

sons in a forward/backward direction. This is different from diagrams with a VBS topology, where the W bosons are predominantly produced in the central region. Therefore, the shape of the QCD background (not shown in the plot) features two peaks at $y_{e^+} = \pm 1.6$. The effects of the different preferences are seen in the relative contributions that become large when the positron is emitted in a very forward or backward direction. Both the relative NLO QCD and EW corrections are close to constant mostly reproducing the value of the integrated cross-section. The NLO QCD corrections become marginally less negative when the positron is emitted in a very forward or backward direction with no differences between the polarisation states.

Figure 5.9 shows the differential cross-section with respect to the invariant mass of the two charged leptons and the two neutrinos. This is not an experimentally observable quantity as it requires the reconstruction of the neutrino momenta. However, it is very useful in understanding features in related observables that can be measured. In the high-invariant-mass region the fall-off depends on the polarisation state. When both bosons are longitudinally polarised the distribution falls off the fastest. The TT polarisation state features the slowest fall-off. The mixed polarisation states have an intermediate behaviour. This effect has been observed in LO polarisation studies of VBS processes [51,85]. The different fall-off rates translate to different normalised shapes of the polarisation states. In particular, the shape of the LL polarised signal has a much sharper peak in the low-invariant-mass region. The slower fall-off at high invariant masses causes the fraction of the TT polarisation state to increase to 80% at $M_{e^+\nu_e\mu^+\nu_\mu} = 1\,\text{TeV}$. While the VBS signal features a peak at $M_{e^+\nu_e\mu^+\nu_\mu} = 200\,\text{GeV}$ the peak of the QCD background is shifted to higher invariant masses. This results in a very large relative contribution in the high-invariant-mass range. The cause of this are the different kinematic preferences of the different diagram topologies already seen in the plots of the rapidity of the positron in Figure 5.8. For diagrams which have the VBS topology, like the one in the top left diagram of Figure 5.1 that give the dominant contribution to the signal, the jets carry the majority of the energy. Therefore, the four-lepton invariant mass is typically only of the order of a few hundred GeV [191]. The t-channel gluon exchange present in diagrams like the top right one in Figure 5.1 produces the bosons preferably in a more forward/backward direction resulting in a larger four-lepton invariant mass for the QCD background. The relative NLO EW corrections become more negative with increasing invariant mass. This is less severe for the LL polarisation state. The large negative corrections are caused by EW Sudakov logarithms. The EW Casimir operators that are the prefactors of the leading double logarithms depend on the polarisation. When the boson is longitudinally polarised they are smaller than when they are transversely polarised. Therefore, as already seen at the integrated level the correction to the longitudinally polarised bosons is smaller. The NLO QCD corrections only slightly decrease in size becoming less negative for high invariant masses with no significant differences between the polarisation states. The size of the QCD scale uncertainties grows with increasing invariant mass. For transversely polarised bosons the growth of the scale uncertainties is larger than for longitudinally polarised ones.

In Figure 5.10 the differential cross-section with respect to the invariant mass of the positron and the antimuon is shown. This observable is highly correlated to the four-lepton invariant mass in Figure 5.9 and has very similar features. As it does not require the reconstruction of the neutrino momenta it is measurable at the LHC. As for the four-lepton invariant mass the fall-off rates in the high-invariant-mass region depend on the polarisation state. Also the effects of the EW Sudakov logarithms on the size of the NLO EW corrections

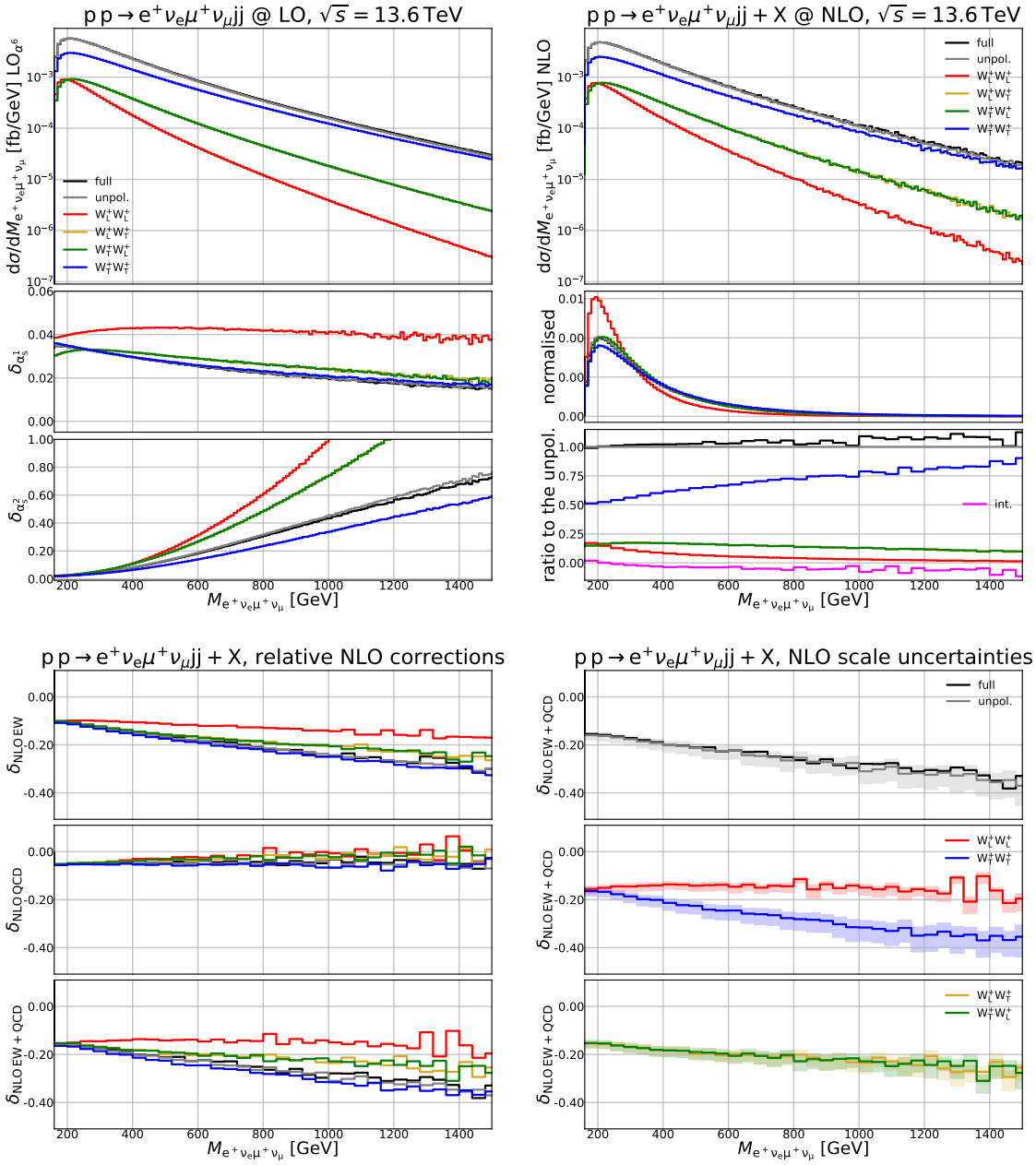

Figure 5.9: Distribution in the invariant mass of the system formed by the two charged leptons and the two neutrinos. Details are described in the main text (first paragraphs of Section 5.2.4).

are clearly visible here. Furthermore, the charged-lepton invariant mass is also sensitive to the different kinematic preferences of the signal and the QCD background.

Figure 5.11 shows the differential cross-section with respect to the transverse momentum of the leading jet. The normalised shapes of the polarised signals show a considerable difference of the LL polarisation state compared to the ones with at least one transversely polarised boson. There is only a very small shape difference between the TT polarisation state and the mixed polarisation states. The shape of the LL polarisation state has a shaper peak at low transverse momenta than the other polarisation states. This makes this

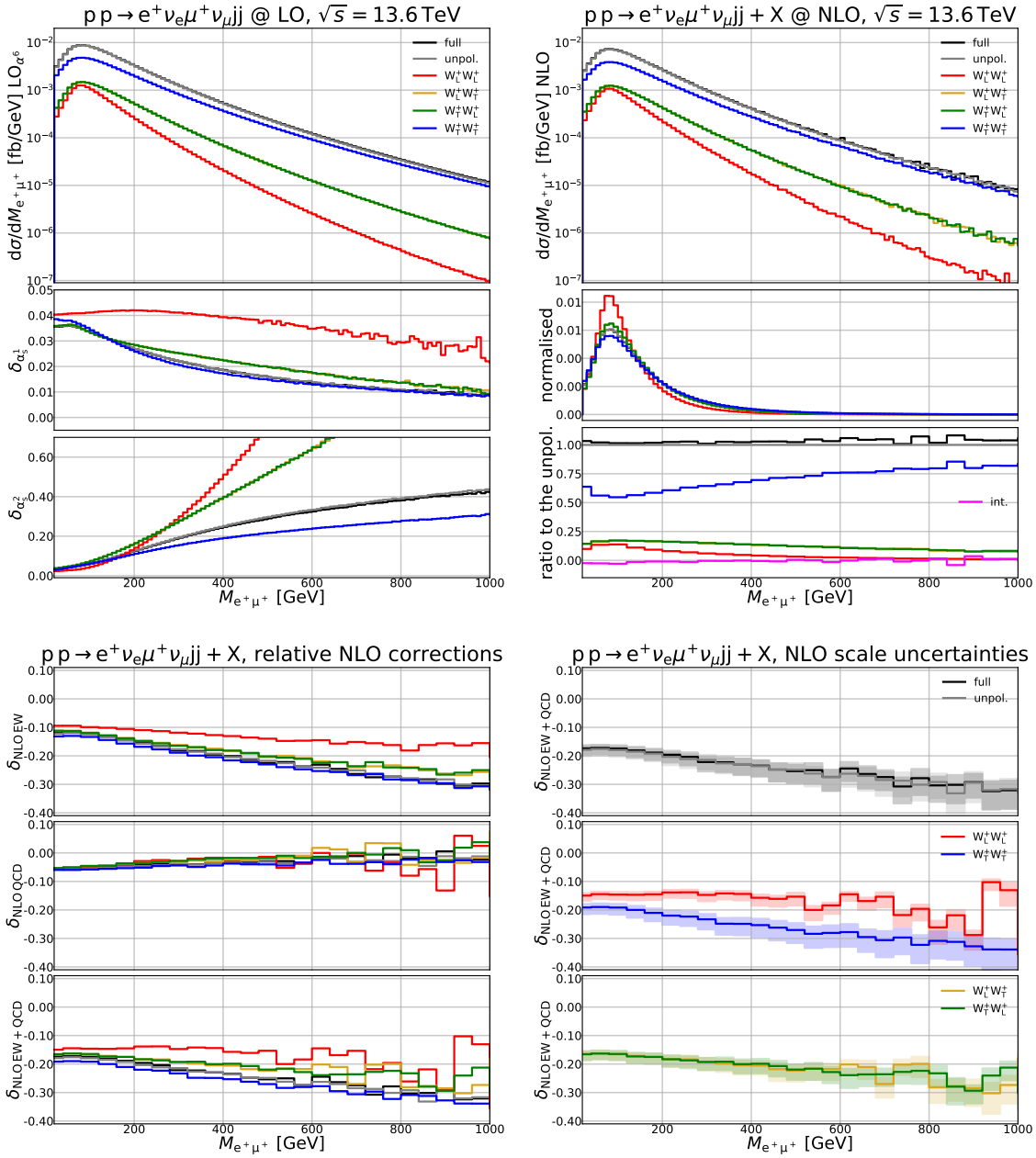

Figure 5.10: Distribution in the invariant mass of the charged-lepton pair. Details are described in the main text (first paragraphs of Section 5.2.4).

observable suited to select the LL polarisation state. As this is a jet observable it has a large dependence on the production subprocess. Therefore, beyond the Standard Model effects can result in potentially large changes of the shapes making it only directly usable in Standard Model studies. The NLO EW corrections become more negative with increasing transverse momentum. Similarly, as for the four-lepton and charged-lepton invariant mass this is caused by the EW Sudakov logarithms, that become more relevant at larger energies. The differences between the LL and the TT state are much smaller compared to the invariant-mass distributions. For transverse momenta $p_{\mathrm{T,j_1}} > 250\,\mathrm{GeV}$ the NLO QCD corrections are constant. When the transverse momentum of the leading jet is small the corrections become

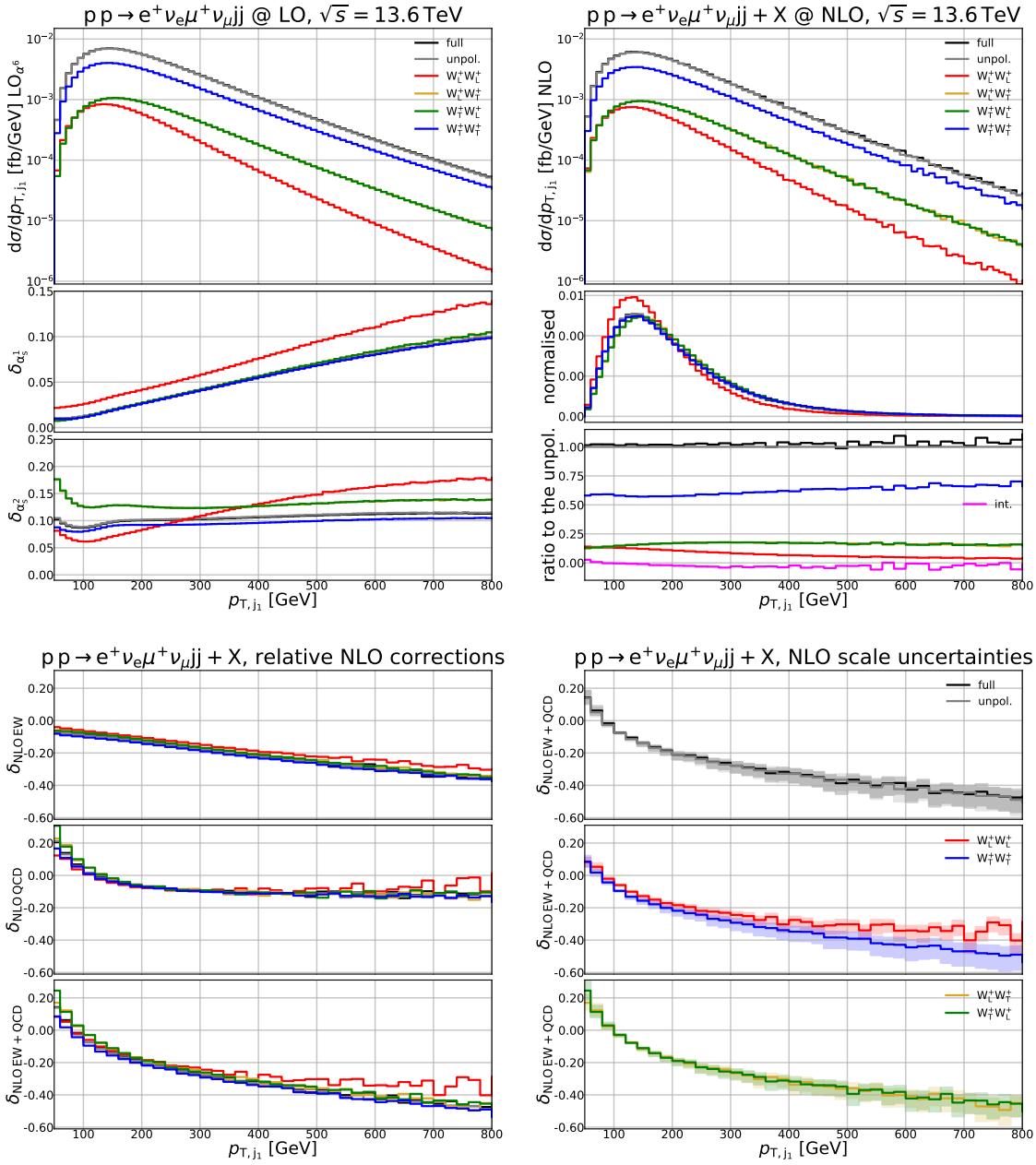

Figure 5.11: Distribution in the transverse momentum of the leading jet. Details are described in the main text (first paragraphs of Section 5.2.4).

large and positive. This behaviour has been observed in other VBS studies [184, 186, 189].

Figure 5.12 presents the differential cross-section with respect to the transverse momentum of the positron. There is a strong dependence on the polarisation of the W^+ boson emitting the positron in the low-transverse-momentum region. When the W^+ boson is longitudinally polarised the distribution features a sharp peak at $p_{T,e^+} = 40\,\text{GeV}$. For a transversely polarised boson the distribution steadily decreases with increasing transverse momentum. The fall-off at high transverse momenta is much faster for a longitudinally polarised boson compared to a transverse one. The reason for these different shapes are the different decay preferences of longitudinal and transverse bosons. A transversely po-

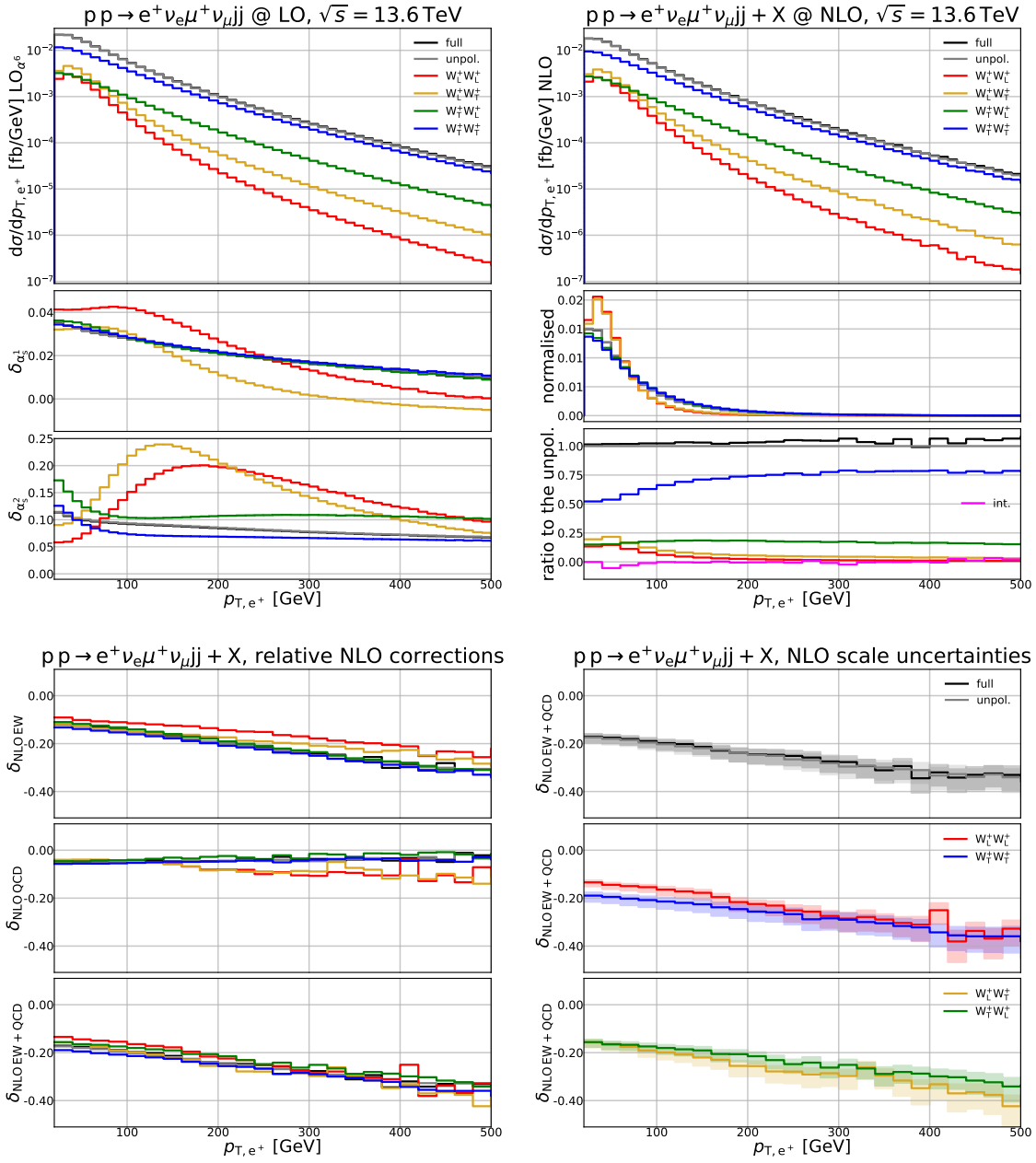

Figure 5.12: Distribution in the transverse momentum of the positron. Details are described in the main text (first paragraphs of Section 5.2.4).

larised boson emits its decay particles preferably in or opposite to its direction in its CM frame. This results in one decay product having more transverse momentum than the other one. Therefore, there are more events where the positron has either a very small transverse momentum or a very large transverse momentum. The decay products of longitudinally polarised bosons favour the emission in a direction orthogonal to the bosons direction in its CM frame. This produces decay particles with the transverse momentum split much more evenly between the two compared to the transverse case resulting in the observed peak. Furthermore, the shape differences result in a change of the polarisation fractions as shown in the ratios to the unpolarised cross-section. The effects from the EW Sudakow logarithms seen

in other observables like the four-lepton invariant mass are also visible in the relative NLO EW corrections that become more negative at high transverse momenta. The polarisation-dependent prefactors of the double logarithms cause the corrections to the states with a longitudinally polarised W^+ boson emitting the positron to be less negative. For transverse momenta $p_{T,e^+} < 150\,\text{GeV}$ the NLO QCD corrections are close to constant and the same for all polarisation states. For higher transverse momenta this changes. The corrections to the TT and TL state become less negative and the LL and LT state become more negative. In the complete NLO picture the differences between the different polarisation states partly cancel resulting very similar NLO EW+QCD corrections. The interference and the QCD background have different shapes compared to the LO signal as is evident by the non-flat corrections. The difference is particularly large when the W^+ boson emitting the positron is longitudinally polarised.

In Figure 5.13 the differential cross-section with respect to the transverse-momentum ratio of the second hardest charged lepton to the hardest charged lepton,

$$R_{21}^{(\ell)} = \frac{p_{T,\ell_2}}{p_{T,\ell_1}}\,, \tag{5.15}$$

is presented. The normalised shapes show a clear difference between the LL polarisation state and the other states. The differences between the mixed polarisation states and the TT polarisation state are only minor. Therefore, this is a great observable to distinguish the purely longitudinal polarisation state. When both bosons are longitudinally polarised there is a preference for the charged leptons to have similar transverse momenta. When at least one transversely polarised boson is present, larger differences are favoured. The reason for the different preferences is the different transverse-momentum distributions of the charged leptons. As shown in Figure 5.12, for the positron, the transverse-momentum distribution for the decay of a longitudinally polarised boson has a sharp peak. The analogous distribution of the antimuon is not shown but has an equivalent feature. Therefore, the probability that the transverse momentum of the positron and the antimuon are similar is greater, when both bosons are longitudinally polarised. The transverse-momentum distribution of a lepton emitted from a transversely polarised W^+ boson is much wider making large transverse-momentum differences more probable. For very small transverse-momentum ratios $\left(R_{21}^{(\ell)} < 0.1\right)$ the NLO EW corrections become very negative. In the event selection it is required that the subleading charged lepton has a transverse momentum of at least 20 GeV. Therefore, in this region of phase space the transverse momentum of the leading charged lepton must be very large. This means one is probing the high-transverse-momentum region, where the Sudakov logarithms cause large negative corrections. The NLO QCD corrections are for the most part constant and the same for all polarisation states. Only in the region $R_{21}^{(\ell)} < 0.2$ the LL polarisation state receives a larger negative correction.

5.2.5 Conclusion for W^+W^+ scattering

There are two key aspects of polarised W^+W^+ scattering that appear in many observables. For the discrimination of the different polarisation states, because of the unobservable neutrinos, one cannot rely on the decay angles of the positron and antimoun. However, the characteristic kinematic preferences of the polarisation states seen in the decay angle, translate to shape differences seen in measurable observables. Such observables are the rapidity

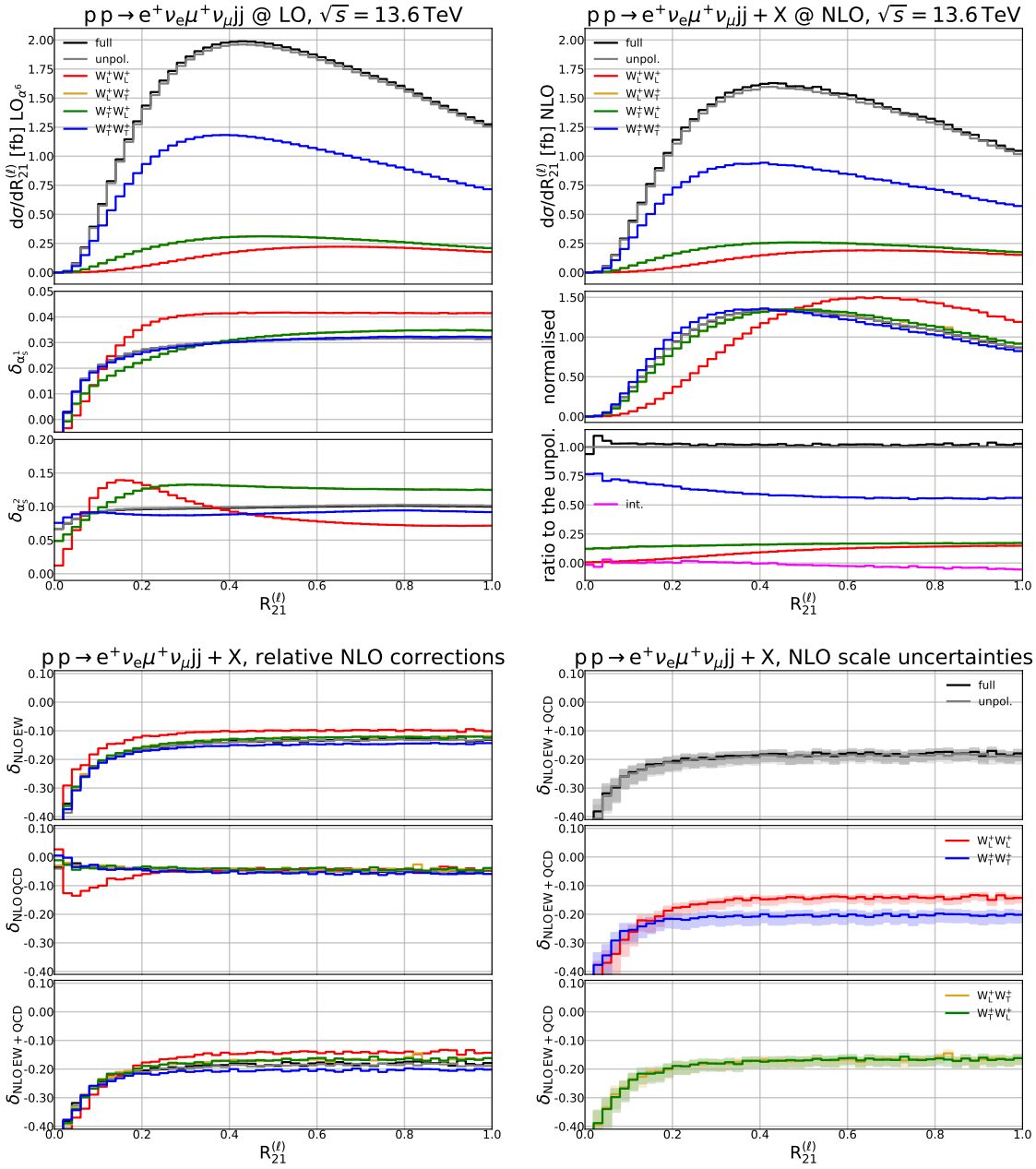

Figure 5.13: Distribution in the ratio of the transverse momenta of the subleading and leading lepton. Details are described in the main text (first paragraphs of Section 5.2.4).

separation of the positron and the antimuon and the transverse-momentum ratio of the subleading and leading charged lepton. They can be used to discriminate the different polarisation states.

Another key feature prominently seen in energy observables are the Sudakov logarithms and how they affect the size of the NLO EW corrections. Already at the integrated level it has been shown that they cause the NLO EW corrections to be large and negative. In the high-energy tails of the differential distributions their effects are even more pronounced. Furthermore, in energy-type observables the energy dependence of the logarithms is clearly visible in the change of the relative size of the NLO EW corrections. The Sudakov logarithms

affect the polarised signals differently. This results in less negative corrections to longitudinally polarised bosons and more negative corrections to transversely polarised bosons.

Chapter 6

Conclusion

The main goal of this thesis has been the implementation and use of the DPA at NLO accuracy to compute polarised VBS processes. To this end the Monte Carlo code BBMC has been extended to compute polarised and unpolarised processes in the DPA. This entailed the implementation of the DPA methods such as the on-shell projection and the boost to the frame in which the polarisation vectors are defined. The main challenge of the extension was the implementation of the NLO corrections. in particular, the NLO EW real-emission contributions with charged resonances. For these processes the massive-resonance counterterms were implemented. With this extension BBMC is capable of computing polarised VBS at NLO QCD and EW accuracy.

To test the used methods, before studying VBS processes, vector-boson pair-production processes were analysed. The lower number of final-state particles and contributing Feynman diagrams makes their computation simpler. As first process I computed polarised ZW^+ production with a leptonically decaying Z boson and a hadronically decaying W^+ boson. To study this process two setups were considered one where the W boson decays into two slim jets (resolved) and one where the W boson decays into one massive fat jet (unresolved). The differences between the two setups from the different jet recombinations were found to give significant effects at LO. When including the NLO QCD corrections, the large contribution from real-emission processes reduced the differences. Therefore, the most significant differences are seen in the K-factors of some differential cross-sections. In both setups the two bosons are strongly boosted enhancing the longitudinal signal compared to more inclusive setups. The main difference to other existing polarisation studies is the hadronically decaying boson. This offers a higher event rate and avoids having to treat part of the W decay as missing transverse momentum. The primary drawbacks are that jets cannot be distinguished by their flavour and that the QCD background can be very large. The shape of the distributions depends greatly on how accurate the selection of the decay jets of the W^+ boson is. Selecting jets as decay jets that do not originate from the W-boson decay adds a background contribution. The misidentification background causes enhancements in otherwise suppressed phase-space regions resulting in large shape changes in both angular and energy observables. The size of this background is found to depend greatly on the studied polarisation state. For the chosen process the TL state features the largest background because of an interplay of the unitarity suppression and the transverse-momentum cut on the jet system. The shape changes of the TL state from misidentification cause the distributions to resemble the ones with a transversely polarised W^+ boson. As seen in the different polarised shapes of

the differential distributions, there are many observables that can be used for discrimination between polarisation states. Even when, as in the unresolved setup, no information on the substructure of the hadronic decay is used, there are many observables that are sensitive to the polarisation of the Z boson. For example the decay angles and the transverse momenta of the charged leptons were found to be suitable for polarisation discrimination. However, resolving the substructure gives access to observables that are sensitive to the decay of the W^+ boson. It has been shown that the decay angle of the leading decay jet is very sensitive to the polarisation of the W^+ boson.

The process studied next was polarised W^+W^- production at the LHC with decays into two different flavour opposite charged leptons. For this process the NLO EW corrections were computed. As the resonant W bosons are electrically charged, the massive-resonance counterterms had to be used to cancel the additional IR singularities. As this process does not have any massless final-state particles, other than the decay particles of the resonances at LO, only a subset of the detailed counterterms were needed for this process. Even though this process features two neutrinos in the final state there are LHC observables, like the angular separation of the positron and muon, suited for the discrimination of the polarised signals. The t-channel top quark present in $b\bar{b}$-induced processes was found to considerably enhance the longitudinal signal. Furthermore, the large negative NLO EW corrections in the tails of energy distributions show the effects from large EW logarithms.

After the study of vector-boson pair-production processes a VBS process was targeted. In VBS the sensitivity to the unitarity cancellations is much greater than for vector-boson pair production making them ideal for testing the Standard Model. The VBS process that was studied here is the scattering of two W^+ bosons. Same-sign W scattering is the VBS process with the cleanest signal, since the backgrounds that complicate other VBS processes are inherently suppressed. For example gluon-induced contributions to the QCD background are only present beyond LO. For this process both the NLO QCD and EW corrections were computed. Compared to vector-boson pair production the hard scattering of VBS processes has two additional final-state quarks; therefore, all massive-resonance counterterms are needed to cancel the IR divergences. Both the QCD and EW corrections were found to be negative. The negative EW corrections are a consequence of large Sudakov logarithms. Furthermore, the size of the NLO EW corrections depends on the polarisation of the W bosons. The correction was found to be the most negative for the TT state and the least negative for the LL state. This is caused by the dependence of the prefactors of the leading double logarithms on the polarisation of the W^+ boson. When the W^+ boson is transversely polarised these prefactors are larger than when the W^+ boson is longitudinally polarised giving the different relative corrections. The effects of the Sudakov logarithms are even more pronounced when analysing energy-type observables because in the high-energy regions they can cause the NLO EW corrections to exceed -40% of the LO. Similarly to W^+W^- production also in W^+W^+ scattering the decays feature two neutrinos that cannot be detected in experiments. Therefore, the decay angle cannot be used as a discriminator for the polarisation states in measurements. However, the different decay kinematics of transverse and longitudinally polarised bosons translate to shape differences in other observables, which are measurable. One of these observables is azimuthal angular separation of the positron and the antimuon. Here the different decay kinematics cause a preference for the positron and the antimuon to be emitted in opposite directions for the TT state. Another observable found to have discriminatory capabilities is the transverse-momentum ratio of the subleading and leading charged

lepton. Here the different decay kinematics manifest in a preference for the decay leptons from longitudinally polarised bosons to have more similar transverse momenta. These observables are ideal candidates to be used in polarisation templates needed for polarisation measurements.

Important advancements have been made to computing polarised di-boson processes with high accuracy. For this thesis only polarised W^+W^+ scattering was computed. In principal also other polarised VBS processes can be computed with the DPA as presented. The method is, however, not yet completely general in the sense that it is not directly applicable to the computation of arbitrary polarised processes. When extending the methods detailed in this thesis for the computation of other polarised VBS processes some of the subtleties may become more important. One of these is the triple-vector-boson production background with the third resonance decaying into jets present in all VBS processes. When the third boson becomes resonant the standard DPA amplitude is singular. Here this was treated by reintroducing the non-zero decay width of the bosons to regulate the divergence. This has the problematic side effect of breaking gauge invariance. For W^+W^+ scattering in the setup here it has been shown that this effect is small. In other VBS processes this does not have to be the case. Therefore to compute polarised cross-sections of other VBS processes a general treatment method that ensures the removal of the singularities while simultaneously conserving gauge invariance is needed. While the process of primary interest has been VBS, the methods can be further extend to processes such as triple-vector-boson production or nested resonances. For the computation of such processes a generalised implementation of the on-shell projection is needed. To summarise, the field of polarised vector bosons still offers many opportunities for advancement in physics.

Appendix A

Mismatch in the local and integrated counterterms

In Section 3.2 it was argued that first applying the subtraction mapping to the off-shell phase-space point and then projecting the reduced momenta on-shell is the preferred method. It was shown that when the subtraction mapping and the on-shell projection are applied in this order the mismatch between the local and integrated counterterms is beyond the intrinsic accuracy of the DPA. In this appendix the reverse order, first applying the on-shell projection and second the subtraction mapping, is analysed. This analysis was already part of Ref. [37]. Here it is shown that this method leads to a mismatch of the local and integrated dipoles. But in contrast to first using the subtraction mapping this approach will give a discrepancy that is not necessarily small and beyond the intrinsic accuracy of the DPA. Therefore, first applying the subtraction mapping is the preferential method.

The argument follows the same partonic process

$$q\,q \to \underbrace{\mu^+(k_1)\,\nu_\mu(k_2)}_{\mathrm{W}^+(k_{12})}\,\underbrace{\mathrm{e}^+(k_3)\,\nu_\mathrm{e}(k_4)}_{\mathrm{W}^+(k_{34})}\,q(k_5)\,q(k_6)\,\gamma(k_7) \tag{A.1}$$

and dipole $\mathcal{D}_{[12]7,5}$ already chosen in Section 3.2. As before any flux factors and symmetry factors are omitted for simplicity. The discussion starts from the subtracted-real contribution $\mathcal{R}-\mathcal{D}$ to the production. Omitting all other counterterms the subtracted-real contribution reads

$$\begin{aligned}(\mathcal{R}-\mathcal{D})_\mathrm{prod} \propto \sum_{\lambda_{12}\lambda_{34}} \Bigg[& \left|\mathcal{M}^{(5)}_{\mathrm{P},\mu\nu}\left(Q;\tilde{k}_{12},\tilde{k}_{34},k_5,k_6,k_7\right)\tilde{\varepsilon}^{\mu,*}_{12}\tilde{\varepsilon}^{\nu,*}_{34}\right|^2 \\ & \times \mathrm{d}\Phi_5\Big(Q;\tilde{k}_{12},\tilde{k}_{34},k_5,k_6,k_7\Big) \\ & - \mathcal{D}_{[12]7,5}(\bar{\tilde{k}}_{12},\bar{k}_5;\tilde{y},\tilde{z},\tilde{\phi})\left|\mathcal{M}^{(4)}_{\mathrm{P},\mu\nu}\left(Q;\bar{\tilde{k}}_{12},\tilde{k}_{34},\bar{k}_5,k_6\right)\tilde{\varepsilon}^{\mu,*}_{12}\tilde{\varepsilon}^{\nu,*}_{34}\right|^2 \\ & \times \mathrm{d}\Phi_\mathrm{rad}\left(\bar{\tilde{k}}_{12}+\bar{k}_5;\tilde{z},\tilde{y},\tilde{\phi}\right)\mathrm{d}\Phi_4\left(Q;\bar{\tilde{k}}_{12},\tilde{k}_{34},\bar{k}_5,k_6\right)\Bigg]\,.\end{aligned} \tag{A.2}$$

The momenta of the two resonances $\tilde{k}_{12}$, $\tilde{k}_{34}$ are projected on-shell. Additionally, as this is only the production sub-process the on-shell phase-space measure is used. As in Section 3.2 the dipole $\mathcal{D}_{[12]7,5}$ regulates the IR singularities associated to a massive final-state resonance

as emitter (here the W boson with momentum $\tilde{k}_{12}$) and a massless final-state spectator with momentum k_5. This is the form of the dipole as used in the literature for radiation off massive final-state particles. Carrying out the integration of the dipole, over the on-shell radiation phase space, results in the integrated dipole that is added back in the DPA calculation.

In the DPA calculation the phase-space integration is performed over the off-shell momenta. The subtracted-real DPA contribution including the decay amplitudes and phase-space measures, when first projecting the momenta on-shell, reads

$$\begin{aligned}
(\mathcal{R}-\mathcal{D})_{\mathrm{DPA}} \propto \sum_{\lambda_{12}\lambda_{34}} \Bigg[& \left| \mathcal{M}^{(5)}_{\mathrm{P},\mu\nu}\left(Q;\tilde{k}_{12},\tilde{k}_{34},k_5,k_6,k_7\right)\tilde{\varepsilon}^{\mu,*}_{12}\tilde{\varepsilon}^{\nu,*}_{34}\right|^2 \\
& \times \mathrm{d}\Phi_5\left(Q;k_{12},k_{34},k_5,k_6,k_7\right) \\
& - \mathcal{D}_{[12]7,5}(\bar{\tilde{k}}_{12},\bar{k}_5;\tilde{y},\tilde{z},\tilde{\phi}) \left|\mathcal{M}^{(4)}_{\mathrm{P},\mu\nu}\left(Q;\bar{\tilde{k}}_{12},\tilde{k}_{34},\bar{k}_5,k_6\right)\tilde{\varepsilon}^{\mu,*}_{12}\tilde{\varepsilon}^{\nu,*}_{34}\right|^2 \\
& \times \mathrm{d}\Phi_{\mathrm{rad}}\left(\bar{k}_{12}+\bar{k}_5;z,y,\phi\right)\mathrm{d}\Phi_4\left(Q;\bar{k}_{12},k_{34},\bar{k}_5,k_6\right)\Bigg] \\
\times & \frac{1}{\mathrm{BW}(k_{12})\,\mathrm{BW}(k_{34})}\left|\tilde{\varepsilon}^{\mu}_{12}\mathcal{M}^{(2)}_{\mathrm{D},\mu}\left(\tilde{k}_{12};\tilde{k}_1,\tilde{k}_2\right)\right|^2\left|\tilde{\varepsilon}^{\mu}_{34}\mathcal{M}^{(2)}_{\mathrm{D},\mu}\left(\tilde{k}_{34};\tilde{k}_3,\tilde{k}_4\right)\right|^2 \\
\times & \frac{\mathrm{d}k^2_{12}}{2\pi}\frac{\mathrm{d}k^2_{34}}{2\pi}\mathrm{d}\Phi_2\left(k_{12};k_1,k_2\right)\mathrm{d}\Phi_2\left(k_{34};k_3,k_4\right)\,.
\end{aligned} \tag{A.3}$$

The Eqs. (A.2) and (A.3) have some differences in particular in the different phase-space measures

$$\mathrm{d}\Phi_5\left(Q;\tilde{k}_{12},\tilde{k}_{34},k_5,k_6,k_7\right) \quad \to \quad \mathrm{d}\Phi_5\left(Q;k_{12},k_{34},k_5,k_6,k_7\right)\,, \tag{A.4}$$

and

$$\begin{aligned}
& \mathrm{d}\Phi_{\mathrm{rad}}\left(\bar{\tilde{k}}_{12}+\bar{k}_5;\tilde{z},\tilde{y},\tilde{\phi}\right)\mathrm{d}\Phi_4\left(Q;\bar{\tilde{k}}_{12},\tilde{k}_{34},\bar{k}_5,k_6\right) \quad \to \\
& \mathrm{d}\Phi_{\mathrm{rad}}\left(\bar{k}_{12}+\bar{k}_5;z,y,\phi\right)\;\mathrm{d}\Phi_4\left(Q;\bar{k}_{12},k_{34},\bar{k}_5,k_6\right)\,.
\end{aligned} \tag{A.5}$$

In the DPA the phase-space integration is performed over the off-shell momenta; therefore, the difference in Eq. (A.4) results in a Jacobian of the on-shell projection. This Jacobian is of the order $\mathcal{O}(M^2_{\mathrm{W}}/k^2_{12})$. Fully differentially this discrepancy is large in particular when the W^+ boson is far off-shell. However, when the integration over the W^+ boson off-shellness k^2_{12} is performed, the Breit-Wigner modulation of the resonant propagator suppresses the far off-shell contributions. Therefore, when studying regions of phase space, which are dominated by the W^+ boson being close to on-shell, this mismatch only gives effects beyond the intrinsic DPA accuracy. The argument for the discrepancy in Eq. (A.5) is more involved as for dipoles that have an intermediate resonance as emitter and/or spectator the on-shell projection and the subtraction mapping do not commute. The IR kernel and the matrix element of the reduced process of the local counterterm are evaluated starting from the on-shell projected real-emission phase-space point. The subtraction mapping is then applied to the on-shell real-emission phase-space point to evaluate the matrix element of the reduced process. In the expressions of the local and integrated counterterms from literature [56], that are reused, the integrated counterterms are evaluated with an on-shell LO phase-space point. For the local counterterms this corresponds to first taking the off-shell phase-space point and applying the subtraction mapping and afterwards projecting it on-shell. As stated before

the used subtraction mapping, the CS-dipole mapping, and the DPA on-shell projection do not commute. Therefore, first applying the on-shell projection leads to a mismatch between the local and integrated counterterms. In contrast to the difference in Eq. (A.5) this one is not beyond the accuracy of the DPA and can be numerically sizeable. This prevents the correct working of the subtraction scheme. This discrepancy could in principle be remedied by introducing the Jacobian of the DPA on-shell mapping. By using the reverse order first using the subtraction mapping and then the on-shell projection this source of discrepancy can be avoided. Using the local and integrated dipoles from the literature with this ordering only results in a mismatch that is beyond the intrinsic accuracy of the DPA.

List of acronyms

ATLAS	A Toroidal LHC Apparatus
CERN	European Organization for Nuclear Research
CKM	Cabibbo-Kobayashi-Maskawa
CM	center of mass
CMS	Compact Muon Solenoid
CS	Catani-Seymour
DPA	double-pole approximation
EW	electroweak
GSW	Glashow-Salam-Weinberg
HL	high-luminosity
IR	infrared
KLN	Kinoshita-Lee-Nauenberg
LHC	Large Hadron Collider
LO	leading-order
LL	longitudinal longitudinal
LT	longitudinal transverse
NLO	next-to-leading-order
NNLO	next-to-next-to-leading-order
PA	pole approximation
PETRA	Positron-Electron-Tandem-Ring Accelerator
PDF	parton-distribution function
PDG	Particle Data Group
PS	parton shower
QCD	quantum chromodynamics
QED	quantum electrodynamics
QFT	quantum field theory
SPS	Super Proton Synchrotron
TL	transverse longitudinal
TPA	triple-pole approximation
TT	transverse transverse
UV	ultraviolet
VBS	vector-boson scattering

List of tables

List of figures

Bibliography

[1] P. A. M. Dirac and N. H. D. Bohr, *The quantum theory of the emission and absorption of radiation*, *Proceedings of the Royal Society of London. Series A, Containing Papers of a Mathematical and Physical Character* **114** (1927) 243–265, [https://royalsocietypublishing.org/doi/pdf/10.1098/rspa.1927.0039].

[2] P. A. M. Dirac, *The quantum theory of the electron*, *Proc. Roy. Soc. Lond. A* **117** (1928) 610–624.

[3] E. Fermi, *Quantum Theory of Radiation*, *Rev. Mod. Phys.* **4** (Jan, 1932) 87–132.

[4] C. D. Anderson, *The Positive Electron*, *Phys. Rev.* **43** (Mar, 1933) 491–494.

[5] F. Bloch and A. Nordsieck, *Note on the radiation field of the electron*, *Phys. Rev.* **52** (Jul, 1937) 54–59.

[6] T. Kinoshita, *Mass singularities of Feynman amplitudes*, *J. Math. Phys.* **3** (1962) 650–677.

[7] T. D. Lee and M. Nauenberg, *Degenerate Systems and Mass Singularities*, *Phys. Rev.* **133** (1964) B1549–B1562.

[8] W. E. Lamb and R. C. Retherford, *Fine Structure of the Hydrogen Atom by a Microwave Method*, *Phys. Rev.* **72** (1947) 241–243.

[9] M. Gell-Mann, *A Schematic Model of Baryons and Mesons*, *Phys. Lett.* **8** (1964) 214–215.

[10] G. Zweig, *An SU(3) model for strong interaction symmetry and its breaking. Version 2*, pp. 22–101. 2, 1964.

[11] H. L. Anderson, E. Fermi, E. A. Long, and D. E. Nagle, *Total Cross Sections of Positive Pions in Hydrogen*, *Phys. Rev.* **85** (Mar, 1952) 936–936.

[12] R. Brandelik, et al., *Evidence for planar events in e^+e^- annihilation at high energies*, *Physics Letters B* **86** (1979) 243–249.

[13] D. P. Barber, et al., *Discovery of Three-Jet Events and a Test of Quantum Chromodynamics at PETRA*, *Phys. Rev. Lett.* **43** (Sep, 1979) 830–833.

[14] C. Berger, et al., *Evidence for gluon bremsstrahlung in e^+e^- annihilations at high energies*, *Physics Letters B* **86** (1979) 418–425.

[15] W. Bartel, et al., *Observation of planar three-jet events in e^+e^- annihilation and evidence for gluon bremsstrahlung*, *Physics Letters B* **91** (1980) 142–147.

[16] E. Fermi, *An attempt of a theory of beta radiation. 1.*, *Z. Phys.* **88** (1934) 161–177.

[17] S. L. Glashow, *Partial Symmetries of Weak Interactions*, *Nucl. Phys.* **22** (1961) 579–588.

[18] S. Weinberg, *A Model of Leptons*, *Phys. Rev. Lett.* **19** (1967) 1264–1266.

[19] A. Salam, *Weak and Electromagnetic Interactions*, *Conf. Proc. C* **680519** (1968) 367–377.

[20] S. L. Glashow, J. Iliopoulos, and L. Maiani, *Weak Interactions with Lepton-Hadron Symmetry*, *Phys. Rev. D* **2** (1970) 1285–1292.

[21] P. Higgs, *Broken symmetries, massless particles and gauge fields*, *Physics Letters* **12** (1964) 132–133.

[22] P. W. Higgs, *Broken symmetries and the masses of gauge bosons*, *Phys. Rev. Lett.* **13** (Oct, 1964) 508–509.

[23] F. Englert and R. Brout, *Broken Symmetry and the Mass of Gauge Vector Mesons*, *Phys. Rev. Lett.* **13** (1964) 321–323.

[24] G. S. Guralnik, C. R. Hagen, and T. W. B. Kibble, *Global conservation laws and massless particles*, *Phys. Rev. Lett.* **13** (Nov, 1964) 585–587.

[25] **UA1** Collaboration, G. Arnison, et al., *Experimental Observation of Isolated Large Transverse Energy Electrons with Associated Missing Energy at $\sqrt{s} = 540$ GeV*, *Physics Letters B* **122** (1983) 103–116.

[26] **UA2** Collaboration, M. Banner, et al., *Observation of Single Isolated Electrons of High Transverse Momentum in Events with Missing Transverse Energy at the CERN anti-p p Collider*, *Physics Letters B* **122** (1983) 476–485.

[27] **UA1** Collaboration, G. Arnison, et al., *Experimental Observation of Lepton Pairs of Invariant Mass Around 95 GeV/c^2 at the CERN SPS Collider*, *Physics Letters B* **126** (1983) 398–410.

[28] **UA2** Collaboration, P. Bagnaia, et al., *Evidence for $Z^0 \to e^+e^-$ at the CERN $\bar{p}p$ Collider*, *Physics Letters B* **129** (1983) 130–140.

[29] **ATLAS** Collaboration, G. Aad et al., *Observation of a new particle in the search for the Standard Model Higgs boson with the ATLAS detector at the LHC*, *Phys. Lett. B* **716** (2012) 1–29, [arXiv:1207.7214].

[30] **CMS** Collaboration, S. Chatrchyan et al., *Observation of a New Boson at a Mass of 125 GeV with the CMS Experiment at the LHC*, *Phys. Lett. B* **716** (2012) 30–61, [arXiv:1207.7235].

[31] J. M. Cornwall, D. N. Levin, and G. Tiktopoulos, *Derivation of Gauge Invariance from High-Energy Unitarity Bounds on the S Matrix*, *Phys. Rev. D* **10** (1974) 1145. [Erratum: Phys. Rev. D 11 (1975) 972].

[32] C. E. Vayonakis, *Born Helicity Amplitudes and Cross-Sections in Nonabelian Gauge Theories*, *Lett. Nuovo Cim.* **17** (1976) 383.

[33] S. Actis, et al., *RECOLA: REcursive Computation of One-Loop Amplitudes*, *Comput. Phys. Commun.* **214** (2017) 140–173, [arXiv:1605.01090].

[34] M. D. Schwartz, *Quantum Field Theory and the Standard Model*. Cambridge University Press, 2013.

[35] C. Itzykson and J. B. Zuber, *Quantum Field Theory*. International Series In Pure and Applied Physics. McGraw-Hill, New York, 1980.

[36] S. Actis, A. Denner, L. Hofer, A. Scharf, and S. Uccirati, *Recursive generation of one-loop amplitudes in the Standard Model*, *JHEP* **04** (2013) 037, [arXiv:1211.6316].

[37] A. Denner, C. Haitz, and G. Pelliccioli, *NLO EW and QCD corrections to polarised same-sign WW scattering at the LHC*, *JHEP* **11** (2024) 115, [arXiv:2409.03620].

[38] A. Denner and S. Dittmaier, *Electroweak Radiative Corrections for Collider Physics*, *Phys. Rept.* **864** (2020) 1–163, [arXiv:1912.06823].

[39] A. Denner and G. Pelliccioli, *NLO EW and QCD corrections to polarized ZZ production in the four-charged-lepton channel at the LHC*, *JHEP* **10** (2021) 097, [arXiv:2107.06579].

[40] R. G. Stuart, *General renormalization of the gauge invariant perturbation expansion near the Z^0 resonance*, *Phys. Lett. B* **272** (1991) 353–358.

[41] R. G. Stuart, *Gauge invariance, analyticity and physical observables at the Z^0 resonance*, *Phys. Lett. B* **262** (1991) 113–119.

[42] A. Aeppli, G. J. van Oldenborgh, and D. Wyler, *Unstable particles in one loop calculations*, *Nucl. Phys. B* **428** (1994) 126–146, [hep-ph/9312212].

[43] A. Denner, S. Dittmaier, M. Roth, and D. Wackeroth, *Electroweak radiative corrections to $e^+e^- \to WW \to 4$ fermions in double-pole approximation: The RACOONWW approach*, *Nucl. Phys. B* **587** (2000) 67–117, [hep-ph/0006307].

[44] W. Beenakker, A. P. Chapovsky, and F. A. Berends, *Non-factorizable corrections to W pair production*, *Phys. Lett.* **B411** (1997) 203–210, [hep-ph/9706339].

[45] A. Denner, S. Dittmaier, and M. Roth, *Non-factorizable photonic corrections to $e^+e^- \to WW \to$ four fermions*, *Nucl. Phys.* **B519** (1998) 39–84, [hep-ph/9710521].

[46] W. Beenakker, A. P. Chapovsky, and F. A. Berends, *Non-factorizable corrections to W pair production: Methods and analytic results*, *Nucl. Phys.* **B508** (1997) 17–63, [hep-ph/9707326].

[47] V. S. Fadin, V. A. Khoze, and A. D. Martin, *Interference radiative phenomena in the production of heavy unstable particles*, *Phys. Rev.* **D49** (1994) 2247–2256.

[48] K. Melnikov and O. I. Yakovlev, *Top near threshold: all α_s corrections are trivial*, *Phys. Lett.* **B324** (1994) 217–223, [hep-ph/9302311].

[49] V. S. Fadin, V. A. Khoze, and A. D. Martin, *How suppressed are the radiative interference effects in heavy instable particle production?*, *Phys. Lett.* **B320** (1994) 141–144, [hep-ph/9309234].

[50] A. Denner, D. Lombardi, and C. Schwan, *Double-pole approximation for leading-order semi-leptonic vector-boson scattering at the LHC*, *JHEP* **08** (2024) 146, [arXiv:2406.12301].

[51] A. Ballestrero, E. Maina, and G. Pelliccioli, *W boson polarization in vector boson scattering at the LHC*, *JHEP* **03** (2018) 170, [arXiv:1710.09339].

[52] A. Denner and G. Pelliccioli, *Polarized electroweak bosons in W^+W^- production at the LHC including NLO QCD effects*, *JHEP* **09** (2020) 164, [arXiv:2006.14867].

[53] A. Denner and G. Pelliccioli, *NLO QCD predictions for doubly-polarized WZ production at the LHC*, *Phys. Lett. B* **814** (2021) 136107, [arXiv:2010.07149].

[54] D. N. Le and J. Baglio, *Doubly-polarized WZ hadronic cross sections at NLO QCD + EW accuracy*, *Eur. Phys. J. C* **82** (2022) 917, [arXiv:2203.01470].

[55] D. N. Le, J. Baglio, and T. N. Dao, *Doubly-polarized WZ hadronic production at NLO QCD+EW: calculation method and further results*, *Eur. Phys. J. C* **82** (2022) 1103, [arXiv:2208.09232].

[56] S. Catani, S. Dittmaier, M. H. Seymour, and Z. Trocsanyi, *The Dipole formalism for next-to-leading order QCD calculations with massive partons*, *Nucl. Phys. B* **627** (2002) 189–265, [hep-ph/0201036].

[57] M. Schönherr, *An automated subtraction of NLO EW infrared divergences*, *Eur. Phys. J. C* **78** (2018) 119, [arXiv:1712.07975].

[58] S. Catani and M. Seymour, *A general algorithm for calculating jet cross-sections in NLO QCD*, *Nucl. Phys. B* **485** (1997) 291–419, [hep-ph/9605323]. [Erratum: Nucl. Phys. B 510 (1998) 503–504].

[59] L. Basso, S. Dittmaier, A. Huss, and L. Oggero, *Techniques for the treatment of IR divergences in decay processes at NLO and application to the top-quark decay*, *Eur. Phys. J. C* **76** (2016) 56, [arXiv:1507.04676].

[60] A. Denner, C. Haitz, and G. Pelliccioli, *NLO EW corrections to polarised W^+W^- production and decay at the LHC*, *Phys. Lett. B* **850** (2024) 138539, [arXiv:2311.16031].

[61] A. Denner, C. Haitz, and G. Pelliccioli, *NLO QCD corrections to polarized diboson production in semileptonic final states*, *Phys. Rev. D* **107** (2023) 053004, [arXiv:2211.09040].

[62] **CMS** Collaboration, S. Chatrchyan et al., *Measurement of the Polarization of W Bosons with Large Transverse Momenta in W+Jets Events at the LHC*, *Phys. Rev. Lett.* **107** (2011) 021802, [arXiv:1104.3829].

[63] **ATLAS** Collaboration, G. Aad et al., *Measurement of the polarisation of W bosons produced with large transverse momentum in pp collisions at $\sqrt{s} = 7$ TeV with the ATLAS experiment*, *Eur. Phys. J.* **C72** (2012) 2001, [arXiv:1203.2165].

[64] **CMS** Collaboration, V. Khachatryan et al., *Angular coefficients of Z bosons produced in pp collisions at $\sqrt{s} = 8$ TeV and decaying to $\mu^+\mu^-$ as a function of transverse momentum and rapidity*, *Phys. Lett.* **B750** (2015) 154–175, [arXiv:1504.03512].

[65] **ATLAS** Collaboration, M. Aaboud et al., *Measurement of the W boson polarisation in $t\bar{t}$ events from pp collisions at $\sqrt{s} = 8$ TeV in the lepton + jets channel with ATLAS*, *Eur. Phys. J. C* **77** (2017) 264, [arXiv:1612.02577]. [Erratum: Eur. Phys. J. C 79 (2019) 19].

[66] **CMS** Collaboration, V. Khachatryan et al., *Measurement of the W boson helicity fractions in the decays of top quark pairs to lepton + jets final states produced in pp collisions at $\sqrt{s} = 8$ TeV*, *Phys. Lett.* **B762** (2016) 512–534, [arXiv:1605.09047].

[67] **ATLAS** Collaboration, G. Aad et al., *Measurement of the angular coefficients in Z-boson events using electron and muon pairs from data taken at $\sqrt{s} = 8$ TeV with the ATLAS detector*, *JHEP* **08** (2016) 159, [arXiv:1606.00689].

[68] **ATLAS** Collaboration, M. Aaboud et al., *Measurement of $W^{\pm}Z$ production cross sections and gauge boson polarisation in pp collisions at $\sqrt{s} = 13$ TeV with the ATLAS detector*, *Eur. Phys. J. C* **79** (2019) 535, [arXiv:1902.05759].

[69] **CMS, ATLAS** Collaboration, G. Aad et al., *Combination of the W boson polarization measurements in top quark decays using ATLAS and CMS data at $\sqrt{s} = 8$ TeV*, *JHEP* **08** (5, 2020) 051, [arXiv:2005.03799].

[70] **CMS** Collaboration, A. Tumasyan et al., *Measurement of the inclusive and differential WZ production cross sections, polarization angles, and triple gauge couplings in pp collisions at $\sqrt{s}$ =13 TeV*, *JHEP* **07** (2022) 032, [arXiv:2110.11231].

[71] **ATLAS** Collaboration, *Observation of gauge boson joint-polarisation states in $W^{\pm}Z$ production from pp collisions at $\sqrt{s} = 13$ TeV with the ATLAS detector*, arXiv:2211.09435.

[72] **CMS** Collaboration, A. M. Sirunyan et al., *Measurements of production cross sections of polarized same-sign W boson pairs in association with two jets in proton-proton collisions at $\sqrt{s} = 13$ TeV*, *Phys. Lett. B* **812** (2021) 136018, [arXiv:2009.09429].

[73] T. Han, D. Krohn, L.-T. Wang, and W. Zhu, *New Physics Signals in Longitudinal Gauge Boson Scattering at the LHC*, *JHEP* **03** (2010) 082, [arXiv:0911.3656].

[74] Z. Bern et al., *Left-handed W bosons at the LHC*, *Phys. Rev.* **D84** (2011) 034008, [arXiv:1103.5445].

[75] W. J. Stirling and E. Vryonidou, *Electroweak gauge boson polarisation at the LHC*, *JHEP* **07** (2012) 124, [arXiv:1204.6427].

[76] A. Belyaev and D. Ross, *What Does the CMS Measurement of W-polarization Tell Us about the Underlying Theory of the Coupling of W-Bosons to Matter?*, *JHEP* **08** (2013) 120, [arXiv:1303.3297].

[77] J. Brehmer, J. Jaeckel, and T. Plehn, *Polarized WW Scattering on the Higgs Pole*, *Phys. Rev. D* **90** (2014) 054023, [arXiv:1404.5951].

[78] J. Searcy, L. Huang, M.-A. Pleier, and J. Zhu, *Determination of the WW polarization fractions in $pp \to W^{\pm}W^{\pm}jj$ using a deep machine learning technique*, *Phys. Rev. D* **93** (2016) 094033, [arXiv:1510.01691].

[79] J. Lee, et al., *Polarization fraction measurement in same-sign WW scattering using deep learning*, *Phys. Rev. D* **99** (2019) 033004, [arXiv:1812.07591].

[80] J. Lee, et al., *Polarization fraction measurement in ZZ scattering using deep learning*, *Phys. Rev. D* **100** (2019) 116010, [arXiv:1908.05196].

[81] S. Brass, C. Fleper, W. Kilian, J. Reuter, and M. Sekulla, *Transversal Modes and Higgs Bosons in Electroweak Vector-Boson Scattering at the LHC*, *Eur. Phys. J. C* **78** (2018) 931, [arXiv:1807.02512].

[82] R. Gauld, A. Gehrmann-De Ridder, T. Gehrmann, E. W. N. Glover, and A. Huss, *Precise predictions for the angular coefficients in Z-boson production at the LHC*, *JHEP* **11** (2017) 003, [arXiv:1708.00008].

[83] R. Frederix and T. Vitos, *Electroweak corrections to the angular coefficients in finite-p_T Z-boson production and dilepton decay*, *Eur. Phys. J. C* **80** (2020) 939, [arXiv:2007.08867].

[84] M. Pellen, R. Poncelet, A. Popescu, and T. Vitos, *Angular coefficients in $W + j$ production at the LHC with high precision*, *Eur. Phys. J. C* **82** (2022) 693, [arXiv:2204.12394].

[85] A. Ballestrero, E. Maina, and G. Pelliccioli, *Polarized vector boson scattering in the fully leptonic WZ and ZZ channels at the LHC*, *JHEP* **09** (2019) 087, [arXiv:1907.04722].

[86] A. Ballestrero, E. Maina, and G. Pelliccioli, *Different polarization definitions in same-sign WW scattering at the LHC*, *Phys. Lett. B* **811** (2020) 135856, [arXiv:2007.07133].

[87] D. Buarque Franzosi, O. Mattelaer, R. Ruiz, and S. Shil, *Automated predictions from polarized matrix elements*, *JHEP* **04** (2020) 082, [arXiv:1912.01725].

[88] R. Poncelet and A. Popescu, *NNLO QCD study of polarised W^+W^- production at the LHC*, *JHEP* **07** (2021) 023, [arXiv:2102.13583].

[89] M. Pellen, R. Poncelet, and A. Popescu, *Polarised W+j production at the LHC: a study at NNLO QCD accuracy*, *JHEP* **02** (2022) 160, [arXiv:2109.14336].

[90] J. Baglio and N. Le Duc, *Fiducial polarization observables in hadronic WZ production: A next-to-leading order QCD+EW study*, *JHEP* **04** (2019) 065, [arXiv:1810.11034].

[91] J. Baglio and N. Le Duc, *Polarization observables in WZ production at the 13 TeV LHC: Inclusive case*, *Commun. Phys.* **30** (2020) 35–47, [arXiv:1910.13746].

[92] Q.-H. Cao, B. Yan, C. P. Yuan, and Y. Zhang, *Probing $Zt\bar{t}$ couplings using Z boson polarization in ZZ production at hadron colliders*, *Phys. Rev. D* **102** (2020) 055010, [arXiv:2004.02031].

[93] E. Maina, *Vector boson polarizations in the decay of the Standard Model Higgs*, *Phys. Lett. B* **818** (2021) 136360, [arXiv:2007.12080].

[94] E. Maina and G. Pelliccioli, *Polarized Z bosons from the decay of a Higgs boson produced in association with two jets at the LHC*, *Eur. Phys. J. C* **81** (2021) 989, [arXiv:2105.07972].

[95] R. Rahaman and R. K. Singh, *Anomalous triple gauge boson couplings in ZZ production at the LHC and the role of Z boson polarizations*, *Nucl. Phys. B* **948** (2019) 114754, [arXiv:1810.11657].

[96] R. Rahaman and R. K. Singh, *Unravelling the anomalous gauge boson couplings in $ZW^{\pm}$ production at the LHC and the role of spin-1 polarizations*, *JHEP* **04** (2020) 075, [arXiv:1911.03111].

[97] R. Rahaman and R. K. Singh, *Breaking down the entire spectrum of spin correlations of a pair of particles involving fermions and gauge bosons*, *Nucl. Phys. B* **984** (2022) 115984, [arXiv:2109.09345].

[98] S. De, V. Rentala, and W. Shepherd, *Measuring the polarization of boosted, hadronic W bosons with jet substructure observables*, arXiv:2008.04318.

[99] T. Kim and A. Martin, *A $W^{\pm}$ polarization analyzer from Deep Neural Networks*, arXiv:2102.05124.

[100] A. Dey and T. Samui, *Jet Substructure and Multivariate Analysis Aid in Polarization Study of Boosted, Hadronic W Fatjet at the LHC*, arXiv:2110.02773.

[101] L. Ricci and M. Riembau, *Energy correlators of hadronically decaying electroweak bosons*, *Phys. Rev. D* **106** (2022) 114010, [arXiv:2207.03511].

[102] V. Cavaliere, R. Les, T. Nitta, and K. Terashi, *HE-LHC prospects for diboson resonance searches and electroweak WW/WZ production via vector boson scattering in the semi-leptonic final states*, arXiv:1812.00841.

[103] J. Roloff, V. Cavaliere, M.-A. Pleier, and L. Xu, *Sensitivity to longitudinal vector boson scattering in semileptonic final states at the HL-LHC*, *Phys. Rev. D* **104** (2021) 093002, [arXiv:2108.00324].

[104] **CMS** Collaboration, A. M. Sirunyan et al., *Search for a heavy resonance decaying into a Z boson and a Z or W boson in 2ℓ2q final states at $\sqrt{s}$ =13 TeV*, *JHEP* **09** (2018) 101, [arXiv:1803.10093].

[105] **ATLAS** Collaboration, M. Aaboud et al., *Combination of searches for heavy resonances decaying into bosonic and leptonic final states using 36 fb^{-1} of proton-proton collision data at $\sqrt{s}$ =13 TeV with the ATLAS detector*, *Phys. Rev. D* **98** (2018) 052008, [arXiv:1808.02380].

[106] **CMS** Collaboration, A. M. Sirunyan et al., *Combination of CMS searches for heavy resonances decaying to pairs of bosons or leptons*, *Phys. Lett. B* **798** (2019) 134952, [arXiv:1906.00057].

[107] **ATLAS** Collaboration, G. Aad et al., *Search for heavy diboson resonances in semileptonic final states in pp collisions at $\sqrt{s}$ = 13 TeV with the ATLAS detector*, *Eur. Phys. J. C* **80** (2020) 1165, [arXiv:2004.14636].

[108] **CMS** Collaboration, A. Tumasyan et al., *Search for heavy resonances decaying to ZZ or ZW and axion-like particles mediating nonresonant ZZ or ZH production at $\sqrt{s}$ =13 TeV*, *JHEP* **04** (2022) 087, [arXiv:2111.13669].

[109] D. Liu and L.-T. Wang, *Prospects for precision measurement of diboson processes in the semileptonic decay channel in future LHC runs*, *Phys. Rev. D* **99** (2019) 055001, [arXiv:1804.08688].

[110] S. Kallweit, J. M. Lindert, S. Pozzorini, and M. Schönherr, *NLO QCD+EW predictions for 2ℓ2ν diboson signatures at the LHC*, *JHEP* **11** (2017) 120, [arXiv:1705.00598].

[111] B. Biedermann, et al., *Next-to-leading-order electroweak corrections to $pp \to W^+W^- \to$ 4 leptons at the LHC*, *JHEP* **06** (2016) 065, [arXiv:1605.03419].

[112] B. Biedermann, A. Denner, S. Dittmaier, L. Hofer, and B. Jäger, *Next-to-leading-order electroweak corrections to the production of four charged leptons at the LHC*, *JHEP* **01** (2017) 033, [arXiv:1611.05338].

[113] B. Biedermann, A. Denner, and L. Hofer, *Next-to-leading-order electroweak corrections to the production of three charged leptons plus missing energy at the LHC*, *JHEP* **10** (2017) 043, [arXiv:1708.06938].

[114] F. Cascioli, et al., *ZZ production at hadron colliders in NNLO QCD*, *Phys.Lett.* **B735** (2014) 311–313, [arXiv:1405.2219].

[115] M. Grazzini, S. Kallweit, and D. Rathlev, *ZZ production at the LHC: fiducial cross sections and distributions in NNLO QCD*, *Phys. Lett.* **B750** (2015) 407–410, [arXiv:1507.06257].

[116] M. Grazzini, S. Kallweit, S. Pozzorini, D. Rathlev, and M. Wiesemann, *W^+W^- production at the LHC: fiducial cross sections and distributions in NNLO QCD*, *JHEP* **08** (2016) 140, [arXiv:1605.02716].

[117] M. Grazzini, S. Kallweit, D. Rathlev, and M. Wiesemann, *$W^{\pm}Z$ production at hadron colliders in NNLO QCD*, *Phys. Lett. B* **761** (2016) 179–183, [arXiv:1604.08576].

[118] G. Heinrich, S. Jahn, S. P. Jones, M. Kerner, and J. Pires, *NNLO predictions for Z-boson pair production at the LHC*, *JHEP* **03** (2018) 142, [arXiv:1710.06294].

[119] M. Grazzini, S. Kallweit, D. Rathlev, and M. Wiesemann, *$W^{\pm}Z$ production at the LHC: fiducial cross sections and distributions in NNLO QCD*, *JHEP* **05** (2017) 139, [arXiv:1703.09065].

[120] S. Kallweit and M. Wiesemann, *ZZ production at the LHC: NNLO predictions for $2\ell 2\nu$ and 4ℓ signatures*, *Phys. Lett.* **B786** (2018) 382–389, [arXiv:1806.05941].

[121] M. Grazzini, S. Kallweit, J. M. Lindert, S. Pozzorini, and M. Wiesemann, *NNLO QCD + NLO EW with Matrix+OpenLoops: precise predictions for vector-boson pair production*, *JHEP* **02** (2020) 087, [arXiv:1912.00068].

[122] F. Caola, K. Melnikov, R. Röntsch, and L. Tancredi, *QCD corrections to W^+W^- production through gluon fusion*, *Phys. Lett. B* **754** (2016) 275–280, [arXiv:1511.08617].

[123] F. Caola, K. Melnikov, R. Röntsch, and L. Tancredi, *QCD corrections to ZZ production in gluon fusion at the LHC*, *Phys. Rev. D* **92** (2015) 094028, [arXiv:1509.06734].

[124] M. Grazzini, S. Kallweit, M. Wiesemann, and J. Y. Yook, *ZZ production at the LHC: NLO QCD corrections to the loop-induced gluon fusion channel*, *JHEP* **03** (2019) 070, [arXiv:1811.09593].

[125] S. Alioli, F. Caola, G. Luisoni, and R. Röntsch, *ZZ production in gluon fusion at NLO matched to parton-shower*, *Phys. Rev. D* **95** (2017) 034042, [arXiv:1609.09719].

[126] E. Re, M. Wiesemann, and G. Zanderighi, *NNLOPS accurate predictions for W^+W^- production*, *JHEP* **12** (2018) 121, [arXiv:1805.09857].

[127] S. Bräuer, A. Denner, M. Pellen, M. Schönherr, and S. Schumann, *Fixed-order and merged parton-shower predictions for WW and WWj production at the LHC including NLO QCD and EW corrections*, *JHEP* **10** (2020) 159, [arXiv:2005.12128].

[128] M. Chiesa, C. Oleari, and E. Re, *NLO QCD+NLO EW corrections to diboson production matched to parton shower*, *Eur. Phys. J. C* **80** (2020) 849, [arXiv:2005.12146].

[129] S. Alioli, et al., *Next-to-next-to-leading order event generation for Z boson pair production matched to parton shower*, *Phys. Lett. B* **818** (2021) 136380, [arXiv:2103.01214].

[130] S. Alioli, S. Ferrario Ravasio, J. M. Lindert, and R. Röntsch, *Four-lepton production in gluon fusion at NLO matched to parton showers*, *Eur. Phys. J. C* **81** (2021) 687, [arXiv:2102.07783].

[131] J. M. Lindert, D. Lombardi, M. Wiesemann, G. Zanderighi, and S. Zanoli, *$W^{\pm}Z$ production at NNLO QCD and NLO EW matched to parton showers with MiNNLO$_{\rm PS}$*, *JHEP* **11** (2022) 036, [arXiv:2208.12660].

[132] S. Groote, J. G. Körner, and P. Tuvike, *$O(\alpha_s)$ Corrections to the Decays of Polarized $W^{\pm}$ and Z Bosons into Massive Quark Pairs*, *Eur. Phys. J. C* **72** (2012) 2177, [arXiv:1204.5295].

[133] S. Groote, J. G. Körner, and P. Tuvike, *Fully analytical $\mathcal{O}(\alpha_s)$ results for on-shell and off-shell polarized W-boson decays into massive quark pairs*, *Eur. Phys. J. C* **73** (2013) 2454, [arXiv:1301.0881].

[134] **Particle Data Group** Collaboration, M. Tanabashi et al., *Review of Particle Physics*, *Phys. Rev. D* **98** (2018) 030001.

[135] D. Bardin, A. Leike, T. Riemann, and M. Sachwitz, *Energy-dependent width effects in e^+e^- annihilation near the Z-boson pole*, *Physics Letters B* **206** (1988) 539–542.

[136] **NNPDF** Collaboration, R. D. Ball et al., *Parton distributions from high-precision collider data*, *Eur. Phys. J. C* **77** (2017) 663, [arXiv:1706.00428].

[137] **NNPDF** Collaboration, V. Bertone, S. Carrazza, N. P. Hartland, and J. Rojo, *Illuminating the photon content of the proton within a global PDF analysis*, *SciPost Phys.* **5** (2018) 008, [arXiv:1712.07053].

[138] A. Buckley, et al., *LHAPDF6: parton density access in the LHC precision era*, *Eur. Phys. J. C* **75** (2015) 132, [arXiv:1412.7420].

[139] S. Dittmaier, *A general approach to photon radiation off fermions*, *Nucl. Phys. B* **565** (2000) 69–122, [hep-ph/9904440].

[140] M. Cacciari, G. P. Salam, and G. Soyez, *The anti-k_t jet clustering algorithm*, *JHEP* **04** (2008) 063, [arXiv:0802.1189].

[141] M. Rubin, G. P. Salam, and S. Sapeta, *Giant QCD K-factors beyond NLO*, *JHEP* **09** (2010) 084, [arXiv:1006.2144].

[142] J. Baglio, N. Le Duc, and M. M. Weber, *Massive gauge boson pair production at the LHC: a next-to-leading order story*, *Phys. Rev. D* **88** (2013) 113005, [arXiv:1307.4331]. [Erratum: Phys. Rev. D 94 (2016) 099902].

[143] M. Klasen and G. Kramer, *Dijet cross-sections at $O(\alpha\alpha_s^2)$ in photon-proton collisions*, *Phys. Lett. B* **366** (1996) 385–393, [hep-ph/9508337].

[144] B. W. Harris and J. F. Owens, *Photoproduction of jets at HERA in next-to-leading order QCD*, *Phys. Rev. D* **56** (1997) 4007–4016, [hep-ph/9704324].

[145] S. Frixione and G. Ridolfi, *Jet photoproduction at HERA*, *Nucl. Phys. B* **507** (1997) 315–333, [hep-ph/9707345].

[146] A. Denner, S. Dittmaier, S. Kallweit, and A. Mück, *Electroweak corrections to Higgs-strahlung off W/Z bosons at the Tevatron and the LHC with HAWK*, *JHEP* **03** (2012) 075, [arXiv:1112.5142].

[147] G. P. Salam and E. Slade, *Cuts for two-body decays at colliders*, *JHEP* **11** (2021) 220, [arXiv:2106.08329].

[148] U. Baur, T. Han, and J. Ohnemus, *Amplitude zeros in $W^{\pm}Z$ production*, *Phys. Rev. Lett.* **72** (1994) 3941–3944, [hep-ph/9403248].

[149] S. S. D. Willenbrock, *Pair Production of W and Z Bosons and the Goldstone Boson Equivalence Theorem*, *Annals Phys.* **186** (1988) 15.

[150] B. W. Lee, C. Quigg, and H. B. Thacker, *Weak Interactions at Very High-Energies: The Role of the Higgs Boson Mass*, *Phys. Rev. D* **16** (1977) 1519.

[151] M. Hoppe, M. Schönherr, and F. Siegert, *Polarised cross sections for vector boson production with Sherpa*, *JHEP* **04** (2024) 001, [arXiv:2310.14803].

[152] F. Caola, K. Melnikov, R. Röntsch, and L. Tancredi, *QCD corrections to W^+W^- production through gluon fusion*, *Physics Letters B* **754** (2016) 275–280.

[153] M. Grazzini, S. Kallweit, S. Pozzorini, D. Rathlev, and M. Wiesemann, *W^+W^- production at the LHC: fiducial cross sections and distributions in NNLO QCD*, *Journal of High Energy Physics* **2016** (Aug., 2016).

[154] Grazzini, M. and Kallweit, S. and Lindert, J.M. and Pozzorini, S. and Wiesemann, M., *NNLO QCD + NLO EW with Matrix+OpenLoops: precise predictions for vector-boson pair production*, *Journal of High Energy Physics* **2020** (Feb., 2020).

[155] Billoni, M. and Dittmaier, S. and Jäger, B. and Speckner, C., *Next-to-leading order electroweak corrections to pp → W+W- → 4 leptons at the LHC in double-pole approximation*, *Journal of High Energy Physics* **2013** (Dec., 2013).

[156] B. Biedermann, et al., *Next-to-leading-order electroweak corrections to $pp \to W^+W^- \to 4$ leptons at the LHC*, *Journal of High Energy Physics* **2016** (June, 2016).

[157] D. Lombardi, M. Wiesemann, and G. Zanderighi, *W^+W^- production at NNLO+PS with MINNLO$_{PS}$*, *JHEP* **11** (2021) 230, [arXiv:2103.12077].

[158] G. Pelliccioli and G. Zanderighi, *Polarised-boson pairs at the LHC with NLOPS accuracy*, *Eur. Phys. J. C* **84** (2024) 16, [arXiv:2311.05220].

[159] P. D. Group, et al., *Review of Particle Physics*, *Progress of Theoretical and Experimental Physics* **2022** (08, 2022) 083C01, [https://academic.oup.com/ptep/article-pdf/2022/8/083C01/49175539/ptac097.pdf].

[160] **CMS Collaboration** Collaboration, A. M. Sirunyan, et al., *W^+W^- boson pair production in proton-proton collisions at $\sqrt{s} = 13$ TeV*, *Phys. Rev. D* **102** (Nov, 2020) 092001.

[161] **ATLAS** Collaboration, M. Aaboud et al., *Measurement of $W^{\pm}W^{\pm}$ vector-boson scattering and limits on anomalous quartic gauge couplings with the ATLAS detector*, *Phys. Rev. D* **96** (2017) 012007, [arXiv:1611.02428].

[162] **CMS** Collaboration, A. M. Sirunyan et al., *Observation of electroweak production of same-sign W boson pairs in the two jet and two same-sign lepton final state in proton-proton collisions at $\sqrt{s} = 13$ TeV*, *Phys. Rev. Lett.* **120** (2018) 081801, [arXiv:1709.05822].

[163] **ATLAS** Collaboration, M. Aaboud et al., *Observation of electroweak production of a same-sign W boson pair in association with two jets in pp collisions at $\sqrt{s} = 13$ TeV with the ATLAS detector*, *Phys. Rev. Lett.* **123** (2019) 161801, [arXiv:1906.03203].

[164] **CMS** Collaboration, A. M. Sirunyan et al., *Measurements of production cross sections of WZ and same-sign WW boson pairs in association with two jets in proton-proton collisions at $\sqrt{s} = 13$ TeV*, *Phys. Lett. B* **809** (2020) 135710, [arXiv:2005.01173].

[165] **ATLAS** Collaboration, G. Aad et al., *Measurement and interpretation of same-sign W boson pair production in association with two jets in pp collisions at $\sqrt{s} = 13$ TeV with the ATLAS detector*, *JHEP* **04** (2024) 026, [arXiv:2312.00420].

[166] **CMS** Collaboration, A. M. Sirunyan et al., *Measurement of vector boson scattering and constraints on anomalous quartic couplings from events with four leptons and two jets in proton–proton collisions at $\sqrt{s} = 13$ TeV*, *Phys. Lett. B* **774** (2017) 682–705, [arXiv:1708.02812].

[167] **ATLAS** Collaboration, G. Aad et al., *Observation of electroweak production of two jets and a Z-boson pair*, *Nature Phys.* **19** (2023) 237–253, [arXiv:2004.10612].

[168] **ATLAS** Collaboration, G. Aad et al., *Differential cross-section measurements of the production of four charged leptons in association with two jets using the ATLAS detector*, *JHEP* **01** (2024) 004, [arXiv:2308.12324].

[169] **ATLAS** Collaboration, M. Aaboud et al., *Observation of electroweak $W^{\pm}Z$ boson pair production in association with two jets in pp collisions at $\sqrt{s} = 13$ TeV with the ATLAS detector*, *Phys. Lett. B* **793** (2019) 469–492, [arXiv:1812.09740].

[170] **CMS** Collaboration, A. M. Sirunyan et al., *Measurement of electroweak WZ boson production and search for new physics in WZ + two jets events in pp collisions at $\sqrt{s} = 13$ TeV*, *Phys. Lett. B* **795** (2019) 281–307, [arXiv:1901.04060].

[171] **ATLAS** Collaboration, G. Aad et al., *Measurements of electroweak $W^{\pm}Z$ boson pair production in association with two jets in pp collisions at $\sqrt{s} = 13$ TeV with the ATLAS detector*, *JHEP* **06** (2024) 192, [arXiv:2403.15296].

[172] **CMS** Collaboration, A. Tumasyan et al., *Observation of electroweak $W^{+}W^{-}$ pair production in association with two jets in proton-proton collisions at $\sqrt{s} = 13$ TeV*, *Phys. Lett. B* **841** (2023) 137495, [arXiv:2205.05711].

[173] **ATLAS** Collaboration, G. Aad et al., *Observation of electroweak production of W^+W^- in association with jets in proton-proton collisions at $\sqrt{s} = 13$ TeV with the ATLAS Detector*, *JHEP* **07** (2024) 254, [arXiv:2403.04869].

[174] **CMS** Collaboration, V. Khachatryan et al., *Study of vector boson scattering and search for new physics in events with two same-sign leptons and two jets*, *Phys. Rev. Lett.* **114** (2015) 051801, [arXiv:1410.6315].

[175] **ATLAS** Collaboration, M. Aaboud et al., *Search for anomalous electroweak production of WW/WZ in association with a high-mass dijet system in pp collisions at $\sqrt{s} = 8$ TeV with the ATLAS detector*, *Phys. Rev. D* **95** (2017) 032001, [arXiv:1609.05122].

[176] **CMS** Collaboration, A. M. Sirunyan et al., *Search for anomalous electroweak production of vector boson pairs in association with two jets in proton-proton collisions at 13 TeV*, *Phys. Lett. B* **798** (2019) 134985, [arXiv:1905.07445].

[177] **ATLAS** Collaboration, G. Aad et al., *Search for the electroweak diboson production in association with a high-mass dijet system in semileptonic final states in pp collisions at $\sqrt{s} = 13$ TeV with the ATLAS detector*, *Phys. Rev. D* **100** (2019) 032007, [arXiv:1905.07714].

[178] **CMS** Collaboration, A. Tumasyan et al., *Evidence for WW/WZ vector boson scattering in the decay channel $\ell\nu qq$ produced in association with two jets in proton-proton collisions at $\sqrt{s} = 13$ TeV*, *Phys. Lett. B* **834** (2022) 137438, [arXiv:2112.05259].

[179] B. Jäger, C. Oleari, and D. Zeppenfeld, *Next-to-leading order QCD corrections to W^+W^- production via vector-boson fusion*, *JHEP* **07** (2006) 015, [hep-ph/0603177].

[180] B. Jäger, C. Oleari, and D. Zeppenfeld, *Next-to-leading order QCD corrections to Z boson pair production via vector-boson fusion*, *Phys. Rev. D* **73** (2006) 113006, [hep-ph/0604200].

[181] G. Bozzi, B. Jäger, C. Oleari, and D. Zeppenfeld, *Next-to-leading order QCD corrections to W^+Z and W^-Z production via vector-boson fusion*, *Phys. Rev. D* **75** (2007) 073004, [hep-ph/0701105].

[182] B. Jäger, C. Oleari, and D. Zeppenfeld, *Next-to-leading order QCD corrections to W^+W^+jj and W^-W^-jj production via weak-boson fusion*, *Phys. Rev. D* **80** (2009) 034022, [arXiv:0907.0580].

[183] A. Denner, L. Hošeková, and S. Kallweit, *NLO QCD corrections to W^+W^+jj production in vector-boson fusion at the LHC*, *Phys. Rev. D* **86** (2012) 114014, [arXiv:1209.2389].

[184] B. Biedermann, A. Denner, and M. Pellen, *Complete NLO corrections to W^+W^+ scattering and its irreducible background at the LHC*, *JHEP* **10** (2017) 124, [arXiv:1708.00268].

[185] A. Ballestrero et al., *Precise predictions for same-sign W-boson scattering at the LHC*, *Eur. Phys. J. C* **78** (2018) 671, [arXiv:1803.07943].

[186] A. Denner, S. Dittmaier, P. Maierhöfer, M. Pellen, and C. Schwan, *QCD and electroweak corrections to WZ scattering at the LHC*, *JHEP* **06** (2019) 067, [arXiv:1904.00882].

[187] A. Denner, R. Franken, M. Pellen, and T. Schmidt, *NLO QCD and EW corrections to vector-boson scattering into ZZ at the LHC*, *JHEP* **11** (2020) 110, [arXiv:2009.00411].

[188] A. Denner, R. Franken, M. Pellen, and T. Schmidt, *Full NLO predictions for vector-boson scattering into Z bosons and its irreducible background at the LHC*, *JHEP* **10** (2021) 228, [arXiv:2107.10688].

[189] A. Denner, R. Franken, T. Schmidt, and C. Schwan, *NLO QCD and EW corrections to vector-boson scattering into W^+W^- at the LHC*, *JHEP* **06** (2022) 098, [arXiv:2202.10844].

[190] S. Dittmaier, P. Maierhöfer, C. Schwan, and R. Winterhalder, *Like-sign W-boson scattering at the LHC — approximations and full next-to-leading-order predictions*, *JHEP* **11** (2023) 022, [arXiv:2308.16716].

[191] B. Biedermann, A. Denner, and M. Pellen, *Large electroweak corrections to vector-boson scattering at the Large Hadron Collider*, *Phys. Rev. Lett.* **118** (2017) 261801, [arXiv:1611.02951].

[192] B. Jäger and G. Zanderighi, *NLO corrections to electroweak and QCD production of W^+W^+ plus two jets in the POWHEGBOX*, *JHEP* **11** (2011) 055, [arXiv:1108.0864].

[193] B. Jäger and G. Zanderighi, *Electroweak W^+W^-jj prodution at NLO in QCD matched with parton shower in the POWHEG-BOX*, *JHEP* **04** (2013) 024, [arXiv:1301.1695].

[194] B. Jäger, A. Karlberg, and G. Zanderighi, *Electroweak $ZZjj$ production in the Standard Model and beyond in the POWHEG-BOX V2*, *JHEP* **03** (2014) 141, [arXiv:1312.3252].

[195] M. Rauch and S. Plätzer, *Parton Shower Matching Systematics in Vector-Boson-Fusion WW Production*, *Eur. Phys. J. C* **77** (2017) 293, [arXiv:1605.07851].

[196] B. Jäger, A. Karlberg, and J. Scheller, *Parton-shower effects in electroweak $WZjj$ production at the next-to-leading order of QCD*, *Eur. Phys. J. C* **79** (2019) 226, [arXiv:1812.05118].

[197] B. Jäger, A. Karlberg, and S. Reinhardt, *QCD effects in electroweak $WZjj$ production at current and future hadron colliders*, *Eur. Phys. J. C* **84** (2024) 587, [arXiv:2403.12192].

[198] J. Baglio et al., *Release Note – VBFNLO 3.0*, arXiv:2405.06990.

[199] B. Jäger and S. L. P. Chavez, *Electroweak W^+W^+ production in association with three jets at NLO QCD matched with parton shower*, arXiv:2408.12314.

[200] M. Chiesa, A. Denner, J.-N. Lang, and M. Pellen, *An event generator for same-sign W-boson scattering at the LHC including electroweak corrections*, *Eur. Phys. J.* **C79** (2019) 788, [arXiv:1906.01863].

[201] A. Ballestrero, A. Belhouari, G. Bevilacqua, V. Kashkan, and E. Maina, *PHANTOM: A Monte Carlo event generator for six parton final states at high energy colliders*, *Comput.Phys.Commun.* **180** (2009) 401–417, [arXiv:0801.3359].

[202] J. Alwall, et al., *The automated computation of tree-level and next-to-leading order differential cross sections, and their matching to parton shower simulations*, *JHEP* **07** (2014) 079, [arXiv:1405.0301].

[203] **Sherpa** Collaboration, E. Bothmann et al., *Event Generation with Sherpa 2.2*, *SciPost Phys.* **7** (2019) 034, [arXiv:1905.09127].

[204] S. Dittmaier and M. Krämer, *Electroweak radiative corrections to W boson production at hadron colliders*, *Phys. Rev. D* **65** (2002) 073007, [hep-ph/0109062].

[205] A. Denner, S. Dittmaier, M. Roth, and L. Wieders, *Electroweak corrections to charged-current $e^+e^- \to 4$ fermion processes: Technical details and further results*, *Nucl. Phys. B* **724** (2005) 247–294, [hep-ph/0505042]. [Erratum: Nucl. Phys. B 854 (2012) 504].

[206] A. Denner and S. Dittmaier, *The Complex-mass scheme for perturbative calculations with unstable particles*, *Nucl. Phys. B Proc. Suppl.* **160** (2006) 22–26, [hep-ph/0605312].

[207] **NNPDF** Collaboration, R. D. Ball et al., *Photons in the proton: implications for the LHC*, *Eur. Phys. J. C* **84** (2024) 540, [arXiv:2401.08749].

[208] A. Denner and S. Pozzorini, *One-loop leading logarithms in electroweak radiative corrections. 1. Results*, *Eur. Phys. J.* **C18** (2001) 461–480, [hep-ph/0010201].

[209] D. Graudenz, *Next-to-leading order QCD corrections to jet cross-sections and jet rates in deeply inelastic electron proton scattering*, *Phys. Rev. D* **49** (1994) 3291–3319, [hep-ph/9307311].

Danksagung

Zu Schluss meiner Arbeit möchte ich die Gelegenheit nutzen, um mich bei allen zu bedanken, die mich während meiner Promotion in den letzten vier Jahren begleitet und tatkräftig unterstützt haben.

Zunächst möchte ich ein großes Dankeschön an meinen Doktorvater und Chef Prof. Ansgar Denner aussprechen. Durch deine Geduld und fachliche Kompetenz hast du mir einen einzigartigen Weg ermöglicht. Du hattest immer ein offenes Ohr und Zeit für Fragen, was mich stetig beeindruckt und motiviert hat.

Darüber hinaus möchte ich mich bei der ganzen Arbeitsgruppe des TP II bedanken. Die angenehme Arbeitsatmosphäre und anregenden fachlichen und nicht fachlichen Unterhaltungen haben die Zeit wie im Flug vergehen lassen. Für die enge Zusammenarbeit und die Einführung in die Polarisation bedanke ich mich bei Dr. Giovanni Pelliccioli, für die Einarbeitung in den BBMC Code und Anregungen zu meinem Manuskript bei Dr. Robert Franken sowie für die Erläuterung zum korrekten Umgang mit git und gutem Programmierstil bei Dr. Christopher Schwan. Des weiteren möchte ich mich bei Dr. Timo Schmidt, Dr. Benjamin Summ, Dr. Daniele Lombardi, Dr. Stefan Rode, Dr. Santiago Lopez Portillo Chavez, Luís Miguel Lourenço Marques und Monika Alexandra Wüst für die vielen gesellige Abende entweder beim Sport oder beim Spielen bedanken.

Während der Promotion gab es nicht nur wissenschaftliche Fragestellungen, die beantwortet werden wollten. Deshalb bedanke ich mich hiermit herzlich bei Karina Zink für die stetige Hilfe beim Überwinden der administrativen Hürden.

Zuletzt geht noch ein großer Dank an meine Familie − für den fortwährenden Rückhalt und bei Fragestellungen außerhalb der Physik.

Es war mir eine Ehre mit euch allen diesen Weg zu gehen und freue mich zu sehen wie es für uns weiter geht.